TOWARDS A METHODOLOGY FOR THE PREDICTION OF FLAME EXTINCTION AND SUPPRESSION IN THREE-DIMENSIONAL NORMAL AND MICROGRAVITY ENVIRONMENTS

Jason A. Sutula

Doctor of Philosophy

The University of Edinburgh

2008

This work is dedicated to my wife, Rebecca E. Sutula. Without your support this thesis would never have been completed. Thank you.

Declaration

This thesis and the research described and reported within have been completed solely by Jason A. Sutula under the supervision of Professor Jose L. Torero, Dr. Stephen Welch, and Dr. Richard J. Roby. Where other sources are quoted, full references are given.

Jason A. Sutula
December, 2008

Abstract

The probability of a fire occurring in space vehicles and facilities is amplified by the amounts of electrical equipment used. Additionally, the lack of egress for space personnel and irreplaceable resources used aboard space vehicles and facilities require a rapid response of a suppression system and quick extinguishment. Current experimental means that exist to gather data in space vehicles and facilities are limited by both size of the experiment and cost. Thus, more economical solutions must be considered. The aim of this research was to develop a reliable and inexpensive methodology for the prediction of flame extinction and suppression in any three-dimensional environment. This project was split into two parts. Part one included the identification and validation of a computational model for the prediction of gas dispersion. Part two involved the development of an analytical parameter for predicting flame extinction. For model validation, an experimental apparatus was constructed. The experimental apparatus was one-eighth of the volume of electronics racks found aboard typical space facilities. The experimental apparatus allowed for the addition of parallel plates to increase the complexity of the geometry. Data acquisition consisted of gas concentration measurements through planar laser-induced fluorescence (PLIF) of nitrogen dioxide and velocity field measurements through particle image velocimetry (PIV). A theoretical framework for a generalized Damköhler number for the prediction of local flame extinction was also developed. Based on complexities in this parameter, the computational code FLUENT was determined to be the ideal means for predicting this quantity. The concentration and velocity field measurements provided validation data for the modelling analysis. Comparison of the modelling analysis with experimental data demonstrated that the FLUENT code adequately predicted the transport of gas to a remote location. The

FLUENT code was also used to predict gas transport at microgravity conditions. The model demonstrated that buoyancy decreases the time to achieve higher gas concentrations between the parallel plates. As an example of the use of this methodology for a combustion scenario, the model was used to predict flame extinction in a blow-off case (i.e., rapid increase in strain rate) and localized flame extinction (i.e., flame shrinking) in a low-strain dilution case with carbon dioxide over time. The model predictions demonstrated the potential of this methodology with a Damköhler number for the prediction of extinction in three-dimensional environments.

Publications

Conference Papers

Sutula, J., Klassen, M., Roby, R, Olenick, S., Gaines, G. and Torero, J., "Flame Extinction Based on a Critical Damköhler Number for the Assessment of Suppression Effectiveness in Reduced Gravity Environments," Proceedings of the 5th International Seminar on Fire and Explosion Hazards, Edinburgh, Scotland, April 23-27, 2007.

Acknowledgements

I would first like to thank my supervisor, Professor Jose Torero, for his offer to start this fantastic voyage several years ago as well as for his advice, guidance, and, of course, patience. I would also like to thank my industrial supervisor, Dr. Richard Roby, for his support, suggestions, guidance, and mentorship on this project as well as many other mutual projects we have completed with Combustion Science & Engineering, Inc.

In consort with Dr. Roby, Dr. Michael Klassen and Douglas Carpenter of Combustion Science & Engineering, Inc. have provided patience, understanding, advice, and fiscal support throughout the duration of this project. Words cannot describe how grateful I am to all of you for your generosity.

I would very much like to thank Glenn Gaines for his heroic efforts and late hours in the laboratory with an Nd:YAG laser and a bottle of nitrogen dioxide in order to provide the nitrogen dioxide concentration measurements used in this study. Similarly, I am extremely grateful to Adam Cowlard, Hubert Biteau, Dr. Pedro Reszka, and Angus Law who generously contributed their time and support to provide the particle image velocimetry measurements without which this project would not have come to fruition.

Ravi Bikkani has been instrumental in providing support and guidance as a master in the realm of computational fluid dynamics. My appreciation for your help in assuring that the FLUENT runs were set up appropriately is beyond measure.

Additional, I want to thank Darin Viehe for his work building the mesh of the FLUENT model.

I would also like to thank Dr. Stephen Welch as co-supervisor for his guidance as well as everyone in the Fire Group at the University of Edinburgh who I have had the great pleasure of getting to know.

To my friends and family who have missed me over the last few years, I want to thank you all for the understanding and support you have given to me while I have dedicated a large portion of my life to this project.

Finally, I want to thank Dr. Gary Ruff, technical monitor, and the United States of America National Aeronautics and Space Administration (NASA) for their support of this work through contract #NNC04CB35C.

Contents

List of Figures

List of Tables

Nomenclature

A	pre-exponential constant (1/s)
a	acceleration (m/s^2)
a	stoichiometric coefficient, strain rate (1/s)
$\grave{a}$	stoichiometric coefficient
B	B-number
$\bar{B}$	frequency factor of the reaction
B_i	body force per unit volume (N/m^3)
C	specific heat (J/kg·K)
C_p	specific heat at constant pressure (J/kg·K)
D	molecular diffusivity (m^2/s)
D_1	first Damköhler number
D_a	Damköhler number derived in present study
d	diameter (m)
E	activation energy (J)
F	force (N)
Fr	Froude number
g	acceleration due to gravity (9.807 m/s^2)
$\dot{H}$	heat generation rate per unit volume by chemical reaction (W/m^3)
ΔH°	heat of reaction per unit mass (J/kg)
ΔH_c	heat of combustion (J/kg)
H_o	the net heat of combustion of the solid (J/kg)
h	enthalpy (J/kg), convective heat transfer coefficient (W/m^2·K)

h_L	flame height
k	thermal conductivity (W/m^2·K)
L	the heat required to produce the volatiles under steady burning conditions (J)
L_c	characteristic length (m)
l	integral scale of turbulence
$\dot{M}$	mass generation rate of species per unit volume (kg/s/m^3)
$\dot{m}$	mass flux of species per unit area (kg/s/m^2)
$\dot{m}"_c$	the critical rate of flow of fuel from the surface per unit area (kg/s/m^2)
m	mass (kg), sum of the molecular weights
m_{fs}	mass of fuel vapor just above the liquid surface per unit mass (kg)
m_{og}	mass of oxygen in the gas distant from the liquid surface per unit mass (kg)
MW	molecular weight (g/mol)
P	pressure (N/m^2)
Q	volumetric flow rate (m^3/s), heat transferred from the flame to the liquid surface per unit mass of liquid evaporated (J/kg), heat release (J)
q	heat flux due to conduction (W/m^2)
R	Universal gas constant (8.315 J/mol·K)
R_a	the heat transfer to the burning surface of the fuel other than by convection
R_s	the heat transfer from the surfaces of the burning fuel to the environment
Re	Reynolds number
r, θ, z	radial coordinates
r	radius (m), mass of oxygen required to completely burn a unit mass of flammable vapor (kg)
S	the net sensible heat that enters the fuel in unit time (J/s)
S_c	critical value of the net sensible heat that enters the fuel in unit time

	(J/s)
T	temperature (°C) and (K)
$\hat{T}_r$	maximum achievable flame temperature (°C) and (K)
t	time (s)
U'	intensity of turbulence
U_c	characteristic velocity (m/s)
u	velocity component (m/s)
V	velocity (m/s)
v_i	stoichiometric coefficient
x, y, z	Cartesian coordinates
x	distance (m), thickness (m)
Y	species mass fraction (kg/kg)
Z	region Z, mixture fraction

Greek letters

α	thermal diffusivity (m^2/s)
ε	turbulent eddy diffusivity (m^2/s)
$\bar{\theta}$	dimensionless activation temperature of the reaction
λ_f	the heat that needs to enter the fuel to produce a unit mass of vapor (J)
μ	viscosity (kg/s·m)
π	pi
ρ	mass density (kg/m^3)
σ	surface stress (N/m^2)
ϕ	maximum fraction of the heat of combustion that the flame reaction zone may lose to the fuel surface by convection
ω	reaction rate term

Subscripts

a	species a

b	species b
c	critical
crit	critical
F	flame
f	fuel
g	gas
H	heat transfer
i	the i^{th} species
M	mass transfer
o	oxidizer
p	pressure
$react$	reaction zone where fuel and oxidizer begin to mix
s	surface
$Turb$	turbulent fuel jet
x, y, z	Cartesian coordinates
Z	mixture fraction
∞	ambient gas conditions
0	initial conditions

Superscripts

m	reaction order exponent for the oxidizer
n	reaction order exponent for the fuel
$*$	dimensionless quantity
$'$	dimensionless quantity

Accents

$\vec{}$	vector form
$\dot{}$	rate quantity
$\bar{}$	dimensionless quantity

Chapter One

1. Introduction

1.1. Background to the Project

There are increasing global efforts to explore and conduct research in space via manned and unmanned missions. As the quantity of both human life and supporting equipment continues to expand into extraterrestrial environments, so will the likelihood of a potentially life-threatening fire occurring within current (or proposed) space facilities and space vehicles. Therefore, a need exists to understand the nature of the behavior of fire in microgravity conditions at a fundamental level.

Space facilities and space vehicles rely on large amounts of electronics and electrical equipment to sustain operability. The electronics provide a potential ignition source of fire when coupled with the close proximity of potential fuel packages such as electric cable insulation. Examples already exist of fire incidents that have resulted from these potentially hazardous situations. In the United States of America Shuttle Orbiter missions, five documented fires have already occurred [1]. In all of these incidents, the fire was precipitated by an electrical or electric component failure, which resulted in smoldering and charring of electrical components.

Even though fire detection systems are present aboard the Shuttle Orbiter, the detection systems did not activate during any of the reported fires. In the majority of the incidents, the crew detected the fire by the odor of the smoldering material and traced the smell to the location of the fire [1]. Further complicating the problem of the lack of detection system response is the knowledge of six smoke detector false alarms and five smoke detector test failures during Shuttle Orbiter missions [1].

Fires that occur in space facilities and space vehicles do not have to be large to cause serious damage to the environment and to place the crew in danger. Small amounts of soot and chlorinated products of combustion can short-circuit electrical components and cause the corrosion of others [2]. Due to the compact environments

and lack of egress options available to the crew in space facilities and space vehicles, any damage that threatens life-support systems is unacceptable.

In each of the previous Shuttle Orbiter fires, the crew recognized the problem immediately and responded by isolating the affected systems and removing power to those locations. If the fire had occurred in a system that was not routinely monitored by the on-board crew, ground-based system monitors would have performed the same role [1]. Both on-board crew and ground-based crew have access to the currently available means of extinguishment: carbon dioxide (CO_2). Carbon dioxide is stored in stand-alone tanks near protected equipment. Additionally, CO_2 is located in portable extinguishers, which the crew can potentially use in areas where a problem exists. Both the stand-alone systems and the portable extinguishers are designed to deliver a total flooding concentration of 50% to any given volume [1]. Thus, the current suppression system depends on the reliable, early detection of a fire and the proper delivery of CO_2 suppressant to the fuel/fire interface.

1.2. Overview of Microgravity Experimentation Methods

The ability to conduct research in a microgravity environment is severely limited. Current research facilities allow for the gathering of microgravity data by four different means: drop tower tests, low-gravity aircraft, sounding rocket, or aboard a space vehicle or space station [3]. All of these options impose restrictions on the type of research being conducted. The drop tower tests allow for the sampling of very short time scales of data (2.2 seconds to 5.2 seconds) over small, compact test equipment [3]. The aircraft tests provide longer durations (approximately 25 seconds) [3], but physical space is limited aboard the aircraft and experimentation is again limited by size. Sounding rocket tests can allow for upwards of 500 seconds of achievable microgravity conditions [3], yet the significant cost of conducting experiments within a sounding rocket can be prohibitive.

The longest achievable microgravity duration is available aboard space vehicles and space facilities (e.g., the Shuttle Orbiter and the International Space Station). While in stable orbit, space vehicles and space facilities achieve 0.1 x 10^{-6} g_e [3]. These levels are ideal for microgravity research. Unfortunately, the cost of conducting research in space vehicles and space facilities is even more prohibitive than conducting experiments using sounding rocket. Additionally, due to the high costs associated with space-based research, the use of space vehicles and space facilities is regulated by international governments, which results in long, competitive processes to have a particular experiment considered for flight on a Shuttle Orbiter Mission or aboard the International Space Station.

In general, microgravity research has been composed of three general branches of investigation. First, research has been conducted that has examined the general structure of various flames in microgravity. Second, research has been conducted on flame extinction limits due to increasing or decreasing flow rates of fuel and oxidizer. Third, research has investigated the insertion of various suppressant gases into the combustion flow field through air or fuel streams. While important for increasing the knowledge base, the existing constraints on the ability to gather microgravity combustion data have resulted only in large amounts of small-scale data. This has contributed greatly to the overall understanding of flame extinction, but large-scale microgravity research of fire behavior is lacking.

With regard to the effectiveness of microgravity flame suppression, the focus of the current areas of microgravity combustion research has been solely on suppression agent effectiveness and the resultant flame structure implications. The research has not considered the aspect of the problem that deals with delivery of the suppressant to the fire, especially in non-idealized, three-dimensional geometric conditions (e.g., a fire starting and burning within a Shuttle Orbiter or International Space Station electrical rack). It is clear that both issues cannot be completely uncoupled, since adequate delivery implies having a delivery device at a correct location to provide enough suppressant gas to extinguish the flame.

1.3. Aims of the Research

The experimental means that currently exist to produce microgravity combustion data are limited by both size of the experiment and cost. Thus, more economical solutions must be considered in the effort to better understand both the suppressant dispersion and flame extinction aspects of the problem.

This project will demonstrate that the use of a validated computational fluid dynamics (CFD) model will accurately predict suppressant dispersion in a complex three-dimensional environment. This project will also demonstrate that an analytical parameter can be developed and coupled with the suppressant dispersion predictions to create a three-dimensional mapping of regions where the conditions for flame extinction are favorable after suppressant delivery. The combined use of computational modelling for the transport aspect of the problem and the use of an analytical parameter to address the flame extinction aspect of the problem will comprise a generalized methodology for the prediction of flame extinction and suppression in any three-dimensional environment.

1.4. Outline of Chapters

Chapter 2

Overview of Diffusion Flames

An overview is provided of diffusion flames with emphasis placed on the structure and analyses of the classical jet diffusion and counter-flow flames. The differences between a laminar diffusion flame and a turbulent diffusion flame are also presented. Additionally, the effects of microgravity conditions on a diffusion flame are examined.

Chapter 3
Fire Suppression and Flame Extinction

The concepts of fire suppression and flame extinction are reviewed, with emphasis being given to the flame extinction of diffusion flames. Traditional flame extinction research is presented via four categories: an asymptotic analysis for flame ignition and extinction, a critical flame temperature for extinction, a critical mass flux of fuel from the surface of the burning material necessary to sustain the flame reaction, and a critical scalar dissipation rate for extinction. Several studies that outline these approaches are examined. Also, a review of current microgravity research, with an emphasis on flame suppression and extinction through the use of Halon alternatives, carbon dioxide, nitrogen, and water mist, is discussed.

Chapter 4
Theoretical Framework

The theoretical framework for the development of a generalized Damköhler number that can be used to predict local flame extinction in any modelled three-dimensional volume is introduced. The development of the conservation of mass, momentum, species, and energy equations is presented, with the emphasis placed on a nonspecific flame in a three-dimensional geometry. Finally, an examination of the characteristic variables within the Damköhler number is provided.

Chapter 5
Experimental Setup

The experimental apparatus and various data acquisition methods used to obtain validation data for this study are described. Additionally, detailed descriptions of the experimental apparatus and the procedures conducted for both a planar laser-induced fluorescence (PLIF) measurement technique and a particle image velocimetry (PIV) measurement technique are provided. An overview of the various data reduction methods is also discussed.

Chapter 6

Experimental Results

The results of the experimental studies utilizing PLIF measurements to determine the resultant average concentration of nitrogen dioxide at various locations between parallel plates in the experimental apparatus are provided. The results of the experimental studies utilizing PIV measurements to determine the velocity flow field of a specific location between the center of the parallel plates and the resultant average velocity of several point measurement locations are also presented.

Chapter 7

Model Development

A background discussion is presented on the use of computational fluid dynamics as a tool for the prediction of various physical phenomena in the scientific and engineering community. A brief review describing the FLUENT code, in particular, is then provided. Finally, a discussion of the variables used to create a model for the current problem using FLUENT is offered.

Chapter 8

Model Comparison and Discussion

A comparison of the experimental data and the modelling predictions using FLUENT is presented. The FLUENT model is expanded to include a combustion problem with gaseous suppression, which is then described. The modelling results of the combustion problem with gaseous suppression are provided. The results demonstrate that the FLUENT code can adequately predict the transport of a gaseous suppressant to a flame in a three-dimensional environment and that the use of the Damköhler number as an analysis parameter in a methodology for the prediction of flame extinction in any three-dimensional environment is a valid approach.

Chapter 9

Conclusions and Further Work

A summary of the work conducted, the results of the experimental and computational work performed, and the conclusions for this project are presented. Ideas for further research direction and goals are discussed.

Chapter Two

2. Overview of Diffusion Flames

2.1. Introduction

The suppression of fire has been and remains a concern when dealing with any naturally occurring fire found in normal or microgravity. The majority of all naturally occurring fires are diffusion flames. In a diffusion flame, as opposed to a premixed flame, the fuel and the oxidizer are initially separated. As the reaction begins, the fuel and the oxidizer must flow towards each other and mix in the same region where the reaction takes place. In general, the combustion depends more on the rate of the mixing of the fuel and oxidizer than it does on the chemical processes involved. The flame occurs where the proportion of the fuel and oxidizer come together within the flammability limits of the reaction mixture.

Diffusion flames exist readily in terrestrial or extraterrestrial environments. Pool fires, campfires, candle flames, flames from gas appliances, and even unwanted wire insulation flames are a few examples of fires that are diffusion flames. An understanding of diffusion flames and their structure is necessary when examining the interaction of fire and suppressant. Chapter 2 provides an overview of diffusion flames and the influences both normal gravity and microgravity have on their structure and behavior.

2.2. Laminar Diffusion Flames

When a diffusion flame is relatively small, the region where the combustion reaction is occurring can appear to be smooth and steady. This smooth and steady flame is commonly referred to as “laminar.” The flow rates of the reactants into the mixing zone are responsible for the laminar nature of the flame. A laminar flame will typically have a low flow rate of reactants into the reaction zone. If the flow rate of the reactants is increased, the flame can become “turbulent.”

Specific types of diffusion flames have been extensively researched to determine the physics and structure of flames. Some of the more common analyses are presented

in various compilation texts [4, 5, 6]. The two main types that have been examined are the laminar fuel jet diffusion flame and the counter-flow (also commonly referred to as opposed-flow) diffusion flame. The laminar fuel jet diffusion flame is produced when a gaseous fuel is ejected from a cylindrical tube into a quiescent oxidizer. This flame configuration allows for a detailed analysis of its structure, both experimentally and computationally. The counter-flow diffusion flame is more complex to establish experimentally, but when created, it produces a stable flame where the overall structure can be examined in detail.

2.2.1. Fuel Jet Diffusion Flame

The shape of a burning laminar fuel jet depends on the environment into which the fuel is being released [4, 5, 6]. If a gaseous fuel jet is released into a quiescent oxidizer and burned, the overall shape of the flame will be a "closed" flame similar to the shape of a candle flame or a Bunsen burner flame. This type of flame is similar to a flame produced from a cylindrical fuel inlet surrounded by an over-ventilated co-flow of air. Figure 2.1 depicts a diagram of a gaseous fuel jet flame in over-ventilated and under-ventilated cylindrical co-flow conditions.

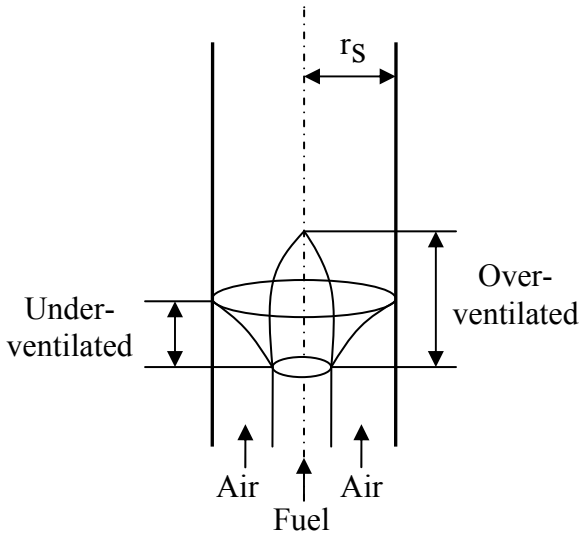

Figure 2.1: Diagram of a gaseous fuel jet flame from a cylindrical co-flow (after Glassman [4]).

If the co-flow of air is large enough to exceed the stoichiometric amount of air necessary for complete combustion, the flame will appear to have a closed shape. If the co-flow of air does not exceed the necessary stoichiometric amount of air needed for combustion, the flame surface will "open" towards the boundaries of the co-flow containment [4].

An analysis of the structure of the open shaped under-ventilated flame is not practical due to the shape, but the over-ventilated closed flame structure has been analyzed in detail [4]. The most significant analyses are of the reactant and product components at various points in the flame and the temperature profile within the flame. Figure 2.2 shows a generalized concentration profile in cross-section through a gaseous fuel jet.

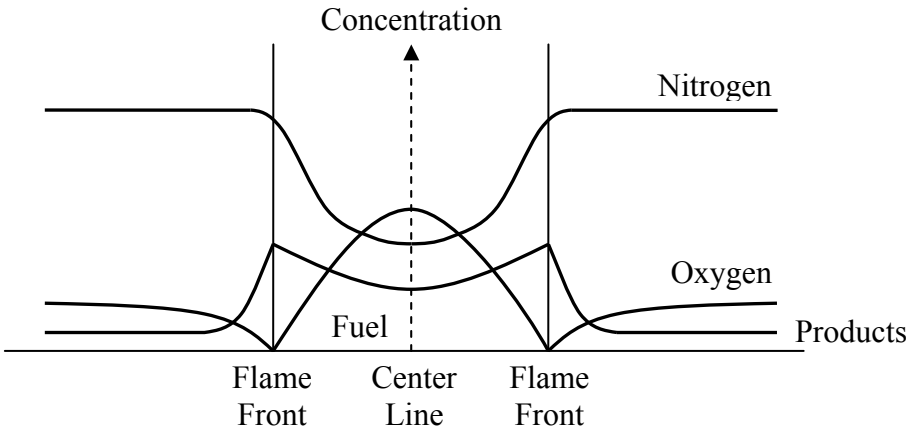

Figure 2.2: Generalized concentration profile of a gaseous fuel jet in cross-section (after Glassman [4]).

The flame front can be considered a boundary that separates the products of combustion from the reactants. While in the oxidizer region outside of the flame, the highest levels of oxygen and nitrogen are available. A move towards the flame front from either side as shown in Figure 2.2 demonstrates that the overall oxygen concentration decreases until it reaches zero at the flame front. The nitrogen concentration decreases only slightly following the same path. Once inside the

boundaries of the flame front, the nitrogen component is lessened due to increases in fuel and combustion product concentrations. Similarly, at the centerline of the gaseous fuel jet, the fuel concentration is at its maximum. A move towards the flame front in either direction shows a decreasing fuel concentration. No fuel is found outside of the flame front. The products of combustion exist both inside the flame front and outside the flame front. When inside the structure of the flame, products of combustion are being created due to the chemical reactions of the flame. Eventually, these products are transported outside of the flame front where their concentrations decrease with as they move away from the flame front [4].

The temperature profile within the gaseous fuel jet cross-section follows a trend similar to the concentration measurements. When outside of the flame front, the temperature of the oxidizer is at ambient conditions. A move towards the flame front will result in an increase in temperature. The maximum temperature is achieved at the point where the maximum concentrations of the major products (e.g., CO_2 and H_2O) exist [4]. The area of maximum temperature is considered to be the location of the flame front. Moving through the flame front into the center of the fuel jet results in lower temperatures, which are due to a lack of oxygen available for maintaining the combustion reaction.

2.2.2. Counter-Flow Diffusion Flame

The counter-flow diffusion flame (or opposed-flow diffusion flame) is one where the gaseous fuel jet and a jet of oxidizer are set in opposition to one another. This experimental setup is more complex to create when compared to the setup of the fuel jet flame. If aligned correctly, this type of diffusion flame can have research advantages. One advantage is that this setup eliminates the ability of the oxidizer to diffuse through to the fuel side [4]. Another advantage is that the flow configuration is easily analyzed [4]. Figure 2.3 depicts an example of a typical counter-flow burner.

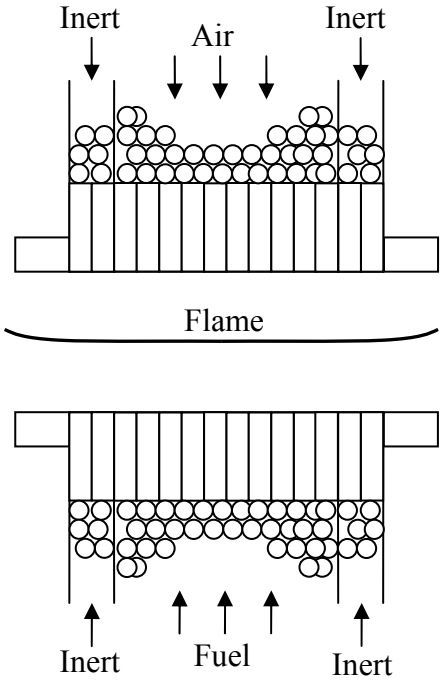

Figure 2.3: Example of a typical counter-flow diffusion flame burner

The counter-flow jets of oxidizer and fuel will typically be constructed in a self-contained burner. As shown in Figure 2.3, each jet can be surrounded by a co-flow of an inert gas designed to exclude the natural atmosphere from interfering with the flame.

2.3 Laminar Diffusion Flame Theory

As mentioned in Section 2.2.1, of greatest interest for diffusion flames is the understanding of the concentration and temperature fields within the flame. To establish the concentration and temperature fields, the steady heat and mass transport equations must be solved. The general form of these equations is for three spatial dimensions. Typically, the problem is defined in terms of one dimension and then expanded to three dimensions.

2.3.1. Generalized Diffusion Flame

Following a similar discussion by Glassman [4], a simple one-dimensional flame geometry is shown in Figure 2.4. This simple geometry can represent a small section of the flame along either a burning gaseous jet or burning in the counter-flow configuration.

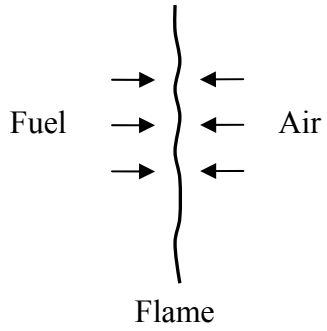

Figure 2.4: One-dimensional diffusion flame geometry.

In a more detailed inspection of differential elements within the flame, the important mass and energy fluxes through a volume element of thickness *dx* at an arbitrary location, *x*, can be obtained through conservation balances. Figure 2.5 depicts a representation of these balances.

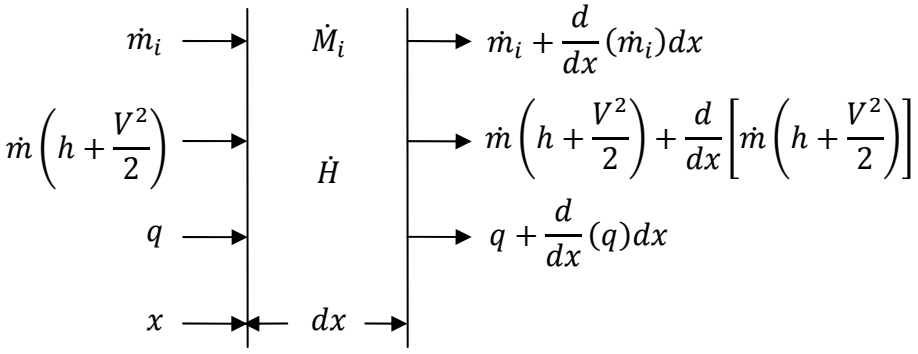

Figure 2.5: Heat and mass flux balances across a differential element within a diffusion flame.

The $\dot{m}_\iota$ term represents the mass flux of species *i* per unit area by convection and diffusion. This term is also equal to $\rho_i V + J_i$ and $\rho V Y_i + J_i$, where $J_i = -\rho D_i \frac{dY_i}{dx}$. $\dot{M}_i$ represents the mass generation rate of species *i* per unit volume by chemical reaction. $q = k\frac{dT}{dx}$ is the amount of energy transported via conduction, and $\dot{H}$ is the heat generation rate per unit volume by chemical reaction. The conservation of mass can be expressed as

$$\dot{m} = \rho V = \text{constant} \tag{2.1}$$

The conservation of mass for species *i* represents the outflow rate minus the inflow rate plus the addition of the storage rate. Since the problem is designed as steady-state, the storage rate is zero. Thus, the inflow rate subtracted from the outflow rate will equal the production rate.

$$\dot{m}_i + \frac{d}{dx}(\dot{m}_i)dx - \dot{m}_i = \dot{M}_i dx \tag{2.2}$$

Substituting for $\dot{m}_\iota$

$$\frac{d}{dx}\left[\rho V Y_i - \rho D_i \frac{dY_i}{dx}\right] = \dot{M}_i \tag{2.3}$$

The conservation of energy can be expressed as

$$\dot{m}\left(h + \frac{V^2}{2}\right) + \frac{d}{dx}\left[\dot{m}\left(h + \frac{V^2}{2}\right)\right] + k\frac{dT}{dx} -$$

$$m\left(h + \frac{V^2}{2}\right) - \left[k\frac{dT}{dx} + \frac{d}{dx}\left(k\frac{dT}{dx}\right)dx\right] = \dot{H}dx \tag{2.4}$$

Assuming that $h \gg \frac{V^2}{2}$ and that there is perfect gas behavior, Equation (2.4) reduces to

$$\frac{d}{dx}\left[\rho V Y C_p T - k\frac{dT}{dx}\right] = \dot{H} \tag{2.5}$$

Equations (2.1), (2.3), and (2.5) may be generalized to three-dimensions as follows:

$$\text{Mass: } \nabla \cdot \rho\vec{V} = 0 \tag{2.6}$$

$$\text{Species: } \nabla \cdot \left[\rho\vec{V}Y_i - \rho D_i \nabla Y_i\right] = \dot{M}_i \tag{2.7}$$

$$\text{Energy: } \nabla \cdot \left[\rho\vec{V}C_p T - k\nabla T\right] = \dot{H} \tag{2.8}$$

These generalized differential equations are inhomogeneous. In order to simplify the solution of these equations, it is desirable to eliminate the inhomogeneous rate terms for the species production and energy generation, $\dot{M}_i$ and $\dot{H}$. To accomplish this, an assumption can be made that the combustion process may be represented by a single-step reaction:

$$\sum_i a_i A_i \rightarrow \sum_i \grave{a}_i A_i \tag{2.9}$$

Reactants Products

Here, A_i represents species i, and a_i, $\grave{a}_i$ are the stoichiometric coefficients of species i. A new variable can be defined as

$$\dot{M} \equiv \frac{\dot{M}_i}{MW_i(\grave{a}_i - a_i)} \tag{2.10}$$

Assuming that the diffusion coefficients for all species, A_i, are the same, Equation (2.7) may be written as

$$\nabla \cdot \left[\rho\vec{V}\left(\frac{Y_i}{MW_i(\grave{a}_i - a_i)}\right) - \rho D \nabla\left(\frac{Y_i}{MW_i(\grave{a}_i - a_i)}\right)\right] = \dot{M} \tag{2.11}$$

Now defining

$$\alpha_i \equiv \frac{Y_i}{MW_i(\grave{a}_i - a_i)} \tag{2.12}$$

Substituting Equation (2.12) into (2.11) results in

$$\nabla \cdot \left[\rho \vec{V} \alpha_i - \rho D \nabla \alpha_i\right] = \dot{M} \tag{2.13}$$

Following a similar procedure with the energy equation, the volumetric energy release rate may be written as

$$\dot{H} = -\dot{M}_\iota \Delta H_i^\circ = -\dot{M} \Delta H_i^\circ \cdot MW_i(\grave{a}_i - a_i) \tag{2.14}$$

where ΔH_i° is the heat of reaction per unit mass of species i. Assuming that $C_p =$ Constant, Equation (2.8) may be written as

$$\nabla \cdot \left[\rho \vec{V} \left(\frac{C_p T}{\Delta H_i^\circ \cdot MW_i(\grave{a}_i - a_i)} - \frac{k}{C_p} \nabla \left(\frac{C_p T}{\Delta H_i^\circ \cdot MW_i(\grave{a}_i - a_i)}\right)\right)\right] = -\dot{M} \tag{2.15}$$

As with the species term, a new variable can be defined:

$$\alpha_T \equiv \frac{C_p T}{\Delta H_i^\circ \cdot MW_i(\grave{a}_i - a_i)} \tag{2.16}$$

Substituting equation (2.16) into (2.15) yields

$$\nabla \cdot \left[\rho \vec{V} \alpha_T - \frac{k}{C_p} \nabla \alpha_T\right] = -\dot{M} \tag{2.17}$$

At this point, it can be assumed that the transport rates of species and energy are the same. Thus, $\frac{k}{C_p} = \rho D$, which implies that α (thermal diffusivity) = D (molecular diffusivity). The energy equation now becomes

$$\nabla \cdot \left[\rho \vec{V} \alpha_T - \rho D \nabla \alpha_T\right] = -\dot{M} \tag{2.18}$$

Both the species and energy equations are of the form $L(\alpha) = \pm\dot{M}$, where the operator $L(\quad)$ is defined as

$$L(\alpha) = \nabla \cdot \left[\rho\vec{V}\alpha - \rho D\nabla\alpha\right] \tag{2.19}$$

Hence, the inhomogeneous rate term, $\dot{M}$, may be eliminated by an appropriate combination of any two of the $L(\quad)$ equations. The above outlined procedure is commonly referred to as the Schvab-Zeldovich transformation. This transformation allows for the elimination of the inhomogeneous terms such that a solvable homogeneous differential equation results.

2.3.2. Confined Axisymmetric Laminar Diffusion Flame

The analysis in the previous section can be used to predict the oxygen and concentration fields for a confined axisymmetric laminar diffusion flame. This analysis was first completed by Burke and Schumann in 1928 [7]. Figure 2.6 depicts the refined problem setup.

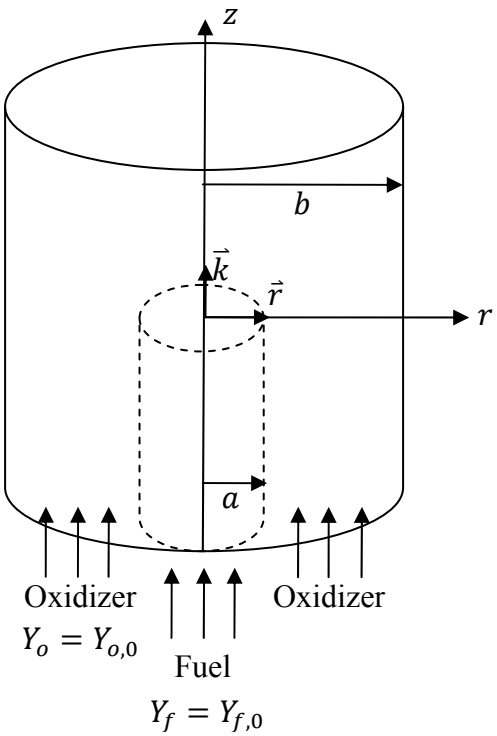

Figure 2.6: Confined axisymmetric laminar diffusion flame problem

A new variable can be defined as

$$\beta_{of} \equiv \alpha_o - \alpha_f \tag{2.20}$$

This variable is designed to facilitate the subtraction of the two species conservation equations for the oxygen and fuel. A homogeneous equation of the form $L(\beta_{of}) = 0$ is obtained and can be solved, subject to appropriate boundary conditions, to yield the oxygen and fuel concentration fields. The $L(\quad)$ equation for $\beta_{of} \equiv \alpha_o - \alpha_f$ is

$$L(\beta_{of}) = \nabla \cdot \left[\rho \vec{V} \beta_{of} - \rho D \nabla \beta_{of}\right] = 0 \tag{2.21}$$

The assumptions for this problem are

1. There is no radial velocity component. $\vec{V} = V\vec{k}$ (axisymmetric)
2. $\rho\vec{V} = \text{constant}$
3. $\rho D = \text{constant}$
4. Terms containing $\frac{d}{dz}$ are $\ll$ than terms containing $\frac{d}{dr}$

The current problem is based on symmetry around an axis, therefore, it is easier to transpose the general Cartesian formulation of the $L(\quad)$ equation in Equation (2.21) into cylindrical coordinates. Using the above assumptions and translating into cylindrical coordinates,

$$\nabla \cdot (\rho \vec{V} \beta_{of}) = \nabla \cdot (\rho V \vec{k} \beta_{of}) = \left(\vec{r}\frac{\partial}{\partial r} + \vec{\theta}\frac{1}{r} + \vec{k}\frac{\partial}{\partial z}\right) \cdot (\rho V \vec{k} \beta_{of}) \tag{2.22}$$

$$\nabla \cdot (\rho \vec{V} \beta_{of}) = \frac{\partial}{\partial z}(\rho V \beta_{of}) = \rho V \frac{\partial \beta_{of}}{\partial z} \tag{2.23}$$

$$\nabla \cdot \rho D \nabla \beta_{of} = \rho D \nabla \cdot \nabla \beta_{of} = \rho D \nabla^2 \beta_{of}$$
$$= \rho D \left[\frac{1}{r} \frac{\partial}{\partial r} \left(r \frac{\partial \beta_{of}}{\partial r} \right) + \frac{1}{r^2} \frac{\partial^2 \beta_{of}}{\partial \theta^2} + \frac{\partial^2 \beta_{of}}{\partial z^2} \right] \tag{2.24}$$

$$\nabla \cdot \rho D \nabla \beta_{of} \cong \rho D \frac{1}{r} \frac{\partial}{\partial r} \left(r \frac{\partial \beta_{of}}{\partial r} \right) \tag{2.25}$$

Thus, the $L(\quad)$ equation in Equation (2.21) can be expressed as

$$L(\beta_{of}) = \rho V \frac{\partial \beta_{of}}{\partial z} - \rho D \frac{1}{r} \frac{\partial}{\partial r} \left(r \frac{\partial \beta_{of}}{\partial r} \right) = 0 \tag{2.26}$$

Dividing through by ρD results in

$$\frac{V}{D} \frac{\partial \beta_{of}}{\partial z} - \frac{1}{r} \frac{\partial}{\partial r} \left(r \frac{\partial \beta_{of}}{\partial r} \right) = 0 \tag{2.27}$$

The boundary conditions for Equation (2.27) are that β_{of} is bounded everywhere and specifically that

$$z = 0\,, \qquad 0 \le r < a \Longrightarrow \beta_{of} \equiv \alpha_o - \alpha_f = -\alpha_{f,0} \tag{2.28}$$

$$z = 0, \qquad a < r < b \Longrightarrow \beta_{of} \equiv \alpha_o - \alpha_f = \alpha_{o,0} \tag{2.29}$$

$$z > 0, \qquad r = b \Longrightarrow \frac{\partial \beta_{of}}{\partial r} = 0 \tag{2.30}$$

For purposes of analysis, the problem can be rewritten in terms of dimensionless axial and radial coordinates. Utilizing Figure 2.6 the following can be defined:

$$\xi \equiv \frac{r}{b} \tag{2.31}$$

$$\eta \equiv \frac{zD}{Vb^2} \tag{2.32}$$

$$\omega \equiv \frac{\alpha_{o,0}}{\alpha_{f,0}} \tag{2.33}$$

$$\gamma \equiv \frac{-\beta_{of}}{\alpha_{f,0}} \tag{2.34}$$

$$c \equiv \frac{a}{b} \tag{2.35}$$

Equation (2.27) can now be written as

$$\frac{\partial \gamma}{\partial \eta} - \frac{1}{\xi}\frac{\partial}{\partial \xi}\left(\xi \frac{\partial \gamma}{\partial \xi}\right) = 0 \tag{2.36}$$

and the transformed boundary conditions are

$$\eta = 0\,, \qquad 0 \le \xi < c \Longrightarrow \gamma = 1 \tag{2.37}$$

$$\eta = 0, \qquad c < \xi < 1 \Longrightarrow \gamma = -\omega \tag{2.38}$$

$$\eta > 0, \qquad \xi = 1 \Longrightarrow \frac{\partial \gamma}{\partial \xi} = 0 \tag{2.39}$$

The solution to Equation (2.36) with the boundary conditions given as Equations (2.37), (2.38), and (2.39) is (as in Glassman [4])

$$\gamma = (1+\omega)c^2 - \omega + 2(1+\omega)c \sum_{j=1}^{\infty} \frac{1}{\phi_j}\left\{\frac{J_1(c\phi_j)}{[J_0(\phi_j)]^2}\right\} J_0(\phi_j \xi)\exp(-\phi_n \eta) \tag{2.40}$$

where J_0 and J_1 are Bessel functions of the first kind and the ϕ_n represent successive roots of the equation $J_1(\phi) = 0$. The flame height and flame shape (i.e., the location of the flame in the ξ, η coordinates) can be obtained from Equation (2.40). The assumption is made that the entire reaction occurs at a flame surface. Thus, the region containing fuel is separated from the region containing oxygen by the flame surface. There is no oxygen in the fuel region, and no fuel in the oxygen region. Hence, in the fuel region

$$\beta_{of} = -\alpha_f = \frac{Y_f}{MW_f a_f} > 0 \tag{2.41}$$

and in the oxygen region

$$\beta_{of} = \alpha_o = -\frac{Y_o}{MW_o a_o} < 0 \tag{2.42}$$

According to Equation (2.40), γ (and thus β_{of}) is a continuous function. At the flame surface

$$0 \leq \beta_{of,\,\text{fuel region}} = \beta_{of,\,\text{oxygen region}} \leq 0 \tag{2.43}$$

Therefore, $\beta_{of} = 0$ and $\gamma = 0$. Thus, $\gamma = 0$ defines the locus of the flame in terms of ξ, η. For a fixed value of c (i.e., the burner geometry) and two different values of ω (i.e., stoichiometries), flame shapes are depicted in Figure 2.7.

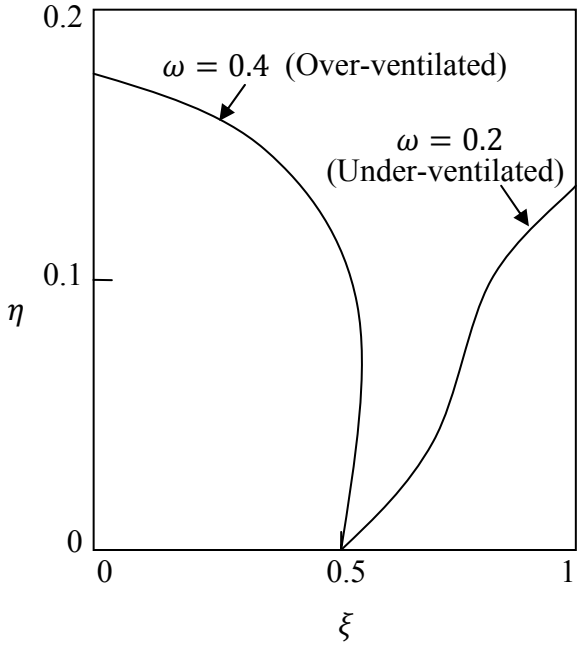

Figure 2.7: Flame shapes as predicted for confined axisymmetric laminar diffusion flame (after Williams [8]).

The flame height can be obtained in terms of a fixed value for η by setting $\xi = 0$ (over-ventilated) or $\xi = 1$ (under-ventilated). Thus, the dimensionless flame height can be expressed as

$$\eta(\xi) \equiv \frac{zD}{Vb^2} = \frac{zD}{Va^2}c^2 = f(\omega) \tag{2.44}$$

For $\xi = 0$ or $\xi = 1$, the dimensionless flame height is equal to the maximum value and can be related to the actual flame height when $z = h_L$, where h_L is the flame height. The relationship between the actual flame height and the dimensionless flame height is then

$$h_L = \eta_{max}\frac{Va^2}{D}c^2 = \eta_{max}\frac{Q}{\pi D}c^2 \tag{2.45}$$

where Q is the volumetric flow rate of the fuel. The above relationship demonstrates that the flame height is directly proportional to the volumetric flow rate of the fuel.

2.4. Turbulent Diffusion Flames

As shown in the previous section, the flame height of a laminar diffusion jet flame is proportional to the ratio of the volumetric flow rate of the fuel and the diffusivity of the fuel

$$h_L \sim \frac{Q}{D} \tag{2.46}$$

As the volumetric flow rate of the fuel is increased, the flow of the fuel becomes turbulent. The system becomes momentum-controlled, and molecular diffusion becomes less important for mass transport [4]. In addition to the flow, the flame behaves differently than a laminar flame. Also, the flame will influence the structure of the turbulent flow field. Within the turbulent mixing zone, the maximum gradient of the mean velocity profile can be steepened, resulting in the generation of vorticity on the opposite sides of the high temperature, low-density reaction region [4].

The rate of entrainment of fluid into the mixing layer is reduced and vortices of larger dimensions are produced due to the development of the decreased overall density [4]. Therefore, the molecular diffusivity observed in previous sections can be substituted with a turbulent eddy diffusivity, ε. Equation (2.46) can be written as

$$h_{L,Turb} \sim \frac{Q}{\varepsilon} \sim \frac{Va^2}{\varepsilon} \tag{2.47}$$

where $h_{L,Turb}$ is the flame height of the turbulent fuel jet. ε is proportional to lU', where l is the integral scale of turbulence. l is proportional to the tube diameter, $2a$. U' is the intensity of turbulence, which is proportional to the mean flow velocity, V, along the axis [4]. Thus,

$$\varepsilon \sim aV \tag{2.48}$$

Combining Equations (2.47) and (2.48) results in

$$h_{L,Turb} \sim \frac{Va^2}{aV} \sim a \tag{2.49}$$

As can be seen in Equation (2.49), the flame height of a turbulent diffusion flame is proportional to the radius of the port through which the fuel flows. Once the flow is fully turbulent, the flame height no longer depends on the volumetric flow rate of the fuel from the burner inlet. Figure 2.8 demonstrates this phenomenon over a range of exit velocities from laminar flow to turbulent flow.

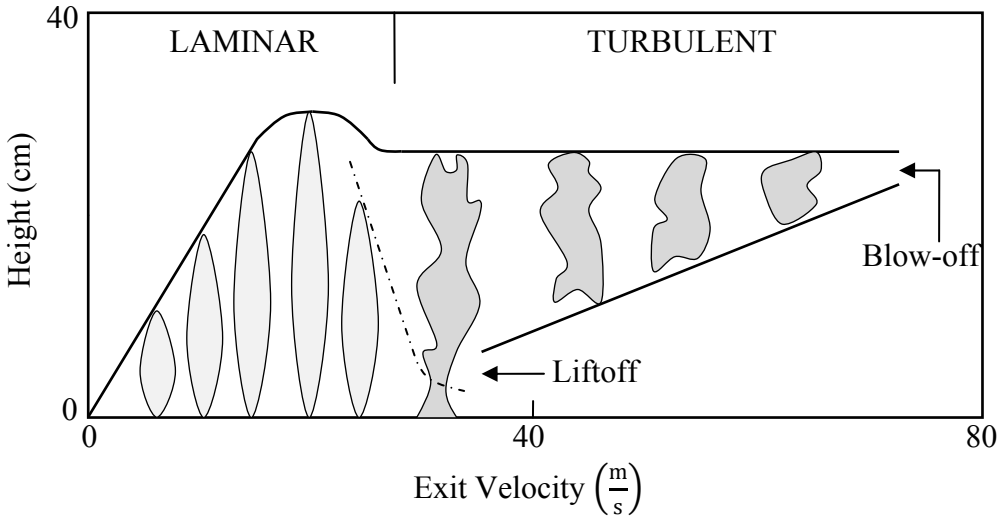

Figure 2.8: Jet diffusion flame heights over a range of exit velocities from the laminar range to fully turbulent (after Glassman [4]).

The figure shows that when in the laminar region, the flame height increases as the exit velocity of the fuel increases. A transition region is achieved between the laminar and turbulent regions. In the transition region, the flame height begins to decrease as eddies begin to form. In the turbulent region, the flame height is no longer dependent on the fuel flow rate. As the exit velocity is increased in the turbulent region, the flame begins to become detached from the exit surface. This phenomenon is typically referred to as "liftoff." If the velocity is increased further, the flame can be extinguished completely by the momentum of the jet overcoming the ability of the combustion reaction to sustain itself, commonly referred to as "blow-off."

2.5. Terrestrial Diffusion Flames

The discussion in the previous sections has focused on simple problem setups that are designed to be easily analyzed. Flames that occur naturally, such as liquid fuel pool fires and flames burning on solid fuels, are much more complicated, but they follow the same physical laws as described in the more simple flame configurations reviewed.

When examining natural flames in a terrestrial environment, it is important to recognize that the momentum and buoyancy in the flame will dictate the behavior of the fire [9]. Typically, the Froude number (Fr) is used as a comparison term to describe various flames and the level of buoyantly-induced turbulence within each type. The Froude number is the ratio of the velocity of the gases in the flame related to the buoyancy of the gases or

$$\mathrm{Fr} = \frac{V^2}{gd} \tag{2.50}$$

where V^2 is the velocity of the gases, g is the acceleration due to gravity, and d is the diameter of the fuel jet or fuel bed.

Turbulent jet flames have high Froude numbers [9] and are easily determined since the inlet velocity is a known quantity. Natural fires depend on the release of fuel vapor from a surface (i.e., either liquid or solid) during the combustion process. As such, the initial velocity of the fuel vapor is difficult to measure. Instead of obtaining a direct measurement, the Froude number is derived from the rate of heat release, $\dot{Q}$, of the burning fuel [9]. If a flame exists over a circular area of diameter, d, the initial velocity of the fuel vapor can be expressed as

$$V = \frac{\dot{Q}}{\Delta H_c \rho \left(\frac{\pi d^2}{4}\right)} \tag{2.51}$$

where ΔH_c is the heat of combustion of the fuel vapor and ρ is the fuel density. Combining Equations (2.50) and (2.51) results in

$$\mathrm{Fr} \sim \frac{\dot{Q}^2}{d^5} \tag{2.52}$$

which is a scaling criterion used to compare the Froude number, the heat release rate of the flame, and the diameter of the fuel bed. The scaling criterion has been used by

Zukoski in previous research [10, 11] to define a dimensionless heat release rate. This rate is commonly expressed as

$$\dot{Q}^* = \frac{\dot{Q}}{\rho_\infty C_p T_\infty \sqrt{gd} \cdot d^2} \tag{2.53}$$

where ρ_∞ is the ambient density of the gases, C_p, is the specific heat, and T_∞ is the ambient temperature. The above equation is used to classify various flame types and to correlate various flame parameters, such as flame height [9].

Figure 2.9 shows a diagram of various turbulent flame regions as defined by the relationship between the flame length of the fire, the dimensionless rate of heat release, and the Froude number.

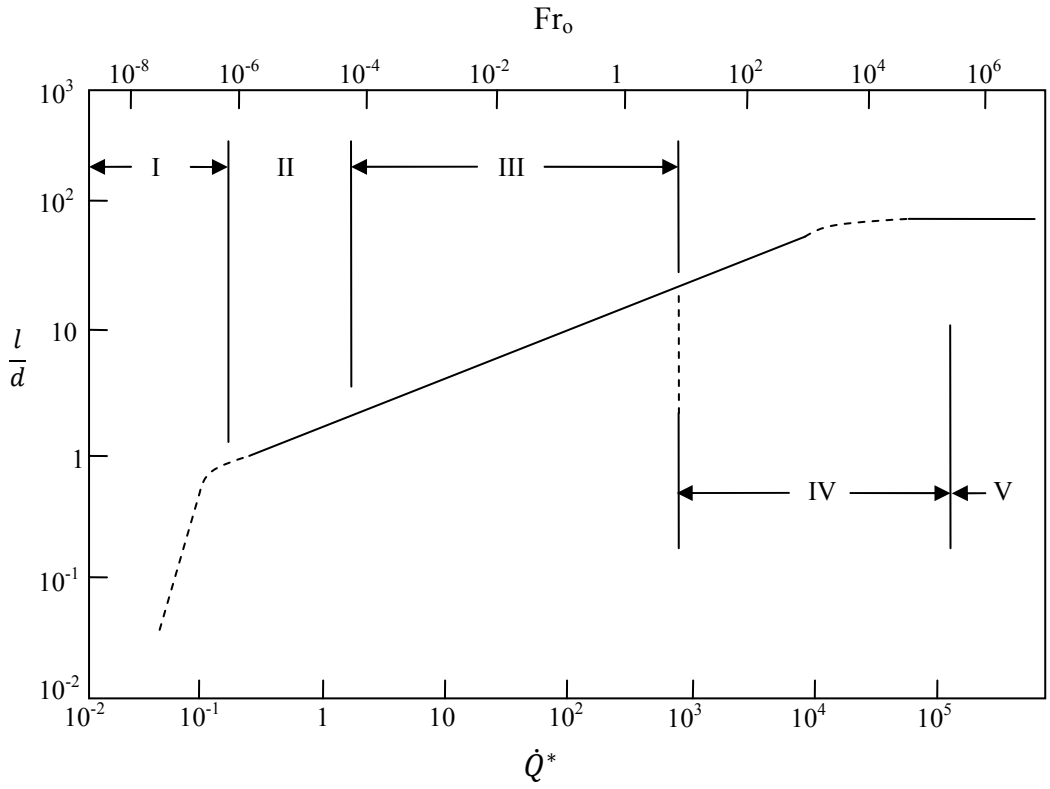

Figure 2.9: Relationship between flame height, Froude number, and dimensionless heat release rate (after Zukoski [11]).

The figure depicts five clear regions with increasing Froude number. On the far right, Region V corresponds to the fully turbulent jet fire. In this region, the momentum of the fuel completely dominates the buoyancy-induced effects from combustion. In the middle, Regions III and IV represent transitional areas where momentum and buoyancy both affect the behavior of the flame. On the left, Regions I and II represent natural turbulent flames that are buoyancy-driven.

2.6. Diffusion Flames in Microgravity

As mentioned previously, buoyancy plays a significant role in the structure and behavior of natural fires in terrestrial environments. When in extraterrestrial environments where microgravity is achieved, buoyancy no longer plays a role in the structure or behavior of fire. The lack of buoyantly-induced flow and turbulence results in conditions where the ambient forced flow of gases through an area of interest is the major determining factor in the observed growth and spread of a fire. It is possible that the free flow of ambient gases in space facilities and space vehicles can be quiescent or can have velocities that will significantly affect the ability of a fire to ignite, grow, and spread.

2.6.1. Microgravity Flames in Quiescent Air

Early flammability and flame spread testing in a quiescent microgravity environment was conducted aboard the Skylab station in 1974. These tests were conducted in a static chamber and involved the observation of flame spread over common materials such as paper, plastics, cotton, and aluminized Mylar [12]. In all cases, flame spread rates in the quiescent environment with microgravity were observed to be slower than flame spread rates observed in similar tests in a terrestrial environment with normal gravity [12]. Later research involving thin sheets of the materials used in the earlier testing aboard the Skylab station verified that flame spread rates in microgravity are much slower if environmental oxygen conditions are maintained at terrestrial limits (i.e., 21% by volume) [13].

Figure 2.10 illustrates the differing flame spread rates for thin fuels in both normal and microgravity conditions.

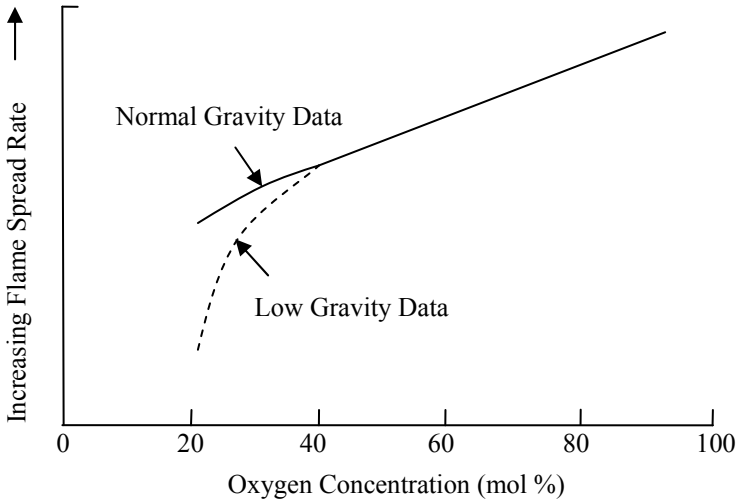

Figure 2.10: Flame spread rates of thin paper sheets in normal gravity and microgravity (after Olson [13]).

It should be noted that as the oxygen concentration is increased, the flame spread values for the normal gravity and microgravity data merge onto the same line. This convergence demonstrates the potential hazard of utilizing high concentration oxygen environments in space facilities and space vehicles. The flame spread reduction observed in a quiescent microgravity environment is completely negated once the local oxygen concentration by volume is increased over 40%. Further research has shown that for thin fuels in microgravity conditions, the fuel mass loss is lower, the flame temperature is lower, and the production of soot is reduced as compared to values observed in normal gravity conditions [3].

Thick sheets of potential fuel materials have also been examined in quiescent microgravity environments. The flame spread over thick sheets of fuel has been observed to decrease with time and to eventually self-extinguish [3]. The self-extinction has been shown to occur over several minutes [3].

For both thin and thick fuels in quiescent microgravity conditions, research has shown that various flame-related experimental results are reduced when compared with results obtained under normal gravity conditions. Thus, quiescent microgravity conditions provide an environment that is more challenging for the establishment, growth, and spread of a fire.

2.6.2. Microgravity Flames in a Forced Flow Environment

Space facilities and space vehicles, with few exceptions, do not provide a quiescent atmosphere. While the quiescent environment described in the preceding section has been well-explored experimentally, the results are not applicable to all microgravity conditions. In particular, space facilities must maintain a small ventilation rate for atmospheric conditioning and component cooling [3]. The continuous flow associated with the ventilation is at a relatively low, superficial velocity, which can range from 6-20 centimeters per second [3]. While this velocity cannot be easily perceived by crew members manning the space facility or space vehicle, the forced flow is great enough to aid in the initiation of a fire and to compensate for the lack of natural buoyancy [14].

Microgravity combustion research has shown that, for thin fuels, the addition of a low velocity forced flow increases the flame spread rates as much as 20% more than a comparable downward flame spread rate found in normal gravity conditions [3]. This increase is not enough for the flame spread rate to match the typical normal gravity "upward" flame spread rates over thin fuels, but the increase is significant and can translate into the potential for difficulty in the suppression of fire in microgravity conditions.

Studies have also examined the flame spread rates over thick fuels with low velocity forced flow rates in microgravity [15, 16, 17]. Tests were conducted at the typical flow velocities found in space facilities and space vehicles. As mentioned previously, the results for the quiescent microgravity conditions indicated that the

flame would self-extinguish. With the introduction of a relatively small forced flow, the flame continued to grow, spread, and sustain itself over the fuel surface.

In general, even the relatively small velocities driven by the circulation of atmospheric gases within space facilities and space vehicles are high enough to strongly influence the potential initiation, growth, and spread of a fire in a microgravity environment. A small forced flow is enough to counter-balance the lack of natural buoyancy found in microgravity environments.

2.7. Conclusions

A review of the basic structure and analyses for simple diffusion flames in normal gravity environments has been presented. The differences between a laminar diffusion flame and a turbulent diffusion flame have been discussed. Additionally, the effects of microgravity conditions on a diffusion flame have been examined.

Most naturally occurring fires in normal gravity or microgravity conditions are diffusion flames. In a terrestrial environment, these fires are turbulent due to the buoyancy of hot combustion products. In microgravity, the fires are more likely to be laminar and are heavily influenced by any forced flow or natural convection within the local area of the flame. This understanding of a diffusion flame behavior in both normal gravity and microgravity environments is necessary to analyze the interaction of a flame with a potential suppressant agent. Chapter 3 will provide further information on how flame suppression is typically defined and how it relates to flame extinction.

Chapter Three

3. Fire Suppression and Flame Extinction

3.1. Introduction

The concepts of fire suppression and flame extinction are intrinsically linked. Fire suppression is a term typically used when referring to an active role in the extinguishment of a fire. Fire service personnel, for example, might use this term to describe the act of extinguishing a fire with water. Flame extinction is a term more often associated with combustion research. The term flame extinction is used when describing the physical phenomenon that results in the extinguishment of a fire or flame. Both terms can be interchangeably used when referring to the process by which the combustion reaction is terminated.

In the combustion literature, flame extinction has been explored through various analyses that approach the problem from different perspectives. In general, the analyses can be divided into four categories: an asymptotic analysis for flame ignition and extinction, a critical flame temperature for extinction, a critical mass flux of fuel from the surface of the burning material necessary to sustain the flame reaction, and a critical scalar dissipation rate for extinction. While distinct in each approach, the physical phenomena described are inherently coupled.

Chapter 3 discusses the basic concept of fire suppression and presents a detailed examination of flame extinction through a review of previous work. Additionally, this chapter will present a review of flame suppression research in microgravity conditions.

3.2. Fire Suppression

Fire suppression is traditionally presented as a visible process by which a flame is extinguished. This process involves the use of a physical suppressant that can be observed during its interaction with the fire. The suppressant agent is applied to the fire in order to facilitate its extinguishment. Typically, the suppressant agent affects the fire through one of four means: the removal of heat, the removal of the oxidizer,

the removal of the fuel, or the interruption of the chain reactions within the combustion process. These four means of extinguishment can be presented in conjunction with the four sides of a geometric shape known as the "Tetrahedron of Fire [18]."

Suppressant agents that are effective at extinguishing a nonspecific fire will be able to affect one or more "sides" of the fire tetrahedron. The possible interactions between various suppressant agents and the sides of the fire tetrahedron represent the basic theory of fire suppression.

3.2.1. The Fire Tetrahedron

As mentioned, the fire tetrahedron is a three-dimensional geometric shape used to visualize the four interdependent aspects of maintaining the combustion process. Figure 3.1 depicts a graphic representation of the fire tetrahedron.

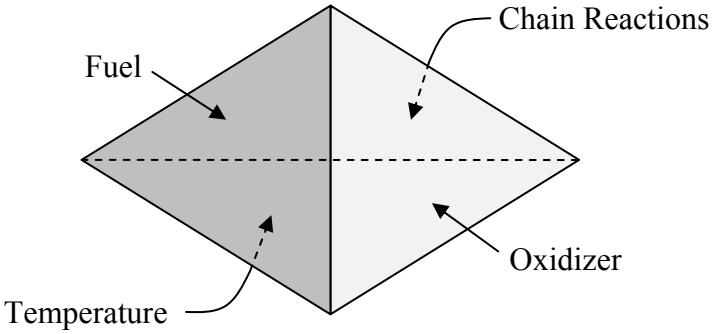

Figure 3.1: The fire tetrahedron (after [19]).

For the combustion process to continue, the fuel must interact with the oxidizer at the appropriate temperature. If the temperature is high enough, the reaction will be able to proceed, and the chain reactions within the chemical process will allow for a self-sustaining flame. If one of the four sides of the fire tetrahedron is removed, the shape cannot maintain its integrity, and the combustion process will cease.

3.2.2. Basic Theory of Fire Suppression

The goal of fire suppression is to interrupt one of the sides of the fire tetrahedron. In order to accomplish this interruption, the suppressant agent must contain some property that will allow it to influence a side or multiple sides of the fire tetrahedron, and it must be delivered to the area where the fire is located.

By examining the four elements in the tetrahedron, a basic method of how to induce the extinguishment of a fire can be determined. First, the fuel can be removed from the local area where the combustion is occurring in order to precipitate extinguishment of the fire. In practice, removal of the fuel can be difficult to facilitate unless the fuel is contained within an area that can be controlled such that the removal is possible. The fuel could also potentially be encapsulated by a barrier that would allow for the separation of the fuel from the reaction zone [19].

Second, removal of the oxidizer will cause the flame to be extinguished. Reducing the local concentration of oxygen at the flame reaction zone will precipitate the extinction of the flame. Normal atmospheric oxygen concentrations are approximately 21% by volume. Extinguishment of the fire will occur by lowering the concentration of oxygen at the reaction zone of the flame to 15% [19]. This is usually accomplished through the introduction of an inert gas with sufficient quantity to reduce the local oxygen concentration.

Third, removal of the heat associated with the combustion process will terminate the reaction. Temperature plays a key role in the reaction chemistry of the combustion process. The addition of a suppressant that removes heat from the reaction will interrupt the combustion process. Due to its high heat capacity and latent heat of vaporization, water is commonly used as a suppressant for its ability to cool the combustion gases involved in the actual reaction as well as to cool the unburned surfaces of the surrounding fuel.

Fourth, the neutralization of chain reactions occurring within the chemical reaction of the fire can cause the extinction of the combustion process. This neutralization is accomplished chemically by absorbing free radicals that are formed in intermediate reaction steps in the combustion process. One of the main radicals is the principle carrier of the chain, the hydroxyl radical [19]. Halon, an extinguishing agent that is now banned throughout the world, was extremely effective due to its ability to grab free radicals and remove them from the reaction zone, thus prohibiting the continuation of chain reactions within the flame chemistry.

While the fire tetrahedron is useful for a general understanding of how a fire can be extinguished, it does not provide detailed information as to how flame extinction actually occurs. As mentioned in the introduction to this chapter, various flame extinction studies have been documented in the combustion literature. An understanding of the main research categories will provide the information necessary to analyze and quantify suppression effectiveness.

3.3. Asymptotic Analysis of Flame Ignition and Extinction

As discussed in Chapter 2, most flames that occur naturally are diffusion flames where the reactants are initially separated. Early experimental work by Potter et al. [20] focused on the counter-flow configuration previously described. The simple analytical nature of the counter-flow configuration and the availability of existing experimental data led to the development of theory for the understanding of when and how a flame established in this manner would ignite or extinguish. The development of the theory for a flame burning in the counter-flow configuration is commonly referred to as an asymptotic analysis.

One of the earliest works in the asymptotic analysis of flame ignition and extinction was conducted by Fendell [21]. A model was presented of an opposed-flow diffusion flame where the oxidizer was a gas, and the fuel was a constant reservoir of liquid or solid. The opposed-flow diffusion flame was arranged in a classic

axisymmetric geometry. Figure 3.2 shows a diagram of the opposed-flow diffusion flame geometry that was analyzed.

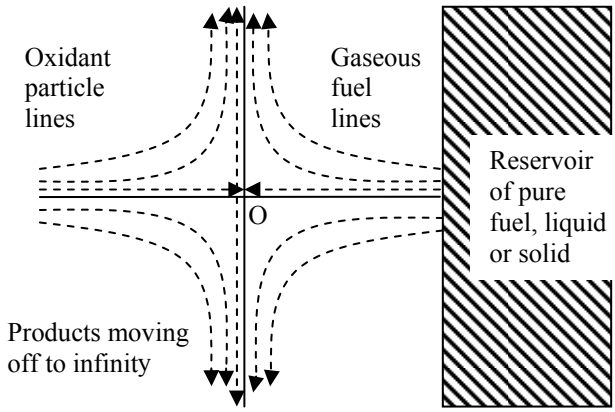

Figure 3.2: Axisymmetric opposed-flow geometry (after Fendell [21]).

Using the above geometry, the opposed-flow diffusion flame problem was developed with a complete description of the governing equations for the conservation of mass, momentum, energy, and species. For the reaction rate term within the equations, second-order Arrhenius kinetics was employed and the following expression resulted

$$-L\bar{T} = L\bar{Y}_f = L\bar{Y}_o = D_1 \bar{Y}_o \bar{Y}_f \exp\left(\frac{-\bar{\theta}}{\bar{T}}\right) \tag{3.1}$$

where $\bar{T}$ was the temperature, $\bar{Y}_f$ was the mass fraction of fuel, $\bar{Y}_o$ was the mass fraction of oxidizer, and $\bar{\theta}$ was the activation temperature of the reaction. L was an operator function that was defined as

$$L = \frac{d^2}{d\bar{z}^2} + \bar{z}\frac{d}{d\bar{z}} \tag{3.2}$$

where $\bar{z}$ was the distance from the fuel reservoir. The bar over each of the above variables indicated that it had been non-dimensionalized. In Equation (3.1), D_1 was the first Damköhler number and was defined as

$$D_1 = \frac{\text{time characterizing the flow}}{\text{time characterizing the chemistry}} = \frac{\rho b d \bar{B}}{2am} \tag{3.3}$$

where ρ was the gas density, b was the stoichiometric coefficient of oxidant, d was the stoichiometric coefficient of fuel, $\bar{B}$ was the frequency factor of the reaction in Arrhenius kinetics, a was the strain rate of the fluid, and m was the sum of the molecular weights of all the reactants times their stoichiometric coefficients.

An examination of the Damköhler number led to the development of three solution methods relative to the size of the Damköhler number. For cases where D_1 was expected to be large, the nearly thin flame approximation which expands on the thin flame solution (Burke-Schumann) via a singular perturbation method was used. For cases where D_1 was small, a conventional perturbation analysis was conducted around the chemically frozen flow limit to describe the asymptotic limit of the small chemical activity. Finally, for intermediate D_1, a numerical integration was conducted to determine the relative importance of the reaction, convection, and diffusion between the two asymptotic limits of intense and weak burning as described by the first and second analyses [21].

As a main discussion point in the analysis by Fendell, the maximum temperature of the reaction was plotted against the first Damköhler number. The result was an S-shaped curve that showed three distinct regions of burning: an area of intense burning, an area of intermediate burning, and an area of weak burning. Figure 3.3 illustrates the plot of the maximum temperature versus the first Damköhler similarity group.

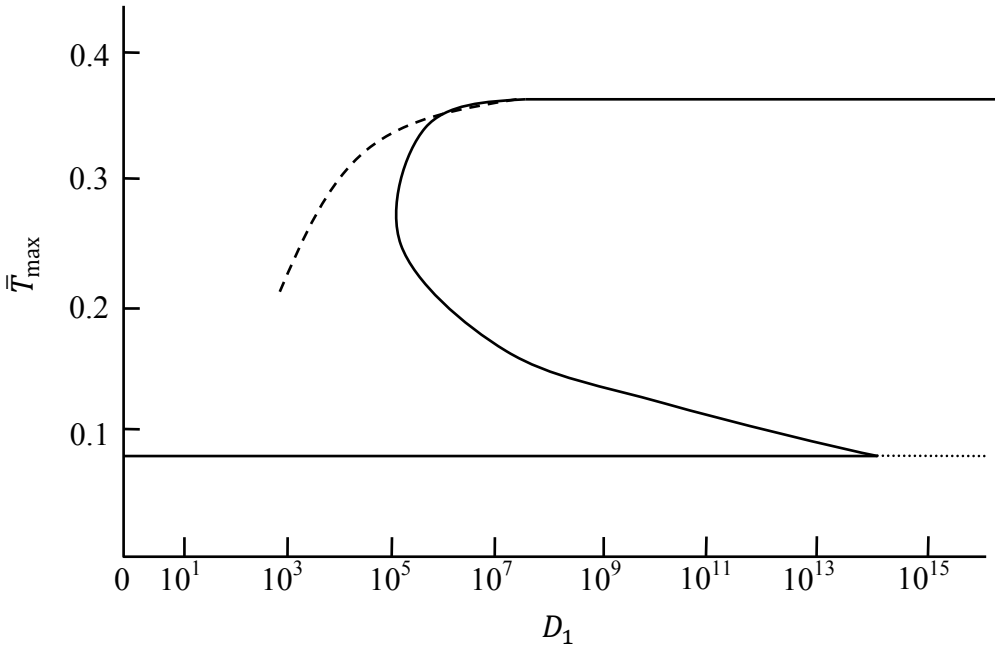

Figure 3.3: Plot of the maximum temperature versus the first Damköhler similarity group (after Fendell [21]).

By examining Figure 3.3, several important conclusions can be made. First, the weak and intense regions are shown to have asymptotic limits at ambient temperature and the flame temperature, respectively. Second, in the frozen flow region, the temperature never increased, and eventually decreased, from the ambient conditions due to heat transfer to the fuel reservoir. Third, in the intermediate burning region, the temperature increased in the reaction zone and fuel and oxidizer were consumed, but the temperature was spread out over a large area and the peak temperature was not very well defined. These results suggested that a wider reaction zone will lower the overall temperature peak such that all of the fuel and oxidizer will have time to participate in the reaction [21]. Fourth, in the intense burning region, the maximum temperature was higher still, and the range over which the elevated temperature was spread was narrower.

The analysis by Fendell concluded that when the first Damköhler number was small, the problem was dominated by diffusion and convection (i.e., losses to the

surroundings do not allow for reactions to occur) [21]. At large values of the Damköhler number, a strong and stable reaction existed in a narrowly confined area. The weak and intense regions were stable, but the intermediate branch was not stable. The system tended towards either the intense or weak if in the intermediate region. Finally, the analysis suggested that a strong enough perturbation as the Damköhler number decreased would cause the system to cross over to the weak branch, and extinction would then occur.

Liñán [22] revisited the counter-flow diffusion flame problem studied by Fendell and predicted that several classes of combustion problems could be linked under a common heading as "boundary-value" problems. Within the linked group, the qualitative aspects of the structure of the diffusion flame were deemed independent of a specific choice for a flame model [22]. In the analysis, Liñán followed a methodology similar to that of Fendell. The analysis resulted in the expansion of the intermediate region into two separate, unsteady branches. While Liñán did not provide a plot of the maximum temperature of the reaction versus the Damköhler number, his analysis suggests a similar S-shaped curve as in Fendell [21], but with four segments. These segments were described as a nearly frozen ignition region, a partial burning region, a premixed flame region, and a near-equilibrium diffusion-controlled region [22].

Law [23] also conducted work using asymptotic analysis when investigating the structure of droplet flames. Building on the previous work with a counter-flow diffusion flame [21, 22], a similar analysis was performed for a spherical droplet problem. The analysis was conducted to understand the influence of a finite gas-phase chemical reaction rate on hydrocarbon droplet evaporation with and without the surrounding diffusion flame [23]. Law proposed that this would determine the ignition-extinction criteria and estimate the effects on evaporation rate, flame standoff distance, and flame temperature [23]. The assumptions for the analysis were a quasi-steady, isobaric, spherically symmetric problem where radiation was negligible [23].

The results of the analysis by Law demonstrated several differences from previous analysis by Fendell and Liñán [21, 22]. The work by Law revealed that the stability regions previously observed did exist for diffusion flame droplets, with the exception of the 1st and higher-order solutions for the nearly frozen region. In the nearly frozen flow region, the flow field was frozen to the zeroth order, and the mass evaporation rate was determined by the classic result for pure evaporation of the drop [23]. The analysis by Law demonstrated that two solutions found in the work by Liñán were not found in the droplet analysis due to the strong nature of a singularity, which rendered convergence impossible [23]. In the partial burning region, a weak flame separated the two regions of frozen flow. Leakage was possible through the zones. In the premixed flame region, only one reactant could leak through the flame. This reactant could be fuel or oxidizer depending on the how the problem was defined. Higher-order solutions did allow a small amount of the second reactant to leak as well. Flame extinction was possible if the leakage became excessive. In the near-equilibrium, diffusion flame region at the low order of approximations, the flame acted as a complete sink for the fuel and oxygen [23]. Leakage was also possible at higher-orders and was responsible for flame extinction [23].

The analysis by Law concluded that even with several differences, the droplet problem was very similar to the counter-flow problem defined in the work by Fendell and Liñán. The exception was in the near frozen flow region. The incorporation of the heat of vaporization and a boundary temperature parameter were taken into account in order to modify the droplet problem accordingly [23]. Results indicated that ignition and extinction criteria for a given droplet in a known atmosphere could be determined.

The analyses conducted by Fendell, Liñán, and Law [21, 22, 23] all provide examples of how examination of a diffusion flame problem yields an extinction parameter, the Damköhler number. By relating the characteristic time of the flow to

the characteristic time of the chemical reaction, the potential for flame extinction could be quantified.

3.4. Critical Flame Temperature for Extinction

Diffusion flame extinction can also be associated with the concept of a critical adiabatic flame temperature below which a flame will extinguish. This temperature is commonly referred to as the "fire point." Several theoretical and experimental studies by Spalding [24] and Roberts and Quince [25] have been conducted with various fuels in order to determine a definition for the fire point and its potential as a flame extinction parameter.

A "flash point" is the lowest surface liquid temperature at which a flammable concentration of vapor above the liquid develops (e.g., the lower flammable limit is reached) [24]. Upon ignition of the vapor, a premixed flame burns back towards the liquid very rapidly. The burning is sufficiently fast such that there is not enough energy returned to the surface of the liquid to heat the liquid to a higher temperature that could support a sustained diffusion flame. The fire point is the lowest surface liquid temperature where, upon ignition of the vapors above the liquid, the result is sustained burning of the liquid as a diffusion flame [24]. These definitions are the result of an analysis of the heat and mass transfer between the surface of the liquid fuel and the flame.

Spalding [24] described this theory of burning liquids using a dimensionless parameter known as a transfer number or B-number. The B-number can be used to describe any conserved property of the liquid fuel system. Definitions of the B-number are typically given for mass transfer and heat transfer. For mass transfer

$$B_M = \frac{m_{fs} + m_{og}/r}{1 - m_{fs}} \tag{3.4}$$

and for heat transfer

$$B_H = \frac{m_{og}\,\Delta H_c/r + C\left(T_g - T_s\right)}{Q} \tag{3.5}$$

where m_{fs} was the mass of fuel vapor just above the liquid surface per unit mass of mixture, m_{og} was the mass of oxygen in the gas distant from the liquid surface per unit mass of mixture, r was the mass of oxygen required to completely burn a unit mass of flammable vapor, ΔH_c was the heat of combustion, C was the specific heat, T_g was the gas temperature, T_s was the surface temperature, and Q was the heat transferred from the flame to the liquid surface per unit mass of liquid evaporated [24].

Roberts and Quince [25] expanded on this analysis by exploring the concept of a limiting condition for the burning of flammable liquids. The expanded analysis was achieved by providing a definition of the B-number at flame extinction. The critical value was given by

$$(B)_{\text{crit}} = \frac{m_{og}}{r}\frac{\hat{T}_r - T_s}{\hat{T}_r - (T_r)_{\text{crit}}} \tag{3.6}$$

where $\hat{T}_r$ was the maximum achievable flame temperature (by setting $Q = 0$), and $(T_r)_{\text{crit}}$ was the value of the flame temperature at which flame failure occurred. Based on the critical value, the analysis concluded that the mass concentration of oxygen in the gas stream divided by the product of the mass of oxygen required for combustion per unit mass of fuel and the B-number, used in conjunction with each other, was a much better distinguishing parameter than solely the B-number [25]. Roberts and Quince also concluded that 1600 K was a theoretical flame temperature below which extinction would occur in most flammable liquids [25].

While the theoretical and experimental studies by Spalding [24] and Roberts and Quince [25] have been beneficial, the use of the fire point as a means to predict flame extinction is limited. The assumptions for this parameter require that the transport

phenomena remain constant, which is a reasonable assumption when buoyancy dominates the problem. Thus, in normal gravity, the fire point is an appropriate, simple tool for the prediction of flame extinction. As gravity is reduced though, the transport phenomena are no longer constant, and the use of the fire point as an extinction parameter can no longer be relied upon. Ultimately, a fire point extinction parameter is a simplified version of the Damköhler number.

3.5. Critical Mass Flux of Fuel for Extinction

Further research by Rasbash [26] and Rasbash et al. [27] has examined the heat flux to the surface of a fuel coupled with a surface temperature as a means to explain the production of volatiles necessary to support combustion [26, 27]. These studies established a link between gas-phase extinction and the condensed fuel feeding the flame by means of a critical mass flux of fuel from a fuel surface to the flame. The critical mass flux of fuel from a fuel surface to the flame is inevitably tied to a heat balance between the flame and the surface of the fuel, and to the critical adiabatic flame temperature for extinction.

In the work by Rasbash, the importance of the critical heat flux was determined through detailed examination of the various parameters affecting the fire point equation [26]. The focus of the analysis by Rasbash was the surplus amount of heat that could enter the fuel and the fraction of the heat of combustion of the fuel that was transferred from the flame to the surface. This phenomenon was expressed through the following relationship:

$$S_c = \left(\phi \Delta H_c - \lambda_f\right) \frac{h}{C} \ln\left(1 + \frac{m_{og}\, \Delta H_c / r + C\left(T_g - T_s\right)}{\phi \Delta H_c}\right) + R_a - R_s \tag{3.7}$$

where S_c was the critical value of the net sensible heat that entered the fuel in unit time, ϕ was the maximum fraction of the heat of combustion that the flame reaction zone lost to the fuel surface by convection, λ_f was the heat that needed to enter the fuel to produce a unit mass of vapor, h was the heat transfer coefficient by

convection, R_a was the heat transfer to the burning surface of the fuel other than by convection, and R_s was the heat transfer from the surface of the burning fuel to the environment [26].

Based on Equation (3.7), other critical parameters were developed by Rasbash that could be associated with critical ignition by a pilot and could also be extended to predict extinction. The three parameters were the critical rate of convective heat transfer from the flame to solid, the critical rate of emission of volatiles, and the critical flame temperature [26].

In a later study by Rasbash et al. [27], the previous analysis was further expanded by focusing on the critical flow of volatiles (i.e., mass flow) that was sufficient to support a flame that could lose heat to the surface of the fuel without the flame temperature being reduced to a point where extinguishment occurred. The study defined three properties of the fuel volatiles that were the most important: the heat of combustion of the volatiles, the heat required to produce the volatiles at the fire point condition, and the maximum fraction of the heat of combustion that a flame could lose to the surface without being extinguished [27].

The maximum fraction of the heat of combustion that a flame could lose to the surface without being extinguished depends on the reactivity of the fuel volatiles (i.e., chemical kinetics). The reactivity cannot be determined independently. It must instead be related to the critical mass flux of fuel volatiles at the fire point [27]. Thus, ignition is a transient phenomenon representing the limiting condition for the establishment of a diffusion flame at the surface. The process is mathematically complex, due the interaction of chemical kinetics, heat and mass transfer, and the precise aero-dynamic conditions existing at the surface at ignition [27].

Rasbash et al. [27] suggested that the ignition condition could only be explored with a B-number, but his suggestion introduced limitations on the problem (e.g., taking radiant heat into account). The direction proposed by Rasbash et al. does provide an

approximate method of relating the critical mass flux of volatiles at the fire point to the stability of the combustion process within the flame [27].

Using a heat and mass balance analysis, Rasbash et al. [27] described some general relationships which were based on various assumptions. Their first assumption was that the reaction rate was infinite. This assumption was not physically possible due to the resulting extinction of the flame becoming extremely difficult. As the flow of fuel vapor decreased below a certain point, extinction would, in fact, occur. For the fuel vapor to flow above its critical level, the flame temperature must exceed a critical value. In this case, the flame temperature remains a component of the Damköhler number, but if the remaining variables in Equation 3.7 remain constant, then the critical temperature can represent an extinction condition. The thickness of this reaction zone is dependent on the aerodynamic conditions and the flame geometry relative to the fuel. If these factors are constant, increasing the reactivity of the fuel will result in lowering the maximum flame temperature. For premixed propagation in diluents, as well as for some diffusion flame studies, this value is approximately 1500K-1600K [27].

According to Rasbash et al., for a flame to exist at the maximum temperature, the mass burning rate must exceed the critical mass burning rate [27]. To further understand this concept, Rasbash et al. developed a test methodology to accurately measure the critical mass flow rate of the volatiles of a solid sample. The critical mass flow rate of the volatiles was determined by examining the limiting slope of the data (i.e., prior to sustained ignition). The results suggested that a fire point can be characterized by a temperature, but the critical flow rate of the volatiles was dependent on experimental parameters. To account for this dependency, the theoretical framework incorporated a critical B-number [27].

Similar to the earlier analysis by Rasbash [26], the fire point equation was expressed as

$$S = \phi H_o + L(\phi - 1)\dot{m}''_c + R_a - R_s \tag{3.8}$$

where S was the net sensible heat that entered the fuel in unit time, ϕ was the maximum fraction of the heat of combustion that the flame reaction zone lost to the fuel surface by convection, H_o was the net heat of combustion of the solid, L was the heat required to produce the volatiles under steady burning conditions, and $\dot{m}''_c$ was the critical rate of flow of fuel from the surface per unit area. Application of a mass transfer approach from Spalding [24] resulted in a relationship between the critical mass flow of fuel and a critical B-number,

$$\dot{m}''_c = \frac{h}{C}\ln(1 + B_c) \tag{3.9}$$

where B_c was the critical value of the B-number and was given by

$$B_c = \frac{m_{og}\,\Delta H_c/r + C(T_g - T_s)}{\phi \Delta H_c} \tag{3.10}$$

Based on an analysis of the data presented by Rasbash et al. [27], the critical mass flow rate of the volatiles increased with an imposed heat flux. This result was not consistent with the proposed theory and suggested that at least one factor that affects the flame stability was changing with the imposed heat flux [27].

The critical mass flux for extinction provides a link between gas-phase extinction and the condensed fuel feeding the flame. In specific cases, the use of this parameter as a means of prediction extinction is valid. However, this use is limited, and the parameter is not broad enough to encompass the varied aspects of flame extinction that can be incorporated through the use of a critical Damköhler number for extinction.

3.6. Scalar Dissipation Rate

More recent combustion studies and researchers [28, 29, 30, 31, 32] have approached flame extinction through the use of a critical scalar dissipation rate. The scalar

dissipation rate represents the rate of the molecular mixing of reactant in a diffusion flame [30, 32]. The rate is typically defined for the mixture fraction, Z, as

$$\chi = 2D_Z(\nabla Z)^2 \tag{3.11}$$

where D_Z is the diffusion coefficient of the mixture fraction. The mixture fraction, Z, is a variable that can be used to relate various gaseous quantities within a particular combustion problem. For example, in a simplified counter-flow flame problem with a one-step reaction in the form of $\upsilon_F \mathrm{F} + \upsilon_O \mathrm{O} \rightarrow \mathrm{P}$, the mixture fraction is defined as

$$Z = \frac{\bar{\upsilon} Y_F - Y_O + Y_{O,2}}{\bar{\upsilon} Y_{F,1} + Y_{O,2}} \tag{3.12}$$

where the subscripts 1 and 2 refer to the fuel stream and oxidizer stream, respectively [30]. Additionally, the term, $\bar{\upsilon}$, is

$$\bar{\upsilon} = \frac{\upsilon_O W_O}{\upsilon_F W_F} \tag{3.13}$$

where W_i is the molecular weight of either the fuel or oxidizer [30]. The use of the mixture fraction is very convenient for reducing the number of variables found in the set of general equations for a nonspecific combustion problem and can lead to simplified solution methods.

In general, the scalar dissipation rate can be described as a characteristic transport time scale for the mixing of reactants in a combustion problem [32]. This definition is very similar to previous definitions of the Damköhler number, as described in Section 3.3. In principal, the use of a critical scalar dissipation rate as a means for predicting flame extinction is viable. However, there are several negative aspects of using a critical scalar dissipation rate as opposed to a critical Damköhler number for extinction.

First, when examining Equation (3.11), a physical understanding of the scalar dissipation rate is less transparent than when examining the Damköhler number. The

Damköhler number exists with a very clear definition: the ratio of the flow time to the chemical time. Second, the experimental measurement of the scalar dissipation rate is problematic due to very demanding spatial and temporal resolutions required to obtain measurements [32]. Additionally, studies that include experimental measurements of the scalar dissipation rate have been conducted utilizing idealized non-premixed jet or counter-flow flame problems and have not been extended to encompass combustion problems in general three-dimensional environments [28, 29, 31, 32]. Third, estimates of the scalar dissipation rate from other measured quantities require many simplifications and must take into account the difference in a global scalar dissipation rate as well as in a local scalar dissipation rate [32].

While the use of a critical scalar dissipation rate is not without its problems, the use of either it or a critical Damköhler number for flame extinction is a valid approach as a means of prediction. This study proposes that the use of a critical Damköhler number for flame extinction is more feasible due to the relative ease with which the terms that compose the Damköhler number can be determined through experimental or computational means. This concept will be explored in greater detail in Chapter 4.

3.7. Fire Suppression Research in Microgravity

Space facilities and space vehicles have traditionally been equipped with fire extinguishers as protection against fires with the potential to spread throughout the facilities [3]. In the past, the extinguishing methods in microgravity environments have been based upon the success of extinguishing methods observed in terrestrial environments. In the Gemini and Mercury space vehicles, a water gun was labeled for use as an emergency extinguisher [3]. In the Apollo space vehicle, foam-based extinguishers were available [3]. For the Shuttle Orbiter, Halon 1301 extinguishers were developed and installed [3].

While Halon 1301 is extremely effective at extinguishing fires due to its ability to interrupt the chemical chain reactions within the flame by grabbing free radicals, the

manufacturing of this gaseous agent is now universally banned due to the potential for ozone depletion. Thus, the Halon class of agents cannot be considered for current use aboard space facilities and space vehicles.

More recently, researchers have focused on a selection of a viable extinguishing agent for the International Space Station (ISS) and the next generation reusable space vehicle [3]. Carbon dioxide, nitrogen, Halon alternatives, and water mist have all been proposed as replacement agents for Halon 1301. Thus, microgravity fire suppression research has focused intensively on the effectiveness of these individual suppression agents. The next four sections in this chapter present research examining the individual effectiveness of Halon alternatives, carbon dioxide, nitrogen, and water mist.

3.7.1. Microgravity Suppression with Halon Alternatives

VanDerWege et al. [33] conducted one of the first studies in microgravity suppression by examining the effects of Halon 1301 (i.e., Bromotrifluoromethane, $CBrF_3$) and a Halon alternative, trifluoromethane (i.e., CF_3H) on the structure and stability of a jet diffusion flame. The experiments were conducted in a 2.2 second drop tower. During testing, the suppression agents were added at varying concentrations to the oxidizer environment.

Experiments were conducted within a matrix of normal and microgravity conditions and atmospheric and low-pressures. VanDerWege et al. determined that the stability limits for the microgravity flames were much greater than corresponding limits observed with terrestrial flames [33]. Additionally, the low-pressure normal gravity flames closely matched the microgravity flames in shape and structure. When the pressure was lowered, the normal gravity flames destabilized to the point of extinction [33]. This result was not observed with the corresponding microgravity flames, which were stable under microgravity conditions [33].

Bundy et al. [34] more thoroughly examined the suppression effectiveness of trifluoromethane, CF_3H, through the use of a counter-flow burner in low strain normal gravity conditions. The strain rate of a flow is directly related to the velocity of the gases in the system. Flame extinction at low strain rates in normal gravity can be compared to flame extinction in microgravity. During the experiment, the suppressant agent was added to both the fuel flow and the oxidizer flow, and the minimum critical concentration for flame extinction at each strain rate was recorded. The results indicated that the critical agent volume fraction for extinction was 0.437 when introduced in the fuel stream and 0.043 when introduced in the oxidizer stream [34]. While not as effective as Halon 1301, the concentration limits of trifluoromethane were promising for suppression. The tradeoff for using this was the potential hazards associated with the use of trifluoromethane in a confined self-contained environment.

3.7.2. Microgravity Suppression with Carbon Dioxide

Carbon dioxide (CO_2) has long been used as a gaseous suppressant agent in terrestrial environments. The process of terrestrial extinguishment with carbon dioxide occurs through several mechanisms. First, the carbon dioxide gas displaces the oxidizer necessary to support combustion. Displacement of the oxidizer causes the flame temperature to drop, as well as the speed at which a flame grows [35]. Second, carbon dioxide cools the reaction zone by increasing the heat capacity of the local atmosphere [35]. This also reduces the flame temperature. Third, carbon dioxide has a small endothermic reaction effect that results in the reduction of the flame temperature [35].

In normal gravity, extinguishment with carbon dioxide is aided by buoyancy. Flame extinction occurs due to the ability to blow-off the flame. The generation of a strong convective flow and a stable fire over a surface allow for the carbon dioxide to be delivered to the reaction zone such that heat losses and kinetic effects lower the rate of the reaction sufficiently below the convective flow of the gases [35]. In quiescent

microgravity environments, the convection term is removed. As a result, suppression can only occur through quenching of the flame [35].

To ensure extinguishment in normal and microgravity conditions, the gaseous agent must remain in place at a particular concentration until the flame extinguishes. In terrestrial applications utilizing carbon dioxide, this is typically accomplished with either a total flooding or local flooding process. NFPA 12 [36] provides guidance on the appropriate percent volume of carbon dioxide needed to ensure extinguishment for both smoldering and flaming fires. Smoldering fires require a 50% volume of carbon dioxide, and flaming fires require 34%. Table 3.1 lists the resulting oxygen concentrations when a 50% or 34% carbon dioxide concentration is required for various initial oxygen conditions as presented by Hirsch et al. [35].

	Residual Oxygen Concentration (% O_2)	
Initial Oxygen %	Using 50% CO_2	Using 34% CO_2
20.9	10.5	13.8
25.0	12.5	16.5
30.0	15.0	19.8

Table 3.1: Calculated residual oxygen concentrations when using carbon dioxide fire suppression (after [35]).

In the table presented by Hirsch et al. [35], the initial concentration was varied based on proposed oxygen environments aboard the ISS. An initial oxygen concentration of 30% would be the most challenging to displace through the use of carbon dioxide flooding. As mentioned previously, lowering the local oxygen concentration to less than 15% will result in extinguishment of the flame when using carbon dioxide in terrestrial applications [19, 35]. At the 25% and 30% initial oxygen concentrations, a 34% volume of carbon dioxide will not reduce the local level of oxygen to a point where extinction would occur. Based on these numbers derived from terrestrial

applications, the recommendation proposed by Hirsch et al. was to design a carbon dioxide system to achieve a concentration of 50% for microgravity suppression [35].

The above recommendation is based on the extinguishing behavior of carbon dioxide in a terrestrial environment. This recommendation is presented as a conservative approach to the design concentration for microgravity. Further research by Bundy et al. [34], Katta et al. [37], and Takahashi [38] has been conducted in microgravity conditions on the suppression effectiveness of carbon dioxide to determine more precisely what carbon dioxide concentration is needed for suppression in microgravity.

Bundy et al. [34] examined the suppression effectiveness of carbon dioxide through the use of a counter-flow burner in low strain normal gravity conditions. During the experiment, the suppressant agent was added to both the fuel flow and the oxidizer flow, and the minimum critical concentration for flame extinction at each strain rate was recorded. The results indicated that the critical agent volume fraction for extinction was 0.773 when introduced in the fuel stream and 0.187 when introduced in the oxidizer stream [34]. This large range was due to the differences in how the CO_2 was introduced into the flow domain. Neither the introduction of the suppressant in either the fuel stream or in the oxidizer stream could completely account for the overall mechanism by which a free-burning diffusion flame (i.e., fuel and oxidizer are converging together at the reaction zone with the suppressant) will be extinguished in microgravity. Thus, the application of the data from this study is limited.

Katta et al. [37] used a cup-burner flame configuration to determine the suppressant effectiveness of carbon dioxide in microgravity conditions. In the study, a methane-oxygen cup-burner diffusion flame was presented experimentally as well as computationally. The results of the computational study suggested that in microgravity conditions a carbon dioxide volume fraction of 19% would be sufficient

to destabilize the base of the flame, resulting in the movement of the reaction zone away from the area where the fuel was being generated [37].

In the study by Takahashi et al. [38], further experiment data using the cup-burner configuration in microgravity conditions was obtained. For these experiments, microgravity was achieved through parabolic flight testing in the National Aeronautics and Space Administration (NASA) Reduced Gravity Aircraft [38]. When microgravity conditions were achieved, various concentrations of carbon dioxide were introduced into the co-flow oxidizer stream of the cup-burner. Tests were conducted for both a 21% initial oxygen atmosphere and a 30% initial oxygen atmosphere. Results for the 21% initial oxygen atmosphere indicated that a carbon dioxide volume fraction of 0.23 was needed to achieve flame extinction. For the 30% initial oxygen atmosphere, a carbon dioxide volume fraction of 0.44 was needed to achieve flame extinction [38].

The research presented by Katta et al. [37] and Takahashi et al. [38] suggests that a design concentration of 50% for carbon dioxide suppression applications is fairly conservative. In atmospheric oxygen conditions of 21%, this number is more than double the needed concentration for suppression in small-scale microgravity experiments. Due to the inherent fire safety concerns within space facilities and space vehicles, the factor of safety built into the higher design value of 50% should not be ignored.

3.7.3. Microgravity Suppression with Nitrogen

Nitrogen (N_2) is an inert, non-toxic gas that has also been used as a suppression agent in terrestrial environments. The process of terrestrial extinguishment with nitrogen is similar to that of carbon dioxide. However, nitrogen is not as effective as carbon dioxide due to the mechanism of suppression for the nitrogen gas. As with carbon dioxide, nitrogen will displace the oxidizer necessary to support combustion. According to Hirsch et al. [35], even though carbon dioxide will induce flame

extinction at reduced local oxygen concentrations of 15% and lower, nitrogen concentrations must be large enough to lower the local oxygen concentration to 12%. Nitrogen will also cool the reaction zone by increasing the heat capacity of the local atmosphere, although this effect is much smaller when compared to carbon dioxide [35].

Bundy et al. [34] also examined the suppression effectiveness of nitrogen through the use of a counter-flow burner in low strain normal gravity conditions. During the experiment, the suppressant agent was added to both the fuel flow and the oxidizer flow, and the minimum critical concentration for flame extinction at each strain rate was recorded. The results indicated that the critical agent volume fraction for extinction was 0.841 when introduced in the fuel stream and 0.299 when introduced in the oxidizer stream [34]. These values are both much higher than similar values observed for carbon dioxide.

Further research by Hamins et al. [39] revisited the concentration of nitrogen needed within the fuel stream to achieve flame extinction. The study utilized a counter-flow burner to gather extinction data as well as companion microgravity modelling predictions. The results of the study reported that a critical volume concentration for extinction was 0.855 [39]. This value was consistent with previous research by Bundy et al. [34] and confirmed that, while nitrogen can be used as a flooding agent for suppression, it is not as effective as carbon dioxide in microgravity conditions.

3.7.4. Microgravity Suppression with Water Mist

According to Abbud-Madrid et al. [40], water mist fire suppression involves the use of very fine water spray with droplet sizes much smaller than those found in typical sprinkler systems. These droplet sizes are extremely small and on the order of less than 200 microns [40]. Based on these small sizes, water mist systems are commonly characterized by a droplet-size distribution. A common mist distribution is represented by either a log-normal curve (e.g., $D_{v,90}$, which is defined as the

diameter below which 90% of the water volume exists), or by the count median diameter (CMD), which is the diameter that divides the number of droplets into two equal halves [40].

Water mist droplets contribute to flame suppression by interacting with a flame through several means. First, the droplets act as a heat sink, absorbing energy from the reaction zone and reducing the overall flame temperature of the reaction. Second, gaseous water vapor acts as an effective third body within the reaction mechanisms of combustion and facilitates radical recombination and a lowering of the reaction rate [40]. Third, surface wetting of the water droplets makes fire growth and spread over wet surfaces more difficult. Fourth, a droplet aerosol that has not been gasified by the heat from the flame zone acts as a radiation shield and prevents the transfer of radiative heat from the flame to other combustible surfaces [40].

Due to the fire suppression benefits and the lack of an effective replacement for Halon 1301, fine water mists have begun to be examined as a potential suppression agent in microgravity conditions [40, 41]. An experiment was designed by Abbud-Madrid et al. [40] to examine the interaction of a propagating premixed flame with various water loadings of a fine water mist. This experiment was conducted aboard the STS-107. The results indicated that as the concentration of water mist increased in the chamber with the premixed flame, the flame speed decreased and the flame became less stable. Near extinction of the flame was achieved at a water loading of 3.3%, and total extinction of the flame was observed at a water loading of 4.8% [40, 41].

The use of water as an extinguishing agent is appealing because water is non-toxic, non-corrosive, and readily available in space facilities and space vehicles [40]. Water mists have been show to be effective in extinguishing over a broad range of applications in terrestrial environments. Additionally, agent cleanup operations in space facilities and space vehicles would be fairly simple after a potential discharge, through the use of dehumidifiers in the ventilation system [40]. These potential

advantages are significant, but further research is necessary to determine the most appropriate means to ensure agent delivery to the combustion zone and the overall effectiveness of water mist in diffusion flame extinction in microgravity.

3.8. Conclusions

In Chapter 3, the concepts of fire suppression and flame extinction have been reviewed, with emphasis being given to flame extinction of diffusion flames. Traditional flame extinction research can be separated into four categories: an asymptotic analysis for flame ignition and extinction, a critical flame temperature for extinction, a critical mass flux of fuel from the surface of the burning material necessary to sustain the flame reaction, and a critical scalar dissipation rate for extinction. Several studies that outline these approaches have been presented. Additionally, a review of the current microgravity research, with emphasis on flame suppression and extinction through the use of Halon alternatives, carbon dioxide, nitrogen, and water mist, has been discussed.

A review of the flame extinction literature suggests that a critical Damköhler number, which relates the characteristic time of the flow to the characteristic time of the chemical reaction, is a strong parameter that can be used to quantify flame extinction in normal and microgravity diffusion flame suppression applications. Conversely, the use of the fire point as a means to predict flame extinction is limited. Ultimately, the fire point as an extinction parameter is a simplified version of the Damköhler number. The critical mass flux for extinction provides a link between gas-phase extinction and the condensed fuel feeding the flame. The use of the critical mass flux for extinction is limited, though, and the parameter is not broad enough to encompass the varied aspects of flame extinction that can be incorporated through the use of a critical Damköhler number for extinction. While the use of a critical scalar dissipation rate for flame extinction is a valid approach as a means of prediction, it is proposed in this study that the use of a critical Damköhler number for flame extinction is more feasible due to the relative ease with which the terms that

compose the Damköhler number can be determined through experimental or computational means.

As has been discussed in Chapter 3, microgravity flame suppression research is currently focused on the evaluation of the effectiveness of various gaseous agents (e.g., Halon alternatives, carbon dioxide, and nitrogen) and water mist as potential replacements for Halons. Based upon the review of flame extinction literature and microgravity flame suppression research, it is suggested that a critical Damköhler number for extinction provides the most complete means of accounting for the addition of a suppressant gas, as well as for quantifying the gas-phase flame extinction and fire suppression over a nonspecific diffusion flame problem in any three-dimensional environment at normal or microgravity conditions.

Chapter Four

4. Theoretical Framework

4.1. Introduction

The goal of designing a methodology for the prediction of flame extinction and suppression in normal gravity or microgravity relies on the fundamental understanding of two equally important aspects of the problem: the delivery of the agent to the reaction zone and the prediction of the agent interaction with the reaction zone upon its arrival. These two aspects are highly coupled and must both be adequately addressed in order to accurately predict flame extinction and suppression.

As was discussed in Chapter 3, the Damköhler number is a derived, non-dimensional parameter that is the ratio of the characteristic time of the flow to the characteristic time of the chemical reaction. A review of the scientific literature suggests that a generalized description and definition of the Damköhler number provides the most complete means of accounting for the addition of a suppressant gas, as well as for quantifying the gas-phase flame extinction and fire suppression over a nonspecific diffusion flame problem in any three-dimensional environment at normal or microgravity conditions.

Chapter 4 presents the theoretical framework for the development of a generalized Damköhler number that can be used to predict local flame extinction. A methodology for application of the theoretical framework will be discussed, with emphasis placed on the coupling of the Damköhler number with computational fluid dynamics modelling for the transport aspect of the problem.

First, the development of a generalized Damköhler number will be presented for any three-dimensional geometry. Second, an analysis of the velocity-strain relationship applicable to the problem will be discussed. Third, velocity deviations influenced by the active combustion reaction zone within the velocity-strain relationship will be addressed. Fourth, an outline for the general problem methodology will be established.

4.2. Development of a Generalized Damköhler Number

A model by Wichman [42] outlined the development of a Damköhler number for use in a two-dimensional diffusion flame spread case. Following a similar procedure to that outlined by Wichman [42], but considering a general three-dimensional volume where the conditions within the volume can change spatially as well as with respect to time, the below analysis can be developed.

4.2.1. Conservation of Mass

The equation for continuity for a mixture of species can be determined by making a mass balance over a differential element. Following Kuo [5], the region of volume in fixed space through which a fluid is flowing depicted in Figure 4.1.

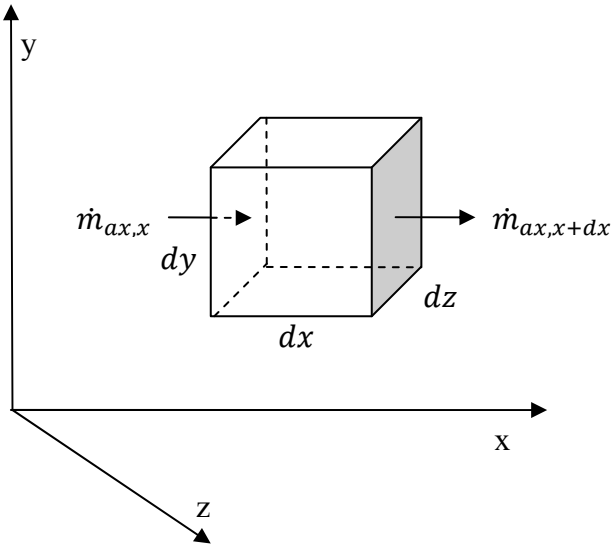

Figure 4.1: A region of volume in space through which a fluid is flowing (after Kuo [5]).

In this space a binary mixture of a and b are flowing through the volume $dxdydz$. Species a could be produced by a reaction, ω_a. Mass balance components are then

$$\frac{\partial \rho_a}{\partial t} dxdydz \tag{4.1}$$

which is the rate change of the mass with respect to time of a in the volume element,

$$\dot{m}_{ax,x} dydz \tag{4.2}$$

which is the input across the face at x,

$$\dot{m}_{ax,x+dx} dydz = \dot{m}_{ax,x} dydz + \frac{\partial \dot{m}_{ax}}{\partial x} dxdydz \tag{4.3}$$

which is the output across the face at $x + dx$, and

$$\omega_a dxdydz \tag{4.4}$$

which is the rate of production of a by chemical reaction. Output and input terms also must be accounted for in the y and z directions. The derivations of these terms are similar to those presented in Equations (4.2) through (4.4). Including these terms in the mass balance yields

$$\frac{\partial \rho_a}{\partial t} + \left(\frac{\partial \dot{m}_{ax}}{\partial x} + \frac{\partial \dot{m}_{ay}}{\partial y} + \frac{\partial \dot{m}_{az}}{\partial z} \right) = \omega_a \tag{4.5}$$

For species b, Equation (4.5) can be written as

$$\frac{\partial \rho_b}{\partial t} + \left(\frac{\partial \dot{m}_{bx}}{\partial x} + \frac{\partial \dot{m}_{by}}{\partial y} + \frac{\partial \dot{m}_{bz}}{\partial z} \right) = \omega_b \tag{4.6}$$

Utilizing the law of conservation of mass, the rate of reaction terms for the two species can be expressed as

$$\omega_a + \omega_b = 0 \tag{4.7}$$

and the mass flow rate of the two species is

$$\left(\frac{\partial \dot{m}_{ax}}{\partial x}+\frac{\partial \dot{m}_{ay}}{\partial y}+\frac{\partial \dot{m}_{az}}{\partial z}\right)+\left(\frac{\partial \dot{m}_{bx}}{\partial x}+\frac{\partial \dot{m}_{by}}{\partial y}+\frac{\partial \dot{m}_{bz}}{\partial z}\right) \tag{4.8}$$

$$=\left(\frac{\partial(\rho u_x)}{\partial x}+\frac{\partial\left(\rho u_y\right)}{\partial y}+\frac{\partial(\rho u_z)}{\partial z}\right)$$

The addition of Equations (4.5) and (4.6) yields

$$\frac{\partial \rho}{\partial t}+\left(\frac{\partial(\rho u_x)}{\partial x}+\frac{\partial\left(\rho u_y\right)}{\partial y}+\frac{\partial(\rho u_z)}{\partial z}\right)=0 \tag{4.9}$$

In vector notation this can be expressed as

$$\frac{\partial \rho}{\partial t}+\left(\nabla \cdot \rho \vec{V}\right)=0 \tag{4.10}$$

4.2.2. Conservation of Momentum

The conservation equation for momentum can be derived from Newton's second law of motion [5]:

$$\sum \vec{F}=\frac{d\left(m\vec{V}\right)}{dt} \tag{4.11}$$

The motion of a fluid particle that is moving through space relative to some fixed coordinate system is described by Equation (4.11). The acceleration of this example particle can be related to other fixed points throughout the domain of the flow field. Figure 4.2 shows an example of an infinitesimal fluid particle moving in a three-dimensional space.

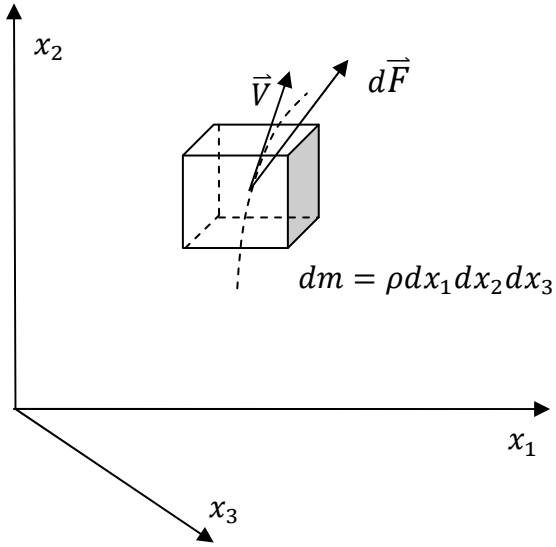

Figure 4.2: An infinitesimal particle moving in a three-dimensional space (after Kuo [5]).

This particle is moving through space with a velocity $\vec{V}$ and has a mass of dm. If the mass is fixed, then the net force, $d\vec{F}$, acting on the particle is given by

$$d\vec{F} = dm\frac{d(\vec{V})}{dt} \tag{4.12}$$

If the particle is observed as it transits through space, then the velocity of the particle can be expressed as the change in the Cartesian coordinates over time. The position of the particle is given by

$$x_1 = x_1(t), \qquad x_2 = x_2(t), \qquad x_3 = x_3(t) \tag{4.13}$$

Thus, the velocity of the particle can be expressed as

$$\vec{V} = \vec{V}[x_1(t), x_2(t), x_3(t), t] = \vec{V}(t) \tag{4.14}$$

And, similarly, the acceleration of the particle can be expressed as

$$\vec{a} = \vec{a}[x_1(t), x_2(t), x_3(t), t] = \vec{a}(t) \tag{4.15}$$

The acceleration can also be written as

$$\vec{a} = \frac{d\vec{V}}{dt} = \frac{\partial \vec{V}}{\partial x_1}\frac{dx_1}{dt} + \frac{\partial \vec{V}}{\partial x_2}\frac{dx_2}{dt} + \frac{\partial \vec{V}}{\partial x_3}\frac{dx_3}{dt} + \frac{\partial \vec{V}}{\partial t} \tag{4.16}$$

It is noteworthy that

$$\frac{dx_1}{dt} = u_1 \tag{4.17}$$

$$\frac{dx_2}{dt} = u_2 \tag{4.18}$$

$$\frac{dx_3}{dt} = u_3 \tag{4.19}$$

where

$$\vec{V} = \vec{\imath}u_1 + \vec{\jmath}u_2 + \vec{k}u_3 = [u_1, u_2, u_3] \tag{4.20}$$

Utilizing Equations (4.17) through (4.20), the acceleration can be expressed as

$$\frac{du_i}{dt} = u_1\frac{\partial u_i}{\partial x_1} + u_2\frac{\partial u_i}{\partial x_2} + u_3\frac{\partial u_i}{\partial x_3} + \frac{\partial u_i}{\partial t} \tag{4.21}$$

Equation (4.21) appears in a standard form that is commonly referred to as the Substantial Derivative. The operator is defined as

$$\frac{d}{dt} \equiv \frac{D}{Dt} \equiv u_1\frac{\partial}{\partial x_1} + u_2\frac{\partial}{\partial x_2} + u_3\frac{\partial}{\partial x_3} + \frac{\partial}{\partial t} \tag{4.22}$$

Equation (4.11) can now be written as

$$dF_i = dm\left[u_1\frac{\partial u_i}{\partial x_1} + u_2\frac{\partial u_i}{\partial x_2} + u_3\frac{\partial u_i}{\partial x_3} + \frac{\partial u_i}{\partial t}\right] \tag{4.23}$$

or

$$dF_1 = dm\frac{Du_1}{Dt} \tag{4.24}$$

$$dF_2 = dm\frac{Du_2}{Dt} \tag{4.25}$$

$$dF_3 = dm\frac{Du_3}{Dt} \tag{4.26}$$

Figure 4.3 depicts a diagram of the forces acting on the fluid particle.

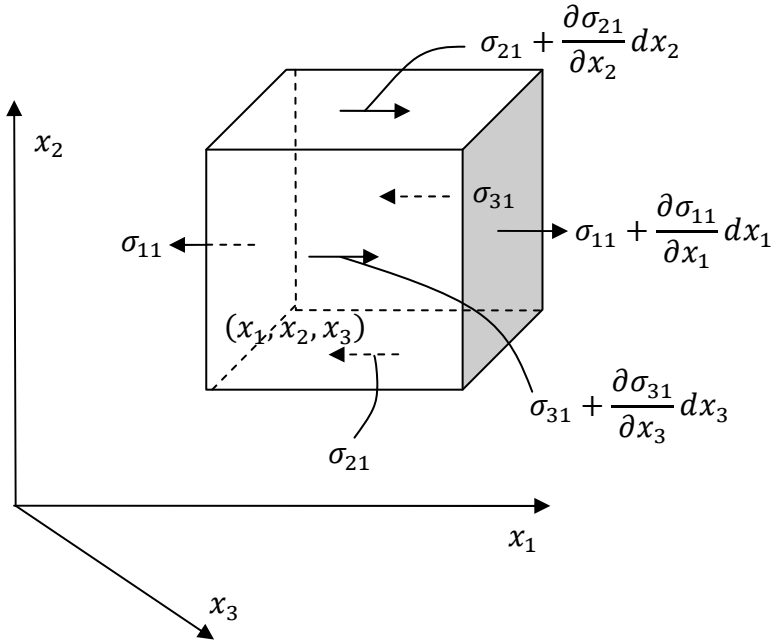

Figure 4.3: Force components (stress) acting on a fluid particle in one direction (after Kuo [5]).

The forces represented in the figure are the surface stress components in one dimension. These can be expanded to the two remaining dimensions. The net surface force acting on the different faces of the particle can be written as

$$df_1 = \left(\frac{\partial \sigma_{11}}{\partial x_1} + \frac{\partial \sigma_{21}}{\partial x_2} + \frac{\partial \sigma_{31}}{\partial x_3}\right) dx_1\, dx_2\, dx_3 \tag{4.27}$$

$$df_2 = \left(\frac{\partial \sigma_{12}}{\partial x_1} + \frac{\partial \sigma_{22}}{\partial x_2} + \frac{\partial \sigma_{32}}{\partial x_3}\right) dx_1\, dx_2\, dx_3 \tag{4.28}$$

$$df_1 = \left(\frac{\partial \sigma_{13}}{\partial x_1} + \frac{\partial \sigma_{23}}{\partial x_2} + \frac{\partial \sigma_{33}}{\partial x_3}\right) dx_1\, dx_2\, dx_3 \tag{4.29}$$

The other force acting on this system is a body force per unit volume, B_i. The particle in Figure 4.3 has a mass, dm, and sides of length dx_1, dx_2, dx_3. The mass of the particle can be expressed as

$$dm = \rho\, dx_1\, dx_2\, dx_3 \tag{4.30}$$

and the differential forces can be expressed as

$$dF_i = df_i + B_i\, dx_1\, dx_2\, dx_3 \tag{4.31}$$

Substituting Equations (4.30) and (4.31) into (4.23) yields

$$\rho\left[u_1 \frac{\partial u_i}{\partial x_1} + u_2 \frac{\partial u_i}{\partial x_2} + u_3 \frac{\partial u_i}{\partial x_3} + \frac{\partial u_i}{\partial t}\right] dx_1\, dx_2\, dx_3 = df_i + B_i\, dx_1\, dx_2\, dx_3 \tag{4.32}$$

After dividing by $dx_1\, dx_2\, dx_3$ and converting into Cartesian tensor notation, Equation (4.32) is

$$\rho\left[u_i \frac{\partial u_i}{\partial x_j} + \frac{\partial u_i}{\partial t}\right] = \frac{\partial \sigma_{ji}}{\partial x_j} + B_i \tag{4.33}$$

Assuming a classical Newtonian fluid, the stress tensor, σ_{ji}, is

$$\sigma_{ji} = \mu\left(\frac{\partial u_i}{\partial x_j} + \frac{\partial u_j}{\partial x_i}\right), \qquad i \neq j \tag{4.34}$$

The general relationship between the strain and stress in the fluid particle [34] is given by

$$\sigma_{ji} = -P\delta_{ij} + \left(\mu' - \frac{2}{3}\mu\right)\frac{\partial u_k}{\partial x_k}\delta_{ij} + \mu\left(\frac{\partial u_i}{\partial x_j} + \frac{\partial u_j}{\partial x_i}\right) \tag{4.35}$$

Assuming that the flow is incompressible, Equation (4.35) can be substituted into Equation (4.33). The result is the Navier-Stokes equation:

$$\rho\left[\frac{\partial u_i}{\partial t} + u_j\frac{\partial u_i}{\partial x_j}\right] = \frac{\partial P}{\partial x_i} + \frac{\partial}{\partial x_j}\left[\mu\left(\frac{\partial u_i}{\partial x_j} + \frac{\partial u_j}{\partial x_i}\right)\right] + B_i \tag{4.36}$$

which can also be expressed in Cartesian coordinates as

$$\rho\left(u_x\frac{\partial u_x}{\partial x} + u_y\frac{\partial u_x}{\partial y} + u_z\frac{\partial u_x}{\partial z} + \frac{\partial u_x}{\partial t}\right) =$$

$$-\frac{\partial P}{\partial x} + \mu\left(\frac{\partial^2 u_x}{\partial x^2} + \frac{\partial^2 u_x}{\partial y^2} + \frac{\partial^2 u_x}{\partial z^2}\right) + \rho B_x \tag{4.37}$$

$$\rho\left(u_x\frac{\partial u_y}{\partial x} + u_y\frac{\partial u_y}{\partial y} + u_z\frac{\partial u_y}{\partial z} + \frac{\partial u_y}{\partial t}\right) =$$

$$-\frac{\partial P}{\partial y} + \mu\left(\frac{\partial^2 u_y}{\partial x^2} + \frac{\partial^2 u_y}{\partial y^2} + \frac{\partial^2 u_y}{\partial z^2}\right) + \rho B_y \tag{4.38}$$

$$\rho\left(u_x\frac{\partial u_z}{\partial x} + u_y\frac{\partial u_z}{\partial y} + u_z\frac{\partial u_z}{\partial z} + \frac{\partial u_z}{\partial t}\right) =$$

$$-\frac{\partial P}{\partial z} + \mu\left(\frac{\partial^2 u_z}{\partial x^2} + \frac{\partial^2 u_z}{\partial y^2} + \frac{\partial^2 u_z}{\partial z^2}\right) + \rho B_z \tag{4.39}$$

or in vector notation as

$$\rho\frac{\partial \vec{V}}{\partial t} + \rho\vec{V}\left(\nabla\cdot\vec{V}\right) = -\nabla P + \mu\nabla^2\vec{V} + \rho B \tag{4.40}$$

4.2.3. Conservation of Energy and Species

With appropriate expressions developed in the previous sections for the conservation of mass and momentum, a qualitative understanding of the application of the conservation of energy and species to a generalized three-dimensional environment is then necessary to define the assumptions and potential limitations of the Damköhler number as an extinction parameter for gas-phase combustion. Figure 4.4 shows a nonspecific fire within a nonspecific three-dimensional geometry.

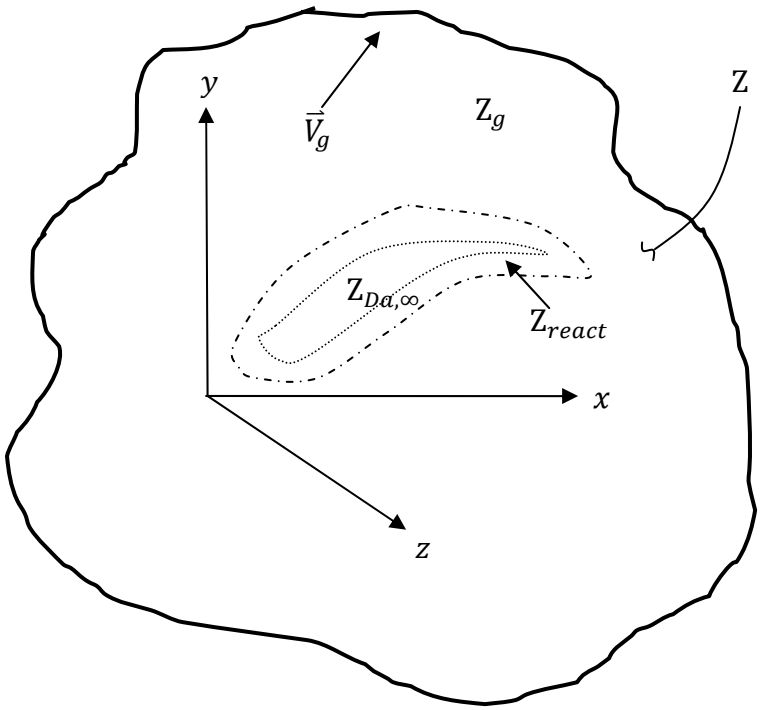

Figure 4.4: Generalized problem setup for nonspecific flame in a three-dimensional environment.

The overall region Z can be subdivided into three zones. Z_g is the region where the gaseous components are in motion throughout the domain. Z_{react} is the zone where the fuel and the oxidizer begin to mix. $Z_{Da,\infty}$ is the zone within the boundaries of the flame where a stable Damköhler number exists.

An analysis similar to that outlined for the conservation of momentum can be performed for the development of the conservation of energy and species equations. For the energy case, the balances in the control volume include the rate of accumulation of internal energy, the net rate of energy entering the problem from convection, the net rate of energy added through a heat flux, the rate of energy added by a heat source, and the net rate of work done on the surroundings [5]. The species equations for both the oxidizer and fuel follow similar reasoning to that of the energy equations.

With the same assumptions listed for the conservation of momentum, a general species equation can be expressed as

$$\frac{\partial Y_i}{\partial t} + \vec{V}(\nabla \cdot Y_i) = D_g \nabla^2 Y_i - \frac{\nu_i \dot{\omega}}{\rho} \tag{4.41}$$

and the energy equation can be written as

$$\frac{\partial T}{\partial t} + \vec{V}(\nabla \cdot T) = \alpha_g \nabla^2 T + \frac{\Delta H_c \dot{\omega}}{\rho C_p} \tag{4.42}$$

where

$$\dot{\omega} = A Y_o^m Y_f^n \exp\left(\frac{-E}{RT}\right) \tag{4.43}$$

$$\Delta H_c = C_p (T_F - T_\infty) \tag{4.44}$$

E is the activation energy of a one-step $(m+n)^{\text{th}}$ reaction where

$$\text{Fuel} + \nu_i \text{Oxidizer} \rightarrow \text{Products} \tag{4.45}$$

and ρ is the density. Equations (4.41) and (4.42) can be non-dimensionalized using the following definitions:

$$x' = \frac{x}{L_c}, y' = \frac{y}{L_c}, z' = \frac{z}{L_c}$$

$$\vec{V}' = \frac{\vec{V}}{U_c}, t' = t\frac{U_c}{L_c}, Y_o' = \frac{Y_o}{Y_{o,\infty}}, Y_f' = \frac{Y_f}{Y_{f,0}}$$

$$T' = \left(\frac{T}{T_F - T_\infty}\right)$$

$$\frac{E}{RT} = \frac{E}{RT_F} + \left(\frac{E}{R}\right)\left(\frac{1}{T} - \frac{1}{T_F}\right) = \frac{E}{RT_F} + \frac{\beta(1-T')}{1-\alpha(1-T')}$$

$$\beta = \left(\frac{E}{RT_F^2}\right)(T_F - T_\infty), \alpha = \left(\frac{T_F - T_\infty}{T_F}\right) \tag{4.46}$$

The exponent in the Arrhenius reaction rate term is non-dimensionalized using the local flame temperature. The β term represents the non-dimensional activation energy, which is much greater than unity. Substituting the preceding definitions into Equation (4.41) yields

$$\frac{\partial\left(Y_f Y_f'\right)}{\partial\left(\frac{L_c}{U_c}t'\right)} + \frac{U_c}{L_c}\vec{V}\cdot\nabla\left(Y_f Y_f'\right) =$$

$$\left(\frac{1}{{L_c}^2}\right)D_{g,f}\nabla^2\left(Y_f Y_f'\right) - \frac{1}{\rho}\left(AY_o^m Y_f^n \exp\left(\frac{-E}{RT_F}\right)Y_o'^m Y_f'^n \exp\left(\frac{-\beta(1-T')}{1-\alpha(1-T')}\right)\right) \tag{4.47}$$

for the fuel and

$$\frac{\partial(Y_o Y_o')}{\partial\left(\frac{L_c}{U_c}t'\right)} + \frac{U_c}{L_c}\vec{V}\cdot\nabla(Y_o Y_o') = \left(\frac{1}{{L_c}^2}\right)D_{g,o}\nabla^2(Y_o Y_o')$$

$$-\frac{\nu_o}{\rho}\left(AY_o^m Y_f^n \exp\left(\frac{-E}{RT_F}\right)Y_o'^m Y_f'^n \exp\left(\frac{-\beta(1-T')}{1-\alpha(1-T')}\right)\right) \tag{4.48}$$

for the oxidizer. Dividing through by $\left(\frac{U_c}{L_c}Y_f\right)$ yields

$$\frac{\partial Y_f'}{\partial t'} + \vec{V} \cdot \nabla Y_f' = \frac{D_{g,f}}{L_c U_c} \nabla^2 Y_f'$$

$$-\frac{1}{Y_f}\left(\left(\frac{A}{\rho \frac{U_c}{L_c}}\right) Y_o^m Y_f^n \exp\left(\frac{-E}{RT_F}\right) Y_o'^m Y_f'^n \exp\left(\frac{-\beta(1-T')}{1-\alpha(1-T')}\right)\right) \tag{4.49}$$

for the fuel, and by $\left(\frac{U_c}{L_c} Y_o\right)$ yields

$$\frac{\partial Y_o'}{\partial t'} + \vec{V} \cdot \nabla Y_o' = \frac{D_{g,o}}{L_c U_c} \nabla^2 Y_o'$$

$$-\frac{\nu_o}{Y_o}\left(\left(\frac{A}{\rho \frac{U_c}{L_c}}\right) Y_o^m Y_f^n \exp\left(\frac{-E}{RT_F}\right) Y_o'^m Y_f'^n \exp\left(\frac{-\beta(1-T')}{1-\alpha(1-T')}\right)\right) \tag{4.50}$$

for the oxidizer. Substituting the definitions from Equation (4.46) into Equation (4.42) yields

$$\frac{\partial\left((T_F - T_\infty)T'\right)}{\partial\left(\frac{L_c}{U_c} t'\right)} + \frac{U_c}{L_c} \vec{V} \cdot \nabla\left((T_F - T_\infty)T'\right)$$

$$= \left(\frac{1}{{L_c}^2}\right) \alpha_g \nabla^2\left((T_F - T_\infty)T'\right)$$

$$+ \frac{C_p(T_F - T_\infty)}{C_p}\left(A Y_o^m Y_f^n \exp\left(\frac{-E}{RT_F}\right) Y_o'^m Y_f'^n \exp\left(\frac{-\beta(1-T')}{1-\alpha(1-T')}\right)\right) \tag{4.51}$$

which then becomes

$$\left(\frac{U_c}{L_c}(T_F - T_\infty)\right)\frac{\partial T'}{\partial t'} + \left(\frac{U_c}{L_c}(T_F - T_\infty)\right)\vec{V} \cdot \nabla T' =$$

$$\left(\frac{(T_F - T_\infty)}{{L_c}^2}\right)\alpha_g \nabla^2 T'$$

$$+(T_F - T_\infty)\left(AY_o^m Y_f^n \exp\left(\frac{-E}{RT_F}\right) Y_o'^m Y_f'^n \exp\left(\frac{-\beta(1-T')}{1-\alpha(1-T')}\right)\right) \tag{4.52}$$

Dividing through by $\frac{U_c}{L_c}(T_F - T_\infty)$ results in

$$\frac{\partial T'}{\partial t'} + \vec{V}\cdot\nabla T' = \frac{\alpha_g}{L_c U_c}\nabla^2 T'$$

$$+\left(\left(\frac{A}{\rho\frac{U_c}{L_c}}\right) Y_o^m Y_f^n \exp\left(\frac{-E}{RT_F}\right) Y_o'^m Y_f'^n \exp\left(\frac{-\beta(1-T')}{1-\alpha(1-T')}\right)\right) \tag{4.53}$$

The reaction rate of both the fuel and the oxidizer can be related if the assumption is made that the flame exists as a flame sheet and that all reactants are consumed in the flame sheet. No fuel is found on the oxidizer side of the flame sheet, and no oxidizer is located on the fuel side of the flame sheet. Additionally, the assumption is made that the Lewis number, Prandtl number, and Schmidt number all are equivalent to unity [5]. This assumption results in the equivalency of the kinematic viscosity, molecular diffusivity, and thermal diffusivity [5]. With these assumptions, a new variable can be defined as

$$f' \equiv Y_f' - \frac{1}{\nu_o} Y_o' \tag{4.54}$$

which reduces Equations (4.49) and (4.50) to

$$\frac{\partial f'}{\partial t'} + \vec{V}\cdot\nabla f' = \frac{D_g}{L_c U_c}\nabla^2 f'$$

$$+\left(\left(\frac{A}{\rho\frac{U_c}{L_c}}\right)Y_o^m Y_f^n \exp\left(\frac{-E}{RT_F}\right)Y_o'^m Y_f'^n \exp\left(\frac{-\beta(1-T')}{1-\alpha(1-T')}\right)\right) \tag{4.55}$$

The similarity of Equations (4.53) and (4.55) allows for a single form of the solution to serve for both of the equations. Additionally, as a result of the kinematic viscosity, molecular diffusion, and thermal diffusion equivalency, the term $\frac{D_g}{L_c U_c}$ is equivalent to $\frac{\frac{\mu}{\rho}}{L_c U_c}$, which is the inverse of the Reynolds number, $\frac{1}{\mathrm{Re}}$. Thus, the most general form of the equation can be expressed as

$$\frac{\partial \Psi}{\partial t'} + \vec{V}\cdot\nabla\Psi = \frac{1}{\mathrm{Re}}\nabla^2\Psi + D_a\dot{\omega}' \tag{4.56}$$

where $\dot{\omega}'$ is the dimensionless reaction rate

$$Y_o'^m Y_f'^n \exp\left(\frac{-\beta(1-T')}{1-\alpha(1-T')}\right) \tag{4.57}$$

and where D_a is the Damköhler number and is

$$D_a = \left(\frac{A}{\rho\frac{U_c}{L_c}}\right)Y_o^m Y_F^n \exp\left(\frac{-E}{RT_F}\right) \tag{4.58}$$

4.3. Examination of the Damköhler number

The terms found in the expression of the Damköhler number in Equation (4.58) are characteristic variables around which the analysis of a critical Damköhler number for flame extinction generally depends. These characteristic variables have little meaning until defined using a method that can assign a local value to them that is problem specific.

Each variable, as it relates to any three-dimensional problem, can be potentially determined at a local level by one of three means: through documentation in the scientific literature, through computer modelling of the problem, or through experimentation. For this study, a variable may be obtained from the scientific literature if it remains a constant throughout the time history of the problem. Experimentation is problematic due to the limitations of measurement equipment. The spatially- and time-dependent variables in Equation (4.58) would be extremely challenging to tabulate over an entire three-dimensional geometry using experimental methods alone. Thus, the ideal solution would be to use computer modelling to predict the transport of reactants, products, and suppressant(s), and to calculate the Damköhler number, which can be used as a means to predict flame extinction within the modelled geometry.

Experimentation must be used in conjunction with the modelling effort as a means to provide validation data to ensure that the chosen modelling code can predict the appropriate and necessary quantities. Additionally, validation data will provide information on the level of accuracy of the model predictions.

An examination of Equation (4.58) can determine which variables are available in scientific literature and which variables must be predicted by computer modelling. Examining each variable in turn will allow for the link from a characteristic value to an actual local value.

The variable, A, is the pre-exponential constant for a particular combustion reaction taking place. The value of A can be obtained through literature sources for a wide variety of combustion reactions. The choice of a specific fuel for use in a particular computational model will define the pre-exponential constant as a local variable relative to the problem.

The variable, E, is the activation energy of a particular combustion reaction. Similar to the pre-exponential constant, this variable can be obtained through literature sources for a diverse group of reaction types and fuels.

The variable, R, is the universal gas constant. This particular variable is a known constant that is applied to most systems involving combustion.

The pre-exponential constant, the activation energy, and the universal gas constant are all terms within Equation (4.58) that are constant values for a particular problem. The remaining variables can change both spatially and with respect to time within a particular problem. Thus, these variables must be determined through an appropriate computational method such as computational fluid dynamics.

The density, ρ, is the local density of the gases throughout a modelled three-dimensional geometry. Computational fluid dynamics modelling can track the local average of this quantity at every node throughout a three-dimensional flow field.

The mass concentration of fuel and oxidizer, $Y_o^m Y_F^n$, can also be determined as local values through the use of computational fluid dynamics modelling. While the model predictions can track these variables globally throughout the model volume, the local values will be of critical importance in the area where the flame exists.

Similarly, model predictions for the local temperature throughout a three-dimensional volume can be determined through computational fluid dynamics modelling. Again, an average local temperature value at a particular node within a model can be determined and compared to other variables.

4.3.1. Determining a Strain Rate in Three Dimensions

The term $\frac{U_c}{L_c}$ is the ratio of a characteristic velocity to a characteristic length scale for the problem. This value is commonly referred to as the "strain" or "strain rate" of a

fluid flow problem. At a local level within a three-dimensional flow, this parameter is, fundamentally, the ratio of the rate of change of the velocity to the rate of change of a differential length scale.

To understand the strain rate for a three-dimensional geometry, the same infinitesimal particle depicted in Figure 4.2 can be considered. If one face of the particle is examined, the geometric changes imposed upon the surface of the particle can be more easily analyzed with regard to the deformation of the particle by the velocity flow over time.

The strain rate can be defined as the angular deformation of each side of the particle volume with respect to time [5]. Figure 4.5 shows an example of the angular deformation of one side of a fluid particle with changing time.

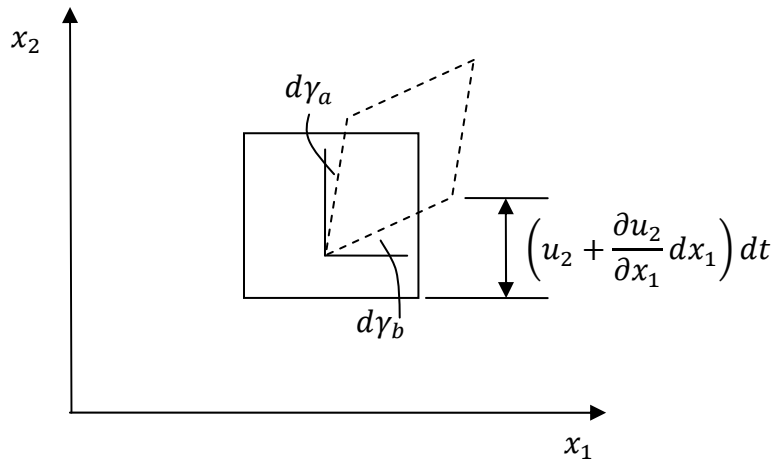

Figure 4.5: The deformation of one side of a fluid particle in two dimensions (after Kuo [5]).

The total angular deformation in Figure 4.5 is given by

$$d\gamma = d\gamma_a + d\gamma_b$$
$$= \frac{\left(u_1 + \frac{\partial u_1}{\partial x_2} dx_2\right) dt - u_1 dt}{dx_2} + \frac{\left(u_2 + \frac{\partial u_2}{\partial x_1} dx_1\right) dt - u_2 dt}{dx_1} \tag{4.59}$$

and thus

$$\frac{d\gamma}{dt} = \frac{\partial u_1}{\partial x_2} + \frac{\partial u_2}{\partial x_1} \equiv 2e_{12} = 2e_{21} \tag{4.60}$$

Equation (4.60) is the strain rate tensor for a general three-dimensional problem. The general form is

$$e_{ij} \equiv \frac{1}{2}\left(\frac{\partial u_1}{\partial x_2} + \frac{\partial u_2}{\partial x_1}\right) \tag{4.61}$$

The tensor form of the strain rate allows for the expansion of the equation into the strain rate of each individual face of the infinitesimal particle shown in Figure 4.2. The i and j terms listed in Equation (4.61) can be substituted with $x, y,$ and z coordinates to form the various strain rates on each face. The process of calculating a strain rate on each surface of a Cartesian infinitesimal particle can be accomplished through the use of a computational fluid dynamics model at each node in a three-dimensional flow field.

Due to the complexity of the strain rate term, a modelling approach is currently the most practical way to predict this quantity over a large three-dimensional volume. In essence, a computational model will calculate the average strain rate at each node refined by the model. This average value will have some error associated with it, but will increase in accuracy as the node resolution is increased.

4.3.2. Velocity Field Deviations due to the Reaction Zone

When examining the local area surrounding a counter-flow diffusion flame, research [43] has demonstrated that the local flow velocity deviates from the predicted “no

flame" velocity as the flow begins to transit into the reaction zone. Tsuji and Yamaoka [43] conducted a counter-flow diffusion flame study where the velocity of the counter-flow was precisely measured with an established diffusion flame. These values were compared with the expected velocity and strain values dictated by the geometric setup of their two-dimensional flow problem. Figure 4.6 presents a graphical representation of the error induced by the presence of the reaction zone.

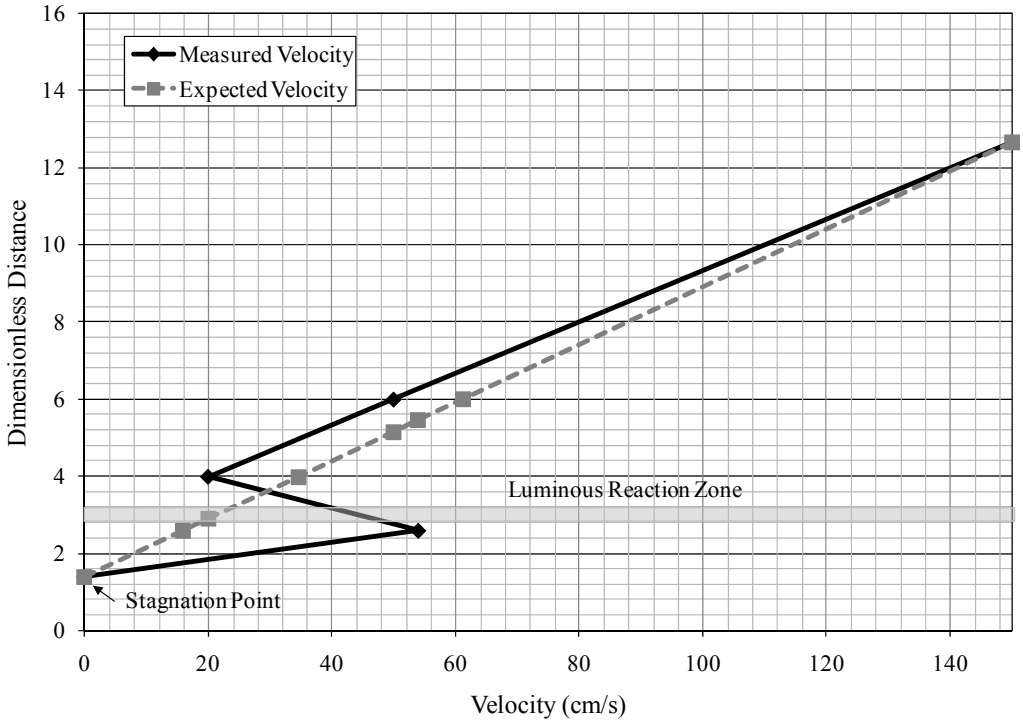

Figure 4.6: Variation of the velocity due to the influence of the reaction zone.

The figure demonstrates that without the influence of the flame, the velocity decreases linearly as it approaches the stagnation point in the counter-flow field. With the reaction zone present, the velocity decreases more slowly when moving from infinity towards the reaction zone. Once a critical distance away from the reaction zone is reached, the velocity increases as the consumption and production of reactants and products exert influence over the local velocity flow field. After

passing through the reaction zone, the velocity decreases very rapidly until the stagnation point is achieved.

While the reaction zone does influence the flow field in the local area of the flame, the actual distances in which this occurs are very small. With a node resolution that is fine enough around the area of the flame, these velocity changes and resultant strain deviations can be directly calculated by a computational model. Thus, the complexity of the flow field requires a robust modelling approach to determine the strain quantity over a three-dimensional volume.

4.3.3. General Problem Methodology

The examination of the characteristic variables in the Damköhler number as presented throughout Chapter 4 has led to the conclusion that all of the characteristic variables have corresponding local values that can be determined through literature sources or can be directly calculated through the use of the three-dimensional computational model. The Damköhler number can be directly applied to determine specific areas within a three-dimensional volume where combustion is present, and can provide a means of determining when and where local flame extinction will occur.

To use the Damköhler number to predict flame extinction in a general three-dimensional environment, the following methodology is proposed:

1. Conduct experimentation to obtain validation data for a particular computer modelling code.
2. Build a representative three-dimensional model of the experimentation into the computational fluid dynamics code.
3. Validate the computational fluid dynamics code through the comparison of the predictions of several variables obtained in the experimentation.

4. Use the validated model to predict the combustion process and track the Damköhler number and composite variables at every local point throughout the domain.
5. Use the Damköhler number parameter to define the region within the three-dimensional domain where an active flame is located.
6. Modify the conditions within the model (i.e., inject a suppressant agent) to determine how the Damköhler number changes due to the new conditions and observe if flame extinction is predicted.

4.4. Conclusions

Chapter 4 has outlined the theoretical framework for the development of a generalized Damköhler number that can be used to predict local flame extinction in any modelled three-dimensional geometry. The development of the conservation of mass, momentum, species, and energy equations has been presented, with the emphasis placed on a nonspecific flame in a three-dimensional geometry. Additionally, an examination of the characteristic variables within the Damköhler number has been presented. When combined with an appropriately validated modelling effort, this theoretical framework will comprise a methodology that allows for the prediction of flame extinction from gaseous suppression in three-dimensional environments.

In general, all of the characteristic variables in the Damköhler number can be translated into actual local values within a three-dimensional geometry through literature sources or through direct calculation from a computational model. Of particular importance is the determination of the velocity-strain relationship throughout the flow field. Based on complexities in this parameter due to the presence of an active flame in the flow field, a computational model with the appropriate resolution becomes the ideal means for predicting this quantity both temporally and spatially.

To initiate the general methodology outlined in this chapter, an appropriate experimental design must be developed to provide experimental data that can be used as validation data for any modelling effort. Chapter 5 will outline the experimental setup used to acquire the validation data for this project. In particular, two variables related to the Damköhler number, the transport of a concentration of a potential suppressant gas (i.e., which would directly influence the local concentrations of fuel and oxidizer) and the measurement of a portion of the velocity flow field, will be experimentally determined. Chapter 6 will present a compilation of this data, which will be used later in a comparison analysis with the modelling effort.

Chapter Five

5. Experimental Setup

5.1. Introduction

The following chapter is devoted to describing the experimental apparatus and various data acquisition methods used to obtain validation data for this study. Chapter 5 first discusses the goals of the experiment. Second, a complete description of the experimental apparatus is presented. Finally, an overview of the various measurement techniques is presented along with a description of the test procedures and data reduction methods.

5.2. Experimental Goal

The experimental goal of this project was to provide data that could be used for the purpose of validating the predictions of a computational fluid dynamics model. To this end, all of the experimental equipment, methods of data acquisition, and test cases were designed so that a three-dimensional computer model of the experiment could be easily produced. A good comparison between the model predictions and the obtained data would allow for the expansion of the predictive capabilities of the computer model to areas where validation data is less available in the scientific literature.

Based on available resources at the time of the experiment design, two different data acquisitions techniques were implemented within the experimental setup. These techniques were Planar Laser-Induced Fluorescence (PLIF) and Particle Image Velocimetry (PIV). The PLIF technique is a data acquisition method commonly used for the measurement of gas concentrations. The PIV data acquisition method is used to gather velocity flow field data in one or two dimensions. Both techniques were identified as necessary to produce validation data for a computational study.

5.3. Experimental Apparatus

As mentioned in Chapter 1, space facilities and space vehicles rely on large amounts of electronics and electrical equipment to sustain operability. Each piece of

electronics equipment provides a potential ignition source of fire, and the close proximity of fuel to the source can be problematic. Due to space constraints, the electronics equipment aboard space facilities and space vehicle are usually enclosed in equipment racks or cabinets that are pressed against the walls of the space module. In general, these cabinets are on the order of 1.0 m wide by 1.0 m long by 2.0 m in height, and they act as small, self-contained compartments. This type of three-dimensional fuel-air arrangement can be challenging for both extinguishment as well as for computational analysis.

In an effort to capture the complexity of the on-board equipment rack configurations, an experimental apparatus was created as a reduced-scale, three-dimensional geometry that was one-eighth of the volume of a typical equipment rack found aboard a space facility or space vehicle. Figure 5.1 shows a perspective view of the experimental apparatus with the nozzle entrance on the right, front-facing side.

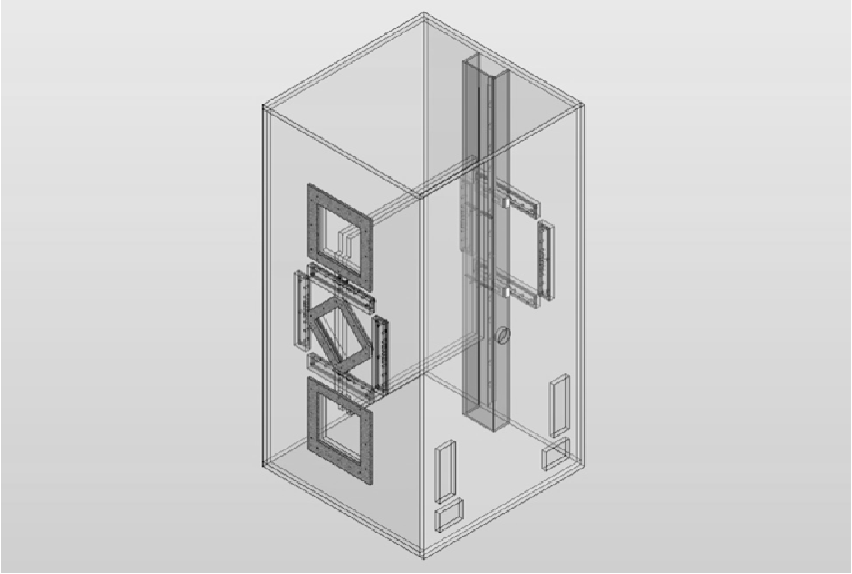

Figure 5.1: Perspective view of the experimental apparatus, nozzle entry in the center of the right, front-facing side.

Figure 5.2 depicts a perspective view of the experimental apparatus, with the side where the camera was positioned on the right, front-facing side.

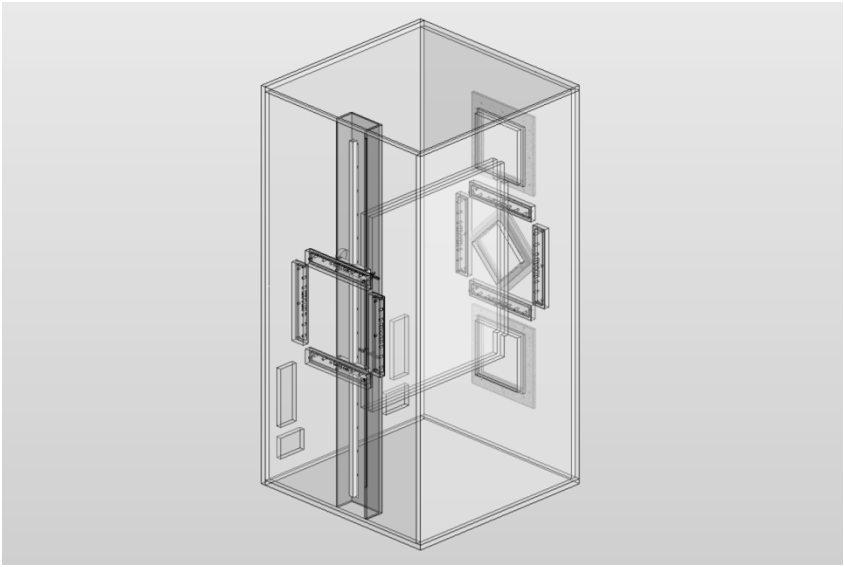

Figure 5.2: Perspective view of the experimental apparatus, camera side on right, front-facing side.

The overall dimensions of the above experimental apparatus were 0.53 m in length by 0.53 m in width by 1.03 m in height. Clear grade acrylic that was nominally 0.127 m in thickness was used for the construction of both the exterior and interior portions. Three quartz windows were installed on one side of the apparatus to allow for the entry of a high-energy laser such that laser diagnostics could be performed at various height locations in the center of the apparatus.

The experimental apparatus was designed to allow for the addition of internal obstructions to increase the internal complexity of the geometry. These obstructions consisted of two parallel plates, where the separation distance between the two plates could be adjusted to various widths. This design allowed for a challenging geometrical configuration for fluid flow and provided a systematic test for model validation through the reduction of the gap distance between the two plates. The dimensions of the test plates were 0.5 m in length by 0.127 m in width by 0.5 m in height. During experimentation, the plates were always positioned directly in the center of the height and width dimensions of the apparatus, and only the separation distance between them was varied.

In the lower portion of the experimental apparatus, four vent holes were located as a means to remove and purge the residual gas from the equipment. These vent holes consisted of two sets: the first set of two with dimensions of 0.051 m by 0.150 m, and the second set of two with dimensions 0.076 m by 0.051 m. The holes were positioned such that the room ventilation could be attached on the exterior of the experimental apparatus to facilitate the removal of testing gases post-experiment. Figure 5.3 shows an expanded view of the experimental apparatus with the left face depicting the location of the ventilation holes.

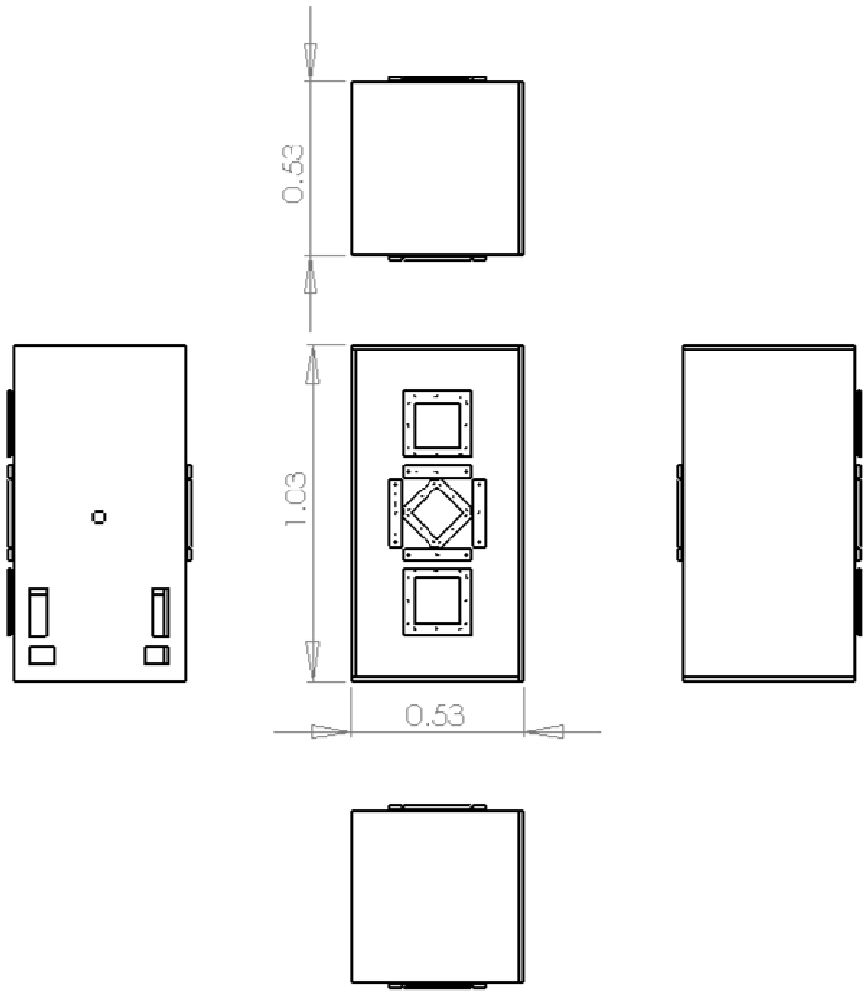

Figure 5.3: Expanded view of the experimental apparatus.

A gas dispersion nozzle was mounted on to the same wall of the experiment containing the four ventilation holes. The nozzle protruded into the experimental apparatus by a distance of 0.102 m and was located directly in the center of the panel comprising the apparatus. Figure 5.4 provides a design diagram of the nozzle annotated with measurement values.

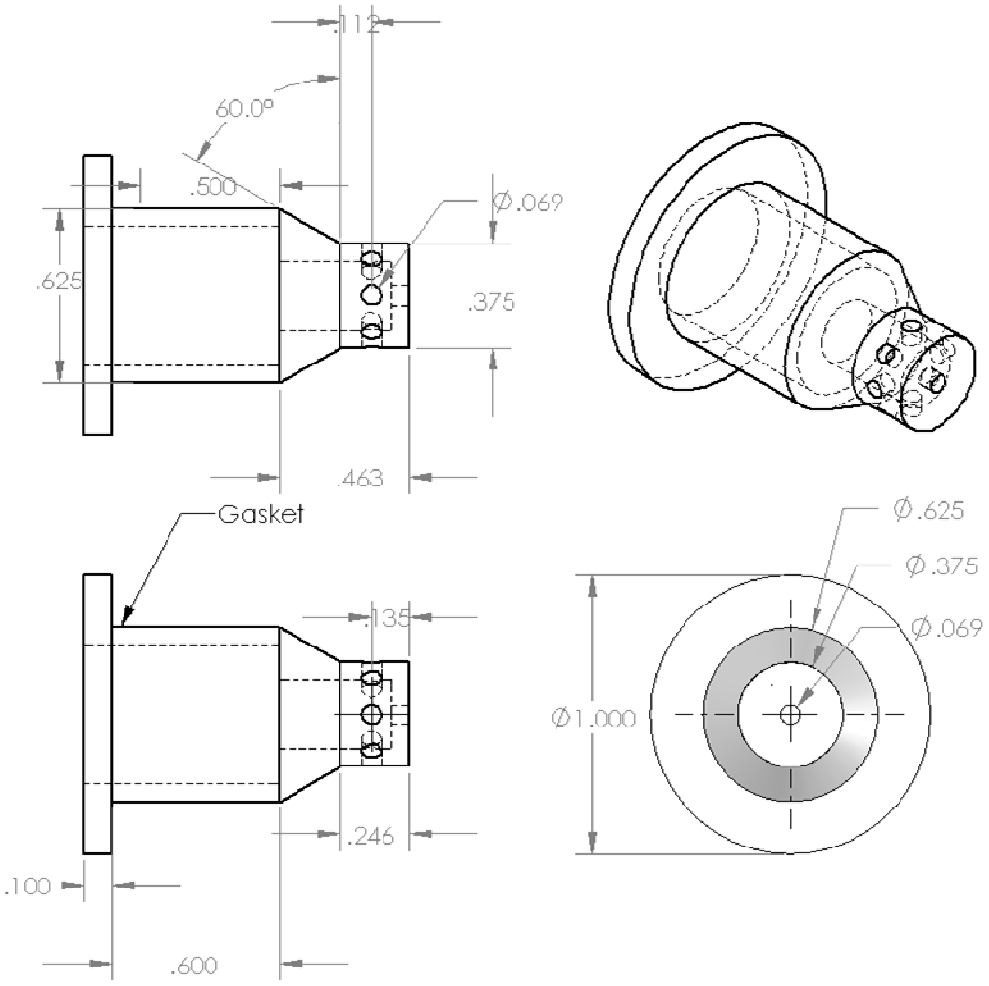

Figure 5.4: Gaseous dispersion nozzle within the experimental apparatus.

The design was based on the standard nozzle currently employed on carbon dioxide extinguishers used aboard the International Space Station. As is shown in Figure 5.4, the tip contains nine small holes through which gas can flow. One hole is designed to allow for parallel flow and is located directly at the tip of the nozzle. The

remaining eight holes are set back in the tip and allow for perpendicular flow to evolve from the nozzle in a radial fashion.

The mounting position of the nozzle was chosen to mimic the insertion of the extinguisher into an equipment rack where a fire has been observed. The manual insertion through a circular hole in the door of the equipment cabinet allows for a penetration into the interior of several tenths of a meter. For purposes of experimentation, the nozzle was rigidly fixed into place throughout all testing. All openings into the experimental apparatus around the nozzle were sealed.

5.4. PLIF Experimental Method

Planar laser-induced fluorescence (PLIF) is a diagnostic technique that is based on the fluorescence of a molecule due to the absorption of energy. PLIF is designed to provide concentration data in two dimensions (i.e., data production over a plane) utilizing a narrow-band laser to induce fluorescence within a gas. Fluorescence occurs when an electron within a molecule is excited to a higher energy state. Figure 5.5 shows a diagram of energy states in the fluorescence process.

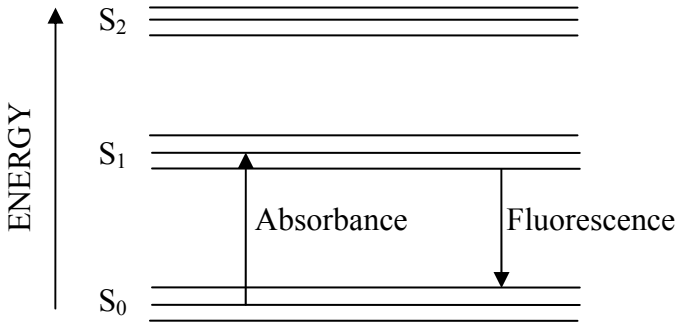

Figure 5.5: Diagram describing the fluorescence process.

In Figure 5.5, S_0 represents the ground state for a general electron located within a gaseous molecule. If this molecule is exposed to an energy source, a general electron within the molecule can absorb the energy. Once the example electron has absorbed

sufficient energy, the electron will transition to a higher energy level. For example, as shown in Figure 5.5, the electron at a ground state of S_0 transitions to S_1. Higher energy levels are unstable, which results in the electron losing energy, usually through the release of a photon. The electron will then release the absorbed energy through various means to return to a lower, more stable energy state.

When a photon is released during the fluorescence process, a specific wavelength is associated with the release. Depending on the wavelength and the type of signal receiving equipment involved, an observation of the release of the energy can be made. If the duration of the release and the signal strength of the release are sufficient, a link can be made between the strength of the signal received and the concentration of the molecules that are undergoing the excitation. This concept is the basic premise behind laser-induced fluorescence.

Within the laser-induced fluorescence technique, a laser acts as the delivery device for energy to the system. A particular gas composed of molecules that are known to absorb the energy from a specific laser wavelength is injected as a tracer gas component (i.e., small concentration) within a main gas. The tracer molecules within the system are excited by the presence of the laser, which results in fluorescence. A camera that is equipped with the appropriate filters and shutter speed is used to record the relative intensity of the fluorescence effect. Based on a simple mass balance relationship between the tracer gas and the main gas, the concentrations of both the tracer gas and the main gas can be quantified.

Various molecules have been researched for their propensity to fluoresce when exposed to a narrow-band laser. In particular, nitrogen dioxide (NO_2) has been well-documented in the diagnostics literature for use in PLIF applications [44, 45, 46, 47]. Nitrogen dioxide has been shown to fluoresce in the range of 400 nm to 750 nm over a variety of laser inputs and test geometries [47]. For the present study, nitrogen dioxide was chosen as an appropriate fluorescing gas for the determination of concentration measurements within the experimental apparatus.

5.4.1. Experimental Setup for PLIF Measurements

Concentration measurements using the PLIF technique were obtained in three locations within the experimental apparatus. The decision to use three locations was based on the limitations of the laser equipment and signal to noise ratio needed to ensure that data could be recorded. The three quartz windows installed in the side of the experimental apparatus allowed for concentration data to be obtained at locations near the top, near the bottom, and in the center between the parallel plates. The use of the quartz windows allowed for the reduction of scatter from the laser source and provided enhanced damage resistance of the experimental apparatus to the effects of the high-energy laser source. Figure 5.6 is a diagram of the PLIF experimental setup needed for an Nd:YAG laser beam to produce a laser sheet projected through a channel between two parallel plates.

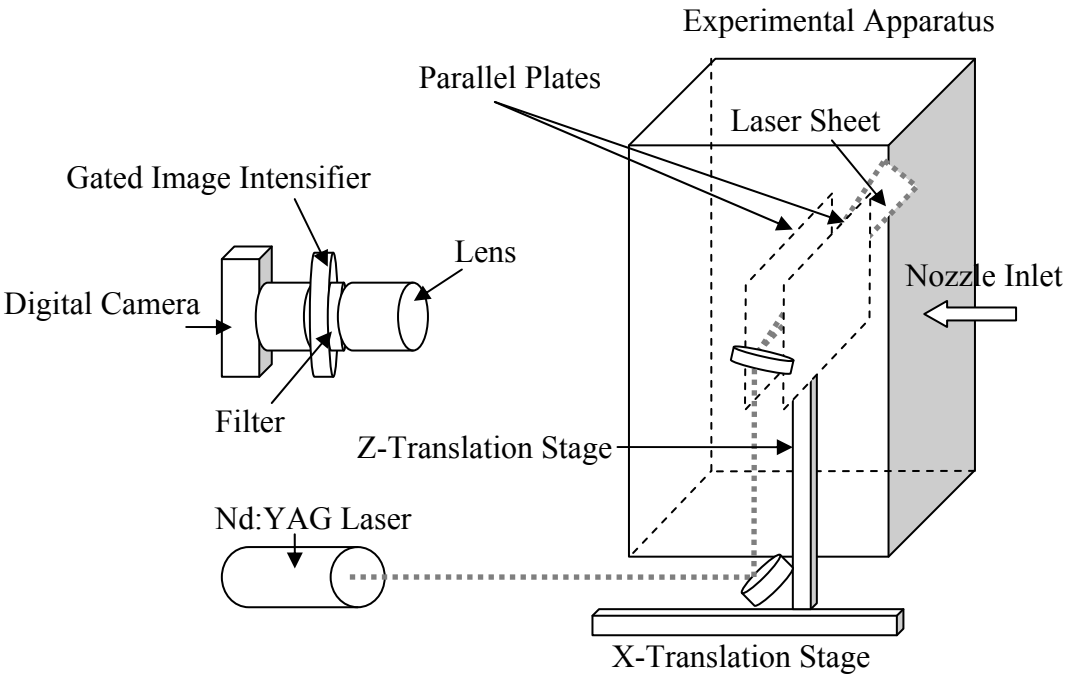

Figure 5.6: Experimental setup for PLIF measurements.

The experimental setup depicted in Figure 5.6 allowed for flexibility in the modification of the X-Z position and direction of the laser sheet as well as the channel gap distance and direction (e.g., horizontal or vertical) of the parallel plates. Because of the relatively weak fluorescence of nitrogen dioxide, an image intensifier and filter to neglect the incident laser light was used. Through precise gating, the intensifier was able to ignore the incident laser pulse and capture the fluorescent event of the nitrogen dioxide, which has a significantly longer lifetime than that of the incident light.

Figure 5.6 shows the camera equipment used in the PLIF experimental setup, as well as the relative positioning of these components. A detailed description of the camera equipment is provided in the list below.

- Digital Camera: The *Imperx* Model 1MP48L was a one megapixel camera capable of running 48 frames per second. For the PLIF application, the camera ran at ten frames per second with an exposure time of one millisecond in order to capture the light decay from the intensifier. The camera ran in "binned" mode, which effectively reduced the resolution (i.e., 496x496 pixels), but increased the sensitivity to light.

- Gated Image Intensifier: *Videoscope* model VS4-1874. This model was equipped with a high quantum efficiency option. The gate delay and exposure were controlled in 20 nanosecond increments. Because the fluorescence lifetime for nitrogen dioxide in air is very short and the intensifier is triggered by the laser Q-switch output, the nominal exposure time used was 50 microseconds with no delay. The gain was adjustable from 2,500 FL/FC to 80,000 FL/FC. Nominal settings for the application were 65,000 FL/FC. The persistence of the intensifier was 1.2 milliseconds to 10%. The camera mounted directly to the rear of the intensifier.

- Filters: Two coated, long-pass filters with approximately 90% transmittance over 550 nm and less than 0.1% below 550 nm filters were used in series after the camera lens.

- Lens: A *Nikkor* 50 mm lens with an F number of 1.4 was coupled to a C-mount adapter, which was then coupled to the intensifier.

Figure 5.6 shows the camera equipment used in the PLIF experimental setup, as well as the relative positioning of these components. A detailed description of the laser and optics used in the PLIF experimental setup is provided in the list below.

- Laser: A *Big Sky* Brilliant B Q-switched Nd:YAG laser running at 10 Hz was used for this portion of the study. The frequency was doubled, making the wavelength 532 nm. The pulse energy was approximately 450 mJ over approximately 4.5 ns.

- Lens 1: A 2.5 cm diameter CVI lens coated for a wavelength of 532 nm with a focal length of 1983 mm was used to thin the laser sheet in the middle of the region between the two parallel plates.

- Mirror 1: A *Newport* model number 20QM20HM.35 high-energy mirror with a 532 nm anti-reflective coating was used just after the laser source.

- Mirror 2: The second mirror was also a *Newport* model number 20QM20HM.35 with a 532 nm anti-reflective coating. This mirror was positioned at the top of the Z-translation stage.

- Cylindrical lens 1: A cylindrical lens was used to expand the beam from the laser source into a thin laser sheet.

- Aperture 1: A custom slot aperture using razor blades to block stray light was manufactured and then installed just prior to the area where the laser entered the experimental apparatus.

- Window 1: The beam entered the experimental apparatus through a 0.64 cm thick quartz window, which was utilized for its broadband transmittance and high damage threshold.

- Aperture 2: A double aperture was located just inside the experimental apparatus within the region of interest between the two parallel plates. This aperture was installed in an effort to minimize scattered light that developed from the laser passing through the quartz window. The aperture was manufactured from aluminum box tubing, painted matte black, with a 0.32 cm slot.

- Aperture 3: An additional aperture was installed between the plates to decrease the background light from the laser. The single slot aperture was positioned up-beam from the viewing area of the camera.

- Sheet Beam Dump: A beam dump was positioned within the experimental apparatus down-beam from the viewing area of the camera. The beam dump consisted of a 0.32 cm wide slot in a 10 cm channel running the full height of the apparatus. Arrays of razor blades were centered inside the channel with the contact surface of the blades approximately 2.5 cm behind the entrance. The laser light was scattered and absorbed by the inside surfaces of the channel, which were painted matte black.

The gaseous agent used to acquire the PLIF concentration measurements was a mixture of 1000 ppm nitrogen dioxide in a balance of nitrogen. Figure 5.7 shows a diagram of the plumbing setup used for the PLIF concentration measurements.

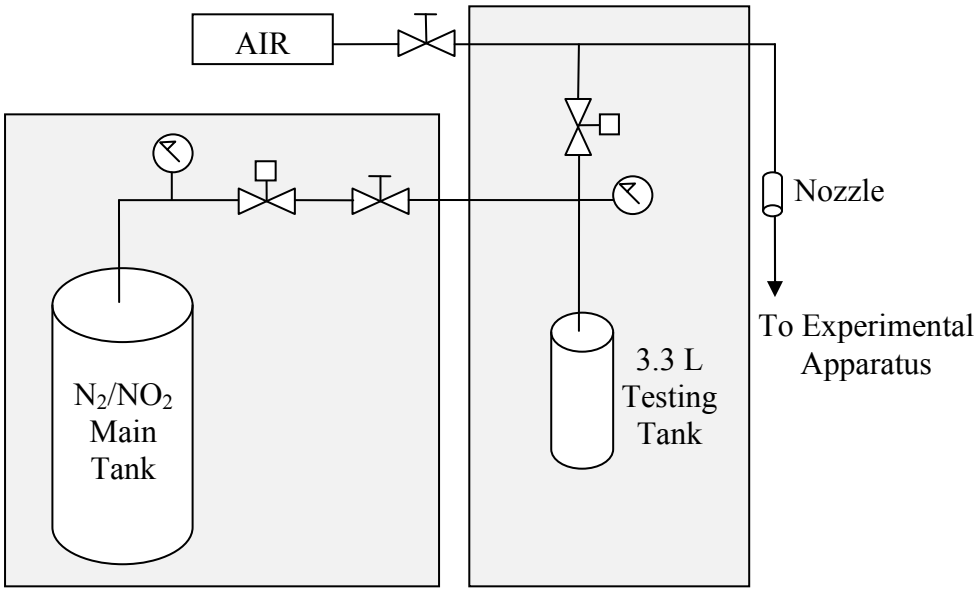

Figure 5.7: Plumbing diagram for PLIF concentration measurements.

As shown in Figure 5.7, the testing gas was stored in a main tank rated for 2068 kPa. A second tank with a volume of 3.3 L was filled from the main tank prior to the initiation of each test. Additionally, an air compressor and holding tank were used as a means to purge gas from the system between tests.

5.4.2. Testing Procedure for PLIF Measurements

Before each test was conducted, the PLIF setup was calibrated to ensure accurate measurements of the NO_2 gas. This calibration was accomplished using a Fourier Transform Infrared (FTIR) Spectroscopy analyzer. In the calibration procedure, NO_2 gas was injected into the experimental apparatus and was sampled by the FTIR analyzer. The digital camera was used to record images of the calibration injection, and the images from the camera were compared with the concentration measurements sampled by the FTIR. These values were used to quantify the fluorescence observed by the camera images during later testing.

The PLIF testing procedure was initiated by ensuring that the intensifier was completely covered and that the gating was set to be under 5 μs. The laser and the camera were both powered on and allowed to warm-up. The camera was configured to have a frame rate of 10 frames per second, a gain of 0-25 dB, and an exposure time of 100 ms. Streampix software was used in conjunction with the camera to observe real-time viewing of the area of interest, as well as for recording of the images.

Once the system was checked to ensure functionality, the gas was injected into the experimental apparatus. The 3.3 L tank was pressurized with the mixture testing gas to approximately 2400 kPa. A solenoid control value system was used to move the testing gas from the main tank into the smaller testing tank. A final solenoid control value was switched to allow for the gaseous mixture to inject into the experimental apparatus. Figure 5.8 depicts the pressure drop in the tank as the mixture was released into the experimental apparatus over three different tests.

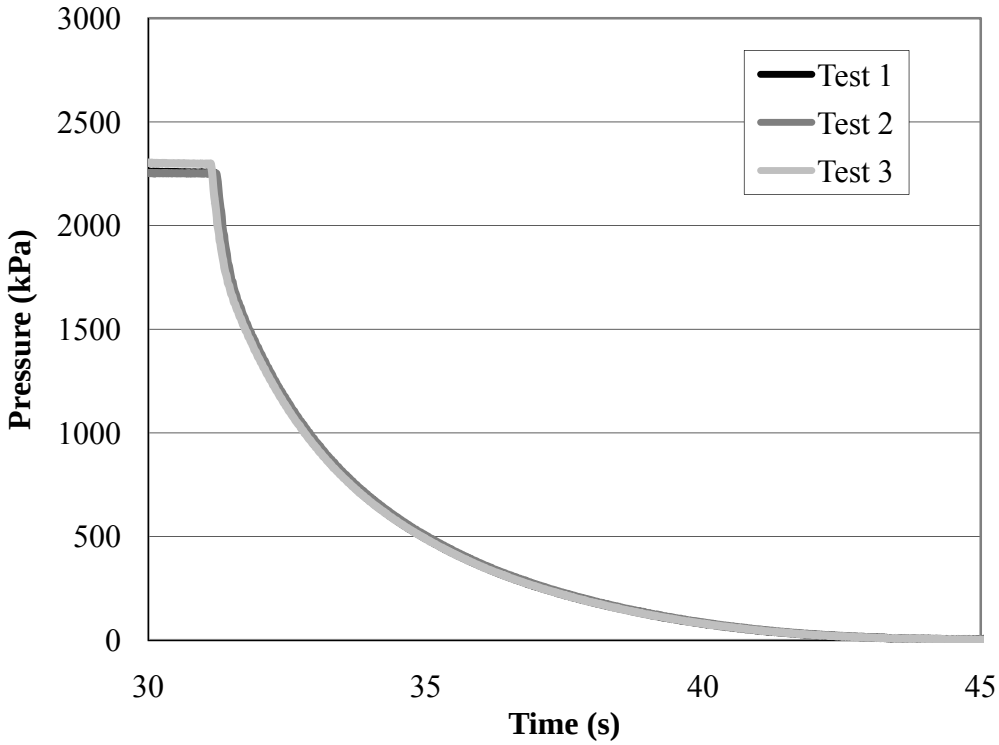

Figure 5.8: Pressure drop within tank containing nitrogen dioxide mixture for PLIF testing.

Data was recorded by the imaging software throughout the duration of the blowdown. After each test, the experimental apparatus was purged with air using the plumbing system. Several air changes were allowed to ensure complete removal of any residual test gas before attempting to conduct the next test.

5.4.3. Data Reduction for PLIF Measurements

Due the large amount of data that can be generated by the use of the PLIF measurement technique, data reduction methods were implemented to allow for a comparison with computational predictions. The data recorded during each test was a series of chronologically recorded images of the concentration of the tracer gas within the experimental apparatus at various locations between the parallel plates. The images recorded a portion of the laser sheet and surrounding area.

To provide a useful quantity of data for comparison with the modelling, a small 2.54 cm by 2.54 cm square of the center of the laser sheet in each image was chosen as the area over which to average the concentration measurements. This same area was averaged at three distinct locations between the plates: a top location, a center location, and a bottom location. All three of the measurement locations followed the progression of the laser sheet through the plates and, thus, were located at the midpoint between the plates when moving from right to left through the gap between the plates. The top and bottom measure locations were located 2.54 cm from the edge of the plates.

To ease the processing of the concentration images, two main programming routines were developed. The first routine was designed to utilize a background image of the area of interest prior to the influx of NO_2 gas with the laser active within the experimental apparatus. Subsequent images recorded during the fluorescent event were subtracted from a background image this routine created. A more detailed recording of the program is located in Appendix A. The second routine processed

the raw images recorded during testing and averaged the measurements over the area of interest after subtracting out the background image. Data was obtained in both graphical and tabular formats. Appendix A also contains the second programming routine. Matlab was used to compose both programming routines.

5.5. PIV Experimental Methods

The Particle Image Velocimetry (PIV) measurement technique works on the premise of tracking the movements of numerous individual particles between two images taken at a known time interval. Figure 5.9 provides an example of the PIV process.

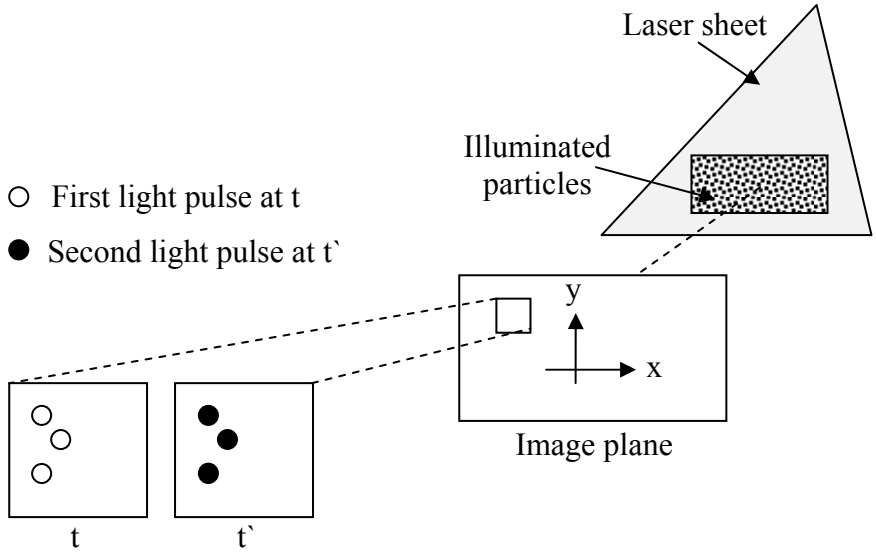

Figure 5.9: Example of the PIV measurement technique (after [48]).

Figure 5.9 depicts an example of the first light pulse, t, and the second light pulse, t`. By evaluating the distance moved by a particle between two consecutive images, and given the known time difference between these images, a velocity vector can be calculated that describes the particle's movement. By tracking many particles between the two images and averaging the movement of particles in a defined space, a map of velocity vectors can be calculated to describe the overall movement over the period of time.

There are four main hardware aspects associated with the capture of PIV images:

1. The insertion of particles into the flow (seeding)
2. The illumination of the particles in the flow
3. The actual capturing of the image (cameras)
4. The electronic timing devices / computers to control all or some of the above

Seeding is the process by which particles are introduced into the flow field. The particles must be present in sufficient quantity that there exist an adequate number of particles in two concurrent images for cross-correlation, which is the tracking of particles from one image to the next, to occur. In order to achieve an appropriate number density, the particles must be injected into the flow by some means. Thus, the challenge is in injecting sufficient particles without disturbing the flow field that will be measured. There are various seeding techniques that have been developed to ensure that the flow field is not disturbed.

In most cases, the illumination of the particles is achieved through the use of a high-power laser. The laser produces pulsed beams of high-energy light that are diverged into a two-dimensional light sheet, which is aligned with the desired measurement plane as shown in Figure 5.9. A fraction of these pulses of light reflect off the artificially introduced seeding particles towards a camera.

Similar to the digital imaging utilized in the PLIF technique, the digital camera used is focused perpendicular to the light sheet in order to capture images of the particles' movement. The main requirements of the camera equipment for PIV are an externally triggered and adjustable shutter speed, exposure time, and frame capturing rate.

The final hardware components that are utilized in the PIV technique are the electronic and computational equipment that trigger the elements of the image acquisition process. The precise triggering of the laser to coincide with the camera exposure must be controlled to a high degree of accuracy. Once the desired image

pairs have been acquired, post-processing is used to create the desired vector maps. The vector maps are created by an iterative process of cross-correlation using an algorithm that tracks the particles between images in a pair. Additionally, a filtering process is used to systematically remove noise found within the images.

5.5.1. Experimental Setup for PIV Measurements

Velocity measurements using the PIV technique were obtained at a central location between the parallel plates within the experimental apparatus. Figure 5.6 is a diagram of the PLIF experimental setup.

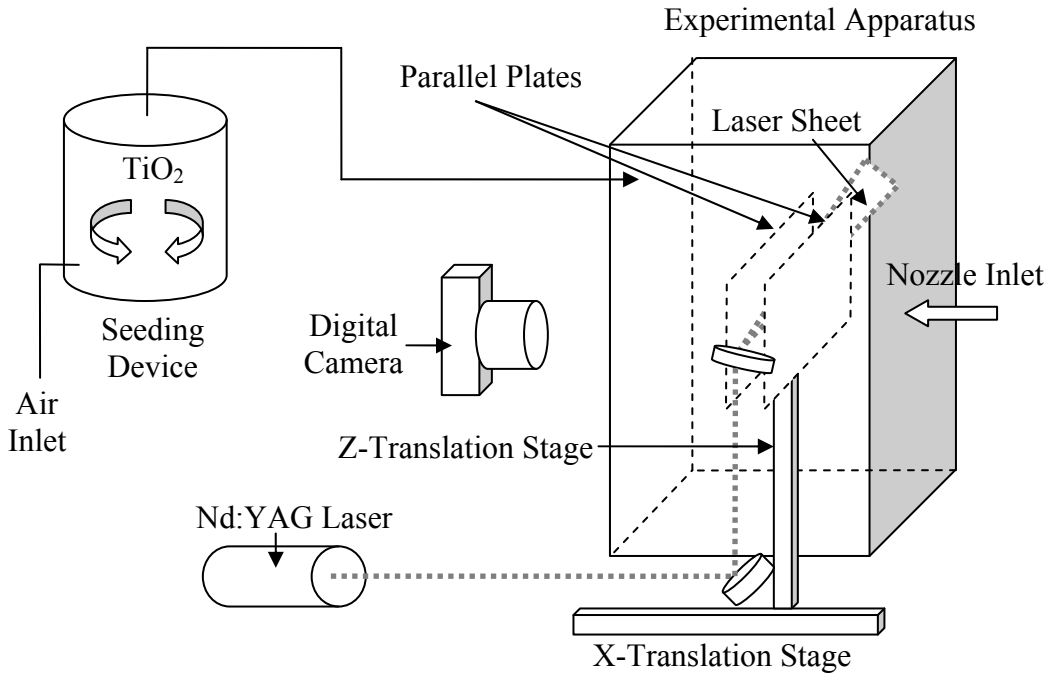

Figure 5.10: Experimental setup for PIV measurement.

Similar to the experimental setup for the PLIF measurements previously described in section 5.4.1, the diagram of the PIV experimental setup shows a graphical representation of an Nd:YAG laser beam producing a laser sheet between two parallel plates. The majority of equipment utilized for the PLIF experimental setup

was also utilized for the PIV measurements. A detailed description of the differing and additional components for the experimental setup is provided in the list below.

- Digital Camera: A *R&D Vision* Firewire CCD camera with a one megapixel 1392 x 1040 pixel resolution was used.

- Laser: A Neo 65-15 twin cavity Nd:YAG laser from *Oxford Lasers* was used for this portion of the study. The two cavities sat side by side with each producing one pulse per image pair. The pulses were passed through optics that again produced a divergent light sheet which aligned with the desired measurement plane, equidistant between and parallel to the plates inside the box. The thickness of the sheet created by this laser was approximately 3 mm.

- Particle Seeder: The particle seeding device was comprised of a cylindrical container containing seeding particles, a brush mounted on a motor, and an air inlet and outlet. The seeding particles used for the PIV measurements were titanium dioxide (TiO_2). TiO_2 is an inert material with a mean particle diameter of 0.5 μm to 1.0 μm. Within the seeder, the brush rotated and excited the particles into the flow created by the air forced though the container. The amount of air passing through the container could be varied to produce an optimum particle entrainment.

5.5.2. Testing Procedure for PIV Measurements

Prior to the start of the testing, the laser and the camera were both powered on and allowed to warm-up. The procedure then began by feeding the outlet pipe of the particle seeding device into the experimental apparatus. Once it was deemed that sufficient particles were present in the box, the outlet pipe was removed and the experimental apparatus was sealed shut. The seeding particles were observed mixing with the natural air flow in the box. The particles remained suspended in the air

throughout the discharge of the test gas. For all of the PIV measurements, the test gas was air.

Similar to the PLIF procedure, the system was checked to ensure functionality prior to the injection of the test gas into the experimental apparatus. A compressed air source with a pressure of approximately 740 kPa was used to provide flow from the nozzle injection point. A manually controlled value system was used to allow the flow of the testing gas from the compressed air source into the experimental apparatus. Figure 5.11 depicts the mass flow rate of air over the injection duration as it was released into the experimental apparatus during the PIV testing.

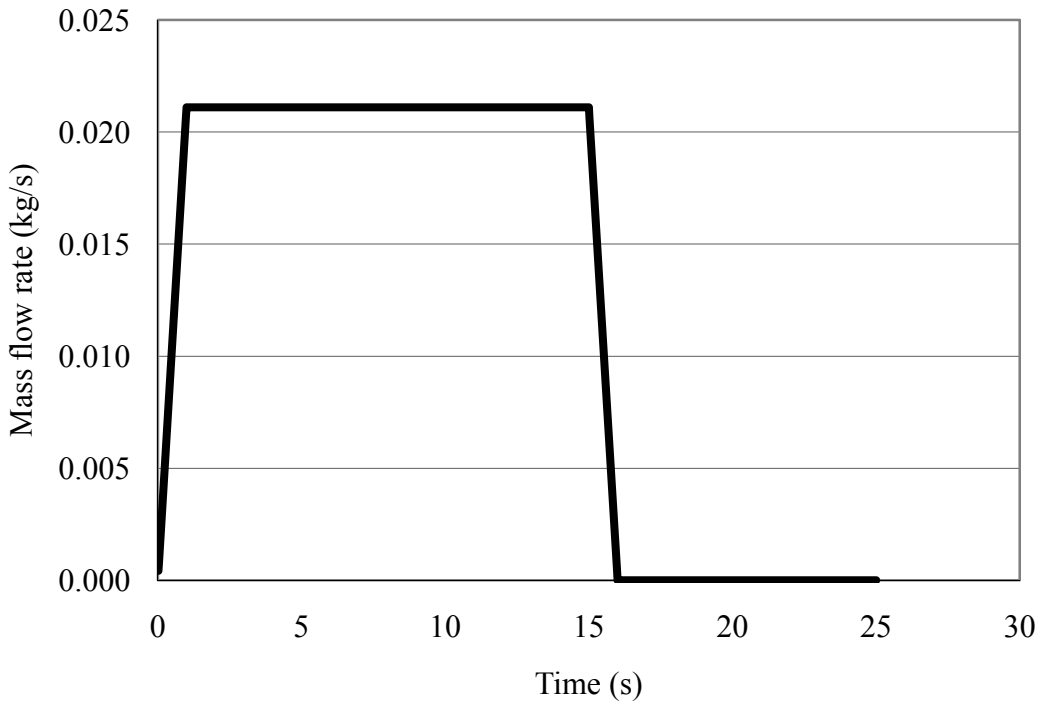

Figure 5.11: Mass flow rate of air into the experimental apparatus during PIV testing.

The gaseous dispersion was next recorded using the camera and image recording system. The PIV system synchronization and image recording were performed with R&D Vision HIRIS software and electronics. A timing diagram was constructed to

ensure that each laser pulse was released during the period of image exposure and that the time delay between pulses (Δt) was maintained. For the PIV experiments, a Δt of 30 ms was used. This value was deemed appropriate for the expected velocities. The image pairs were then captured at a rate of 5 Hz.

After each test, the experimental apparatus remained sealed so that the natural convective currents would be minimized. Several minutes were allotted between repetitive tests to allow for a dampening of internal velocities.

Post-processing of the image pairs to calculate the velocity vector maps was performed using VidPIV software from Intelligent Laser Applications (ILA). VidPIV uses a tree structure which iteratively cross-correlates and filters the results until a satisfactory resolution of accurate velocity vectors is obtained. The incorrect vectors removed through the filtering processes are replaced by interpolated values, the percentage numbers of which can be monitored to assess reliability of the results.

5.5.3. Data Reduction for PIV Measurements

The use of PIV also produces a large amount of visual data. Data reduction methods were implemented to allow for the flow velocity data to be compared with the computational predictions. The data recorded during each PIV test was a series of recorded image pairs that, when analyzed, produce two-dimensional velocity components. These measurements were obtained over a rectangular area directly in the center of and between the parallel plates.

To provide a useful quantity of data for comparison with the modelling, a programming routine was developed to facilitate the processing of the results. The programming routine imports the raw file data and allows for the specific examination of a single velocity vector over time. Additionally, the routine was designed to tabulate the maximum velocity components found in each examined set of data. This routine was written using Matlab and is reproduced in Appendix A.

5.6. Conclusions

Chapter 5 has outlined both the experimental setup and the equipment used to obtain data for this current study. Both of the experimental setups have been designed to provide normal gravity data that can be used to validate computational modelling predictions. The demonstration of good agreement between the experiment data and modelling predictions will allow for the use of computational modelling as an appropriate means for the potential determination of suppressant delivery in any three-dimensional environment.

Chapter Six

6. Experimental Results

6.1. Introduction

The experimental apparatus and two experimental setups presented in Chapter 5 were used to gather data for the comparison of modelling predictions with the experimental data. Chapter 6 presents the results of those experimental studies and is divided into two halves. The first half of the chapter discusses the results of the planar laser-induced fluorescence (PLIF) measurements. The second half of the chapter discusses the results of the particle image velocimetry (PIV) measurements. Presented within each half is an example of the raw data, the reduced results, and an error analysis of the measurements.

6.2. PLIF Measurement Results

As mentioned in Chapter 5, the PLIF technique measured the concentration of the nitrogen dioxide gas between the parallel plates located within the experimental apparatus. Three plate separations were chosen in an effort to determine a minimum spacing where entrance of the tracer gas into the space between the parallel plates would become more difficult. Table 6.1 shows the test matrix that was developed based on the limitations of the experimental apparatus and equipment used for the PLIF measurements.

Plate Separation (cm)	Test #1	Test #2 (1st Repeat)	Test #3 (2nd Repeat)
1.27	Test #1 at 1.27	Test #2 at 1.27	Test #3 at 1.27
1.91	Test #1 at 1.91	Test #2 at 1.91	Test #3 at 1.91
3.18	Test #1 at 3.18	Test #2 at 3.18	Test #3 at 3.18

Table 6.1: Testing matrix for PLIF concentration measurements.

Due to constraints imposed by backscattering of the laser off of the acrylic plates, 1.27 cm was determined to be the smallest separation gap that provided meaningful data. In addition to the 1.27 cm gap, plate separation distances of 1.91 cm and 3.18 cm were also examined. These two separation distances were used within the testing due to the restrictions imposed by the experimental apparatus when widening the gap between the plates. The plates were moveable based solely on a pin and peg system, which allowed for the separation distance between the plates to be increased by 0.64 cm with each transition.

6.2.1. Raw PLIF Images

Figure 6.1 depicts a typical PLIF raw data image of the nitrogen dioxide fluorescence for the 1.27 cm plate separation. The horizontal and vertical scales depict the horizontal and vertical positions within the camera view area. Additionally, the vertical axis contains a second scale that is artificially colored to represent the residual percentage of the initial concentration of nitrogen dioxide injected into the testing apparatus.

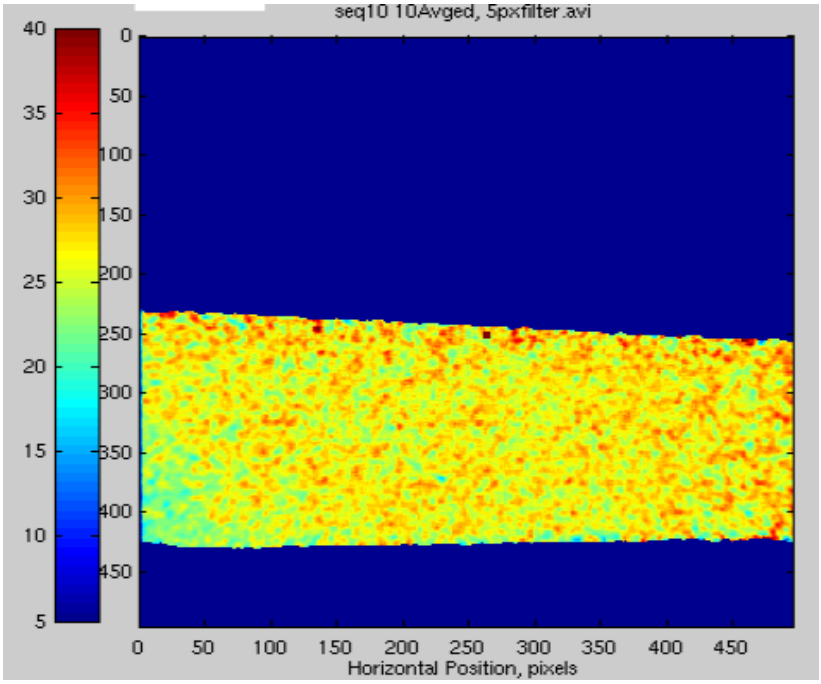

Figure 6.1: Example of PLIF raw image (measurement in $\%NO_2$ remaining of initial 1000 ppm concentration) at the center of the plates for the 1.27 cm separation.

The raw image presented in Figure 6.1 shows that approximately 260 ppm of nitrogen dioxide had penetrated into the middle of the parallel plates at the 1.27 cm separation after the initial injection into the experimental apparatus had been concluded (i.e., an approximate steady-state condition had developed). Figure 6.2 shows a typical PLIF raw data image of the nitrogen dioxide fluorescence for the 1.91 cm plate separation.

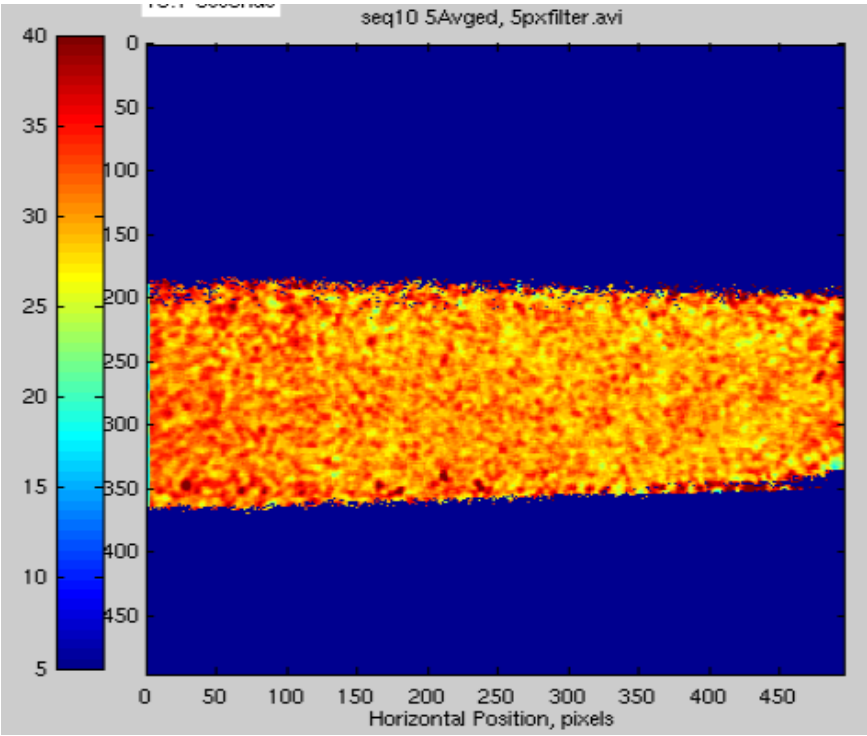

Figure 6.2: Example of PLIF raw image (measurement in $\%NO_2$ remaining of initial 1000 ppm concentration) at the bottom of the plates for the 1.91 cm separation.

The raw image presented in Figure 6.2 demonstrates that approximately 290 ppm of nitrogen dioxide had penetrated into the middle of the parallel plates at the 1.27 cm separation after the initial injection into the experimental apparatus had been concluded. Figure 6.3 depicts a typical PLIF raw data image for the 3.18 cm plate separation.

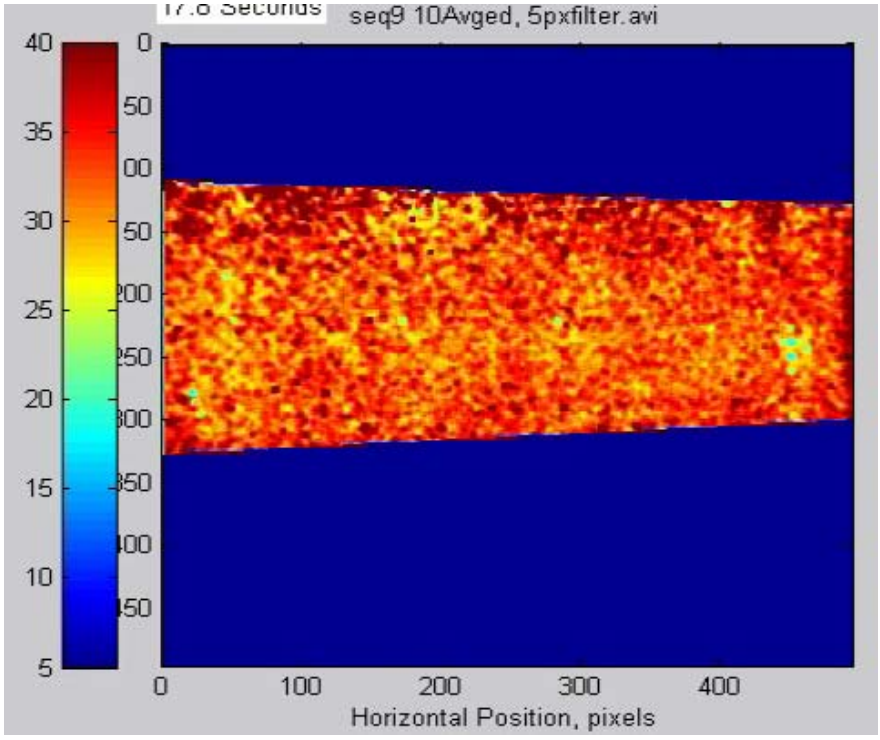

Figure 6.3: Example of PLIF raw image (measurement in $\%NO_2$ remaining of initial 1000 ppm concentration) at the top of the plates for the 3.18 cm separation.

In the raw image shown in Figure 6.3, approximately 330 ppm of nitrogen dioxide was observed at the top of the plates for the 3.18 cm separation after the initial injection into the experimental apparatus had been concluded. The observed range of 260 ppm to 330 ppm was typical when comparing the smallest plate separation to the largest plate separation at each of the three test locations between the plates (e.g., top, center, and bottom).

6.2.2. PLIF Concentration Results

As detailed in Chapter 5, the raw images recorded by the digital camera were compiled into concentration histories by examining a 2.54 cm by 2.54 cm square area in the middle of the laser sheet at each location (i.e., top, center, and bottom) during each test. The recorded concentrations of nitrogen dioxide within the analysis area were averaged to produce a numerical concentration value for that particular area.

Concentration history plots were created for each test conducted. Figure 6.4 shows typical area averaged concentration histories over a three test series. It should be noted that in the first five seconds of data, the concentrations remain at 0 ppm. After five seconds of recording data, a solenoid value was commanded to open releasing the flow of gas into the experimental apparatus. The complete set of concentration history data is included in Appendix B.

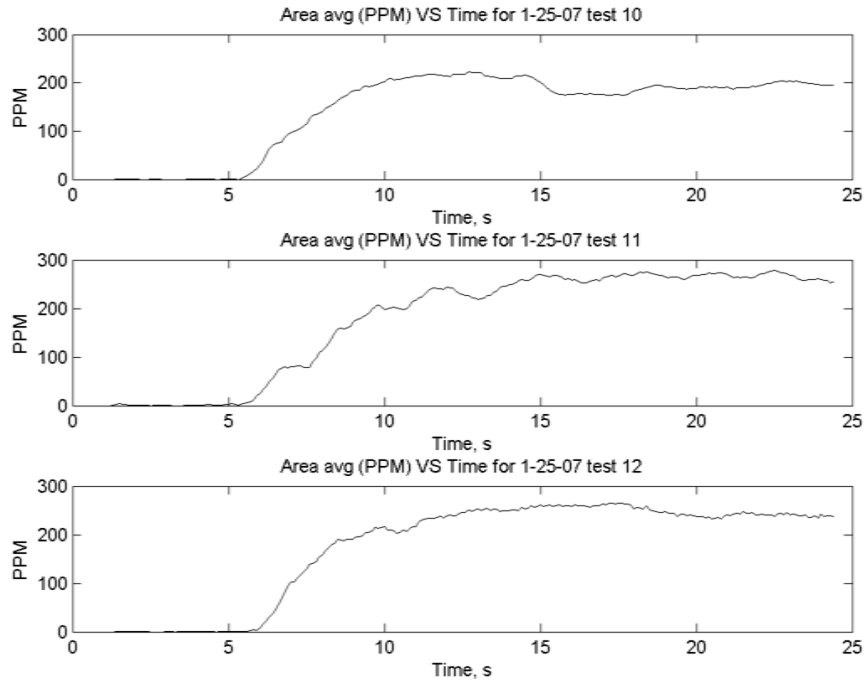

Figure 6.4: Example concentration histories for three tests conducted at the 1.27 cm plate separation distance and processed at the top measurement location.

To better interpret the data and to facilitate the ease of comparison with the computer modelling results, the concentration history data from the triplicate tests was averaged together resulting in one average time history plot of the nitrogen dioxide concentration. This averaging was conducted for each plate separation and plate measurement location. The averaged results for each plate location (i.e., top, center, and bottom) were then plotted on one graph for each plate separation.

Figure 6.5 depicts the average concentration history for the nitrogen dioxide dispersion at the 1.27 cm plate separation.

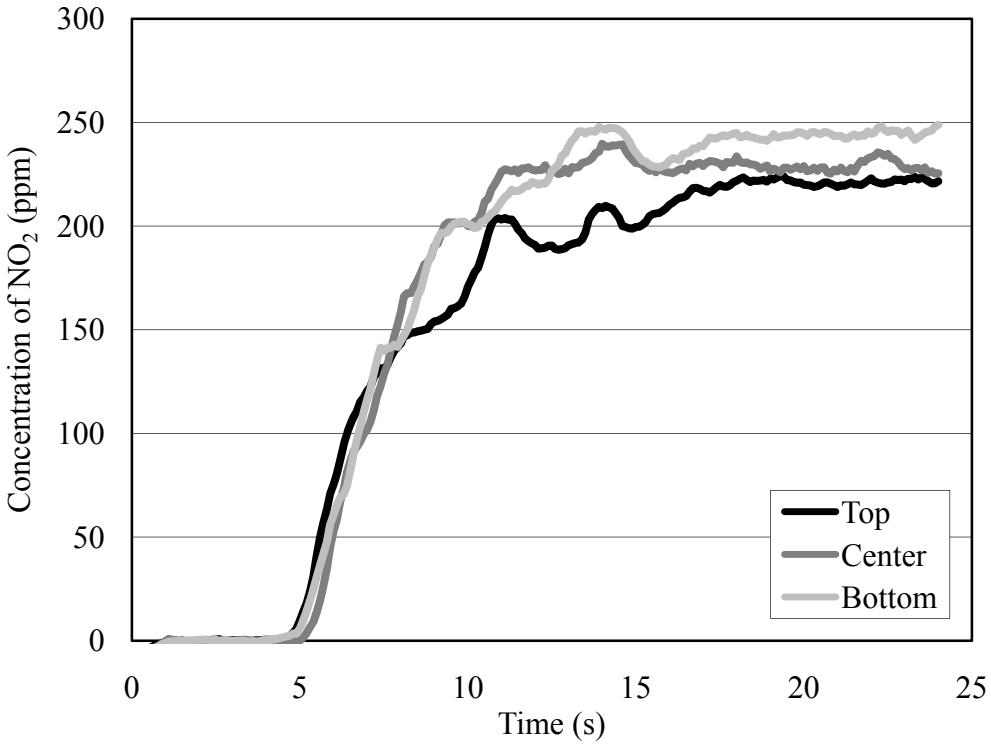

Figure 6.5: Average concentration history of NO_2 for the 1.27 cm plate separation distance processed at the top, center, and bottom locations.

At this spacing, the greatest maximum steady-state concentration of nitrogen dioxide was 248 ppm, which occurred at the bottom measurement location. The lowest maximum steady-state concentration of nitrogen dioxide was 224 ppm, which occurred at the top measurement location.

Figure 6.6, shows the average concentration history for the nitrogen dioxide dispersion at the 1.91 cm plate separation.

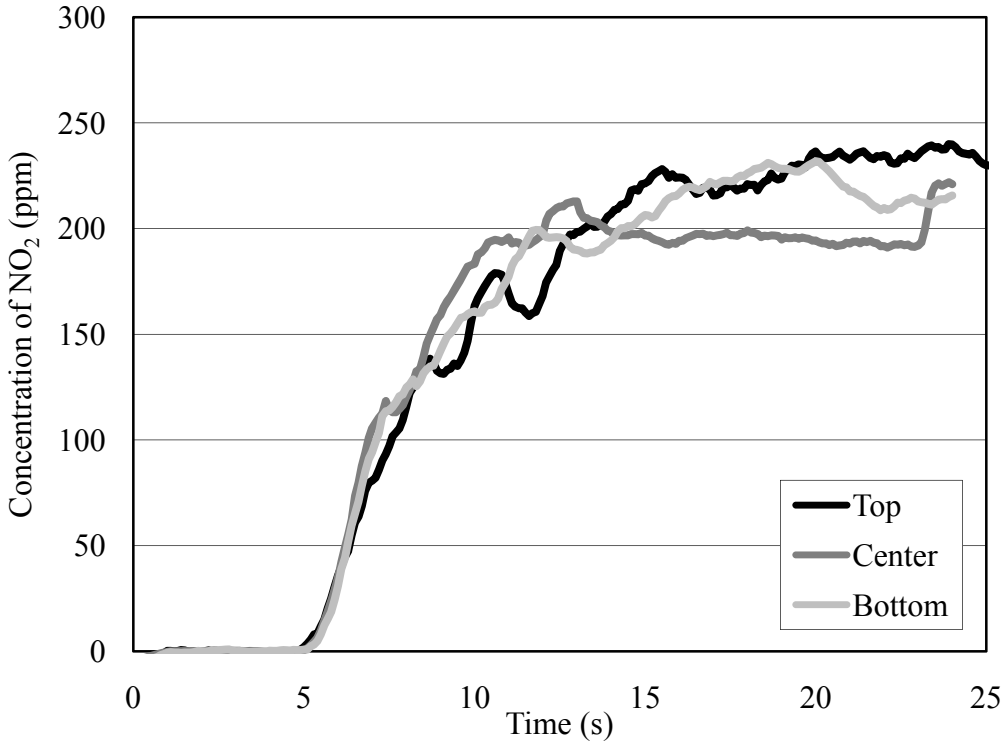

Figure 6.6: Average concentration history of NO_2 for the 1.91 cm plate separation distance processed at the top, center, and bottom locations.

At this spacing, the greatest maximum steady-state concentration of nitrogen dioxide was 240 ppm, which occurred at the top measurement location. The lowest maximum steady-state concentration of nitrogen dioxide was 222 ppm, which occurred at the center measurement location.

Figure 6.7, shows the average concentration history for the nitrogen dioxide dispersion at the 3.18 cm plate separation. At this spacing, the greatest maximum steady-state concentration of nitrogen dioxide was 250 ppm, which occurred at the top measurement location. The lowest maximum steady-state concentration of nitrogen dioxide was 225 ppm, which occurred at the bottom measurement location.

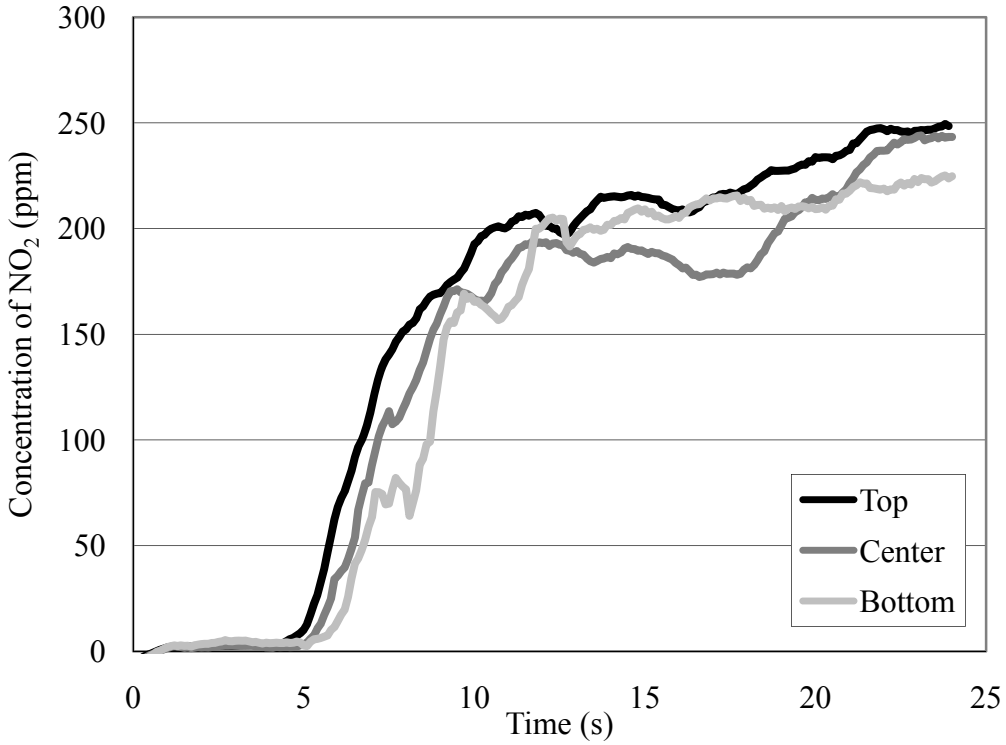

Figure 6.7: Average concentration history of NO_2 for the 3.18 cm plate separation distance processed at the top, center, and bottom locations.

The release of the testing gas into the experimental apparatus occurred over approximately 13 seconds. After this blowdown period from the supply tank, the concentration between the various plate separations was allowed to achieve a steady-state. This period was observed to have developed approximately 15 seconds after the initial influx of gas. Table 6.2 lists the various steady-state averages for the concentration results at the tested plate separations.

Plate Separation (cm)	Top (ppm)	Center (ppm)	Bottom (ppm)
1.27	221.0	228.9	244.8
1.91	234.5	198.0	216.1
3.18	242.7	232.5	219.0

Table 6.2: Steady-state concentration average at each location and plate separation.

Figures 6.5, 6.6, and 6.7 follow similar trends for the evolution of tracer gas build-up between the plates. At each plate separation, a distinct difference in the concentration exists at each measurement location. This observed difference, while not large, suggests that momentum dominates the early distribution of the gases between the plates, which results in higher concentrations of the tracer gases at the top and bottom locations before moving to the center location. As the flow conditions begin to relax, diffusion and buoyancy of the gases start to dominate the problem, resulting in a more uniform distribution of gases between the measurement locations. The remaining differences in concentration are due to diffusive effects and buoyancy. It can be inferred that with an infinitely long mixing time within the experimental apparatus, diffusion would allow for a completely uniform concentration of the tracer gas at each measurement location.

6.2.3. PLIF Measurement Error Analysis

To determine the level of confidence of the concentration results, a statistical analysis was performed with the data presented in the previous section to determine the standard error between measurements. The error was calculated using the steady-state average of the three measurements taken at each plate separation and position between the plates. The standard deviation was calculated using the following formula:

$$\sigma = \sqrt{\frac{1}{N}\sum_{i=1}^{N}(x_i - \bar{x})^2} \tag{6.1}$$

where N is the number of measurements, x_i is the i^{th} measurement, and $\bar{x}$ is the average value of the measurements. The standard error was calculated by

$$S.Err = \frac{\sigma}{\sqrt{N}} \tag{6.2}$$

Table 6.3 lists the various measurement locations and plate separations and their corresponding standard deviations and standard errors.

Plate Separation (cm)	Measurement Location	Average Concentration (ppm)	Standard Deviation (ppm)	Standard Error (ppm)
1.27	Top	221.0	12.2	7.0
1.27	Center	228.9	28.9	16.7
1.27	Bottom	244.8	16.1	9.3
1.91	Top	234.5	8.3	4.8
1.91	Center	198.0	14.6	8.4
1.91	Bottom	216.1	24.2	14.0
3.18	Top	242.7	16.4	9.5
3.18	Center	232.5	2.9	1.7
3.18	Bottom	219.0	2.4	1.4

Table 6.3: Standard deviation and standard error for all concentration measurements.

Figure 6.8 shows a plot of the steady-state average concentration of nitrogen dioxide for each measurement location and plate separation. Figures 6.9, 6.10, and 6.11 are graphical representations of the overall error associated with the measurements.

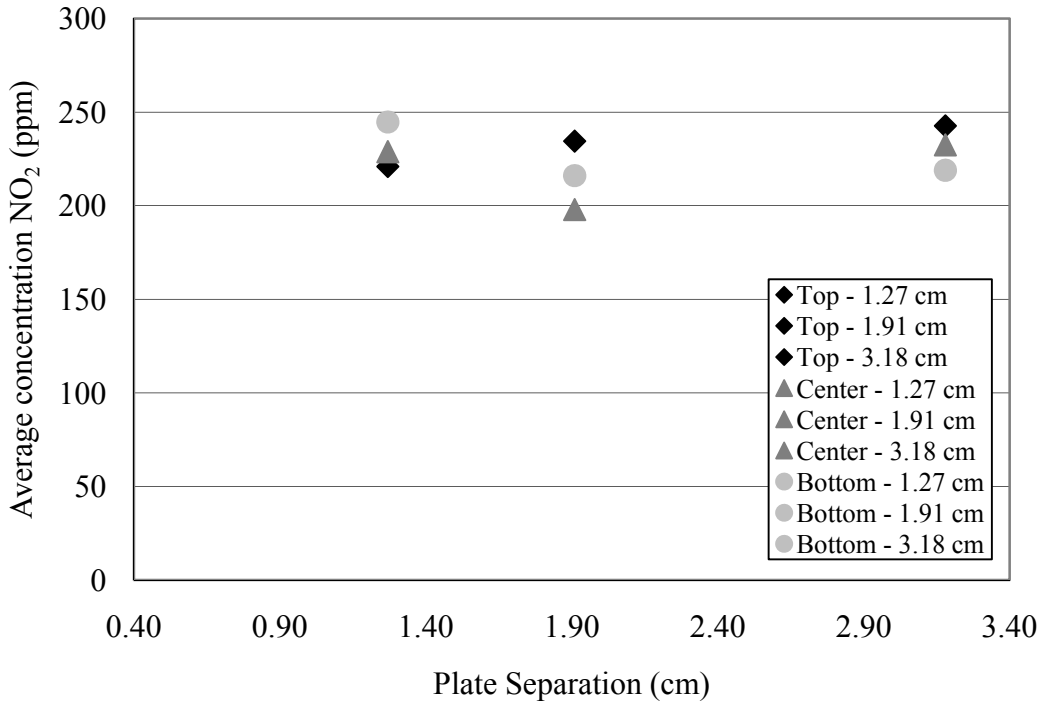

Figure 6.8: Steady-state average concentration of NO_2 at each measurement location.

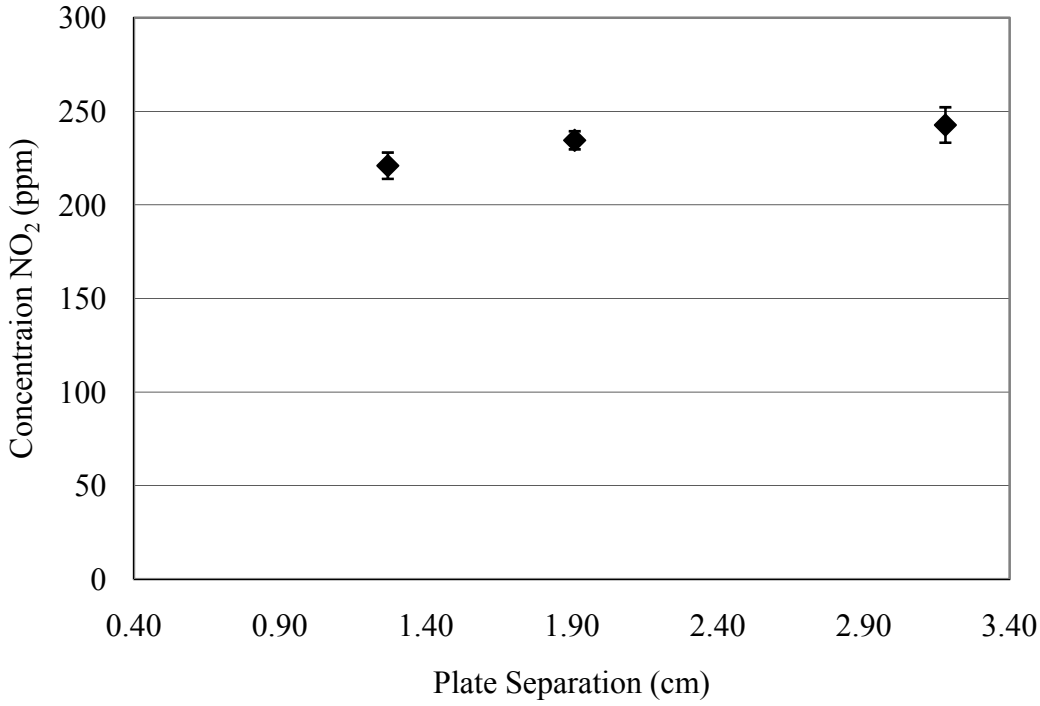

Figure 6.9: Average concentration of NO_2 at the top location for each plate separation (with error bars).

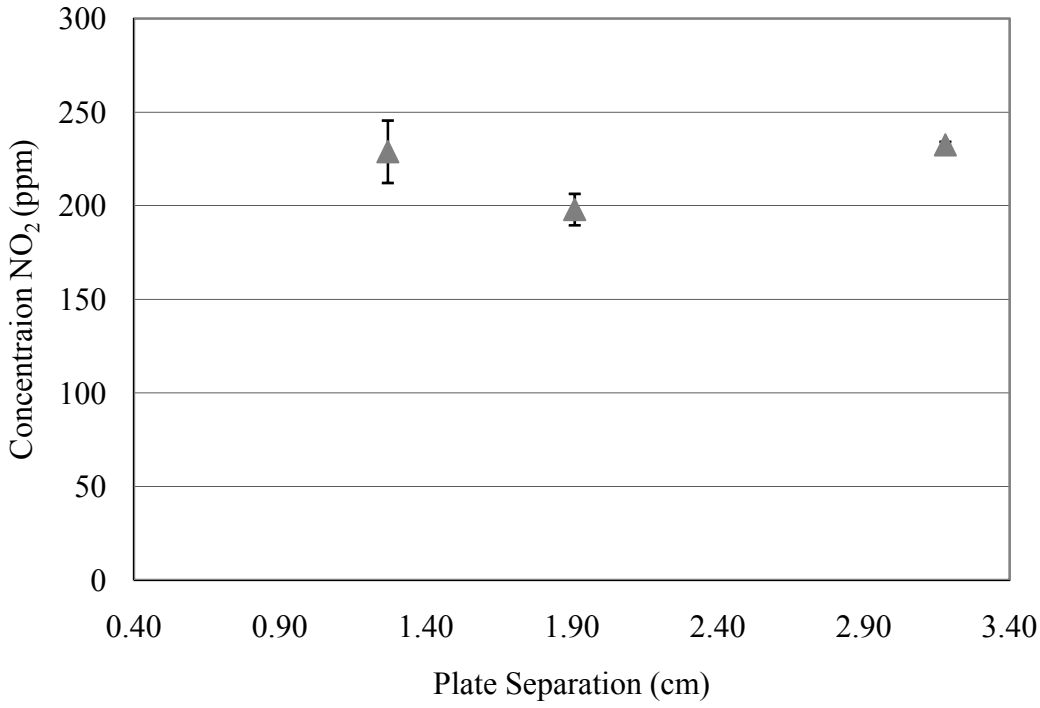

Figure 6.10: Average concentration of NO_2 at the center location for each plate separation (with error bars).

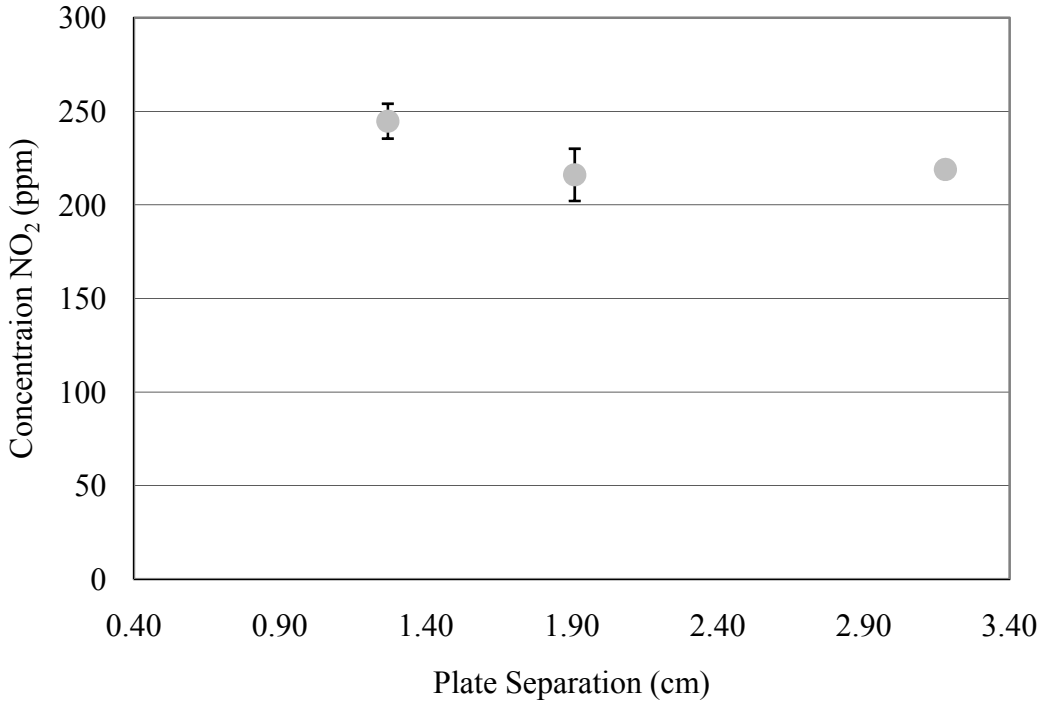

Figure 6.11: Average concentration of NO_2 at the bottom location for each plate separation (with error bars).

The plot shown in Figure 6.8 demonstrates the relatively small amount of variation between the three locations at each plate separation. Additionally, no clear trend is apparent when examining the steady-state average concentration amounts at each plate separation.

In each of the plots depicts in Figure 6.9, 6.10, and 6.11, a point represents the steady-state concentration of nitrogen dioxide. The error bars shown are taken directly from the values reported in Table 6.3. Again, it should be noted that the scatter in the data is fairly well confined.

6.3. PIV Measurement Results

As mentioned in Chapter 5, the PIV technique measured the velocity flow field between the parallel plates located within the experimental apparatus. Three plate separations were again chosen in an effort to determine a minimum spacing where entrance of the tracer gas into the space between the parallel plates would become more difficult. Identical to the PLIF concentration measurements, the plate separations were a 1.27 cm separation, a 1.91 cm separation, and a 3.18 cm separation.

The limitations of the hardware allowed for the gathering of velocity data over only a small plane located parallel to the plates. The velocity plane was centered at the midpoint between the top and bottom of the plates. The viewable area of the camera measured 10.5 cm in height by 14.0 cm in width.

6.3.1. PIV Vector Map

The velocity field was calculated by an examination of an array of point measurements within the viewable field. Overall, there were 24 measurement locations in the width direction and 19 measurement locations in the height direction. The total amount of point measurements was 456. Figure 6.12 is a raw data example of one time-step as a "snapshot" of the overall velocity flow field.

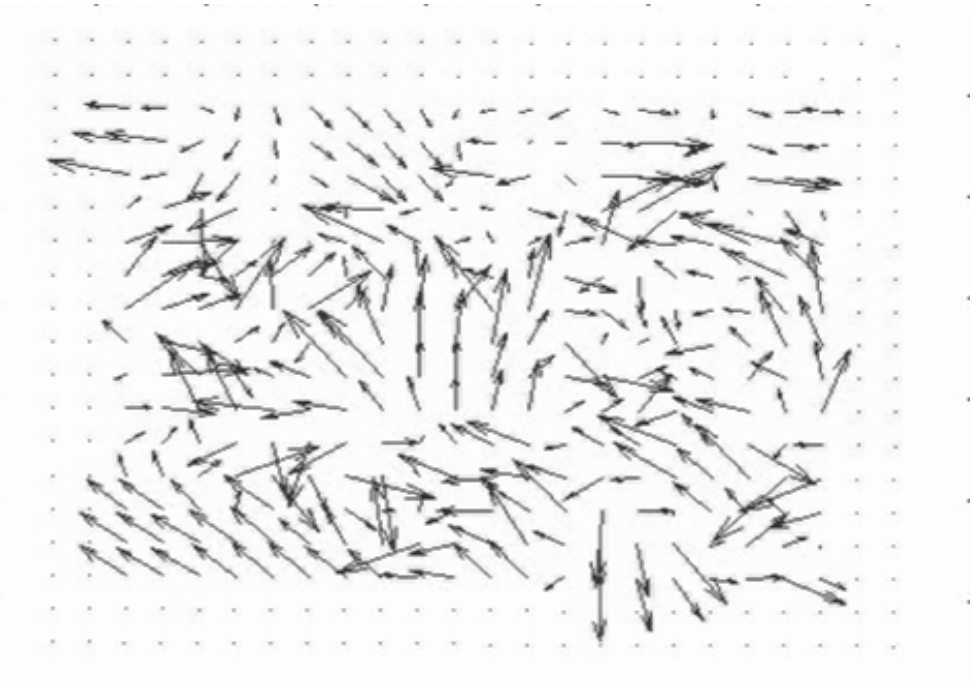

Figure 6.12: Raw data example of the overall velocity flow field.

To reduce the data for comparison with the modelling results, five point measurement locations were processed. Figure 6.13 depicts the locations of the spot velocity measurement locations.

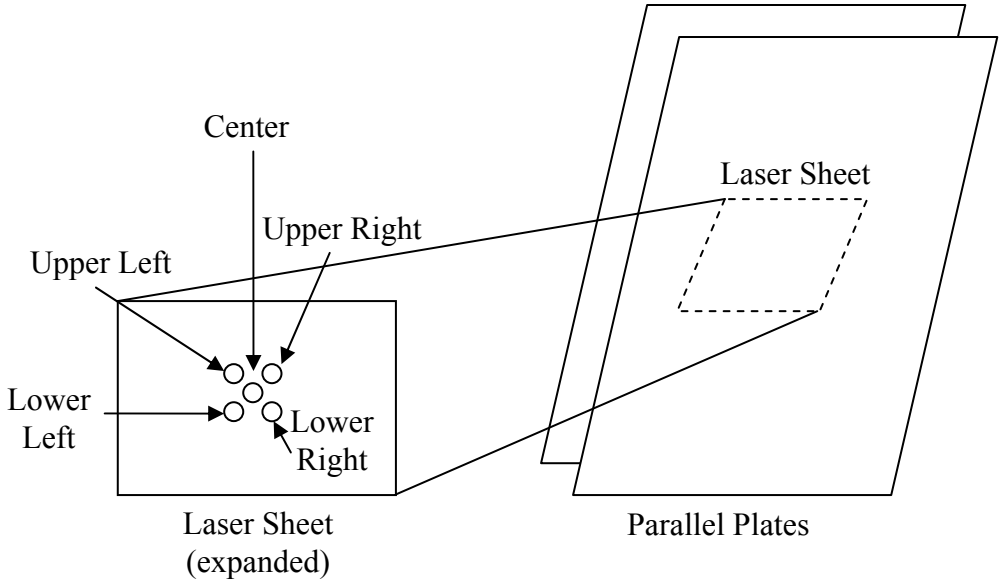

Figure 6.13: Diagram of PIV measurement locations within the laser sheet.

As can be seen in Figure 6.13, the measurement locations included one point closest to the center of the laser plane and four points immediately adjacent to and surrounding the center point. These locations, relative to the central point were labeled upper left, upper right, lower left, and lower right.

6.3.2. PIV Point Velocity Results

The raw images recorded by the digital camera were compiled into time histories of the horizontal and vertical velocity components of the flow between the plates. Figures 6.14 through 6.16 depict the resulting velocity components for the center point locations for each of the plate separation distances. Additionally, the velocity magnitude of the flow field at each of the point measurements was calculated and plotted. This data is presented in Figures 6.17 through 6.19.

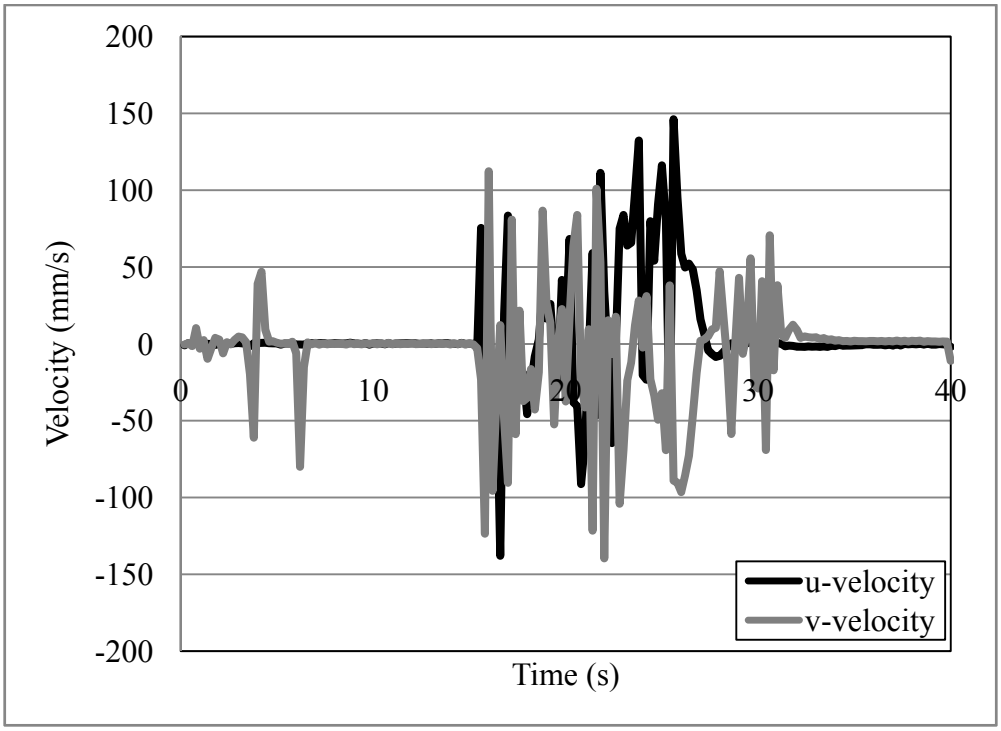

Figure 6.14: Center point velocity component data for the 1.27 cm plate separation.

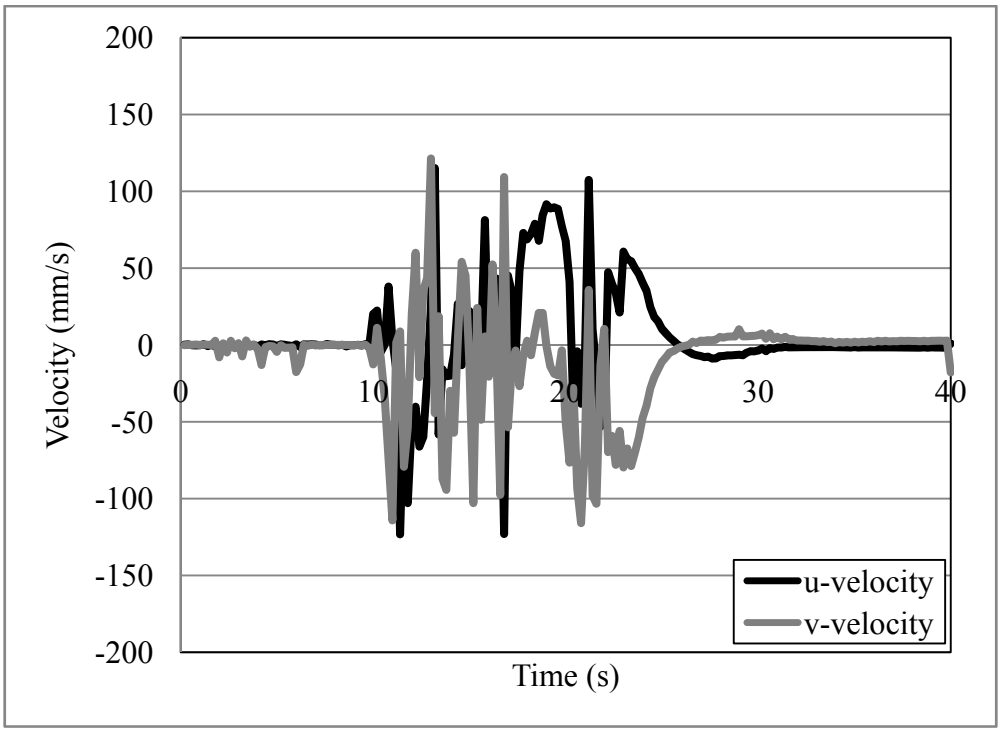

Figure 6.15: Center point velocity component data for the 1.91 cm plate separation.

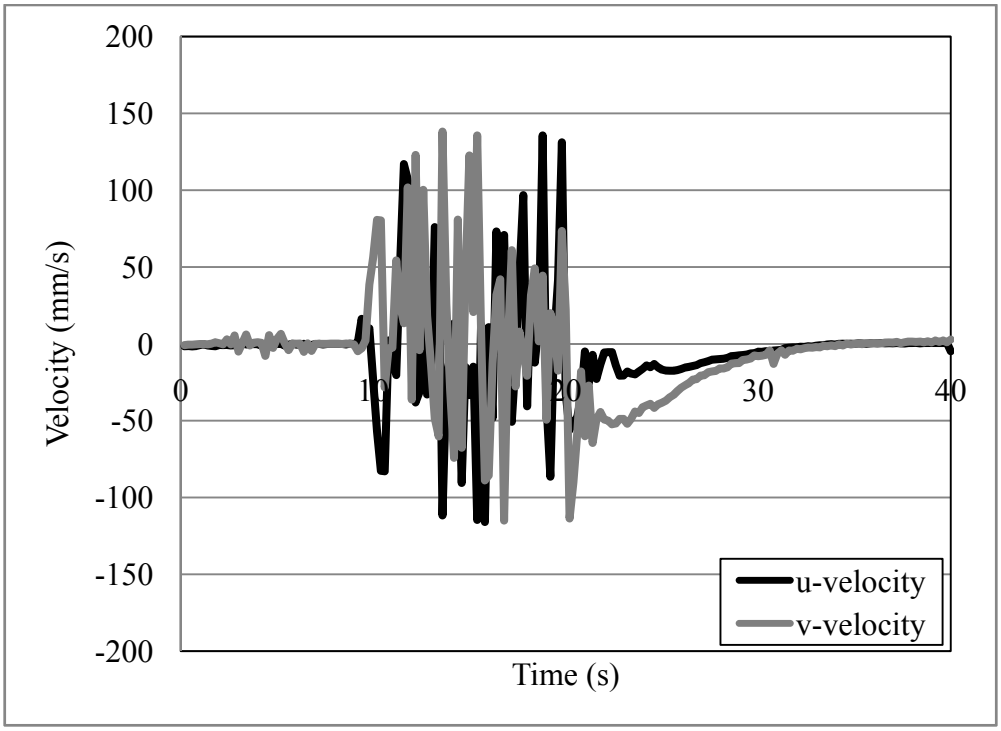

Figure 6.16: Center point velocity component data for the 3.18 cm plate separation.

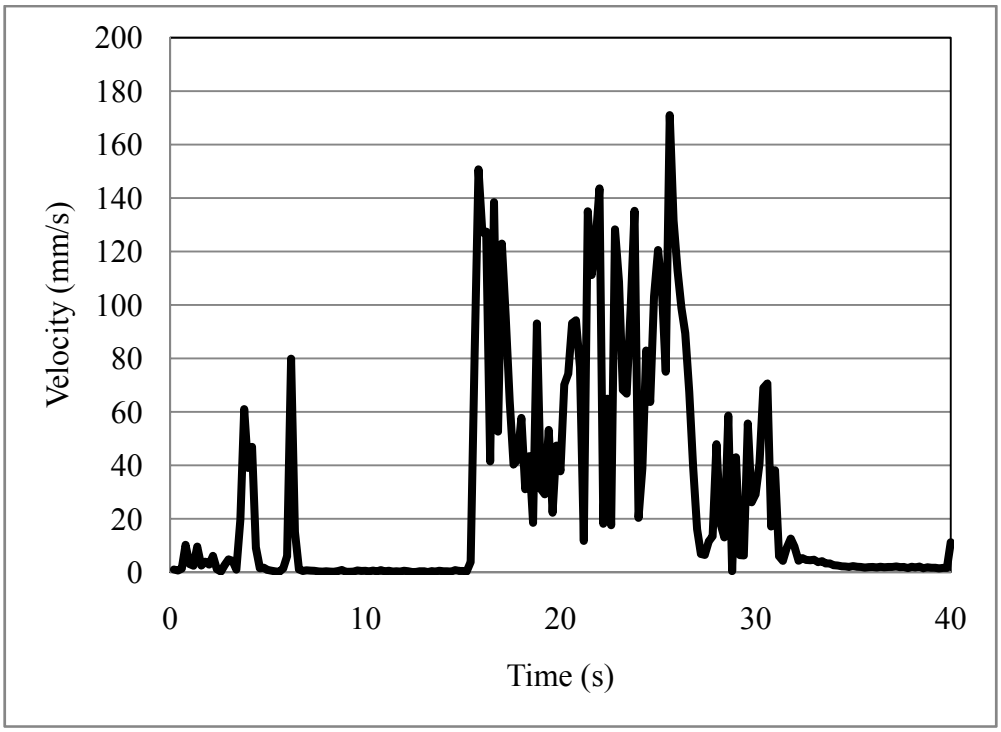

Figure 6.17: Center point velocity magnitude data for the 1.27 cm plate separation.

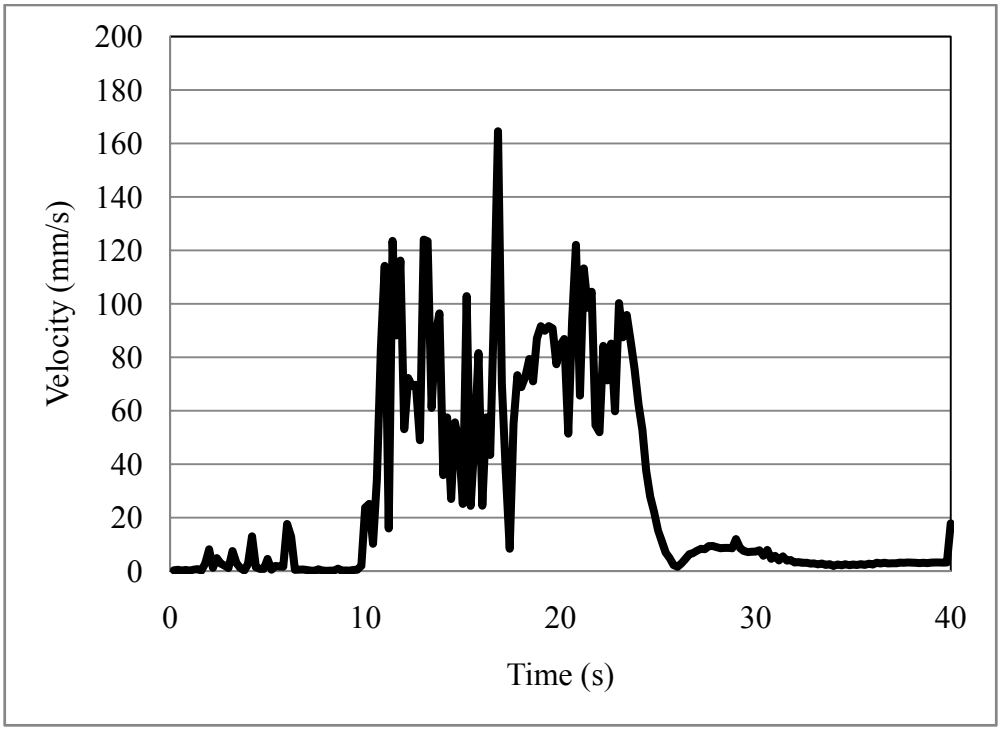

Figure 6.18: Center point velocity magnitude data for the 1.91 cm plate separation.

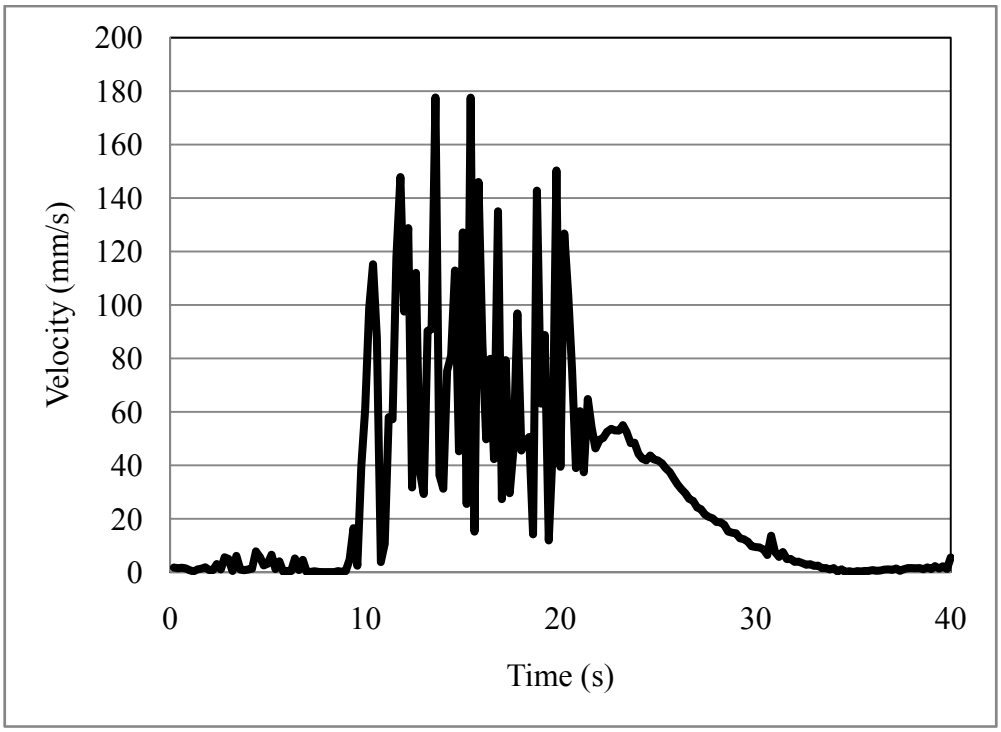

Figure 6.19: Center point velocity magnitude data for the 3.18 cm plate separation.

As shown in Figures 6.14, 6.15, and 6.16, the u-velocity component represents the horizontal movement of the flow between the plates, and the v-velocity component represents the vertical component of the flow between the plates. Data was gathered over a total time period of 40 seconds. The complete set of component velocity data is presented in Appendix C.

Similarly, as depicted in Figures 6.17, 6.18, 6.19, the total time period that data was gathered for the velocity magnitude data was 40 seconds. The complete set of velocity magnitude data is also presented in Appendix C.

6.3.3. PIV Measurement Error Analysis

To determine the level of confidence of the velocity results, a statistical analysis was performed with the data to determine the standard error among the measurements located around the center point location. The error was calculated using the average velocity magnitude of the five measurement locations taken at each plate separation distance. The standard deviation and the standard error were calculated using Equations 6.1 and 6.2, respectively. Table 6.4 lists the measurement location and plate separations and their corresponding standard deviations and standard errors.

Plate Separation (cm)	Measurement Location	Average Velocity Magnitude (mm/s)	Standard Deviation (mm/s)	Standard Error (mm/s)
1.27	Center	61.19	3.02	1.51
1.91	Center	72.67	2.62	1.17
3.18	Center	64.55	3.92	1.75

Table 6.4: Standard deviation and standard error for all velocity measurements.

Figure 6.20 shows a plot of the average velocity magnitude for each measurement location and plate separation.

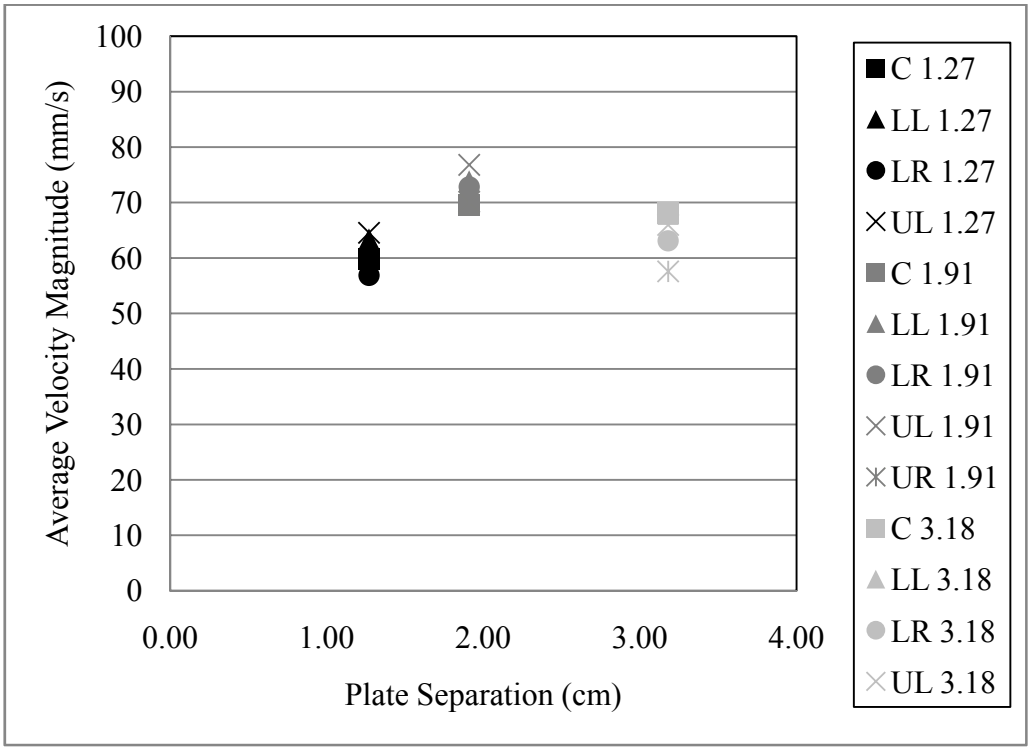

Figure 6.20: Average velocity magnitude at each measurement location and plate separation distance.

The plot shown in Figure 6.20 demonstrates the relatively small amount of variation between the locations at each plate separation. Additionally, no clear trend is apparent when examining the average velocity magnitude at each plate separation distance.

Figure 6.21 is a graphical representations of the overall error associated with the measurements.

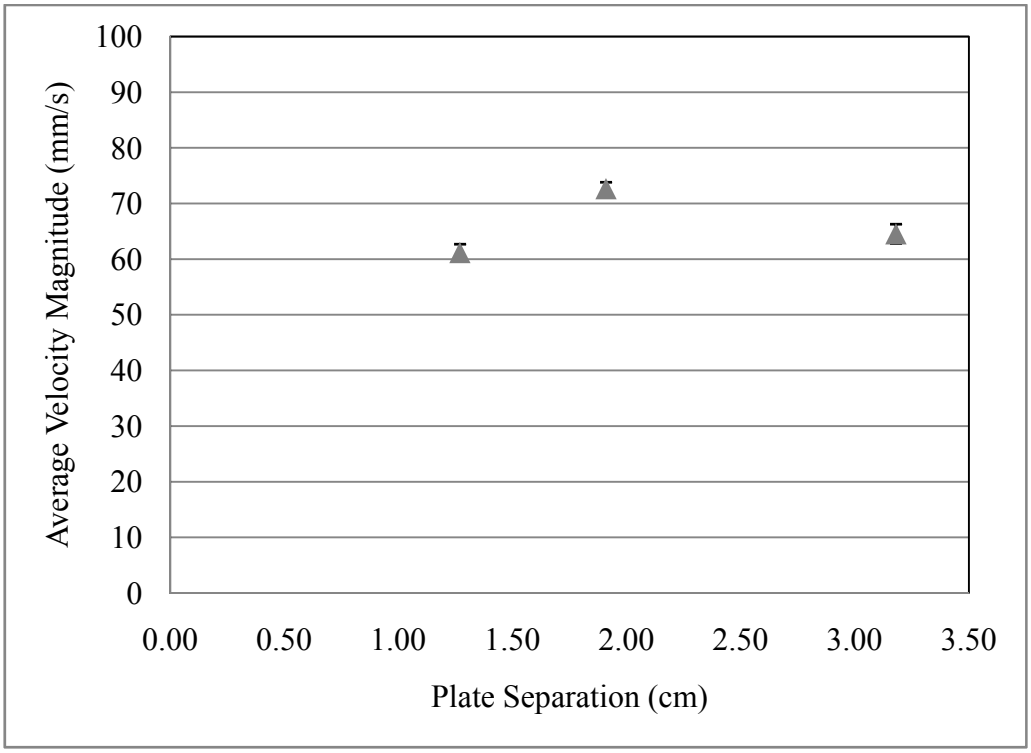

Figure 6.21: Average velocity magnitude at the center location for each plate separation (with error bars).

As depicted in Figure 6.21, each point represents the average velocity magnitude over the five measurement locations for each plate separation distance. The error bars shown are taken directly from the values reported in Table 6.4.

6.4. Conclusions

Chapter 6 has presented the results of the experimental studies utilizing PLIF measurements to determine the resultant average concentration of nitrogen dioxide at various locations between parallel plates and plate separation distances. This chapter has also presented the results of the experimental studies utilizing PIV measurements to determine the velocity flow field of a specific location between the center of the parallel plates and the resultant average velocity of several point measurement locations.

An error analysis of the concentration results indicated a relatively small variation in the range of data collected from test to test over the entire test matrix. Additionally, the analysis demonstrated that the error bars of the average concentration were relatively small, with the largest error occurring with a value of 228.9±16.7 ppm of nitrogen dioxide at the center location of the 1.27 cm plate separation distance.

Similarly, an error analysis of the velocity magnitude results indicated a small variation in the measurement locations surrounding the central measurement point between the parallel plates. The error bars in this analysis were small, with the largest error occurring with a value of 64.29±1.84 mm/s at the center location of the 3.18 cm plate separation distance.

The two parameters experimentally determined and presented in this chapter, the measurement of a concentration of a gas and the measurement of velocity flow field, provide validation data for use with a modelling analysis. The experimental apparatus used in this study provides a challenging configuration for both the measurement and modelling of these variables. Additionally, the experimentally measured parameters are consistent with the characteristic variables compiled in the Damköhler number as outlined in the theoretical framework of Chapter 4.

The next step in a flame extinction prediction methodology is to utilize a computational model that can predict the quantities measured experimentally and presented in this chapter. Chapter 7 will present the background for the use of a computational code and illustrate the procedure used to produce a modelling representation of both the geometry and boundary conditions associated with the experimental apparatus. The modelling comparison between the experimentally determined parameters and the modelling predictions of the computational code will be discussed in Chapter 8.

Chapter Seven

7. Model Development

7.1. Introduction

Chapter 7 is devoted to describing the details of the development of an appropriate computational model that accurately describes the physical geometry and parameters used in the experimental studies and can predict the results of gas concentration and velocity that were presented in Chapter 6. This chapter first reviews the background of the use of computational fluid dynamics as a tool for the prediction of various physical phenomena in the engineering community. Secondly, a brief review describing the Fire Dynamics Simulator (FDS) code and the FLUENT code as potentially appropriate codes for a modelling analysis and comparison with the experimental data is presented. Finally, a discussion of the variables used to create a model for the current problem using FLUENT is offered.

7.2. Computational Fluid Dynamics

Only within the last 40 years has computational fluid dynamics become a useful tool within the engineering community. The usefulness of this tool has been closely tied to the advent of the personal computer and increase in processor speed. The mathematics behind the code algorithms, though, had been developed much earlier. Numerical schemes for iterative solutions to various equations now computed using the CFD methodology were outlined in the early 1900's [49].

The aerospace industry was the first to take advantage of the abilities of CFD modelling, and developed codes and computer resources to understand lift and drag forces caused by fluid flow surrounding aerospace designs. The biggest challenge that arose in using the CFD methodology was how to properly handle turbulence within the calculation.

Three main modelling techniques were developed to deal with turbulent flows: Direct Numerical Simulation (DNS), the Reynolds Averaged Navier-Stokes (RANS) technique, and the Large Eddy Simulation (LES) technique [50]. In general, all three

of these techniques allowed for three-dimensional modelling of complex system geometries. Codes utilizing each technique have been written to allow for flexible geometric production or meshing of surfaces to describe minute details of physical surfaces within a model. The main difference between the three techniques was how turbulence was treated.

DNS would be ideal for most problems because it resolves turbulence within the calculation over all length and time scales. DNS directly solves the Navier-Stokes equations when given appropriate initial and boundary conditions. However, the main problem with using this technique is that it is very computationally intensive. Depending on the size of the geometry used within a DNS model, currently available computational technology can be inadequate to completely resolve the model solution. For an appropriate DNS solution, the grid resolution must be as small as the Kolmogorov length scale, which is the theoretical smallest length scale of turbulence first proposed by Kolmogorov. Additionally, all of the turbulent eddies must be simulated completely to achieve accurate results. The large computational time required and the lack of available computational technology available make the DNS scheme unfeasible for a majority of practical applications.

The RANS technique preferentially models only some aspects of the flow field. This is due, in part, to the impracticality of predicting the full solution to the Navier-Stokes equations. The RANS technique uses an approximation where simplified, averaged Navier-Stokes equations are solved through the use of turbulence modelling. The largest eddies are solved directly, but the smaller scales (i.e., scales smaller than the largest eddy) are modelled. Thus, dynamic information for the movement (and other predicted variables) of the flow at the smaller scales is not predicted.

The RANS technique can be further categorized into utilizing several turbulent sub-grid models. These include the commonly used k-ε (k-epsilon) model, the k-ω (k-

omega) model, and the Reynolds stress model (RSM). Additionally, the RANS technique can be designed to compute steady-state or transient solutions.

LES, a third commonly used modelling technique, directly resolves large-scale turbulence within the code, and uses a sub-grid model to account for the small-scale turbulence. The LES technique is inherently time-dependent (i.e., producing a transient solution), since the Navier-Stokes equations are not time-averaged as is the case with the RANS technique. Both the LES and RANS techniques have methods for predicting the turbulent components of the flow field when at the smaller scales. The main difference between the two techniques is what the small-scale represents. In an LES code, the small-scale is defined as the information located below the size of the grid cell. In a RANS code, the small-scale is defined as the flow information located in the scale smaller than that of the largest eddy.

From a computational time perspective, a DNS code fundamentally requires the most computational resources and time to achieve a solution. The LES technique typically requires more computational resources than a model utilizing a transient version of the RANS technique. Ultimately, the needs and overall goals of the modelling study will dictate which modelling method is most appropriate. For this project, both a LES code and a RANS code were explored.

7.3. Fire Dynamics Simulator (FDS)

As a code that utilizes a LES technique, the Fire Dynamics Simulator (FDS) was first explored as a means to predict the velocities and concentration found during experimentation. FDS is a code that uses computational fluid dynamics to model hydrodynamic flow and fire phenomenon. The code was developed at the National Institute of Standards and Technology (NIST) by Dr. Kevin McGrattan and co-workers [51, 52]. The code solves a form of the Navier-Stokes equations for low-speed, thermally-driven flow conditions [52].

The FDS code contains a collection of several sub-models that allow for a user to explore various problems through user-defined modelling inputs for various boundary conditions. These include a hydrodynamic model, a combustion model, and a radiation transport model. Additionally, FDS provides the functionality to construct detailed geometric configurations through the use of multiple meshing structures. FDS can be run in serial or parallel modes [52].

The hydrodynamic sub-model used in FDS is based on an explicit predictor-corrector scheme, which is second-order accurate in space and time [52]. The model incorporates an LES technique to solve for the flow field within the computational space. DNS is available as an option within the code, but requires an appropriate level of grid resolution to achieve accurate results.

The combustion sub-model within FDS utilizes a single-step chemical reaction. The products of combustion are tracked through the use of a two-parameter mixture fraction model [52]. The mixture fraction is defined as a conserved scalar quantity that represents the mass fraction of the various components of the gas within the flow field [52]. The combustion sub-model also contains a multiple-step finite rate model.

The radiation transport sub-model within FDS incorporates the solution of the radiative heat transfer equation for a gray gas [52]. The technique used to solve the equation is based on a finite volume method traditionally used in convective transport. The sub-model includes methods for both the calculation of gas-phase radiative transfer and the accounting for the presence of water droplets and their impact on the absorption and scattering of radiation [52].

FDS is a unique LES code that was specifically created to deal with problems related to fire, but the code has been shown in validation studies to be useful in a variety of applications. Many of the validation studies have used FDS due to the ability to quickly achieve the temporal results of a model. The solver routine within the code was written to be computationally efficient. The speed of the computation is

generated through geometry restrictions which only allow for a system to be fully rectilinear. Hence, all curved or angled surfaces described within the model must be described as rectilinear. The effects of this approximation can be minimized if the grid density is very high. Body-fitted meshes used in other commercial codes cannot be implemented into this model without losing the large computational speed increase. Even so, complex geometries can be generated in FDS.

7.4. FLUENT

As a code that utilizes a RANS technique, FLUENT was also explored as a means to predict the velocities and concentration found during experimentation. FLUENT, a commercial computational fluid dynamics code, was developed in the early 1980's by a group of private researchers as a tool that provided an interactive CFD code for engineers and scientists. The continuing enhancement of the code has proceeded uninterrupted until the present day. In general, the FLUENT code is a well-developed CFD program that allows for a user to model fluid flow and heat transfer in complex geometries.

Unlike FDS, FLUENT is produced and supported through commercial enterprise. The increased resources and support have resulted in a complex code that has a vast array of tools and potential applications. The negative aspect of the enhanced functionality is the financial cost of the code (i.e., FLUENT licenses much be purchased on a yearly basis).

Many of the enhanced features of FLUENT when compared to FDS are associated with the mesh flexibility inherent to the FLUENT code. FLUENT supports an unstructured mesh type that includes a variety of cell definitions: two-dimensional triangular and quadrilateral and three-dimensional tetrahedral, hexahedral, pyramid, wedge, and polyhedral cell definitions. This refinement allows for extremely accurate geometric representation of the structure being modelled.

In addition to a refined expression of the modelled geometry, FLUENT utilizes sub-model routines for use in analyses. These include a hydrodynamic sub-model that can be solved using LES, RANS, or DNS methods; a combustion sub-model that can utilize a single or multiple-step chemical reaction; conduction, convection, and radiation transport sub-models; as well as many other features expected in commercial software. Some of these sub-models/features include the ability to model steady-state or transient flows, incompressible or compressible flows, Newtonian or non-Newtonian flows, and detailed mixing models.

7.5. Model Development

A virtual representation of the experimental apparatus was created for the present study using the FDS code, version 5.1.6. As mentioned previously, the goal was to establish what type of computational model was appropriate for predicting the dispersion aspect of the overall problem. The FDS code was unable to predict the overall dispersion of the high-momentum gaseous jet slowing to laminar flow between parallel plates. Appendix D contains a more detailed account of the various failed modelling attempts used to predict the dispersion and some possible reasons for the failure.

A virtual representation of the experimental apparatus was also created using the FLUENT code, version 6.4. Similar to using the FDS code, the goal was to establish whether or not FLUENT was appropriate for predicting the dispersion aspect of the overall problem by examining the comparison of the experimental data with the modelling results.

The geometry of the experimental apparatus was constructed to scale within the FLUENT model. The overall dimensions of the apparatus were identical to those outlined in Chapter 5. All geometry features found in the experimental apparatus were included in the FLUENT model. These included the apparatus exterior walls, the ventilation areas located near the base of the apparatus, the laser beam dump

structure, and the inlet nozzle used to release the gaseous mixture into the internal chamber. Figure 7.1 shows a diagram of the FLUENT model representation of the experimental apparatus.

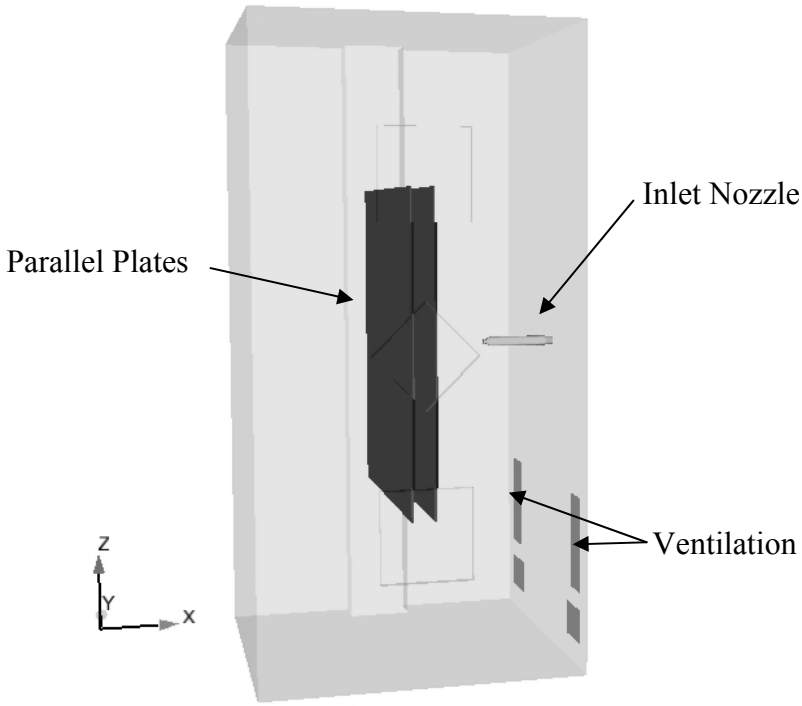

Figure 7.1: FLUENT modelling representation of the experimental apparatus.

The strength of using the FLUENT model was readily apparent with regard to the model description of the inlet nozzle. As mentioned, FLUENT is structured to allow for the construction of an adaptive body-fitted mesh within the model, which resulted in a complete physical representation of the nozzle geometry. The boundary condition of the flow was applied at the interface of the nozzle with the wall of the experimental apparatus. The flow field was then directly calculated within the nozzle, out of the nozzle, and throughout the interior of the experimental apparatus. Figure 7.2 depicts a view of the relative location of the inlet nozzle with respect to the parallel plates and the ventilation from the experimental apparatus.

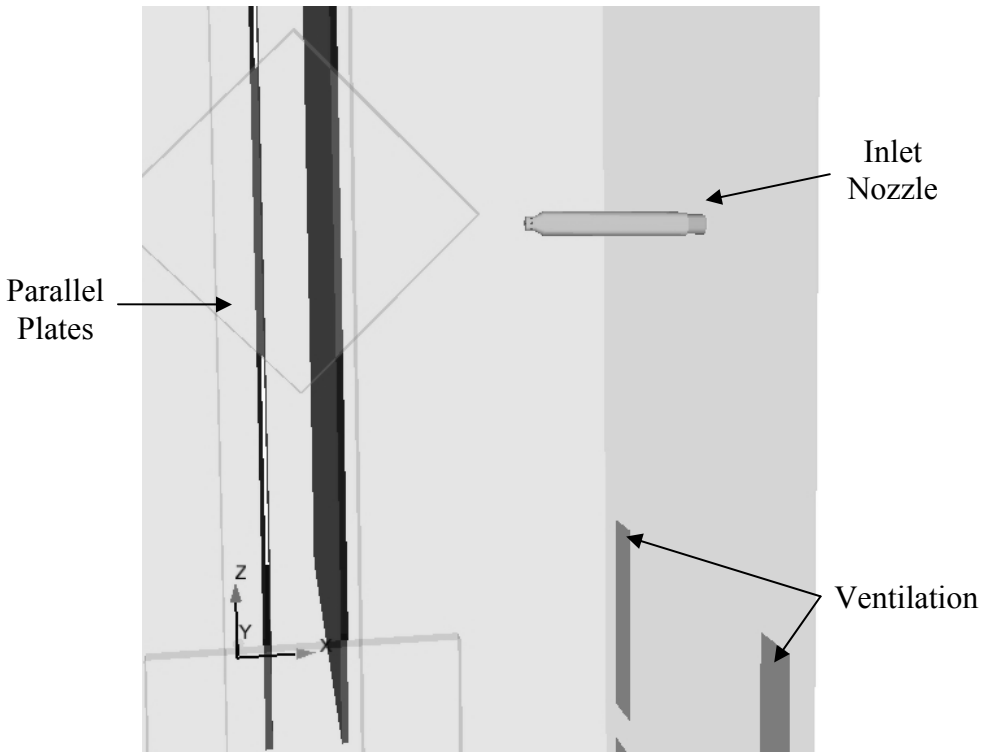

Figure 7.2: Closer view of inlet nozzle representation within the FLUENT model.

Overall, the model contained 820,443 nodes. The node density varied throughout the model, with increased resolution in the local area around the plates, in the area within the plates, near all solid obstructions, and in the area within and surrounding the inlet nozzle. The increase in the node density in these areas resulted in a corresponding increase in cell density. The increase in cell density was necessary for the model to solve more accurately the fluid flow in the boundary layers that developed close to the solid obstructions. Additionally, the increased cell density, near and within the nozzle, allowed for an accurate prediction of the flow from the initial high-momentum gaseous jet into the model domain. Figure 7.3 illustrates the increasing node density of the FLUENT model at a slice through the center of the experimental apparatus.

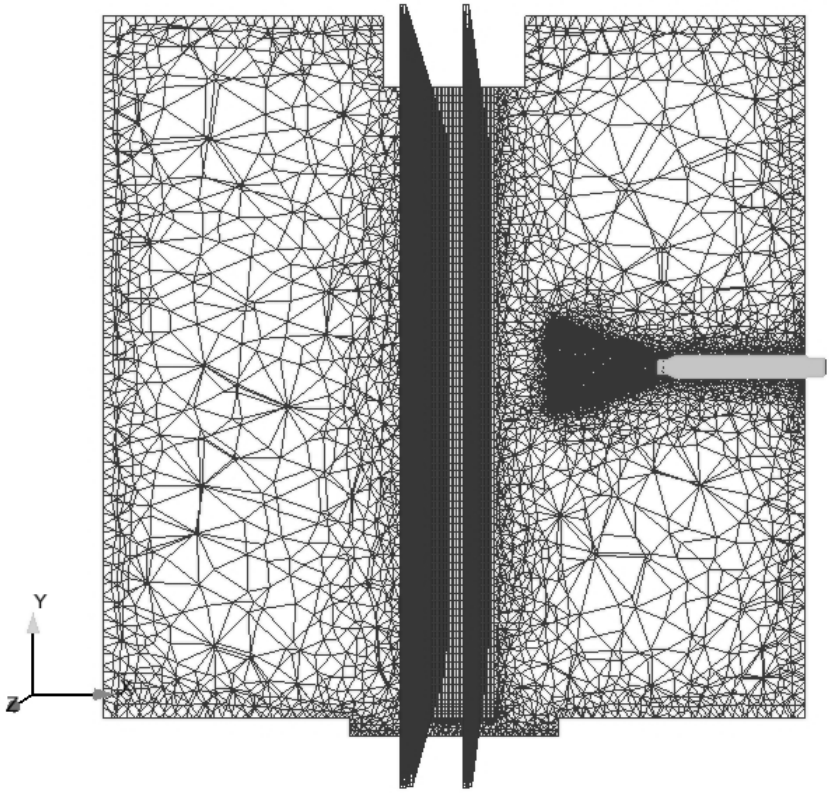

Figure 7.3: Node density displayed for a center slice through the experimental apparatus.

Two FLUENT model variations were created to match the experimental geometry and testing conditions as outlined in Chapters 5 and 6. These model variations were conducted using a pressure-based Navier-Stokes solver. The data obtained for the transient results was second-order implicit in time. As per typical implicit methods, the Navier-Stokes equations are solved both at the current time-step and next time-step while iterating to cancel errors within the approximation such that an acceptable level of error is maintained. The code also contains an adaptive time-step routine to facilitate maximum computational efficiency.

A standard k-ε turbulence model was used with standard wall functions. This turbulence model follows the general methodology whereby two additional transport equations are solved by the code: a transport equation for the turbulent kinetic energy, k, and a transport equation for the turbulent diffusivity, ε. In general, this

computational method has been demonstrated to provide accurate predictions for the convective flow of gases as well as the diffusion of turbulent energy.

The first model variation tracked the flow of the inlet gas mixture (e.g., nitrogen and nitrogen dioxide mixture) over a 30-second period. The initial time-step was 0.02 seconds. The inlet boundary condition was represented by the introduction of the gaseous mixture into the domain. This boundary condition was previously presented in graphical format in Figure 5.8 in Chapter 5. Data collection from the model was focused on matching the experimentally measured concentration values for the seeded flow of nitrogen dioxide into the space between the parallel plates of the experimental apparatus.

The second model variation again tracked the flow of the inlet gas mixture over a 30-second period. The initial time-step was 0.02 seconds. In this case, though, the inlet boundary condition was represented by a release of gaseous agent that was composed completely of air into the domain at a reduced tank pressure. This boundary condition was previously presented in graphical format in Figure 5.11 in Chapter 5. Data collection from this model was focused on matching the experimentally measured velocity field measurements that were obtained through the use of the PIV technique between the parallel plates of the experimental apparatus.

7.4. Conclusions

Chapter 7 has outlined the details of the development of an appropriate computational model that accurately describes the physical geometry and parameters used in the experimental studies. The background of the use of computational fluid dynamics as a tool for the prediction of various physical phenomena has been presented. Additionally, a brief description of the FLUENT code has been offered. This chapter concluded by providing detailed information on the modelling representation for the current problem using the FLUENT code.

As mentioned in Chapter 4, all of the variables that comprise the Damköhler number as outlined in the theoretical framework are characteristic variables that must be determined through appropriate means. A computational model and, in particular, a model utilizing the FLUENT code, provides the ideal way to calculate and track the local values of the variables that comprise the Damköhler number within a model representation of a combustion problem in a three-dimensional environment.

For a potential FLUENT model that employs the combustion process, several variables of the Damköhler number are constants that must be accounted for within the model through various inputs. These variables include the pre-exponential constant, the activation energy, and the universal gas constant. The remaining variables can change both spatially and with respect to time within a particular problem. These variables include the local gas density, the local mass concentration of the fuel, the local mass concentration of the oxidizer, the local gas temperature, and the local strain rate of the flow.

As with any modelling analysis, comparison of the modelling analysis with experimental data provides a means to assess the accuracy of the model. This comparison between the experimental data and the modelling predictions is presented in Chapter 8. Additionally, a discussion of the comparison is offered, and the modelling analysis is expanded to demonstrate the use of the Damköhler number as an extinction parameter in a FLUENT model developed to predict the gaseous suppression of a flame.

Chapter Eight

8. Model Comparison and Discussion

8.1. Introduction

The preceding chapters have presented a foundation for the determination of flame extinction and flame suppression through the use of a generalized Damköhler number in conjunction with a computational model capable of directly calculating the local variables for the Damköhler number at each point in the analysis geometry. Validation data for the model was gathered using PLIF and PIV techniques. The data obtained through these methods was presented in Chapter 6. Chapter 8 will compare the validation data with the FLUENT model that was described in Chapter 7. Comparison of the modelling analysis with experimental data will provide a means to assess the accuracy of the model and the expected error rates. Additionally, an example of a modelling case with active combustion will be presented to demonstrate the process of using the methodology proposed in this work for the prediction of flame extinction. The example model will include a combustion process between the parallel plates of the experimental apparatus and the interaction of the combustion zone with an influx of a suppressant agent.

Chapter 8 will begin by first presenting the comparison of the modelling predictions for the nitrogen dioxide (NO_2) concentrations. Second, the comparison of the velocity modelling predictions will be provided. Third, a description of an example combustion problem involving gaseous suppression will be offered. Finally, the modelling results of the example combustion problem with gaseous suppression will be used to demonstrate the potential application of the use of the Damköhler number as the focal analysis parameter in a methodology for the prediction of flame extinction in any three-dimensional environment.

8.2. Comparison of Experimental Data with FLUENT Modelling Results

As discussed in Chapter 7, two FLUENT model variations were created to match the experimental geometry and testing conditions created during the experimental

studies. Both of the model variations were conducted using a pressure-based Navier-Stokes solver. As mentioned, the data obtained for the transient results was second-order implicit in time and the turbulence model used was the standard k-ε model with standard wall functions.

The models varied only by the boundary condition for the input of the gaseous agent into the experimental apparatus. For the model of the PLIF concentration measurements, a boundary condition associated with a mass flow influx of a mixture of nitrogen and nitrogen dioxide was assigned at the nozzle. (Refer to Figure 5.8). For the model of the PIV velocity measurements, the boundary condition was adjusted for a slightly smaller mass flux and to account for the release of air from the inlet as opposed to the nitrogen and nitrogen dioxide mixture. (Refer to Figure 5.11).

8.2.2. PLIF Concentration Comparison

Chapters 5 and 6 described the location and sizing of the measurement locations where the concentration data was recorded. These average point measurements located between the parallel plates were referred to as the top, center, and bottom measurement locations. The FLUENT model was interrogated to provide modelling predictions as concentration histories for these corresponding locations within the modelled geometry.

Figure 8.1 depicts a planar slice of concentration data predicted by the FLUENT model. A scale colored-coded according to volume fraction is used to represent the amount of nitrogen dioxide predicted by the model.

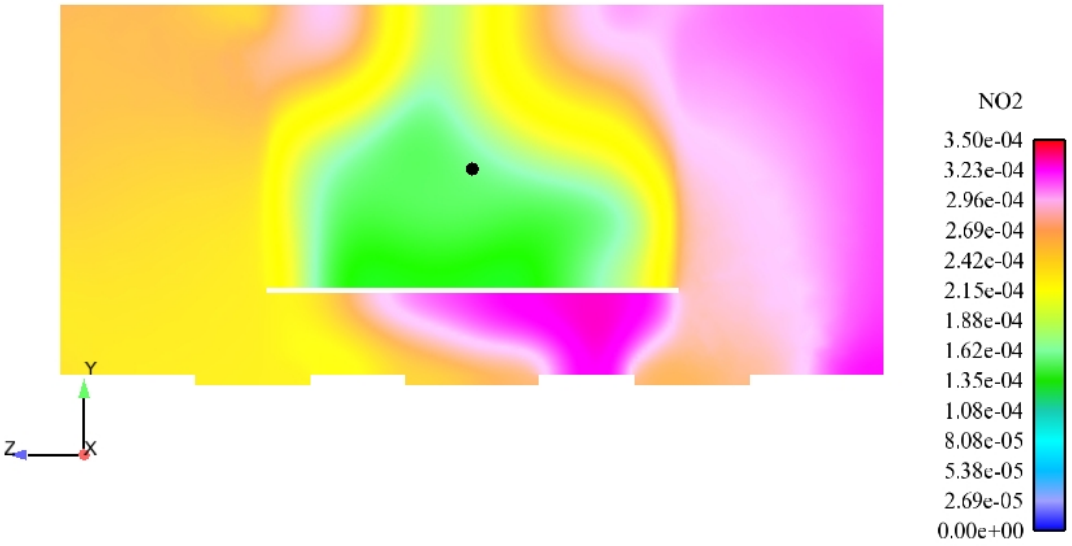

Figure 8.1: Example nitrogen dioxide data slice at the midpoint between the parallel plates for the 1.27 cm plate separation.

As depicted in Figure 8.1, the slice was positioned at the midpoint between the plates for the 1.27 cm plate separation. The slice is turned on its side, with the left portion of the picture representing the "top" of the experimental apparatus. The reference dot depicted in the slice is the location of the center measurement point between the parallel plates.

Figure 8.2 shows the comparison of the experimental data with the FLUENT modelling predictions at the 1.27 cm plate spacing.

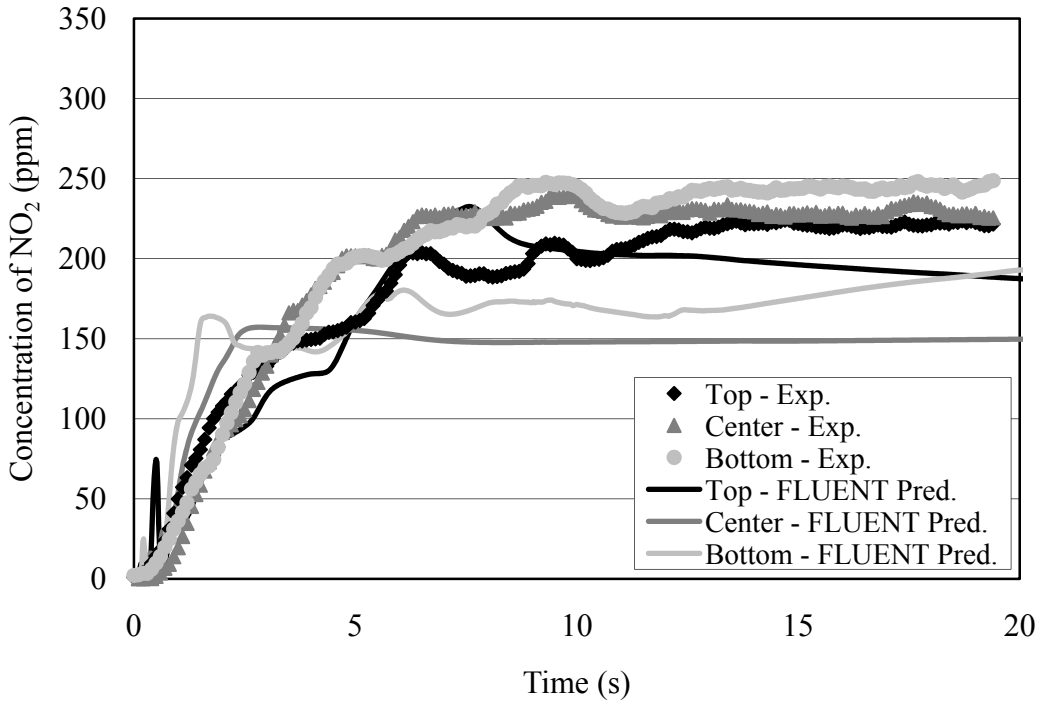

Figure 8.2: Comparison between nitrogen dioxide experimental values and FLUENT model predictions at the 1.27 cm plate separation.

Figure 8.2 demonstrates, in general, that the overall trend of the concentration development between the plates was well-predicted by the FLUENT model. The initial concentration rise is rapid in both the experimental data and in the modelling predictions. This rise is due to the nature of the influx of the gaseous boundary condition at the nozzle. The maximum steady-state average concentration from the experimental data was 244.8 ppm, which occurred at the bottom measurement location. The maximum steady-state average for the FLUENT modelling predictions was 193.2 ppm, which occurred at the top measurement location. The overall steady-state solution at all three locations underpredicts the values observed in the experiments.

Figure 8.3 shows the comparison of the experimental data with the FLUENT modelling predictions at the 1.91 cm plate spacing. Similar to the comparison for the

1.27 cm spacing, the overall trend of the concentration development between the plates was reasonably predicted by the FLUENT model.

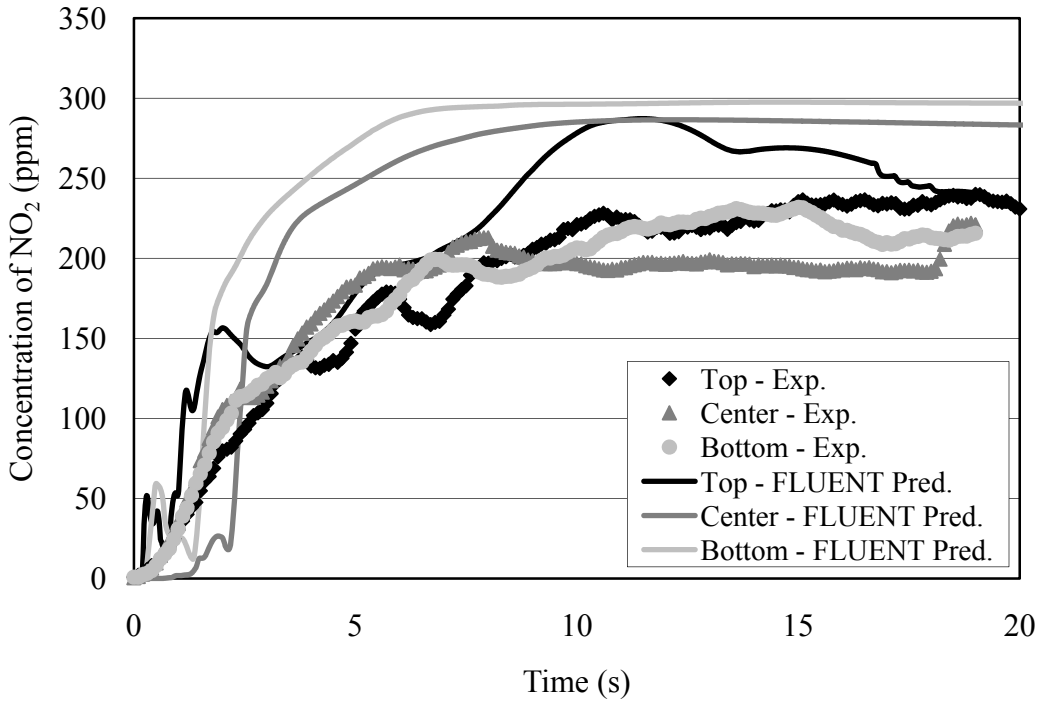

Figure 8.3: Comparison between nitrogen dioxide experimental values and FLUENT model predictions at the 1.91 cm plate separation.

As shown in Figure 8.3, the maximum steady-state average concentration from the experimental data was 234.5 ppm, which occurred at the top measurement location. The maximum steady-state average for the FLUENT modelling predictions was 296.0 ppm, which occurred at the bottom measurement location. The overall steady-state solution at all three locations over predicts the values observed in the experiments.

In comparison, the initial concentration rise is more rapid in the model predictions than seen in the experimental data. Overall, the time to achieve steady-state conditions as predicted by the model matches well with the actual time observed in the experimental data. The difference between the experimental concentration data

and the modelling predictions is due to the impact of the boundary layer resolution in the model. Further refinement of the grid would be expected to improve upon these results.

Figure 8.4 shows the comparison of the experimental data with the FLUENT modelling predictions at the 3.18 cm plate spacing. Similar to the comparison for the 1.91 cm spacing, the initial concentration rise is more rapid and contains greater fluctuations in the model predictions than seen in the experimental data.

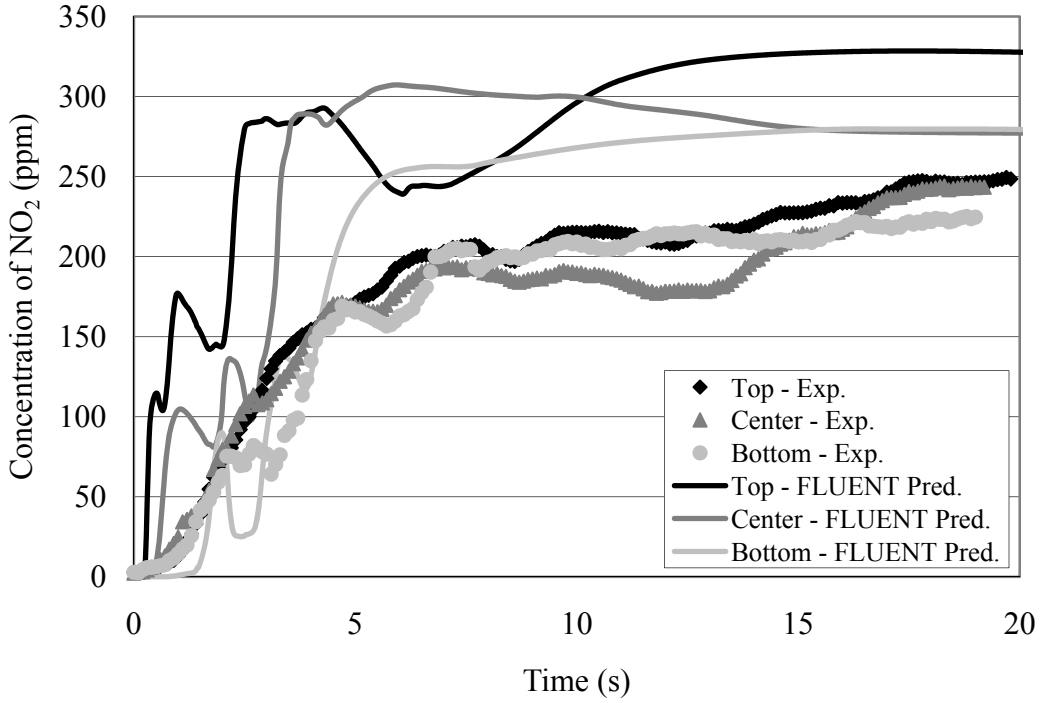

Figure 8.4: Comparison between nitrogen dioxide experimental values and FLUENT model predictions at the 3.18 cm plate separation.

As depicted in Figure 8.4, the maximum steady-state average concentration from the experimental data was 242.7 ppm, which occurred at the top measurement location. The maximum steady-state average for the FLUENT modelling predictions was 309.0 ppm, which also occurred at the top measurement location. The overall steady-state solution at all three locations clearly over predicts the values observed in the experiments.

Again, the overall time to achieve steady-state conditions as predicted by the model matches fairly well with the actual time observed in the experimental data. The difference between the experimental concentration data and the modelling predictions is due to the impact of the boundary layer resolution in the model. Further refinement of the grid would be expected to improve upon these results.

Table 8.1 shows a compilation of the comparison of the average steady-state nitrogen dioxide concentration values with the average steady-state modelling predictions of nitrogen dioxide concentration at the three plate separations and measurement locations. The percent error in the nitrogen dioxide concentrations is calculated with the following formula:

$$Err = \frac{\left|\mathrm{ppm}_{\mathrm{ex}} - \mathrm{ppm}_{\mathrm{pred}}\right|}{\left|\mathrm{ppm}_{\mathrm{ex}}\right|} \times 100 \tag{8.1}$$

Plate Separation (cm)	Measurement Location	Average Experiment Concentration (ppm)	Average FLUENT Model Concentration (ppm)	Percent Error
1.27	Top	221.0	193.2	12.6
1.27	Center	228.9	150.4	34.3
1.27	Bottom	244.8	187.3	23.5
1.91	Top	234.5	237.0	1.1
1.91	Center	198.0	280.0	41.4
1.91	Bottom	216.1	296.0	37.0
3.18	Top	242.7	309.0	27.3
3.18	Center	232.5	282.0	21.3
3.18	Bottom	219.0	273.0	24.7

Table 8.1: Comparison of the average steady-state nitrogen dioxide concentration values with the average steady-state modelling predictions of nitrogen dioxide concentration at the three plate separations and measurement locations.

Overall, the results of the modelling predictions are fairly good. Even though an initial assessment of the range of error of 1.1% to 41.4% suggests that the model error is substantial, the focus of the error analysis should be more on the transport of the major gas in the injected mixture. The nitrogen component in the mixture represents the bulk of the fraction of the mixture.

Table 8.2 provides a practical assessment of the accuracy of the model through examination of the prediction of the nitrogen gas transport.

Plate Separation (cm)	Measurement Location	Average Experimental Nitrogen Concentration (%)	Average FLUENT Nitrogen Concentration (%)	Nitrogen Error Bounds (±%)
1.27	Top	21.2	18.6	2.3
1.27	Center	22.0	14.5	5.0
1.27	Bottom	23.5	18.0	4.2
1.91	Top	22.5	22.8	0.2
1.91	Center	19.0	26.9	11.2
1.91	Bottom	20.8	28.5	10.5
3.18	Top	23.3	29.7	8.1
3.18	Center	22.4	27.1	5.8
3.18	Bottom	21.1	26.3	6.5

Table 8.2: Error bounds of the concentration of nitrogen in the FLUENT predictions.

The data in Table 8.2 demonstrates that even a relatively high error rate of 41% for the prediction of the nitrogen dioxide results in only a ±11% error bound in the prediction of the percent concentration of the nitrogen in the mixture. This error can be interpreted as a requirement for a safety factor when utilizing a FLUENT model for the prediction of gas concentration in a three-dimensional environment.

8.2.3. PIV Velocity Comparison

The PIV measurement locations were described in Chapters 5 and 6. The point measurements interrogated for presentation in the results section were tabulated from a center position and center plane between the parallel plates. (Refer to Figure 6.13). The FLUENT model for the PIV velocity comparison was designed to report the velocity in that identical location within the modelled geometry.

For illustrative purposes, Figure 8.5 shows the velocity field surrounding the nozzle seven seconds after the initiation of the blowdown into the experimental apparatus. The vectors are color-coded according to velocity magnitude.

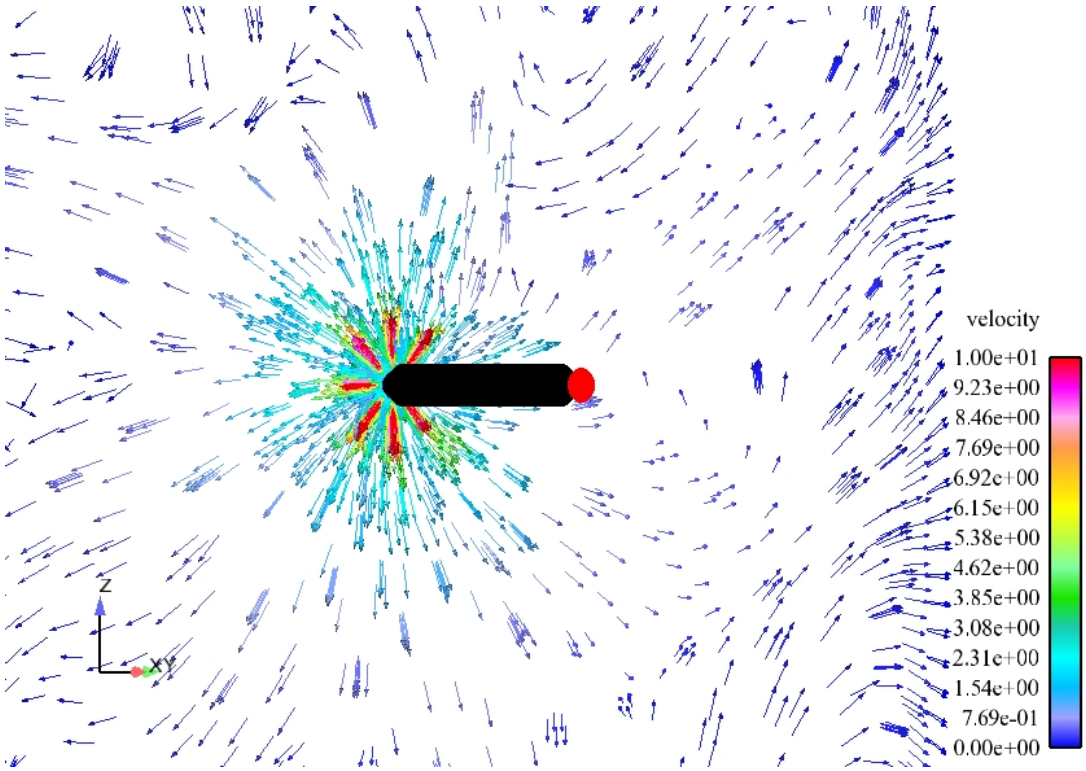

Figure 8.5: Predicted velocity flow field seven seconds after blowdown initiation.

Figure 8.5 provides an example of how the velocity field evolves within the experimental apparatus due to the influx of gas through the nozzle boundary condition. It should be noted that the distribution in the near field of the nozzle is in

a radial pattern demonstrating the flow through the eight radial inlet holes located at the tip of the nozzle.

Figure 8.6 depicts the velocity disparity between the areas of fluid outside the parallel plates and the area of fluid located between the plates. The graphic represents a slice through the midpoint of the parallel plates at the 1.27 cm plate separation. The scale is colored according to velocity magnitude with units of m/s. Similar to Figure 8.1, the left side of the slice represents the "top" of the experimental apparatus.

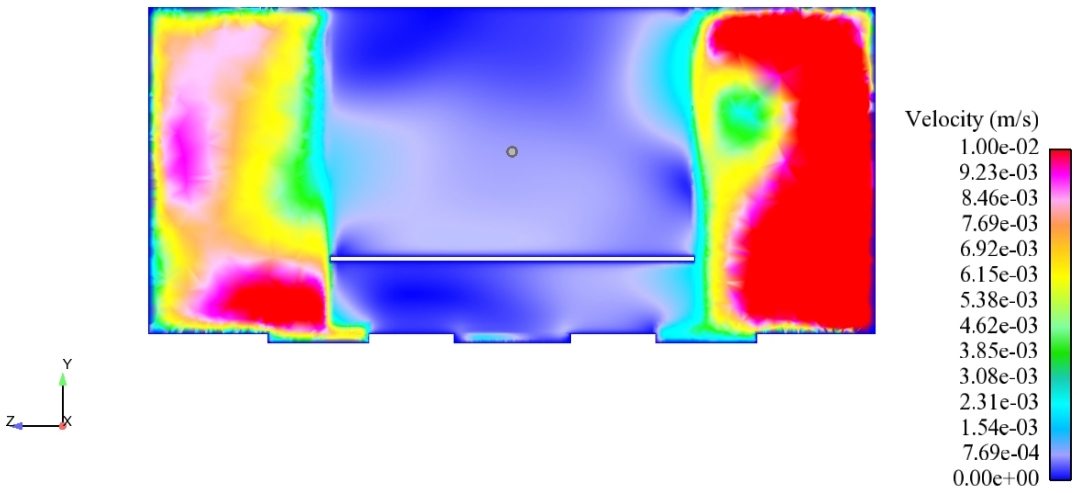

Figure 8.6: Example velocity magnitude slice at the midpoint between the parallel plates for the 1.27 cm plate separation after 0.6 seconds.

As shown in Figure 8.6, at 0.6 seconds after the release of the gas from the inlet nozzle into the experimental apparatus, the velocity has yet to penetrate into the space between the parallel plates. The fluid spaces that have no obstructions quickly build to a maximum velocity in only tenths of seconds, while flow into the area between the plates is at first delayed and then slowed, due to the constriction of the small separation distance.

Figure 8.7 shows the model comparison between the FLUENT predictions and the experimental data in terms of velocity magnitude for the 1.27 cm plate separation.

The peak velocity magnitude obtained in the experimental studies at this separation was 171 mm/s. The corresponding peak velocity magnitude predicted by the FLUENT model was 333 mm/s. The average velocity magnitude in the experimental study over the steady period of the test data was 61 mm/s. The corresponding average velocity magnitude predicted by the FLUENT model was 61 mm/s.

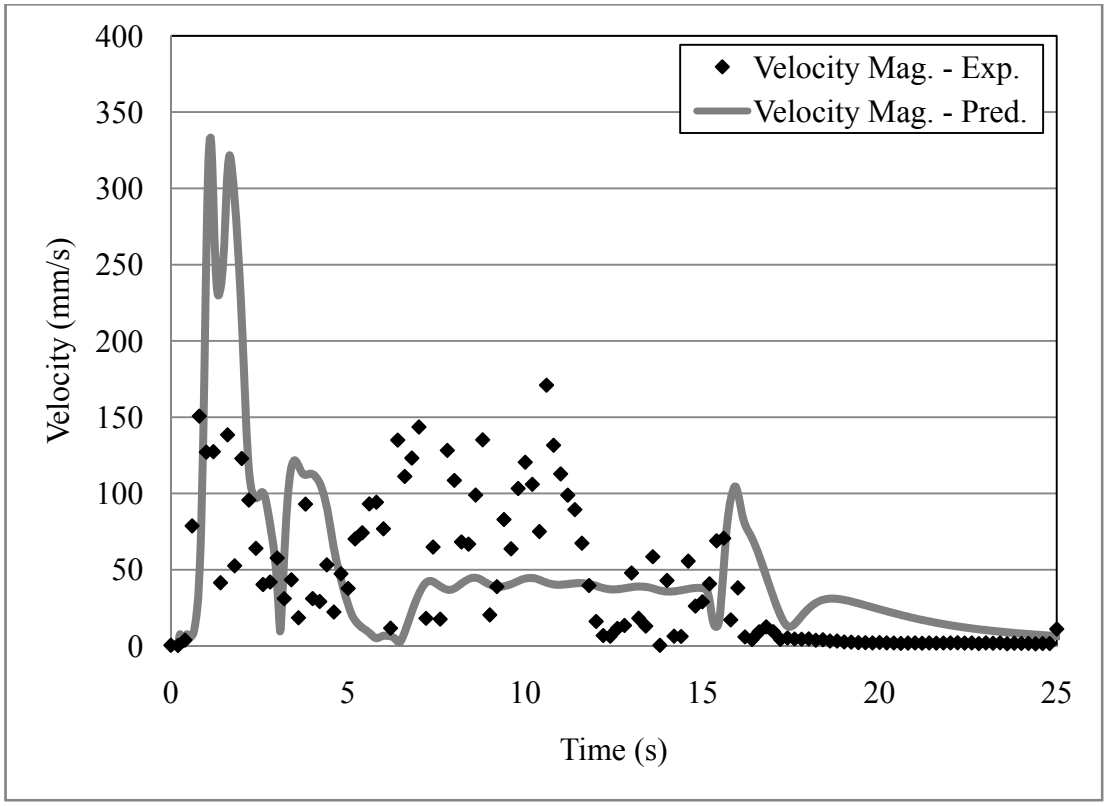

Figure 8.7: Comparison between PIV velocity magnitude experimental values and FLUENT model predictions at the 1.27 cm plate separation.

As depicted in Figure 8.7, in general, the velocity predictions achieved a reasonable agreement with the experimental values obtained for the order of magnitude of the peak velocity, as well as the average velocity magnitude, over the influx between the parallel plates.

Figure 8.8 shows the model comparison between the FLUENT predictions and the experimental data in terms of velocity magnitude for the 1.91 cm plate separation.

The peak velocity magnitude obtained in the experimental studies at this separation was 165 mm/s. The corresponding peak velocity magnitude predicted by the FLUENT model was 142 mm/s. The average velocity magnitude in the experimental study over the steady period of the test data was 73 mm/s. The corresponding average velocity magnitude predicted by the FLUENT model was 92 mm/s.

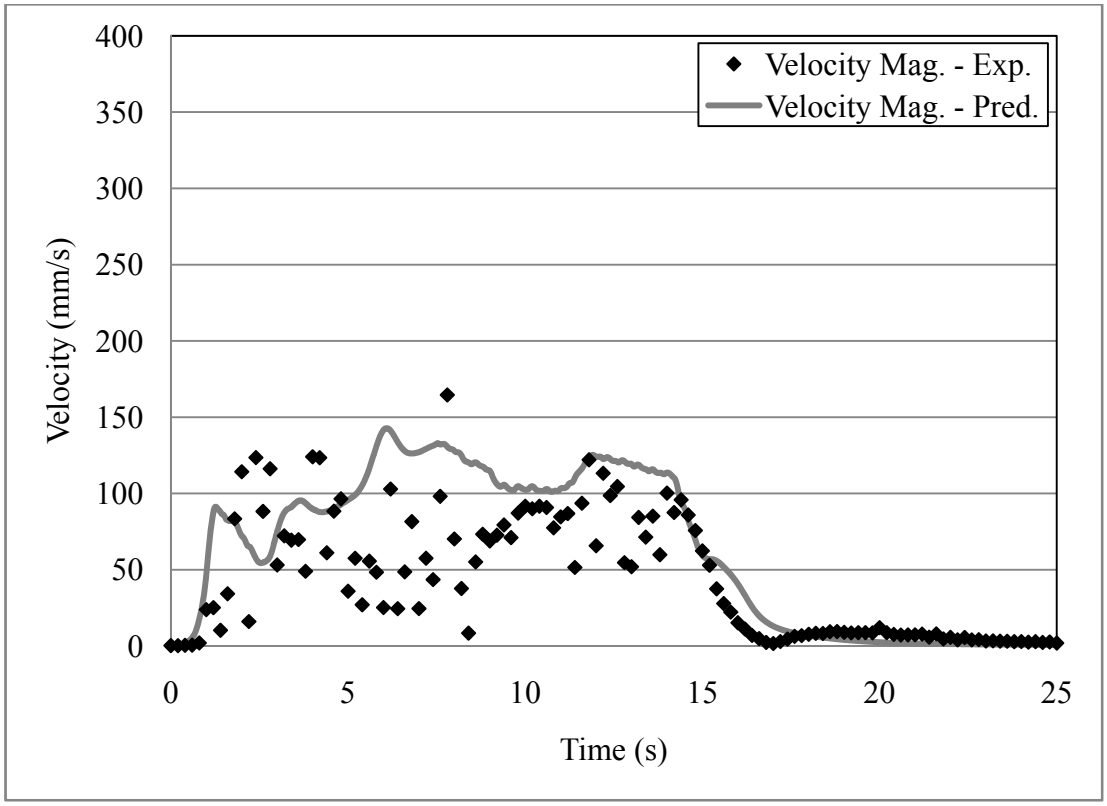

Figure 8.8: Comparison between PIV velocity magnitude experimental values and FLUENT model predictions at the 1.91 cm plate separation.

Similar to the 1.27 cm plate separation, Figure 8.8 demonstrates that the velocity predictions achieved a reasonable agreement with the experimental values obtained for the order of magnitude of the peak velocity, as well as the average velocity magnitude, over the initial influx between the parallel plates.

Figure 8.9 shows the model comparison between the FLUENT predictions and the experimental data in terms of velocity magnitude for the 3.18 cm plate separation.

The peak velocity magnitude obtained in the experimental studies at this separation was 177 mm/s. The corresponding peak velocity magnitude predicted by the FLUENT model was 213 mm/s. The average velocity magnitude in the experimental study over the steady period of the test data was 65 mm/s. The corresponding average velocity magnitude predicted by the FLUENT model was 77 mm/s.

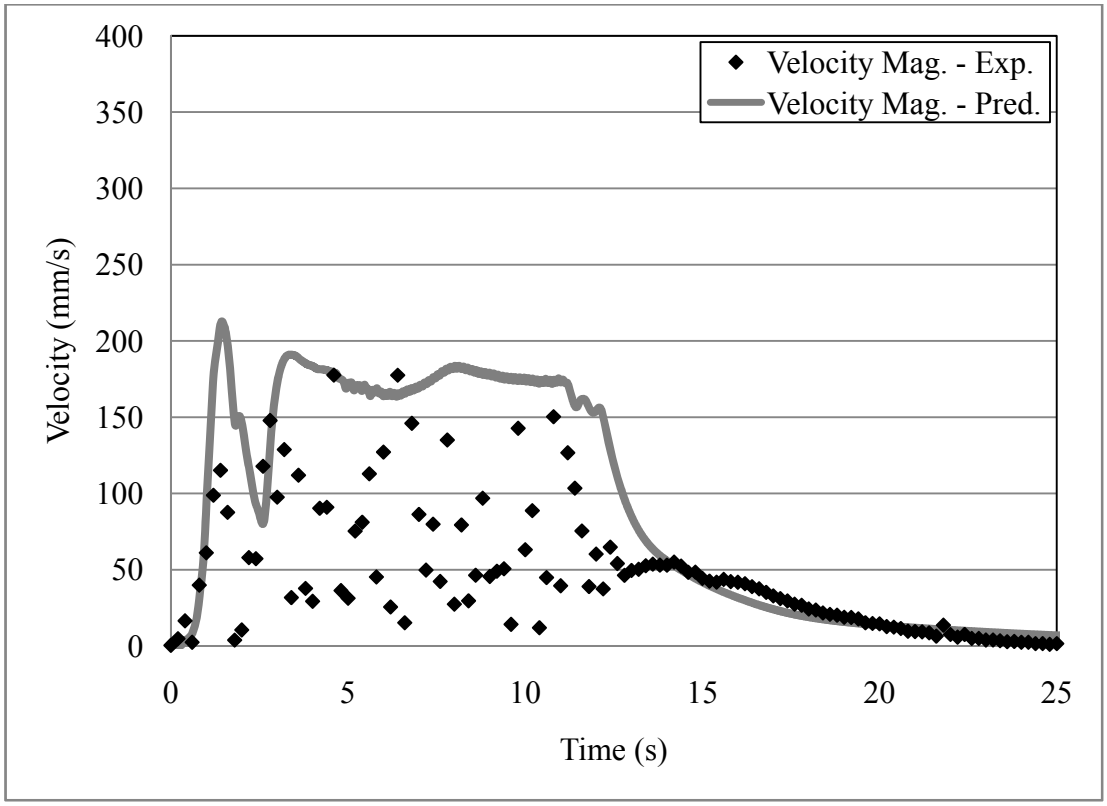

Figure 8.9: Comparison between PIV velocity magnitude experimental values and FLUENT model predictions at the 3.18 cm plate separation

Similar to the comparison for the 1.27 cm and the 1.91 cm plate separations, Figure 8.9 shows that the velocity predictions achieved a reasonable agreement with the experimental values obtained for the order of magnitude of the peak velocity, as well as the average velocity magnitude, over the initial influx between the parallel plates.

Table 8.3 presents the results of the velocity comparison in terms of the average velocity magnitude taken over the steady portion of the velocity increase. The

percent error in the modelling results was calculated using the formula shown in Equation (8.1), but with the values of ppm interchanged with velocity magnitude.

Plate Separation (cm)	Measurement Location	Average Experiment Velocity Magnitude (mm/s)	Average FLUENT Velocity Magnitude (mm/s)	Percent Error
1.27	Center	61.19	61.23	0.1
1.91	Center	72.67	92.37	27.1
3.18	Center	64.55	76.10	17.9

Table 8.3: Comparison of average velocity magnitude and model percent error.

The percent error range of 0.1% to 27.1% in the average values of the steady portion of the velocity magnitude suggests that the model is capable of accurately predicting the local velocity conditions at each node in a complex three-dimensional environment. As with the concentration predictions, when translating any modelling results to actual suggestions for a potential gaseous flame extinction engineering analysis, the potential error must be taken into account through a factor of safety.

Examination of the concentration and velocity predictions suggests that with a reasonable safety factor, the subroutines within the FLUENT code are valid for predicting the concentration transport of gaseous species in complex three-dimensional environments. Thus, the three-dimensional model constructed using FLUENT can be extended to predict flame extinction of a combustion problem through the introduction of a gaseous suppressant agent.

8.3. Prediction of Concentration Results in Microgravity

Section 8.2 demonstrates that with an appropriate factor of safety, the FLUENT model can be used to predict the transport of a suppressant gas in generalized three-dimensional geometries. A validated model can be expanded to examine conditions

that cannot be readily reproduced experimentally. For the present work, interest lies in the ability to translate the transport results obtained in normal gravity conditions into predictions for gaseous transport under microgravity conditions. Thus, the FLUENT model was modified to eliminate the influence of gravity on the flow field.

Figure 8.10 depicts a comparison between the FLUENT modelling results for nitrogen dioxide concentration at normal and microgravity conditions for the 1.27 cm plate separation.

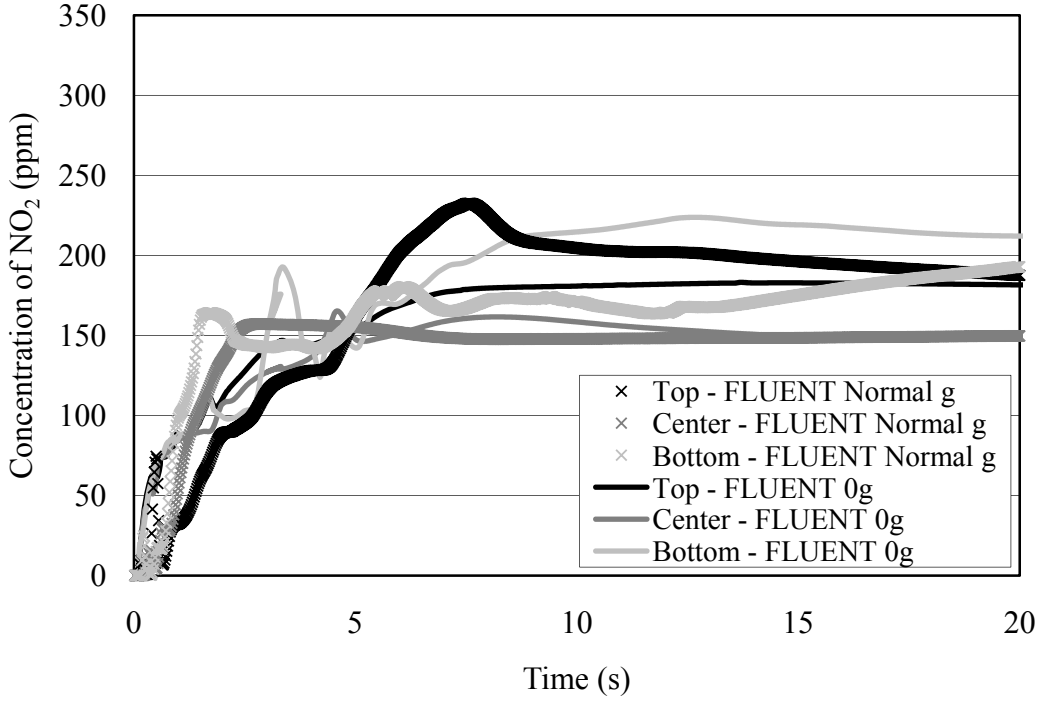

Figure 8.10: Comparison of FLUENT results for normal and microgravity conditions at the 1.27 cm plate separation.

In general, Figure 8.10 demonstrates that the microgravity results and normal gravity results are fairly consistent when compared with each other. An approximate steady-state condition develops after a similar amount of time has passed in both the normal and microgravity predictions. The initial evolution of the nitrogen dioxide between the plates is varied. In the normal gravity case, increased fluctuations are observed early in the time history of concentration. These fluctuations are damped in the

results for the microgravity conditions. These observations suggest that the initial momentum of the influx into the domain dominates the arrival of the nitrogen dioxide at the measurement locations, but the quantity of the nitrogen dioxide that is predicted is dependent on the influence of gravity. Buoyancy of the nitrogen dioxide drives both increased fluctuations and an increase in the amount of nitrogen dioxide predicted at each location.

Figure 8.11 depicts a comparison between the FLUENT modelling results for nitrogen dioxide concentration at normal and microgravity conditions for the 1.91 cm plate separation.

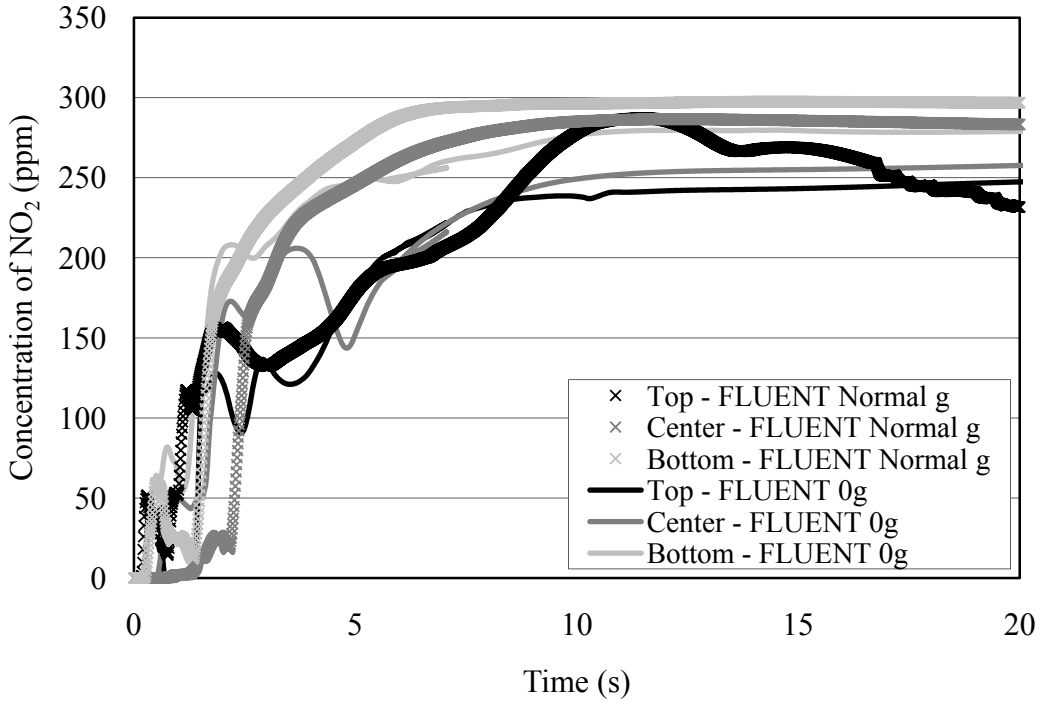

Figure 8.11: Comparison of FLUENT results for normal and microgravity conditions at the 1.91 cm plate separation.

As seen in Figure 8.11, the microgravity results and normal gravity results at a steady-state are fairly consistent with each other. Similar to the 1.27 cm separation, the initial evolution of the nitrogen dioxide between the plates is widely varied. In both normal gravity conditions and microgravity conditions, increased fluctuations

are observed early for the prediction of the nitrogen dioxide concentration. Observations for this plate separation distance show that the concentration of nitrogen dioxide increases much more rapidly at the measurement locations for the normal gravity conditions than for the microgravity conditions. This increase again suggests that the initial momentum of the gas influx into the domain dominates the arrival of the nitrogen dioxide at the measurement locations, but the quantity of the nitrogen dioxide that is predicted is dependent on the influence of gravity. Buoyancy of the nitrogen dioxide drives the increase in the amount of nitrogen dioxide predicted at each location.

Figure 8.12 depicts a comparison between the FLUENT modelling results for nitrogen dioxide concentration at normal and microgravity conditions for the 3.18 cm plate separation.

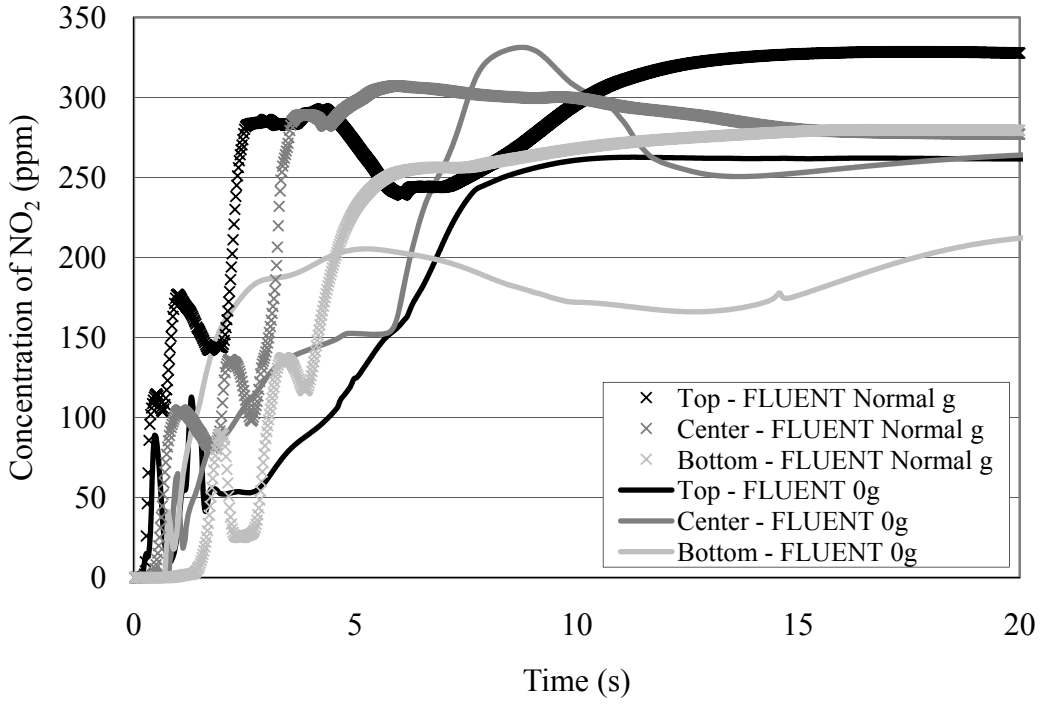

Figure 8.12: Comparison of FLUENT results for normal and microgravity conditions at the 3.18 cm plate separation.

Similar to Figures 8.10 and 8.11, Figure 8.12 also shows that the microgravity results and normal gravity results at a steady-state are fairly consistent with each other. However, at this plate separation, the difference between the microgravity results and normal gravity results is greater than that observed at the smaller separations. The initial evolution of the nitrogen dioxide between the plates is the most widely varied of all the plate separations. Similar to the comparison at the 1.27 cm plate separation for the normal gravity predictions, increased fluctuations are observed early in the time history of concentration. These fluctuations are damped in the results for the microgravity conditions. Observations for the 3.18 cm plate separation distance demonstrate that the concentration of nitrogen dioxide increases much more rapidly at the measurement locations for the normal gravity conditions than for the microgravity conditions. This increase again suggests that the initial momentum of the gas influx into the domain dominates the arrival of the nitrogen dioxide at the measurement locations, but the quantity of the nitrogen dioxide that is predicted is dependent on the influence of gravity. Buoyancy of the nitrogen dioxide drives the increase in the amount of nitrogen dioxide predicted at each location.

8.4. Prediction of Flame Extinction

Chapters 1 and 3 discussed the current state of fire protection aboard space facilities and space vehicles. One of the most challenging potential fires aboard these facilities and vehicles is a fire that initiates due to the overheating of a wire in a narrowly confined space (e.g., between two component circuit boards). The overheated wire would produce vaporized fuel from the insulation materials and, with enough heating, would transition into a flaming fire.

The experimental apparatus developed in this study was designed to replicate the above described fire scenario. As such, the FLUENT model of the experimental apparatus used for the validation studies was adapted to explore the ability of the FLUENT code and the methodology detailed in this project to predict flame

extinction and suppression for an example fire scenario due to the introduction of a gaseous suppressant agent into the geometry.

This section is designed to supply the final piece of the methodology for predicting flame extinction due to gaseous suppression in a generalized three-dimensional environment through the use of a simplified example fire scenario. To demonstrate this part of the methodology using the FLUENT model, an assumption must be made that FLUENT can accurately predict the combustion process and the associated consequences of the combustion (e.g., temperature fields, consumption of fuel and oxidizer, and the production of products of combustion), even though the particular fire scenario modelled has not been validated through experimentation.

8.4.1. FLUENT Modelling Setup

The geometry of the model used in this expanded analysis was identical to the geometry of the experimental apparatus as presented in Chapters 5 and 7. Several modifications were made to the boundary conditions in addition to the model inputs to account for both the combustion reaction and the injection of carbon dioxide as a suppressant gas.

The combustion reaction was defined as a fuel point source located in the center of the parallel plates. A node was assigned to release fuel in a constant distribution spherically around the point source. The fuel flow rate was 1.0e-5 kg/s. This number is consistent with a mass flow rate slightly more than that of a candle flame [53]. Additionally, this size flame is representative of the initial growth phase of a potential fire due to a wire overheat.

A single-step stoichiometric reaction for methane burning in air was used.

$$CH_4 + 2(O_2 + 3.76N_2) \rightarrow CO_2 + 2H_2O + 7.52N_2 \quad (8.2)$$

This particular single-step reaction for methane burning in air was chosen specifically for its simplicity to reduce the computational requirements for the model.

The activation energy for the reaction was constant for the problem and was 2.027e5 (J/mol). The pre-exponential constant for the reaction was 2.119e11 (1/s). Order of reaction exponents for the fuel and oxidizer were 0.2 and 1.3, respectively.

The inlet boundary condition was significantly modified from the original boundary condition defined in the validation modelling effort. First, the gaseous suppression agent was redefined as carbon dioxide. Second, the mass flow rate of the gas through the nozzle was increased to 2.0 kg/s. Finally, the inlet conditions were modified so that the mass flow rate would start two seconds after the start of the calculation and that the flow rate would remain constant for the duration of the model.

8.4.2. Flame Extinction Results and Discussion

To track extinction within the model, the Damköhler number as derived in Chapter 4 was used. From Chapter 4, the Damköhler number was defined as

$$D_a = \left(\frac{A}{\rho a}\right) Y_o^m Y_F^n \exp\left(\frac{-E}{RT}\right) \tag{8.3}$$

where A is the pre-exponential coefficient, ρ is the density, a is the local strain rate, Y_o^m is the oxygen mass fraction, Y_F^n is the methane mass fraction, E is the activation energy for methane and air, R is the universal gas constant, and T is the local gas temperature.

From Section 8.4.1, the pre-exponential coefficient, the activation energy, the reaction coefficients, and the universal gas constants were held steady and garnered from typical sources for methane-air reactions. The remaining variables were directly calculated within the FLUENT model. The entire Damköhler number was

placed into the FLUENT as a user-defined function and directly predicted throughout the entire domain at every time-step.

Figure 8.13 depicts a slice view through the center of the plates of the model representation of the experimental apparatus at the 1.27 cm plate separation. The model is tilted on its side to maximize the amount of the modelled apparatus that can be shown in one picture. In this instance, the z-direction runs from the left to the right with the right-hand side of the image representing the "up" direction. The plot is color-coded according to the Damköhler number with the maximum value being 1e-03 and the minimum value being effectively zero.

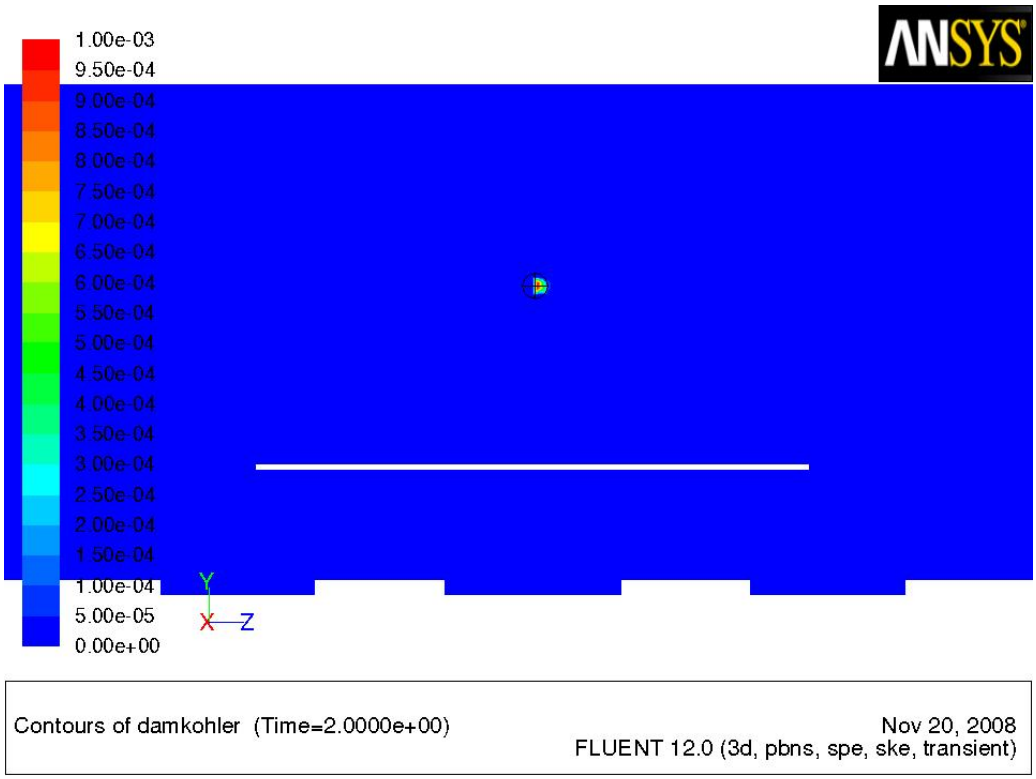

Figure 8.13: FLUENT plot of the Damköhler number after 2.0 seconds.

In this case as shown in Figure 8.13, 2.0 seconds have passed. The Damköhler number has reached a peak, representing that the flame is well established on the predefined node within the model.

Figure 8.14 shows a plot of the static temperature surrounding the single point fuel node. The maximum flame temperature is over 800°C, which indicates the presence of a strong combustion reaction surrounding the node. The temperature is rising along a thermal plume consistent with buoyancy induced by gravity.

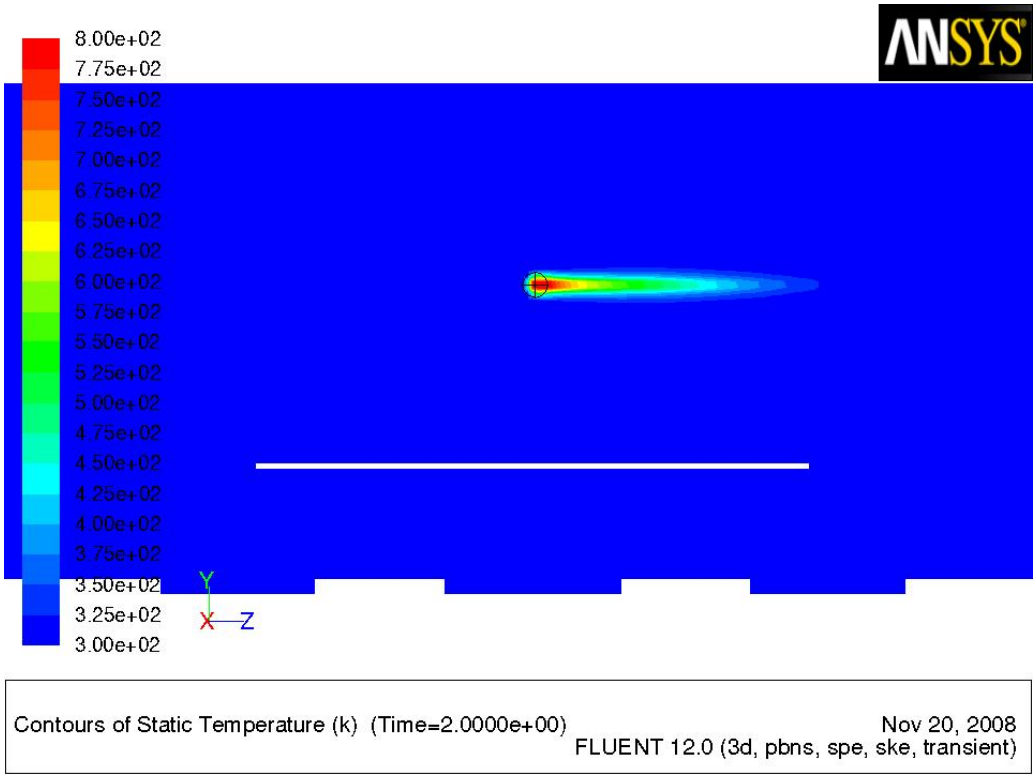

Figure 8.14: FLUENT plot of static temperature after 2.0 seconds.

As depicted in Figure 8.14, at two seconds, the model boundary condition for the introduction of carbon dioxide was initiated. The carbon dioxide was released into the model and the resultant conditions were predicted. The velocity within the nozzle increased to over 3000 m/s in one time-step, forcing out the air that was located in the nozzle at great velocities due to the small openings that comprised the nozzle tip. This rapid development of the velocity flow field created challenging velocity and strained flow conditions between the parallel plates.

Figure 8.15 depicts a plot of the Damköhler number at 2.5 seconds.

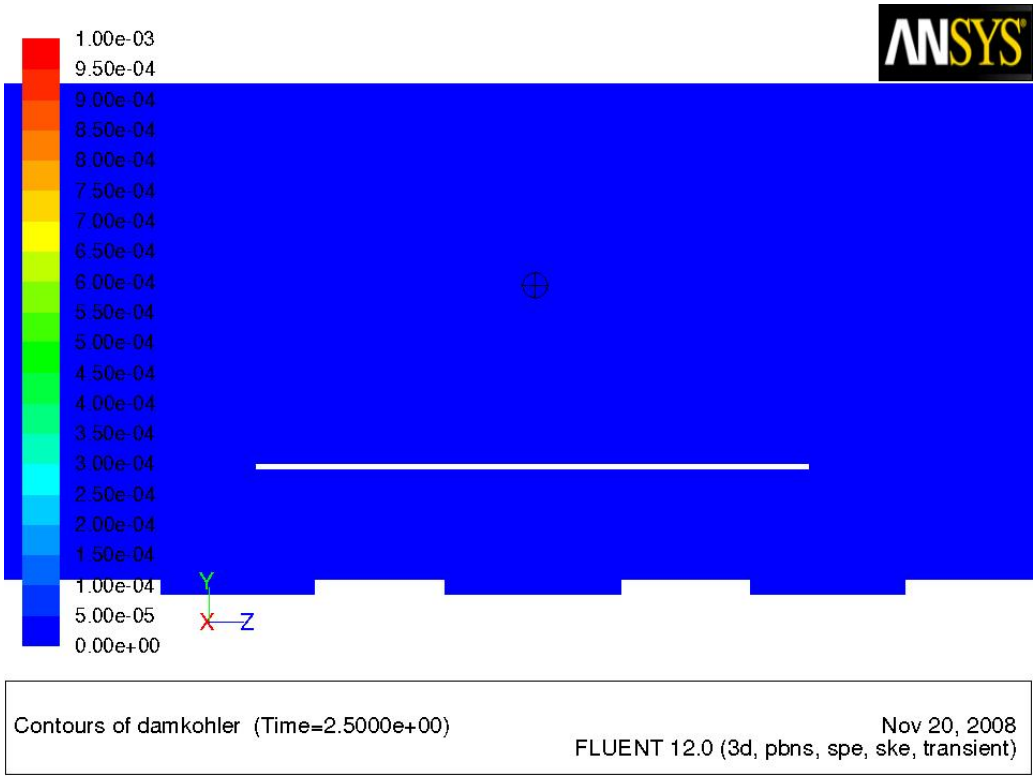

Figure 8.15: FLUENT plot of the Damköhler number after 2.5 seconds.

As shown in Figure 8.15, the plot demonstrates that the Damköhler number has been reduced effectively to zero at 2.5 seconds. This reduction in Damköhler number represents an extinction condition at the flame node between the plates. Based on the Damköhler number plot, conditions for an active flame are not favorable at any location along the slice plane.

Figure 8.16 shows the plot of carbon dioxide mass fraction at 2.5 seconds.

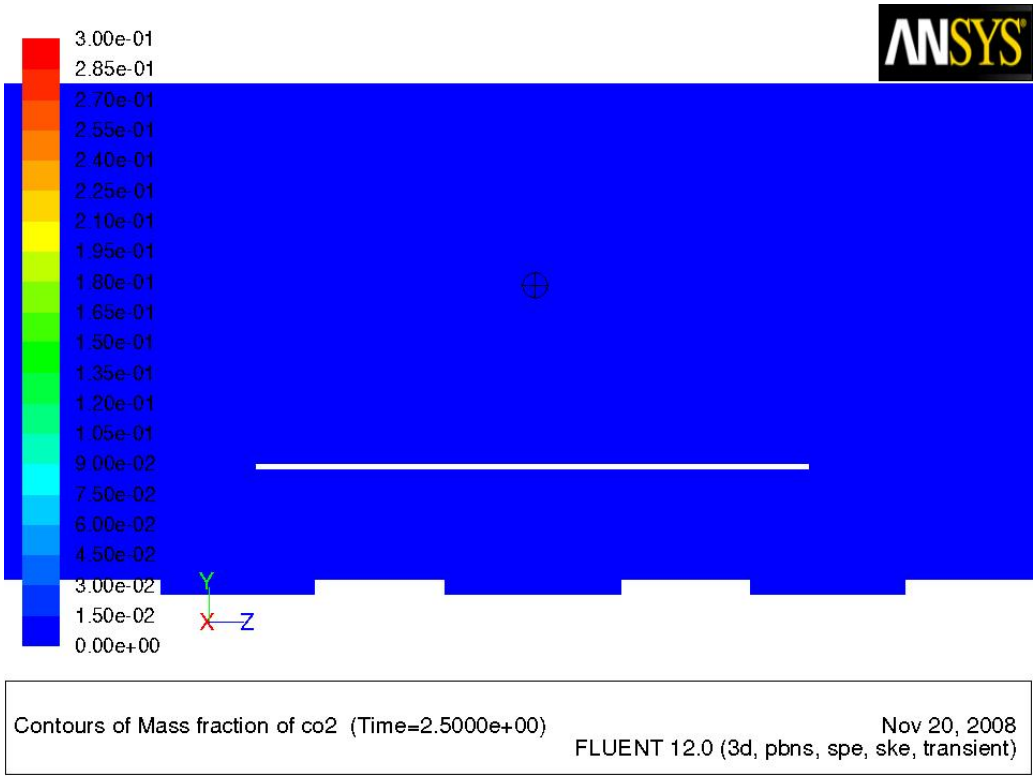

Figure 8.16: FLUENT plot of carbon dioxide mass fraction after 2.5 seconds.

As depicted in Figure 8.16, the carbon dioxide mass fraction between the plates has yet to increase above ambient conditions. This lack of increase in the carbon dioxide concentration is appropriate, as the transport of the carbon dioxide from the nozzle to the center of the plates occurs over approximately five seconds. The carbon dioxide has not penetrated between the plates after only 2.5 seconds.

Figure 8.17 is a plot of the static temperature at 2.5 seconds.

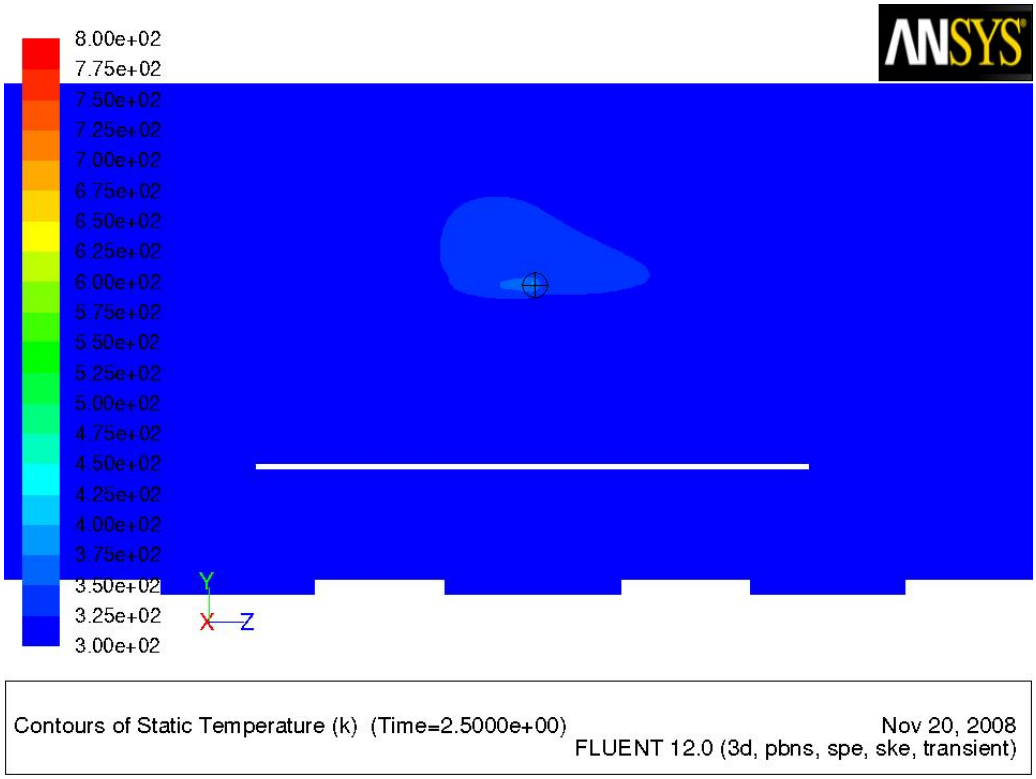

Figure 8.17: FLUENT plot of static temperature after 2.5 seconds.

As can be seen in Figure 8.17, the temperature in the vicinity of where the flame was located has cooled considerably. The temperature has dropped by over 500°C within a time frame of 0.5 seconds, providing further confirmation that the flame has been extinguished.

Figure 8.18 is a time history graph of a single point located one node away from the fuel source point between the parallel plates. This graph shows the evolution of the carbon dioxide mass fraction, the oxygen mass fraction, and the Damköhler number.

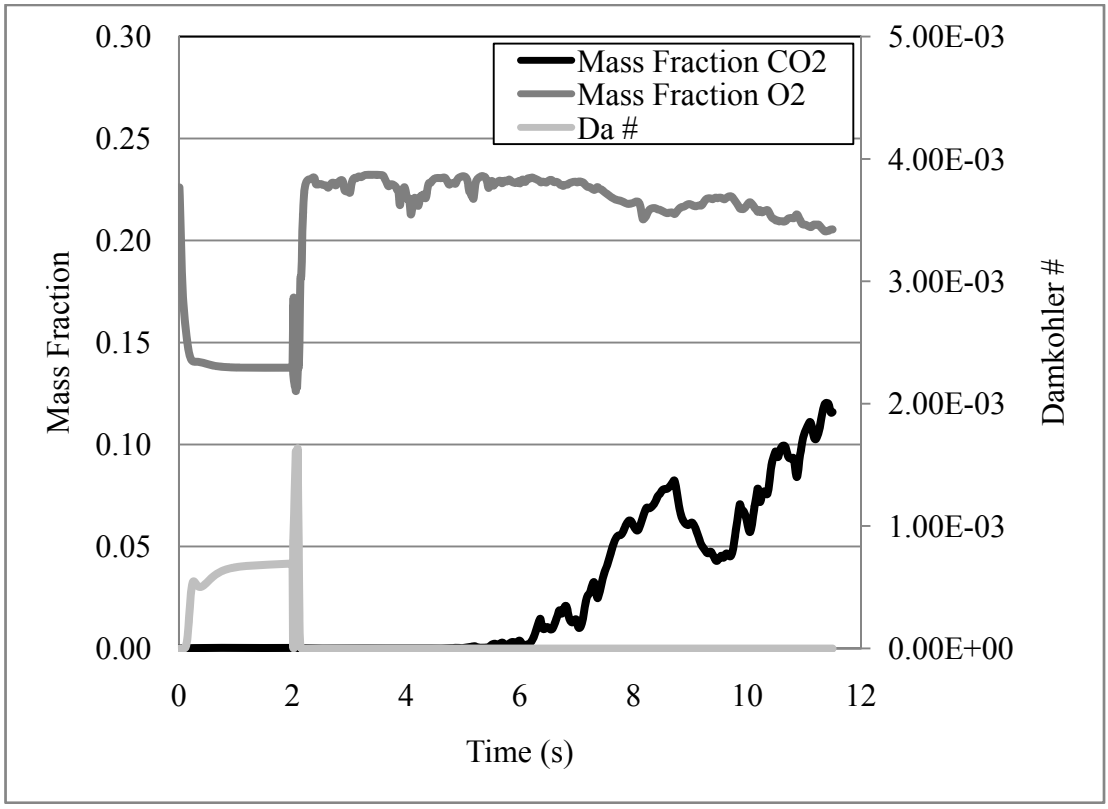

Figure 8.18: Time history of carbon dioxide mass fraction, oxygen mass fraction, and Damköhler number in example combustion scenario.

Initially, the oxygen mass fraction begins to decrease as the local oxygen is entrained by the nearby flame surface. The Damköhler number conversely increases rapidly until a plateau is reached and maintained prior to 2.0 seconds into the model development. Once the inlet boundary condition for the carbon dioxide suppression is initiated, both the Damköhler number and the oxygen mass fraction spike over a very short period of time. This spike is due to the rapid increase in the influx of fresh oxygen and a corresponding increase in the reaction rate. The Damköhler number increases rapidly and is then effectively reduced to zero. The oxygen mass fraction decreases and then returns to near ambient conditions.

The carbon dioxide mass fraction did not begin to increase near the location where the flame had been established until five seconds into the model development. From that point, the mass fraction continued to rise steadily until the model was

terminated. Thus, the mass fraction of carbon dioxide had not increased to a level that would have been able to influence flame extinction at the point in the model where extinction occurs. It can be concluded, then, that flame extinction was due to the rapid increase in the strain rate of the flow field between the parallel plates. This result demonstrates the potential ability of both the FLUENT model and the Damköhler number to predict flame extinction due to the development of blow-off conditions at high strain rates.

This initial modelling result was not an expected goal of the model analysis; thus, a subsequent model was modified to determine if the FLUENT model was capable of predicting the flame extinction due solely to the increase in the mass fraction of the carbon dioxide suppressant gas. In the modified model, the carbon dioxide mass flow rate was lowered from 2.0 kg/s to 0.2 kg/s in an effort to reduce the high initial flow velocities. Additionally, the area of the boundary condition inlet for the carbon dioxide was increased from 2e-4 m^2 to 5e-3 m^2. This area was increased to lower the high initial flow velocities stemming from the inlet boundary condition. All other conditions within the FLUENT model were maintained.

Figure 8.19 again depicts a slice view through the center of the plates of the model representation of the experimental apparatus.

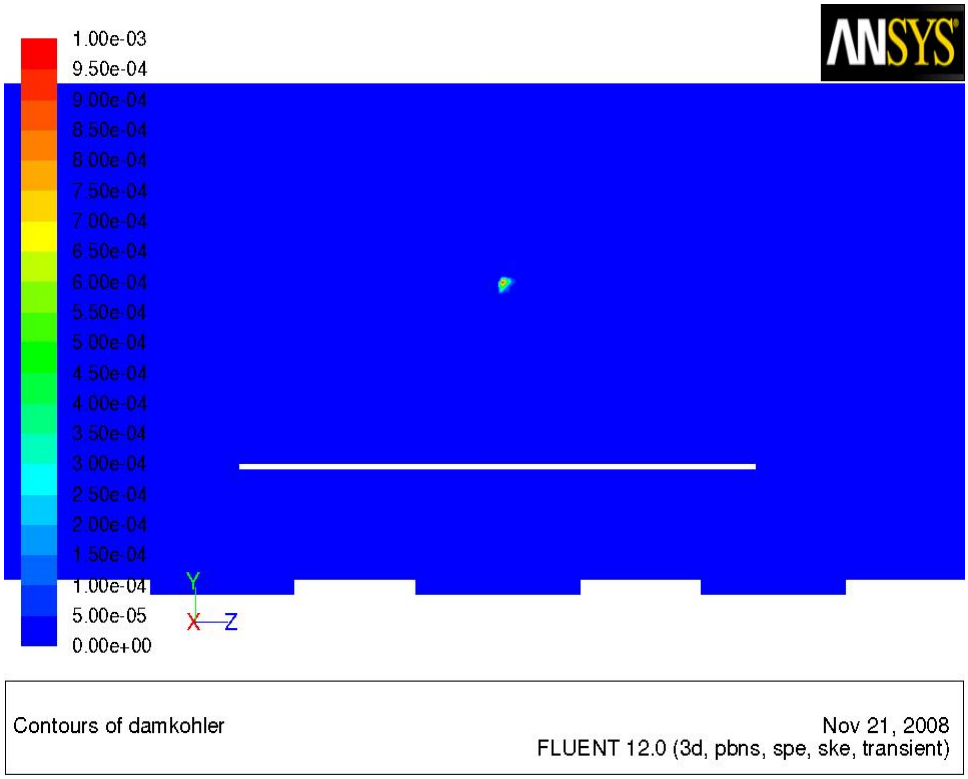

Figure 8.19: FLUENT plot of the Damköhler number after 1.8 seconds.

The plot shown in Figure 8.19 is color-coded according to the Damköhler number. After 1.8 seconds have passed, the Damköhler number has remained fairly constant representing that the flame is well established at the reporting node within the model.

Figure 8.20 shows a plot of the static temperature surrounding the single point fuel node at 1.8 seconds. The maximum flame temperature is over 800°C, which again indicates the presence of a strong combustion reaction surrounding the node. The temperature is rising along a thermal plume consistent with buoyancy induced by gravity.

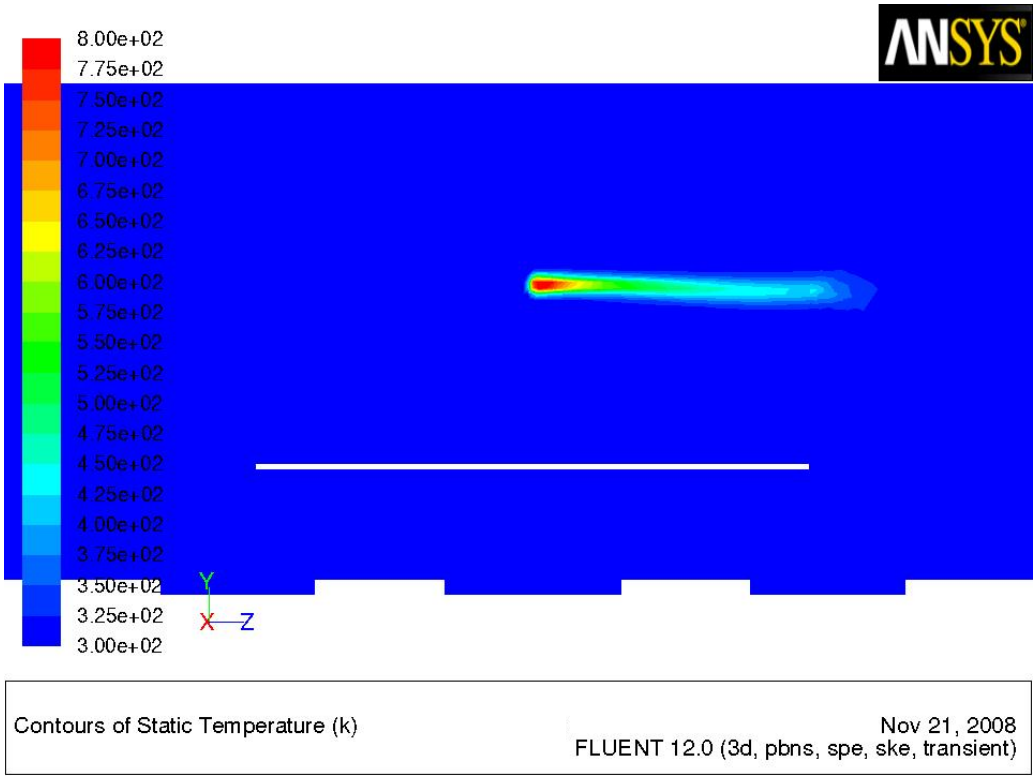

Figure 8.20: FLUENT plot of static temperature after 1.8 seconds.

As depicted in Figure 8.20, at two seconds, the model boundary condition for the introduction of carbon dioxide was initiated. The carbon dioxide was released into the model as per the new boundary condition restrictions, and the resultant conditions between the parallel plates were predicted over time. The carbon dioxide mass fraction increases steadily after three seconds and continues to climb until the end of the run at 12 seconds.

Figure 8.21 depicts a plot of the carbon dioxide mass fraction at 3.6 seconds. This time is just prior to the arrival of the carbon dioxide wave at the flame node.

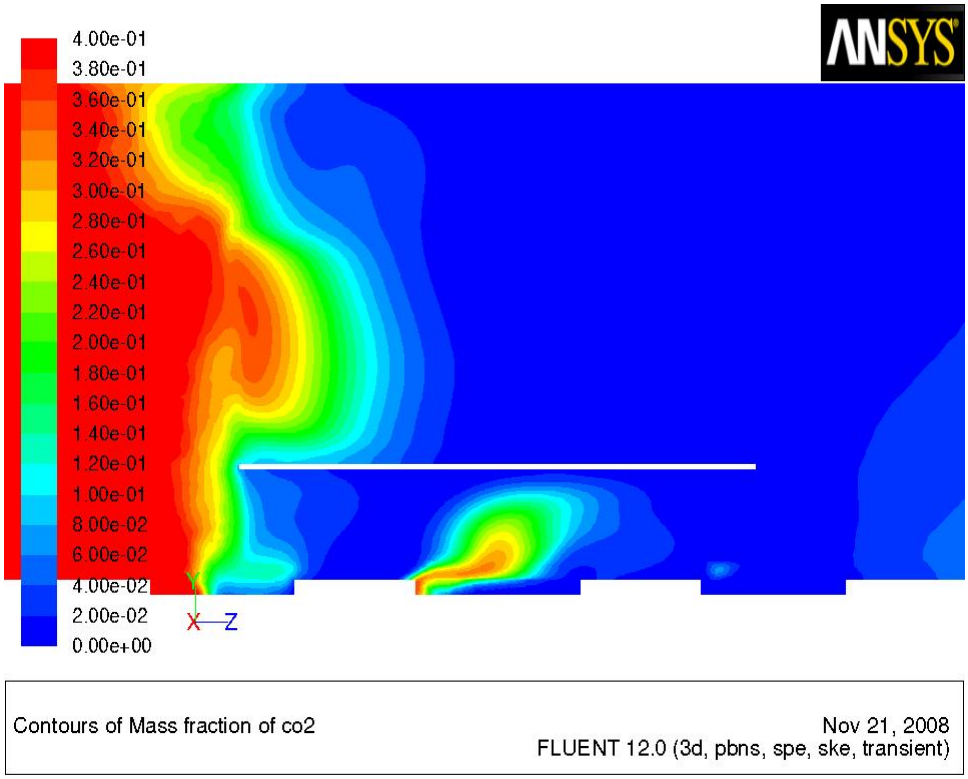

Figure 8.21: FLUENT plot of carbon dioxide mass fraction after 3.6 seconds.

As shown in Figure 8.21, the color contours show a preferential distribution of carbon dioxide gas located at the "bottom" (left side) of the color plot with a small amount beginning to infiltrate from the bottom edges of the plates.

Figure 8.22 shows a plot of the carbon dioxide mass fraction at 5.5 seconds into the run. It should be noted that the local mass fraction has increased to 0.40 or a 40% concentration by mass.

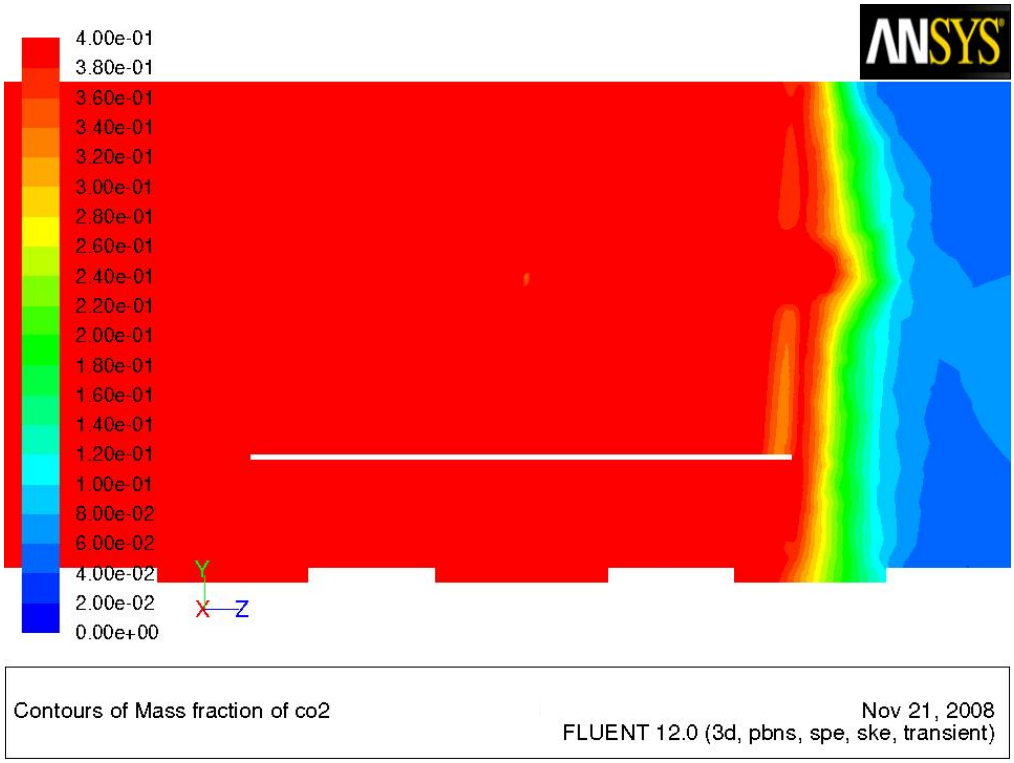

Figure 8.22: FLUENT carbon dioxide mass fraction after 5.5 seconds.

The effect of the increased carbon dioxide as shown in Figure 8.22 is reflected in the size of the Damköhler node shown in the FLUENT results, but total extinction is not captured by the FLUENT model. At a mass fraction of 0.40, literature [19, 35] suggests that the flame should extinguish. Total flame extinction is not observed within the FLUENT modelling results.

Figure 8.23 shows a plot of the Damköhler number at 12.0 seconds after the initiation of the run.

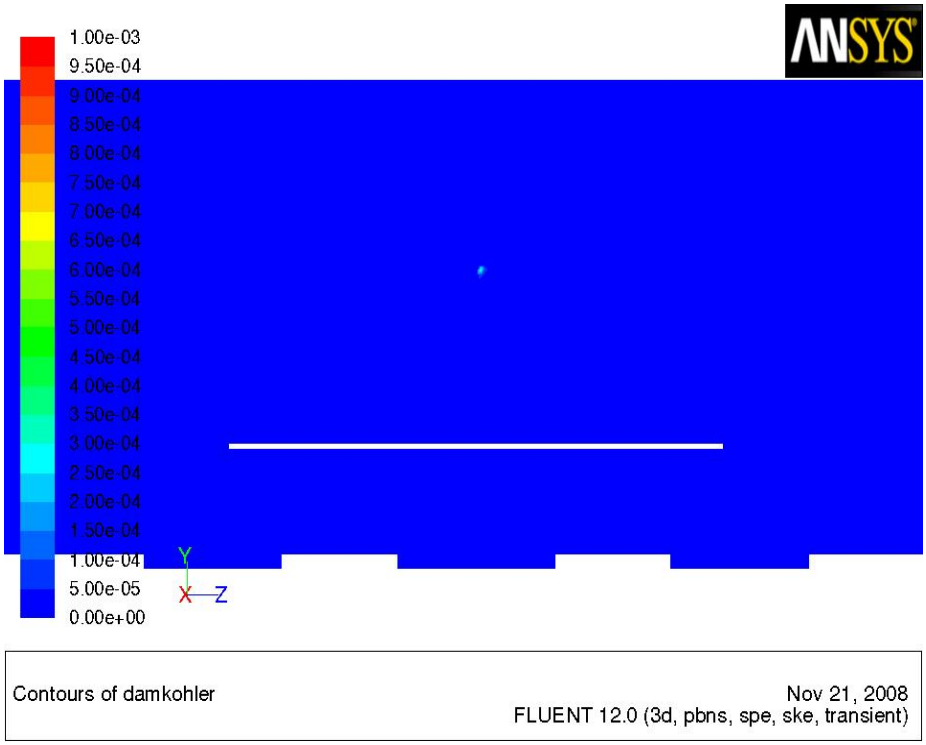

Figure 8.23: FLUENT plot of the Damköhler number after 12.0 seconds.

As shown in Figure 8.23, the Damköhler number region in the model has decreased in size considerably when compared with Figure 8.19. Observation of the plot reveals that the FLUENT model is predicting some localized extinction of the flame. Yet, even as the oxygen levels are continually displaced to a level of 0.005 mass fraction by the increasing accumulation of the carbon dioxide, the flame never fully extinguishes.

Figure 8.24 is a time history graph of a tracking point located one node away from the fuel source point between the parallel plates. This graph depicts the evolution of the carbon dioxide mass fraction, the oxygen mass fraction, the methane fuel mass fraction, and the Damköhler number.

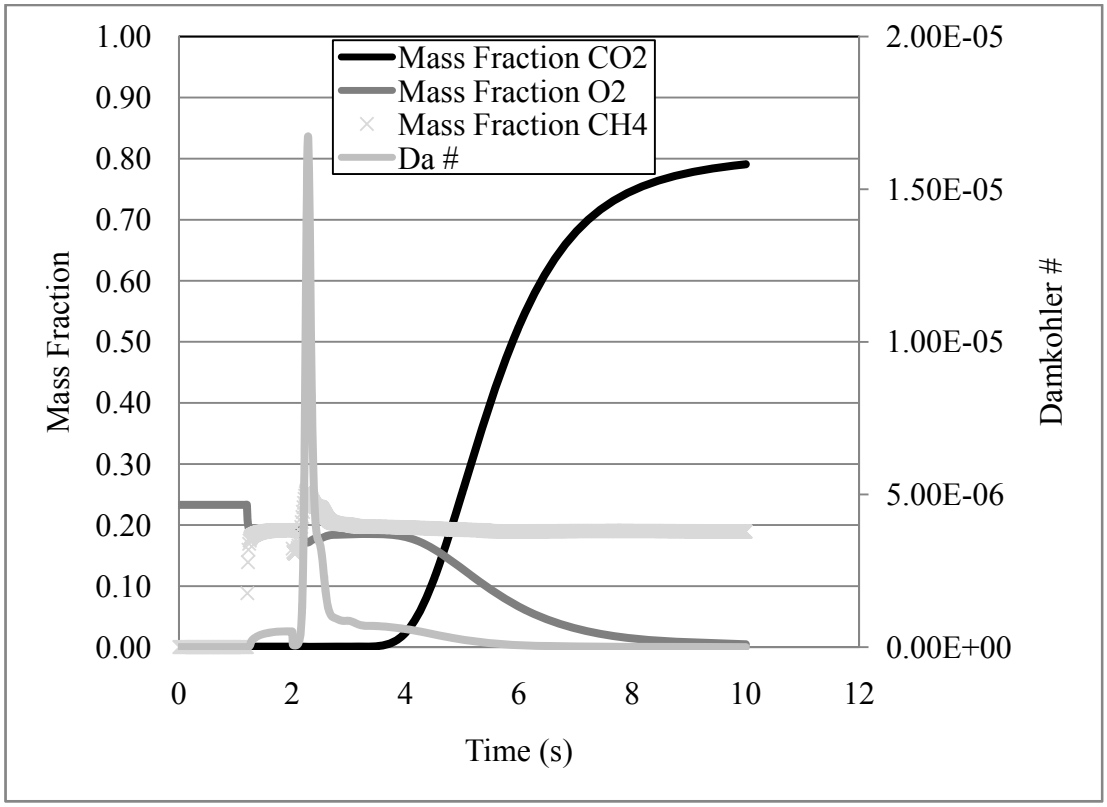

Figure 8.24: Time history of carbon dioxide mass fraction, oxygen mass fraction, methane mass fraction, and Damköhler number.

In Figure 8.24, the concentration levels and initially non-existent Damköhler number remain constant until one second has passed. This initial time of one second in the model is used to ramp up the flow of gas from the nozzle in an effort to minimize the instabilities produced as the flow field develops between the plates. Ignition of the flame is then established, which is verified by decreases in the oxygen mass fraction and increases in the methane mass fraction and Damköhler number.

The carbon dioxide is released into the system and begins to build in the area between the plates at approximately 3.6 seconds. By 8.0 seconds, the concentration of the carbon dioxide is approaching 0.80 mass fraction, while the oxygen mass fraction is reduced to 0.01. As mentioned in the discussion of Figure 8.23, total flame extinction has not occurred.

The lack of total extinction of the flame node is inconsistent with literature studies that suggest that flame extinction due to gaseous suppression with carbon dioxide will occur when the local level of oxygen is reduced below 15% [19] and when the concentration of carbon dioxide has increased to over 34% [35]. This result suggests that modifications are needed in describing the reaction chemistry within FLUENT to more accurately reflect the influence of a suppressant agent on the rate of the reaction. The result also suggests that the Damköhler number has the potential to fill the gap in predicting extinction. Instead of using the Damköhler number as a tracking parameter calculated directly by the model, the calculation of the Damköhler number could be completed through post-processing or through a user programmed sub-routine.

With this method, the Damköhler number would rely on the FLUENT model to predict the transport of the gases and the resulting gas and temperature fields. The sub-routine would then be designed to interrogate the conditions for variable changes that cause known instabilities within the flame structure (e.g., when the oxygen concentration surrounding the flame is reduced below 15%). The sub-routine would modify the reaction chemistry based on an appropriate sub-model of the phenomenon and would potentially provide feedback into the computational model.

8.5. Conclusions

This chapter has compared the validation data presented in Chapter 6 to the FLUENT model that was described in Chapter 7. Comparison of the modelling analysis with experimental data demonstrated that the FLUENT model can predict the transport of a gaseous agent to a location between the parallel plates with a reasonable amount of error, ±11% concentration. It has also been shown that the FLUENT model can predict the local velocity conditions between the parallel plates with an expected error no greater than ±27.1%. These deviations in the predictions from the experimental values can be accounted for, when using the methodology outlined in this work for an engineering analysis, by implementing an appropriate factor of

safety. In general, the FLUENT code is appropriate for predicting the transport of an injected suppression agent in a three-dimensional environment.

The FLUENT model used in the validation studies was adapted to explore the effects of a microgravity condition on the predictions of nitrogen dioxide concentration between the parallel plates. The results indicated that the momentum of the initial jet of gas into the model domain is the most dominant factor in determining the transport of the gas between the plates. After the initial influx, buoyancy plays a strong role in determining how quickly the concentration builds between the plates. In general, buoyant effects shorten the time needed to build to higher concentration levels.

The FLUENT model was also adapted to explore the ability of the FLUENT code along with the methodology detailed in this project to predict flame extinction and suppression in an example fire scenario. The first case involving this model predicted extremely high velocities between the parallel plates. Based on the results of the modelling, it was concluded that flame extinction occurred due to the rapid increase in the strain rate of the flow field between the parallel plates. These results demonstrated the potential of the FLUENT model and the Damköhler number to predict flame extinction due to the development of blow-off conditions at high strain rates.

The FLUENT model was then modified to explore only the interaction of the flame and the low velocity injection of the suppressant agent. Based on the results of the modelling, the FLUENT model predicted some localized extinction of the flame, although the model predicted that the flame never fully extinguishes. The lack of total extinction of the flame node is inconsistent with previous studies. This result suggests that modifications are needed in describing the reaction chemistry within FLUENT to more accurately reflect the influence of a suppressant agent on the rate of the reaction. The result also suggests that the Damköhler number has the potential to fill the gap in predicting extinction. Instead of using the Damköhler number as a

tracking parameter calculated directly by the model, the calculation of the Damköhler number should be completed through post-processing or through a user programmed sub-routine.

Chapter Nine

9. Conclusions and Further Work

9.1. Introduction

The research presented in this thesis has been inspired by the knowledge that the probability of a fire occurring in space vehicles and facilities is amplified by the vast amounts of electronic and electrical equipment used. Additionally, the lack of egress for space personnel and the irreplaceable resources used aboard these space vehicles and facilities require a rapid response of any suppressant system or method and quick extinguishment of any fire.

The experimental means that currently exist to gather data in space vehicles and facilities are limited by both size of the experiment and cost. Thus, more economical solutions must be considered in the effort to better understand both the suppressant dispersion and flame extinction aspects of the problem. Thus, the goal of this research has been to develop a reliable and inexpensive methodology for the prediction of flame extinction and suppression in any three-dimensional environment in normal gravity or microgravity.

To achieve this goal, the project was effectively split into two segments. The first segment was to identify and validate a computational model that was capable of predicting the dispersion aspect of the problem. The second segment was to develop an analytical parameter that was able to predict flame extinction utilizing the dispersion predictions of the computational model.

The purpose of this chapter is to summarize the process of the theoretical development for this methodology, the experimental studies, the computational modelling development, and the modelling predictions. Additionally, the main conclusions from this work will be presented.

9.2. Summary and Conclusions

This work first presented a brief review of the basic structure and analyses for simple diffusion flames in normal gravity environments. The simple analyses were followed by a discussion of both laminar diffusion flames and turbulent diffusion flames and the influence that microgravity conditions have on diffusion flames.

Once the foundation of the structure of a diffusion flame was defined, this work illustrated the basic concept of fire suppression and presented a more detailed examination of flame extinction through a review of previous work. Additionally, a review was offered of flame suppression research in microgravity conditions. This information was used to provide background for the development of the theoretical framework for the project.

Next, the theoretical framework for the development of a generalized Damköhler number that could be used to predict local flame extinction was presented. The analysis utilized, incorporated, and expanded on previous research that developed this parameter. A methodology was also outlined for application of the theoretical framework with emphasis placed on the coupling of the Damköhler number with computational fluid dynamics modelling for the transport aspect of the problem.

In an effort to provide validation data for the computational aspect of this research, experimentation was conducted. The experimental apparatus and various data acquisition methods used to obtain validation data for this study were next presented in detail. The results of those experimental studies were then discussed, and an error analysis of each of the methods was illustrated.

A computational representation was produced using the FLUENT code. The background of the use of computational fluid dynamics as a tool for the prediction of various physical phenomena in the engineering community was discussed in this work. This section included a brief review describing both the FDS and the

FLUENT code. Additionally, a discussion of the variables used to create the chosen FLUENT model was provided.

Finally, this work presented the comparison of the FLUENT modelling results with the experimental data. Once the comparisons were demonstrated to validate the model predictions, further modelling work was developed and discussed, with the emphasis on the potential ability of the Damköhler number to predict flame extinction through the use of the FLUENT code.

A summary of the main conclusions made throughout this research is listed below:

- Most naturally occurring fires in normal gravity or microgravity conditions are diffusion flames. In a terrestrial environment, these fires are turbulent due to the buoyancy of hot combustion products. In microgravity, the fires are more likely to be laminar and are heavily influenced by any forced flow or natural convection within the local area of the flame. This understanding of diffusion flame behavior in both normal gravity and microgravity environments is necessary in order to analyze the interaction of a flame with a potential suppressant agent.

- The current direction of microgravity flame suppression research is focused on the evaluation of the effectiveness of various gaseous agents (e.g., Halon alternatives, carbon dioxide, and nitrogen) and water mist as potential replacements for Halons. Based upon the review of the flame extinction literature and microgravity flame suppression research, a critical Damköhler number for extinction provides the most complete means of accounting for the addition of a suppressant gas, as well as for quantifying the gas-phase flame extinction and fire suppression over a nonspecific diffusion flame problem in any three-dimensional environment at normal gravity or microgravity conditions.

- In general, all of the characteristic variables in the Damköhler number can be translated into actual local values within a three-dimensional geometry through literature sources or through direct calculation from a computational model. Of particular importance when using this method is the determination of the velocity-strain relationship throughout the flow field. Based on complexities in this parameter due to the presence of an active flame in the flow field, a computational model with the appropriate resolution becomes the ideal means for predicting this quantity, both temporally and spatially.

- The two parameters experimentally determined in this research, the measurement of a concentration of a gas and the measurement of velocity flow field, provide validation data for use with a modelling analysis. These experimentally measured parameters are significant due to their consistency with the characteristic variables compiled in the Damköhler number as outlined in the theoretical framework.

- As outlined in the theoretical framework, the Damköhler number is comprised of characteristic variables that must be determined through appropriate means. A computation model and, in particular, a model utilizing the FLUENT code, provides the ideal way to calculate and track the local values of the variables that comprise the Damköhler number within a modelled representation of a combustion problem in a three-dimensional environment.

- Comparison of the modelling analysis with experimental data demonstrated that the FLUENT model can predict the transport of a gaseous agent to a location remote from the inlet conditions in a three-dimensional space with a reasonable amount of error. The comparison also showed that the FLUENT model can predict the local velocity conditions in a three-dimensional space. In general, the FLUENT code is appropriate for predicting the transport of an injected suppression agent in a three-dimensional environment.

- The FLUENT model used in the validation studies was adapted to explore the effects of a microgravity condition on the predictions of nitrogen dioxide concentration between the parallel plates. The results indicated that the momentum of the initial jet of gas into the model domain is the most dominant factor in determining the transport of the gas between the plates. After the initial influx, buoyancy plays a strong role in determining how quickly the NO_2 concentration builds between the plates. In general, buoyant effects shorten the time needed to build to higher concentration levels.

- The FLUENT model used in the validation studies was also adapted to explore the potential of the FLUENT code and the methodology detailed in this project to predict flame extinction and suppression in an example fire scenario. The first case involving this model predicted extremely high velocities in the local area of the flame. Flame extinction occurred due to the rapid increase in the strain rate of the flow field. These results demonstrated the potential of both the FLUENT model and the Damköhler number to predict flame extinction due to the development of blow-off conditions at high strain rates.

- The FLUENT model was also modified to explore only the interaction of the flame and the low velocity injection of the suppressant agent. Based on the results of the modelling, the FLUENT model predicted some localized extinction of the flame, although the model predicted that the flame never fully extinguishes. The lack of total extinction of the flame node is inconsistent with previous studies. This result suggests that modifications are needed in describing the reaction chemistry within FLUENT to more accurately reflect the influence of a suppressant agent on the rate of the reaction. This result also suggests that the Damköhler number has the potential to fill the gap in predicting extinction. The calculation of the Damköhler number should be completed through post-processing or through

a user programmed sub-routine that can take advantage of inputted physiological models based on previous literature that will provide feedback to the reaction chemistry within the computational model.

9.3. Further Work

A main conclusion of this research is that the methodology for predicting flame extinction presented in this work is applicable to any three-dimensional environment in normal or microgravity conditions. This conclusion has not been rigorously investigated due to the lack of experimental data related to the combustion aspect of the problem. To effectively demonstrate this applicability, suppressant transport experimentation with combustion in a three-dimensional environment must be conducted. Additionally, experimentation at microgravity conditions would be valuable and would help to focus the use of this methodology for space facilities and space vehicles. With this information, a similar project could be developed to further refine any potential modifications to the methodology or the Damköhler number developed.

A secondary line of further work would be related to the ignition aspect of the Damköhler number analysis. The focus of this study has been to explore the condition of a stable Damköhler number and to observe how a model perturbation results in the forcible extinction of the flame. As shown in the work by Fendell [21] and Liñán [22], the branch of the Damköhler number that leads to ignition of a flame can also be examined. An analysis of this kind could produce a means to model general combustion problems involving ignition or potentially exotic combustion problems that are not as common and extremely complex.

References

[1] Friedman, R., "Risks and Issues in Fire Safety on the Space Station", NASA TM 106430, 1994.

[2] Tanaka, T. J., Korsah, K. and Antonescu, C., "Preliminary Studies on the Impact of Smoke on Digital Equipment," Proceedings of the U.S.N.R.C. Twenty Third Water Reactor Safety Information Meeting, October, 1995.

[3] *Microgravity Combustion: Fire in Free Fall*, Ross, Howard, ed., Academic Press, San Diego, 2001.

[4] Glassman, Irvin, *Combustion*, 3rd Edition, Academic Press, San Diego, 1996.

[5] Kuo, Kenneth, *Principles of Combustion*, John Wiley & Sons, New York, 1986.

[6] Turns, Stephen, *An Introduction to Combustion*, 2nd Edition, McGraw Hill, Boston, 2000.

[7] Burke, S. and Schumann, T., *Ind. Eng. Chem.*, 20, p. 998, 1928.

[8] Williams, Forman A., *Combustion Theory: The Fundamental Theory of Chemically Reacting Flow Systems*, 2nd Edition, Westview Press, 1985.

[9] Drysdale, Dougal, *An Introduction to Fire Dynamics*, 2nd Edition, John Wiley & Sons, New York, 1999.

[10] Zukoski, E., "Convective Flows Associated with Room Fires," Semi-Annual Progress Report, National Science Foundation Grant No. GI 31892 X1, Institute of Technology, Pasadena, California, 1975.

[11] Zukoski, E., "Fluid Dynamic Aspects of Room Fires," *Proceedings of the 1st International Symposium on Fire Science*, Hemisphere Publishing Corporation, Washington, 1986.

[12] Kimzey, J., Skylab Results, Proceedings of the 3rd Space Processing Symposium, NASA Marshall Space Flight Center, M-74-5, NASA TM-X-70752, 1, pp. 115-130, 1974.

[13] Olson, S., "The Effect of Microgravity on Flame Spread over a Thin Fuel," NASA TM-100195, 1987.

[14] Friedman, R., *Fire Mater*. 2, pp. 235-243, 1996.

[15] Olson, S., "Fuel Thickness Effects on Flame Spread and Extinction Limits in Low Gravity as Compared to Normal Gravity," The Combustion Institute, Eastern States Section, Fall Technical Meeting, 1991.

[16] Egorov, S. Belyaev, A., Klimin, L., Voiteshonok, V., Ivanov, A., Semenov, A., Zaitsev, E., Balashov, E., and Andreeva, T., In the 3rd International Microgravity Combustion Workshop (H.D. Ross, ed.), NASA CP-10174, pp. 195-199, 1995.

[17] Ivanov, A., Balashov, Y, Andreeva, T., and Melikhov, A., "Experimental Verification of Material Flammability in Space," NASA CR-1999-209405, 1999.

[18] Haessler, W., *The Extinguishment of Fire*, Quincy, MA, National Fire Protection Association, 1974.

[19] Bryan, J., *Fire Suppression and Detection Systems*, Prentice Hall, Englewood Cliffs, NJ, 1993.

[20] Potter, A., Jr., Heimel, S., and Butler, J., *Eighth Symposium (International) on Combustion*, Williams and Wilkins, New York, p. 1027, 1962.

[21] Fendell, F., "Ignition and extinction in combustion of initially unmixed reactants," *Journal of Fluid Mechanics*, 21, pp. 282-303, 1965.

[22] Liñán, A., "The asymptotic structure of counterflow diffusion flames for large activation energies," *Acta Astronautica*, 1, pp. 1007-1039, 1974.

[23] Law, C.K., "Asymptotic Theory for Ignition and Extinction in Droplet Burning," *Combustion and Flame*, 24, pp. 89-98, 1975.

[24] Spalding, D., *Some Fundamentals of Combustion*, Buttersworth, London, 1955.

[25] Roberts, A., and Quince, B., "A Limiting Condition for the Burning of Flammable Liquids," *Combustion and Flame* 20, pp. 245-251, 1973.

[26] Rasbash, D., "Relevance of Fire Point Theory to the Assessment of Fire Behaviour of Combustible Materials," International Symposium of Fire Safety and Combustible Materials, Edinburgh University, pp. 169-178, 1975.

[27] Rasbash, D.J., Drysdale, D.D., Deepak, D., "Critical Heat and Mass Transfer at Pilot Ignition and Extinction of a Material," *Fire Safety Journal*, 10, pp. 1-10, 1986.

[28] Dibble, R., Kollmann, W., and Schefer, R., "Measurement and Predictions of Scalar Dissipation in Turbulent Jet Flames," Combustion Institute/Western States Section. Spring Meeting. Boulder, CO, 1984.

[29] Muss, J., Dibble, R., and Talbot, L., "Measurement of Mixture Fraction and Scalar Dissipation in Non-Premixed Reacting Flows Using Rayleigh Scattering," Combustion Institute/Western States Section. Spring Meeting. University of California at Davis, 1994.

[30] Pitsch, H. and Fedotov, S., "Investigation of Scalar Dissipation Rate Fluctuations in Non-Premixed Turbulent Combustion Using a Stochastic Approach," *Combustion Theory and Modelling*, 5, pp. 41-57, 2001.

[31] Personal communication on scalar dissipation rate with J. Quintiere, January 13, 2009.

[32] Williamson, J., Marshall, A., and Trouve, A., "Developing Extinction Criteria for Fires," *Proceedings of the 11th Interflam Conference*, 2, pp. 849-860, 2007.

[33] VanDerWege, B., Bush, M., and Hochgreb, S., "Effect of CF3H and CF3Br on Laminar Diffusion Flames in Normal and Microgravity," *Third International Microgravity Combustion Conference*, Cleveland, Ohio, April 11-13, 1995.

[34] Bundy, M., Hamins, A., Lee, K., "Suppression Limits of Low Strain Rate Non-Premixed Methane Flames," *Combustion and Flame*, 133, pp. 299-310, 2003.

[35] Hirsch, D., Hshieh, F., Beeson, H., and Pedley, M., "Carbon Dioxide Fire Suppressant Concentration Needs for International Space Station Environments," *Journal of Fire Sciences*, 20, pp. 391-399, 2002.

[36] *NFPA 12 Standard on Carbon Dioxide Extinguishing Systems*, 2008 Edition, NFPA, 1 Batterymarch Park, Quincy, MA.

[37] Katta, V., Takahashi, F., Linteris, G., "Suppression of cup-burner flames using carbon dioxide in microgravity," *Combustion and Flame*, 137, pp. 506-522, 2004.

[38] Takahashi, F., Linteris, G., and Katta, V., "Extinguishment of methane diffusion flames by carbon dioxide in coflow air and oxygen-enriched microgravity environments," *Combustion and Flame*, in press, accepted 10 March, 2008.

[39] Hamins, A., Bundy, M., Oh, C., Kim, S., "Effect of buoyancy on the radiative extinctions limit of low-strain-rate nonpremixed methane-air flames," *Combustion and Flame*, 151, pp.225-234, 2007.

[40] Abbud-Madrid, A., Amon, F., McKinnon, J., "The MIST Experiment on STS-107: Fighting Fire in Microgravity," 42nd AIAA Aerospace Sciences Meeting and Exhibit, Reno, Nevada, 5-8 January, 2004.

[41] Abbud-Madrid, McKinnon, J., A., Amon, F., Gokoglu, S., "Suppression of Premixed Flames by Water Mist in Microgravity: Findings from the MIST Experiment on STS-107," Proceedings of the 14th Halon Options Technical Working Conference, Albuquerque, New Mexico, May 4-6, 2004.

[42] Wichman, Indrek, "A Model Describing the Influences of Finite-Rate Gas-Phase Chemistry on Rates of Flame Spread over Solid Combustibles," *Combustion Science and Technology*, 40, Nos. 5&6, pp. 233-255, 1984.

[43] Tsuji, H. and Yamaoka, I., "Structure Analysis of Counterflow Diffusion Flames in the Forward Stagnation Region of a Porous Cylinder," Thirteenth Symposium (International) on Combustion, The Combustion Institute, Pittsburg, PA, pp. 723-731, 1971.

[44] Neuberger, D., and Duncan, A., "Fluorescence of Nitrogen Dioxide," *The Journal of Chemical Physics*, 22, No. 10, pp. 1693-1697, 1954.

[45] Schwartz, S., and Johnston, H., "Kinetics of Nitrogen Dioxide Fluorescence," *The Journal of Chemical Physics*, 51, No. 4, pp. 1286-1302, 1969.

[46] Cattolica, R., "Combustion-Torch Ignition: Fluorescence Imaging of NO_2," Twenty-first Symposium (International) on Combustion, The Combustion Institute, pp. 1551-1559, 1986.

[47] Patten, K., Jr., Burley, J., and Johnston, H., "Radiative Lifetimes of Nitrogen Dioxide for Excitation Wavelengths from 400 to 750 nm," *J. Phys. Chem.*, pp. 7940-7969, 1990.

[48] Raffel, M., Willert, C., Kompenhans, J., *Particle Image Velocimetry*, Springer, New York, 1998.

[49] Versteeg, H.K., and Malalasekera, W., *An Introduction to Computational Fluid Dynamics: The Finite Volume Method*, Adison Wesley Longman Limited, London, 1995.

[50] Anderson, D.A., Tannehill J.C. and Pletcher, R.H., *Computational Fluid Mechanics and Heat Transfer*, Hemisphere, New York, N.Y., 1997.

[51] McGrattan, K., Klein, B., Hostikka, S., and Floyd, J. "Fire Dynamics Simulator (Version 5) User's Guide," NIST Special Publication 1019-5, 2008.

[52] McGrattan, K., Hostikka, S., Floyd, J., Baum, H., Rehm, R., Mell, W., and McDermott, R. "Fire Dynamics Simulator (Version 5) Technical Reference Guide Volume 1: Mathematical Model," NIST Special Publication 1018-5, 2008.

[53] Hamins, A., Bundy, M., and Dillon, S., "Characterization of Candle Flames," *Journal of Fire Protection Engineering*, Vol. 15, 2005.

Appendix A – Data Reduction Routines

PLIF Background Image

%This program creates the background image which will be later subtracted. The format is makebg(series,b) where 'series' is the series in quotes and 'b' is the number of images to average. The background images should be in the set path and named 'series_XX' where the filename is NOT padded with zeros. The resulting image from this should be saved in memory as "bgimage"

```
function bgimage=makebg4cal(bgfile,numimages,name4calbg);
numimages=uint32(numimages);

for i=1:numimages  %To average "" images
   if i==1
      lastfile=imread(sprintf('%s_%d.tif',bgfile,i));  %read the first image in
      lastfile=uint32(lastfile);
   else
      currentfile=imread(sprintf('%s_%d.tif',bgfile,i));   %read the next image
      currentfile=uint32(currentfile);
      currentfile=lastfile+currentfile;
%       currentfile=imadd(lastfile,currentfile);           %add the current image to the
last one
      lastfile=currentfile;
   end
end

if max(max(currentfile))>2^32
   disp('BG saturated')
   return
end
%bgimage=imdivide(currentfile,numimages);
bgimage=currentfile./numimages;
bgimage=uint16(bgimage);
%bgimage=uint16(currentfile);
clear currentfile;
imwrite(bgimage,'bg4calimage.tiff','tiff');
imwrite(bgimage,sprintf('bgimage%s.tiff',name4calbg),'tiff');

disp('Finished writing background image to disk...');


clear bgfile, clear origfile, clear currentfile
```

PLIF Averaging Routine

This program is a way to plot an average of the sheet area with time-averaging and scaling (to convert to PPM and % concentration). Use "makebg4cal.m" to generate a background image which was used for the calibration.

```
%global shotscaler;

close all hidden;
%clear SCALEDIMAGES lastfile currentfile AVGEDIMAGES
%aviobj/work24a/
clear all
disp('Always pay close attention to working directories')
disp('TLcoords are not top left, they are center of ROI')
% USER INPUTS
%channelgap=1.25
%testdate='2-22-06'

writefiles='y';
gap=input('What is the gap (format 0.75 for 3/4") ');
switch gap
   case 0.5
      SEQUENCES2PROCESS=[11:13; 12:14; 10:12] %halfingap
      TESTDATES={'2-15-07' '2-06-07' '1-25-07'}  %halfingap
      TLcoords=[280 184+10;250 170; 282 371]  %halfingap
      CALBGSEQ=[10 1 1];  %background sequence used to calibrate for respective
days
      windowlabels={'Top' 'Bottom' 'Middle'};
      t4avging=[210 240; 210 240; 210 240]
   case 0.75
      SEQUENCES2PROCESS=[10:12;2,3,16; 10:12]    %0.75" gap
%       SEQUENCES2PROCESS=[12]
      TESTDATES={'1-02-07' '12-12-06' '3-06-07'}    %0.75" gap
%       TESTDATES={'3-06-07'}
      TLcoords=[250 270;266 196; 286 220]  %0.75in gap
%       TLcoords=[286 220]
      CALBGSEQ=[1 1 1];  %background sequence used to calibrate for respective
days
      windowlabels={'Bottom' 'Middle' 'Top'};
      t4avging=[170 200;200 230;210 230]
   case 1.25
      SEQUENCES2PROCESS=[8:10;9:11;9:11];  %1.25IN GAP
      TESTDATES={'2-22-07' '2-21-07' '3-01-07'} %1.25" gap
      TLcoords=[346,180; 306,250; 285,215]  %1.25" gap
      windowlabels={'Middle' 'Top' 'Bottom'};
```

```
    CALBGSEQ=[1 1 1];  %background sequence used to calibrate for respective
days
    t4avging=[210 240; 210 240; 210 240]
end

TOTALIMAGES=250*ones(1,length(SEQUENCES2PROCESS))
sourceconc=1020  %PPM NO2
query1='n';%input('Use standard shot intensity rather than input files? y/n ','s');
rootdir='d:\NASA\Good'

images2avg=10   %user input
shotscaler=1
filterwidth=5
imfilterwidth=5%33/2    %about     0.1in
injectionframe=50
%maskfile='immask';
%seqfileoffset=1

%mask=imread('immask.tif');  %load image mask
%mask=uint32(mask./max(max(mask)));  %get just 1's and 0's
%sheetpixels=numel(mask)-sum(sum(mask));
%[junk,TLcoord]=imcrop(double(mask));
squaresize=102/2+1; %pixels, so 102=1"
for dateindex=1:length(TESTDATES);
   sprintf('Processing %s',char(TESTDATES(dateindex)));
   TLcoord=TLcoords(dateindex,:);
   h=ones(filterwidth,filterwidth)/filterwidth^2;
   h2=ones(imfilterwidth,imfilterwidth)/imfilterwidth^2;
   %MB=dlmread(sprintf('MB_%d_images.txt',images2avg),'\t');
MB=dlmread(sprintf('%s\\%s\\MB_%d_images.txt',rootdir,char(TESTDATES(datei
ndex)),images2avg),'\t');
   %MB=uint16(MB.*1000);
   M=MB(:,1:length(MB)/2);     %selects M values from combined matrix loaded as
MB
   B=MB(:,length(MB)/2+1:length(MB));  %selects B values from combined matrix
loaded as MB
   Msquare=M((TLcoord(2)-squaresize/2):(TLcoord(2)+squaresize/2),(TLcoord(1)-
squaresize/2):(TLcoord(1)+squaresize/2));
   %Msquare=M((TLcoord(1)-
squaresize/2):(TLcoord(1)+squaresize/2),(TLcoord(2)-
squaresize/2):(TLcoord(2)+squaresize/2));
   Bsquare=B((TLcoord(2)-squaresize/2):(TLcoord(2)+squaresize/2),(TLcoord(1)-
squaresize/2):(TLcoord(1)+squaresize/2));
   Msquare=repnonzero(Msquare,mean(Msquare(1,:)));
   %Msheet=double(uint32(M*1e6).*mask);Bsheet=B.*double(mask);  %makes all
elements outside of the sheet zero
```

```
   figure(4);imagesc(Msquare,[0 .1]);axis square; colorbar;title('Msquare');
   frames(1)=getframe(4);
   Mwithbox=drawbox(M,TLcoords(dateindex,:),squaresize);
   testdate=char(cell2mat(TESTDATES(dateindex)));
   figure(5);imagesc(Mwithbox,[0 .1]);axis square; colorbar;title('M full image');
   Mwithboxframe=getframe(5);
   hgsave(5,sprintf('Mwithbox%s_dateavgs.fig',testdate));
   %Msheettimes1MM=uint32(Msheet.*1e6);
%Msheetavg=double(sum(sum(Msheet)))/double(sheetpixels)/1e6;Bsheetavg=sum(s
um(Bsheet))/sheetpixels;
   % IMAGE FILTERING (BLURRING OF CONSTANTS);
   %Mquery1='y';%input('Use standard shot intensity rather than input files? y/n
','s');=.001*imfilter(M*1000,h);
   %B=0.001*imfilter(1000*B,h);M1
   for iseq=1:length(SEQUENCES2PROCESS(dateindex,:))
      %bgsequence=SEQUENCES2PROCESS(iseq);    %changed from a string to a
number

name4calbg=sprintf('%s_seq%dbg',char(TESTDATES(dateindex)),CALBGSEQ(dat
eindex));    %the bgfile will get this in the name

bgfromcal=makebg4cal(sprintf('%s\\%s\\seq%dbg\\seq%d',rootdir,char(TESTDATE
S(dateindex)),CALBGSEQ(dateindex),CALBGSEQ(dateindex)),images2avg,name4
calbg);
      bgfromcalsquare=bgfromcal((TLcoord(2)-
squaresize/2):(TLcoord(2)+squaresize/2),(TLcoord(1)-
squaresize/2):(TLcoord(1)+squaresize/2)); %cropped section of background used for
calibration
      bgcalfileavg(dateindex,iseq)=mean(mean(bgfromcalsquare));

      bgsequence=SEQUENCES2PROCESS(dateindex,iseq);
      %bgfile=makebg(sprintf('seq%d',bgsequence),images2avg);

bgfile=makebg(sprintf('%s\\%s\\seq%ddump\\seq%d',rootdir,char(TESTDATES(dat
eindex)),bgsequence,bgsequence),images2avg);  %rootdir\testdate\sequence#\
      bgfile=uint32(bgfile);
      bgfilesquare=bgfile((TLcoord(2)-
squaresize/2):(TLcoord(2)+squaresize/2),(TLcoord(1)-
squaresize/2):(TLcoord(1)+squaresize/2));%cropped bgfile
      bgfileavg(dateindex,iseq)=mean(mean(bgfilesquare));
      %maskedbgfile=bgfile.*mask;
      %bgsheetavg=sum(sum(maskedbgfile))/sheetpixels;  %this is the average
intensity of the background file in the sheet area only
      %seriesnumber=9 %offset=findfirstlaserimages(seriesnumber)-2;    %user input
series#
      seriesnumber=SEQUENCES2PROCESS(iseq);
```

```
totalimages=TOTALIMAGES(iseq);

%seriesname=sprintf('seq%d',seriesnumber); %user input

seriesname=sprintf('%s\\%s\\seq%ddump\\seq%d',rootdir,char(char(TESTDATES(da
teindex))),SEQUENCES2PROCESS(dateindex,iseq),SEQUENCES2PROCESS(date
index,iseq));%user input
imagewidth=size(bgfile);imagewidth=imagewidth(1,1);
for k=1:totalimages-images2avg;
  jstart=k;   %defines imagBG4minusBG2es to be added start point
  jend = k+images2avg-1;

  for j=jstart:jend;  %to add images
    filenum=j;%+seqfileoffset;
    if j==jstart
      lastfile=imread(sprintf('%s_%d.tif',seriesname,filenum));  %read the
first image in
      lastfile=uint32(lastfile((TLcoord(2)-
squaresize/2):(TLcoord(2)+squaresize/2),(TLcoord(1)-
squaresize/2):(TLcoord(1)+squaresize/2)));
      %%lastfile=lastfile./(SHOTFILE(j));
      %lastfile=lastfile(ystart:yend,xstart:xend);%-bgfile;
    else
      currentfile=imread(sprintf('%s_%d.tif',seriesname,filenum));%read the
next image
      currentfile=uint32(currentfile((TLcoord(2)-
squaresize/2):(TLcoord(2)+squaresize/2),(TLcoord(1)-
squaresize/2):(TLcoord(1)+squaresize/2)));
      %%currentfile=currentfile./(SHOTFILE(j));
      %currentfile=currentfile(ystart:yend,xstart:xend);%-bgfile;
      currentfile=lastfile+currentfile;          %add the current image to the last
one
      lastfile=currentfile;
    end
  end
  %lastfile=uint16(lastfile/SHOTFILE(j))-bgfile;   %removes the background.
the background must have the same number of images added and no averaging
  %lastfileavg=(double(lastfile)/images2avg)-double(bgfile);  %having
  %problems 7-25-06 AM, trying to repair issue with double VS uints
  seqintensity(iseq,k)=mean(mean(lastfile));  %average intensity of selected
location, including the background
  LASTFILEAVG=(lastfile/uint32(images2avg))-uint32(bgfile((TLcoord(2)-
squaresize/2):(TLcoord(2)+squaresize/2),(TLcoord(1)-
squaresize/2):(TLcoord(1)+squaresize/2)));
  %LASTFILEAVG=LASTFILEAVG.*mask;
```

```
lastfileavg(iseq,k)=mean(mean(LASTFILEAVG));%double(sum(sum(LASTFILEA
VG))/squaresize^2);

%lastfilesheetavgscaledppm(iseq,k)=lastfileavg(iseq,k)*double(Msheetavg)+double(
Bsheetavg);

LASTFILESQUAREAVGSCALEDPPM=double(LASTFILEAVG).*double(Msquar
e)+double(Bsquare);

%LASTFILESQUAREAVGSCALEDPPM=double(LASTFILEAVG).*double(Msq
uare)+double(Bsquare)+Msquare.*(double(bgfilesquare)-double(bgfromcalsquare));
%4-12-07 accounts for background changes after calibration

lastfilesquareavgscaledppm(iseq,k)=mean(mean(LASTFILESQUAREAVGSCALE
DPPM));

%lastfilesheetavgscaledppm(iseq,k)=mean(mean(Msquare))*lastfileavg(iseq,k)+mea
n(mean(Bsquare));

%lastfilesheetavgscaledpercent(iseq,k)=100*(sum(sum(lastfileavg.*mask))/sheetpixe
ls*Msheetavg+Bsheetavg)/sourceconc;

lastfilesquareavgscaledpercent(iseq,k)=100*lastfilesquareavgscaledppm(iseq,k)/sour
ceconc;
      end
      figure(1);plot(lastfilesquareavgscaledppm);
      %if and(iseq==1, dateindex==1); pause; end
      %sprintf('The average sheet value is %d (intensity',bgsheetavg)
      if writefiles=='y';imwrite(bgfile,sprintf('bg%d.tiff',bgsequence),'tiff');end
      biasppm(dateindex,iseq)=mean(lastfilesquareavgscaledppm(iseq,20:30));
   end %sequence loop
   SEQAVG=mean(lastfilesquareavgscaledppm,1);
   %dlmwrite(sprintf('%s_seqaverage%imgs',
   figure(1);plot(lastfilesquareavgscaledppm);title('Scaled PPM');
xlabel('frame');ylabel('concentration, PPM');
   numseq=length(SEQUENCES2PROCESS)

   avgscaledpercent(dateindex,:)=mean(lastfilesquareavgscaledpercent,1);
   stdbetweenseq_ppm(dateindex,:)=std(lastfilesquareavgscaledppm,1);
   DATEAVG(dateindex,:)=mean(lastfilesquareavgscaledppm,1);

lastfilesquareavgscaledppm(1+height(lastfilesquareavgscaledppm),:)=mean(lastfilesq
uareavgscaledppm,1);  %adds an average to the bottom row

   TIMESCALE=[images2avg/10/2:0.1:(TOTALIMAGES(1)-images2avg/2)/10-.1];
```

```
   figure(10+dateindex);
   for i=1:length(SEQUENCES2PROCESS)

%subplot(numseq,1,i);plot(TIMESCALE,lastfilesheetavgscaledpercent(i,:));title(spri
ntf('Illuminated area average VS Time for %s test
%d',testdate,SEQUENCES2PROCESS(i)));xlabel('Time,
s');ylabel('AOI/Injected,%');
      linecolors=['r' 'g' 'b'];
      subplot(length(SEQUENCES2PROCESS),2,2*i-
1);plot(TIMESCALE,lastfilesquareavgscaledppm(i,:)-
biasppm(dateindex,i));title(sprintf('Area avg (PPM) VS Time for %s test
%d',testdate,SEQUENCES2PROCESS(dateindex,i)));xlabel('Time, s');ylabel('PPM');
      axis([0 totalimages/10 0 300]);
      subplot(length(SEQUENCES2PROCESS),2,[2 4
6]);plot(TIMESCALE,lastfilesquareavgscaledppm(i,:)-
biasppm(dateindex,i),linecolors(i));axis([0 25 0 300]);title(sprintf('Area avg (PPM)
VS Time for %s test
%d',testdate,SEQUENCES2PROCESS(dateindex,i)));xlabel('Time,
s');ylabel('PPM');hold on;legend;grid
      SSsectionoftest=lastfilesquareavgscaledppm-biasppm(dateindex,i);
      individualtests(dateindex,:,:)=SSsectionoftest;

testavgs(i,dateindex)=mean(mean(SSsectionoftest(i,t4avging(dateindex,1):t4avging(
dateindex,2))));
      if i==length(SEQUENCES2PROCESS);

portionavg(dateindex,:)=[mean(mean(individualtests(dateindex,:,t4avging(dateindex,
1):t4avging(dateindex,2)))),
std(std(individualtests(dateindex,:,t4avging(dateindex,1):t4avging(dateindex,2))))];

      end%average and stdev for a time range
   end
   figure(10+dateindex);legend 1 2 3

   if writefiles=='y';
      hgsave((10+dateindex),sprintf('AreaavgVStime%s.fig',testdate));

dlmwrite(sprintf('%s_AreaAvg%d_img.txt',char(TESTDATES(dateindex)),images2a
vg),[lastfilesquareavgscaledppm;stdbetweenseq_ppm(dateindex,:)],'delimiter','\t','pre
cision',6);
      saveas((10+dateindex),sprintf('%ggapAreaavgVStime%s.jpg',gap,testdate),'jpg')
   end



   clear lastfilesquareavgscaledppm stdbetweenseq_ppm %
```

```
   %out
   %clear lastfilesheetavgscaledpercent;
end   %date loop

figure(1);
for i=1:length(TESTDATES)

%subplot(numseq,1,i);plot(TIMESCALE,lastfilesheetavgscaledpercent(i,:));title(spri
ntf('Illuminated area average VS Time for %s test
%d',testdate,SEQUENCES2PROCESS(i)));xlabel('Time,
s');ylabel('AOI/Injected,%');
   testdate=char(cell2mat(TESTDATES(i)))

subplot(length(SEQUENCES2PROCESS),1,i);plot(TIMESCALE,DATEAVG(i,:));ti
tle(sprintf('Area avg (PPM) VS Time for %s',testdate));xlabel('Time,
s');ylabel('PPM');
end
biasppmdateavg=mean(biasppm,2);
figure(2);
%plot(TIMESCALE,DATEAVG);title('Average for day,
PPM');legend(windowlabels);xlabel('Time, s');ylabel('Concentration, PPM');%legend
Top Bottom Middle
%for i=1:numseq
for i=1:height(DATEAVG)
   DATEAVG2PLOT(i,:)=DATEAVG(i,:)-biasppmdateavg(i);
end
plot(TIMESCALE,DATEAVG2PLOT);title(sprintf('Average for %gcm
Gap',gap*2.54));axis([0,max(TIMESCALE),0,300]);legend(windowlabels);xlabel('Ti
me, s');ylabel('Concentration, PPM');%legend Top Bottom Middle
%
subplot(numseq,1,i);plot(TIMESCALE,lastfilesquareavgscaledppm(i,:));title(sprintf('
Illuminated area average VS Time for %s test
%d',testdate,SEQUENCES2PROCESS(i)));xlabel('Time, s');ylabel('NO2 conc, PPM
');
%end

%figure(3);
%    plotyy(TIMESCALE,lastfilesquareavgscaledpercent,
TIMESCALE,lastfilesquareavgscaledppm);
%    [AX,H1,H2] =plotyy(TIMESCALE,lastfilesquareavgscaledpercent,
TIMESCALE,lastfilesquareavgscaledppm,'plot');
%    set(get(AX(1),'Ylabel'),'String','AOI/Injected')
%    set(get(AX(2),'Ylabel'),'String','NO2 conc, PPM')
%    ylim(AX(1),[0 20])
%    ylim(AX(2),[0 .20*sourceconc])
%    SEQUENCENAMES=sprintf('Sequence%d ',SEQUENCES2PROCESS);
```

```
%    legend(sprintf('Sequence%d
',SEQUENCES2PROCESS));%SEQUENCENAMES);
%    title(sprintf('Illuminated area average VS Time for %s test
%d',testdate,SEQUENCES2PROCESS(i)));xlabel('Time, s');
if writefiles=='y';hgsave(2,sprintf('AreaavgVStime%s_dateavgs.fig',testdate));end
disp('Background adjustment (%)');
100*((bgfileavg-bgcalfileavg)./bgcalfileavg)
```

PIV Data Reduction Routine

```
% import data from files

path = % path to the results being analyzed

for i = 200:1:399                                   % file numbers i.e., ImportXXX -
ImportXXX

   ii = ['Import' num2str(i)];
   filepath2 = [path (ii) '.dat'];
   velocity = textread(filepath2);                  % this is the raw matrix

   u = velocity(:,3);                               % vector of u velocity values
   v = velocity(:,4);                               % vector of v velocity values
   x_coord = velocity(:,1);                         % vector of x coordinates
   y_coord = velocity(:,2);                         % vector of y coordinates

%    quiver(x_coord,y_coord,u,v,2,'-r')             % plots vector map
%    xlabel('x coordinate (mm)')
%    ylabel('y coordinate (mm)')


% extract velocity vector at a user chosen coordinate

   x = 102.8023911;                                 % x coordinate of desired vector
   y = 95.54721069;                                 % y coordinate of desired vector

   [r,c] = size(velocity);

   for i = 1:1:r
      if velocity(i,1) == x && velocity(i,2) == y
         out = [velocity(i,3), velocity(i,4)];
         break
      end
   end
```

```
   fid=fopen('spec_position.csv','a');                    % creates and writes out to a
.csv file

   for i=1:1:2
      fprintf(fid,'%d,',out(1,i));
   end

   fprintf(fid,'\n');

   fclose(fid);


% extract max u and v velocity vector

   vel_uv = velocity(:,3:4);
   uv = [ min(vel_uv(:,1)) max(vel_uv(:,1)) min(vel_uv(:,2)) max(vel_uv(:,2))];

   fid=fopen('max_min.csv','a');                          % creates and writes out to a
.csv file

   for i=1:1:4
      fprintf(fid,'%d,',uv(1,i));
   end

   fprintf(fid,'\n');

   fclose(fid);

end
```

Appendix B – PLIF Concentration History

Test data for the 1.27 cm plate separation

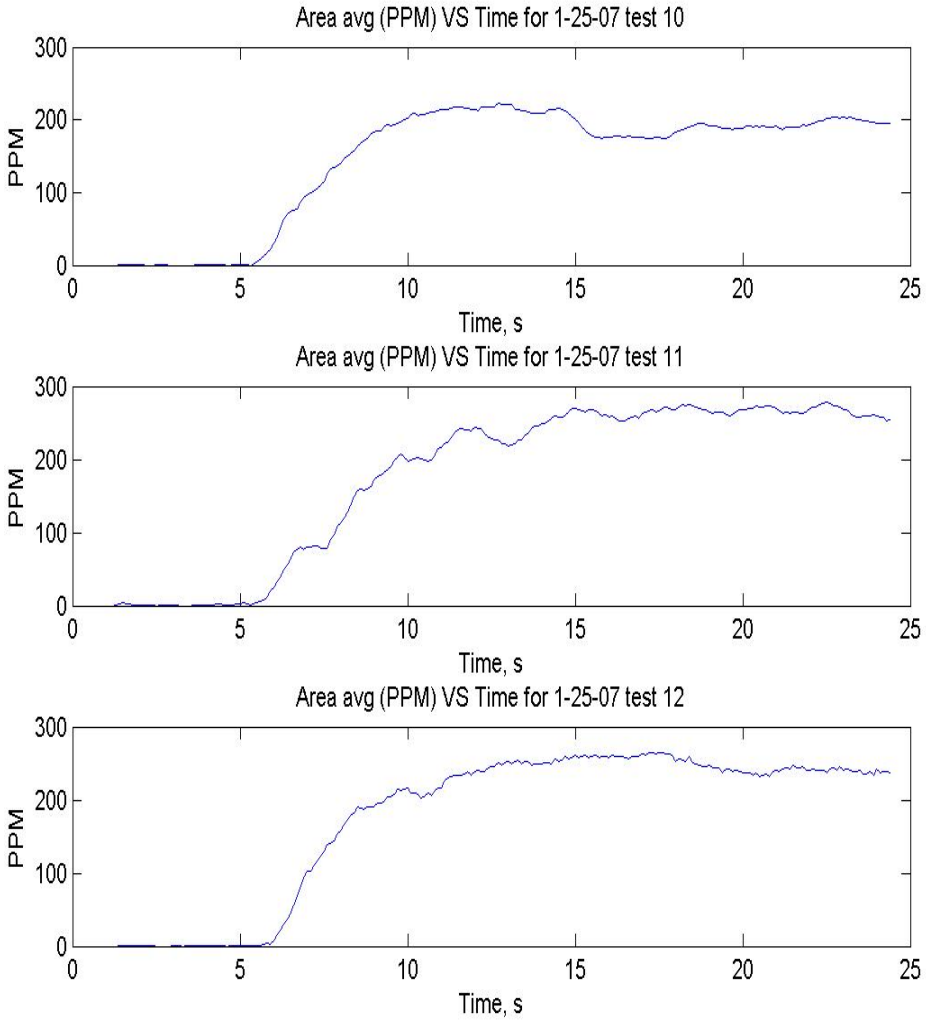

Figure B.1: Concentration histories for tests 10, 11, and 12 at the 1.27 cm plate separation on 1-25-07.

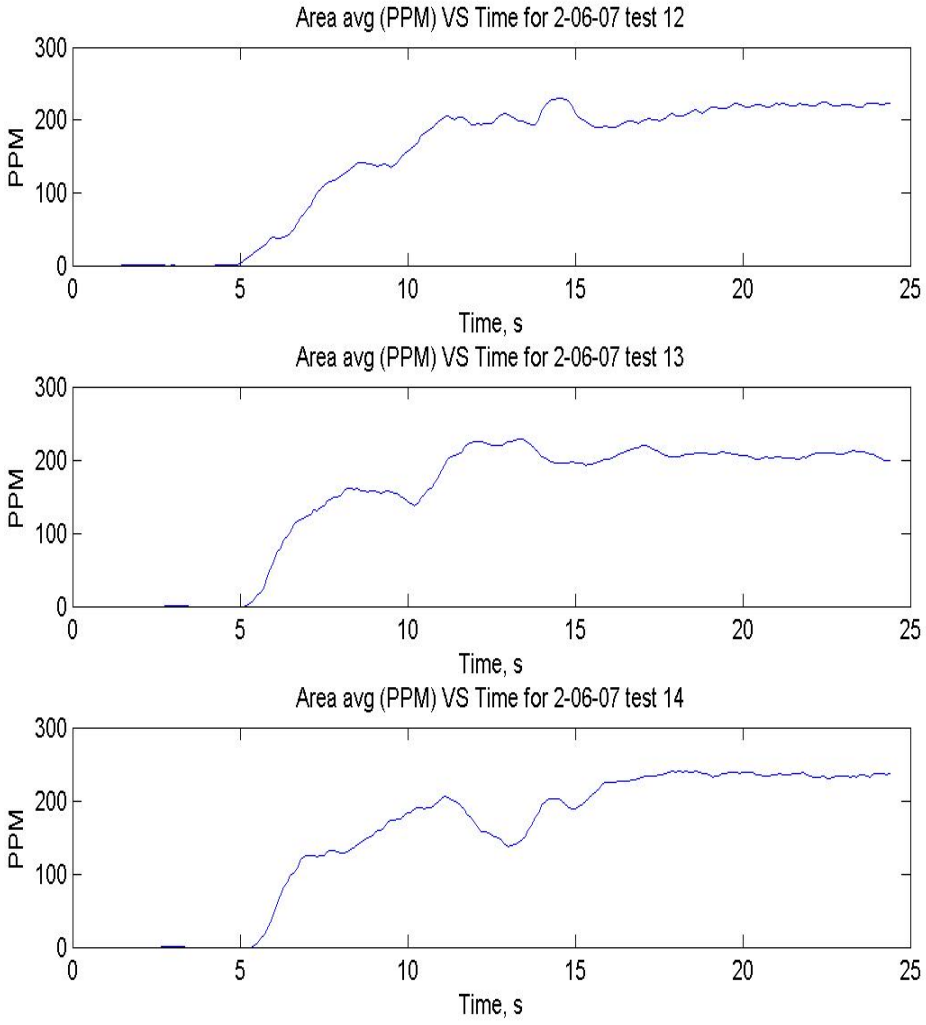

Figure B.2: Concentration histories for tests 12, 13, and 14 at the 1.27 cm plate separation on 2-06-07.

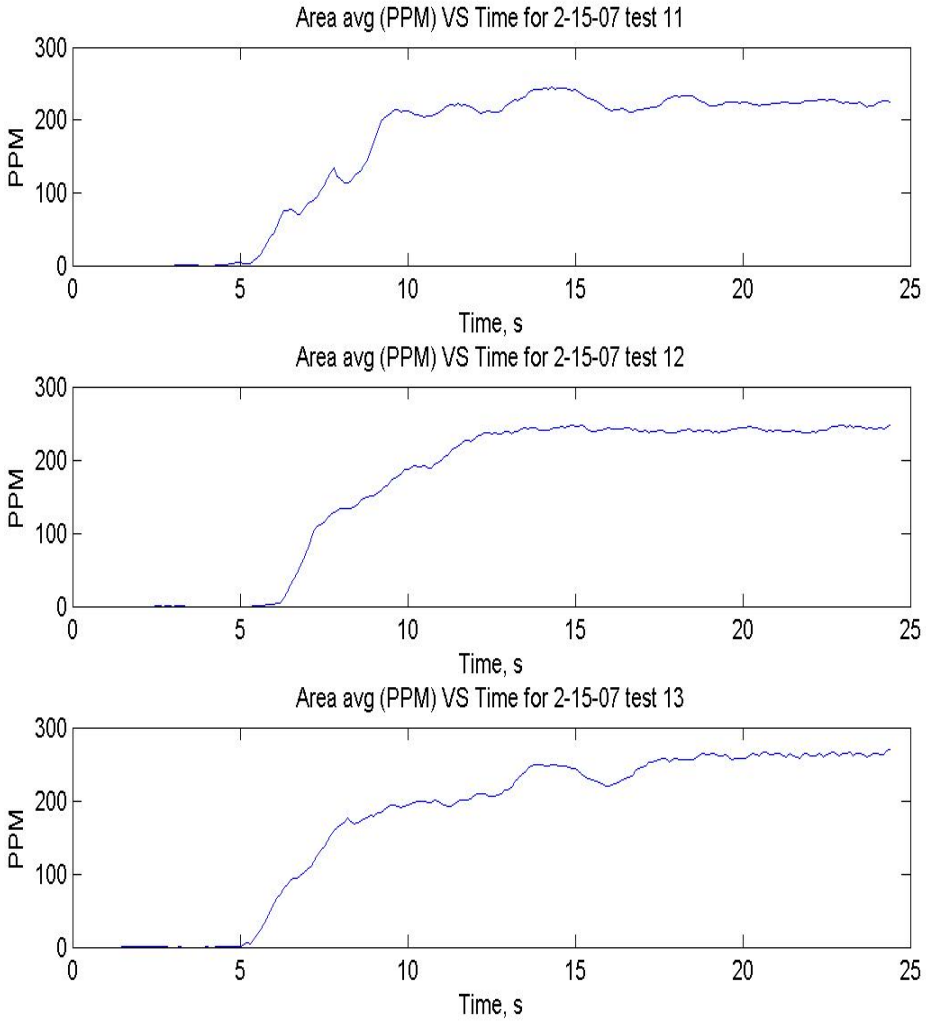

Figure B.3: Concentration histories for tests 11, 12, and 13 at the 1.27 cm plate separation on 2-15-07.

Test data for the 1.91 cm plate separation

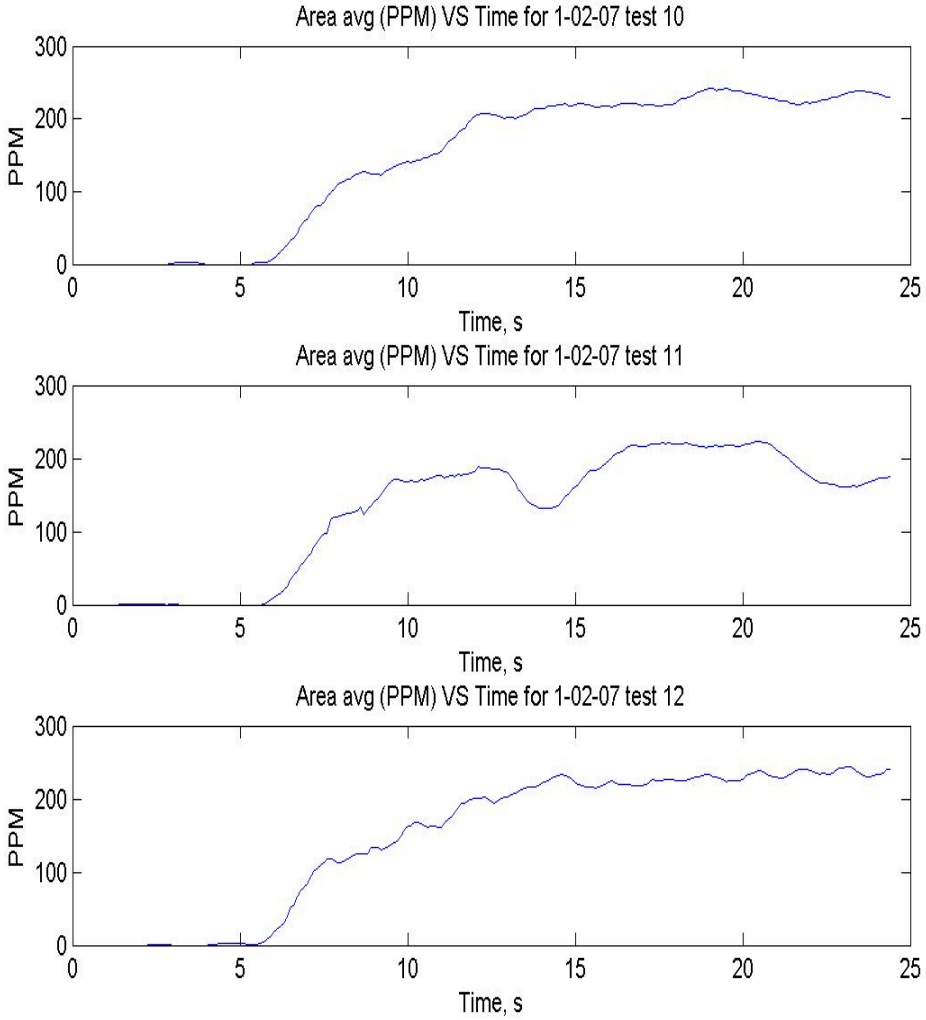

Figure B.4: Concentration histories for tests 10, 11, and 12 at the 1.91 cm plate separation on 1-02-07.

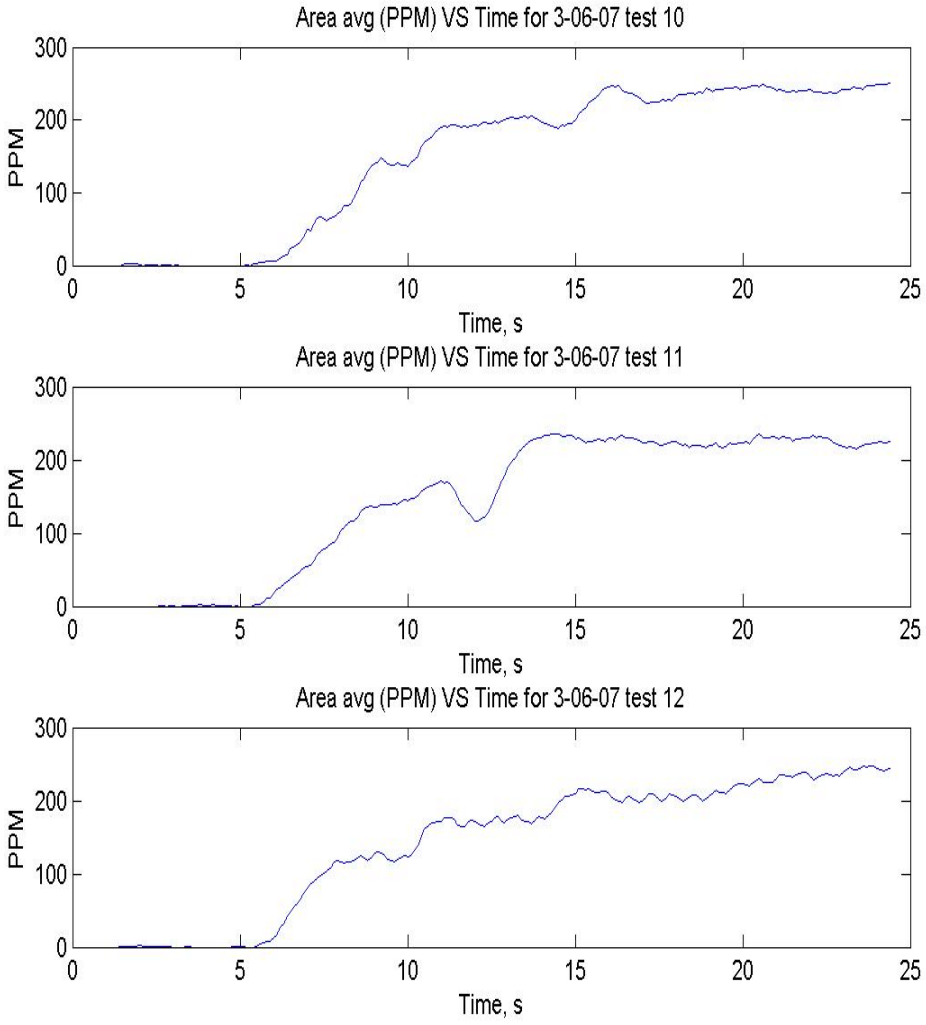

Figure B.5: Concentration histories for tests 10, 11, and 12 at the 1.91 cm plate separation on 3-06-07.

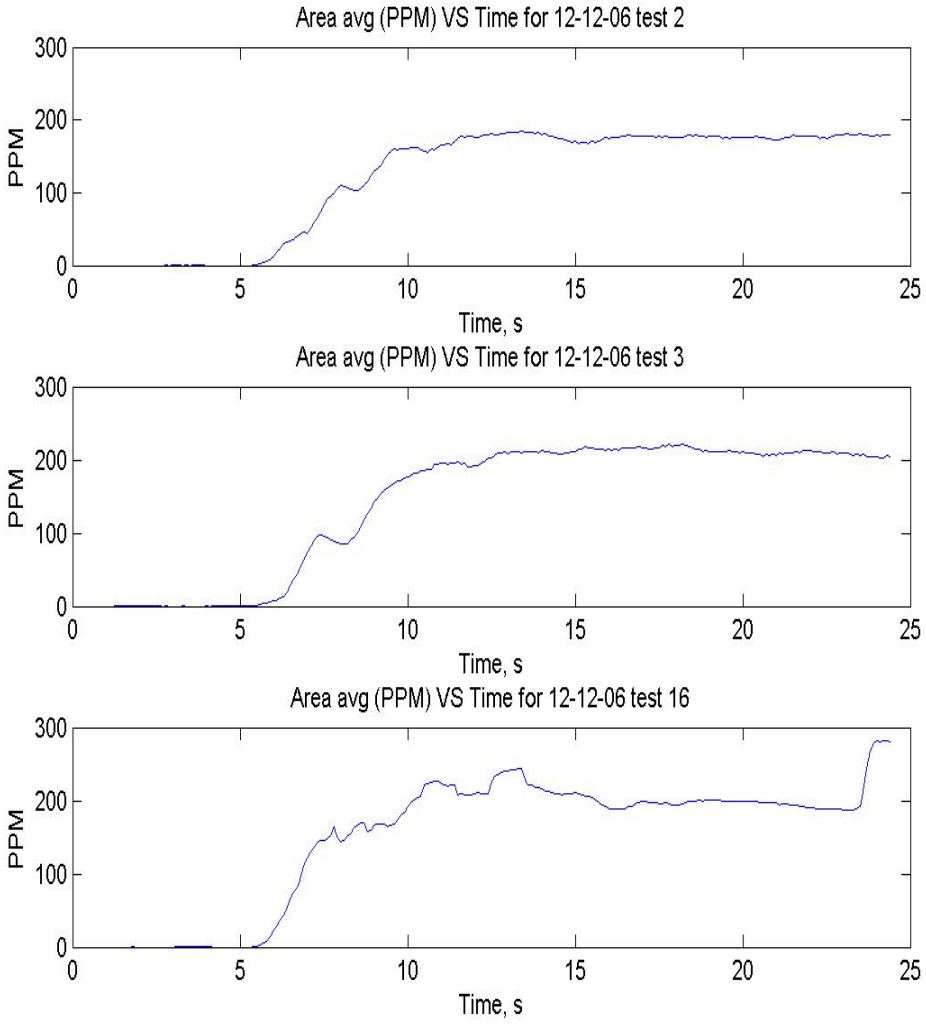

Figure B.6: Concentration histories for tests 2, 3, and 16 at the 1.91 cm plate separation on 12-12-06.

Test data for the 3.18 cm plate separation

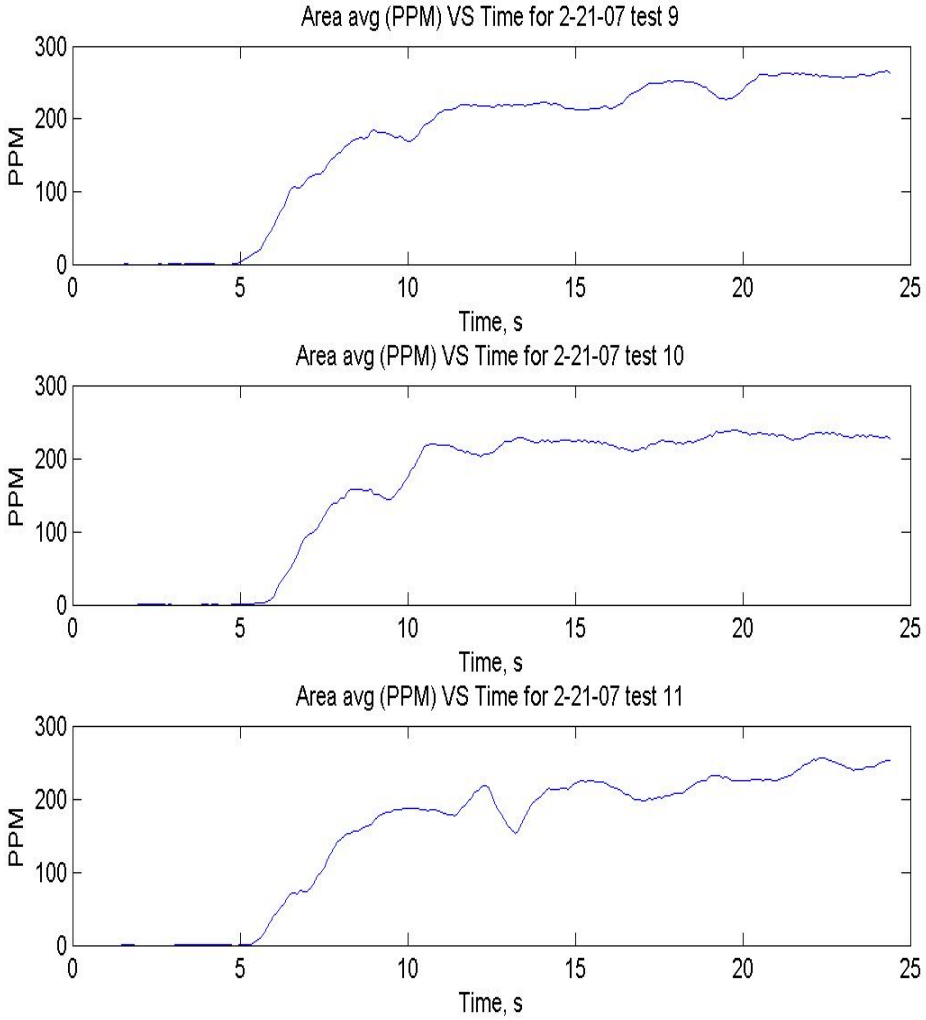

Figure B.7: Concentration histories for tests 9, 10, and 11 at the 3.18 cm plate separation on 2-21-07.

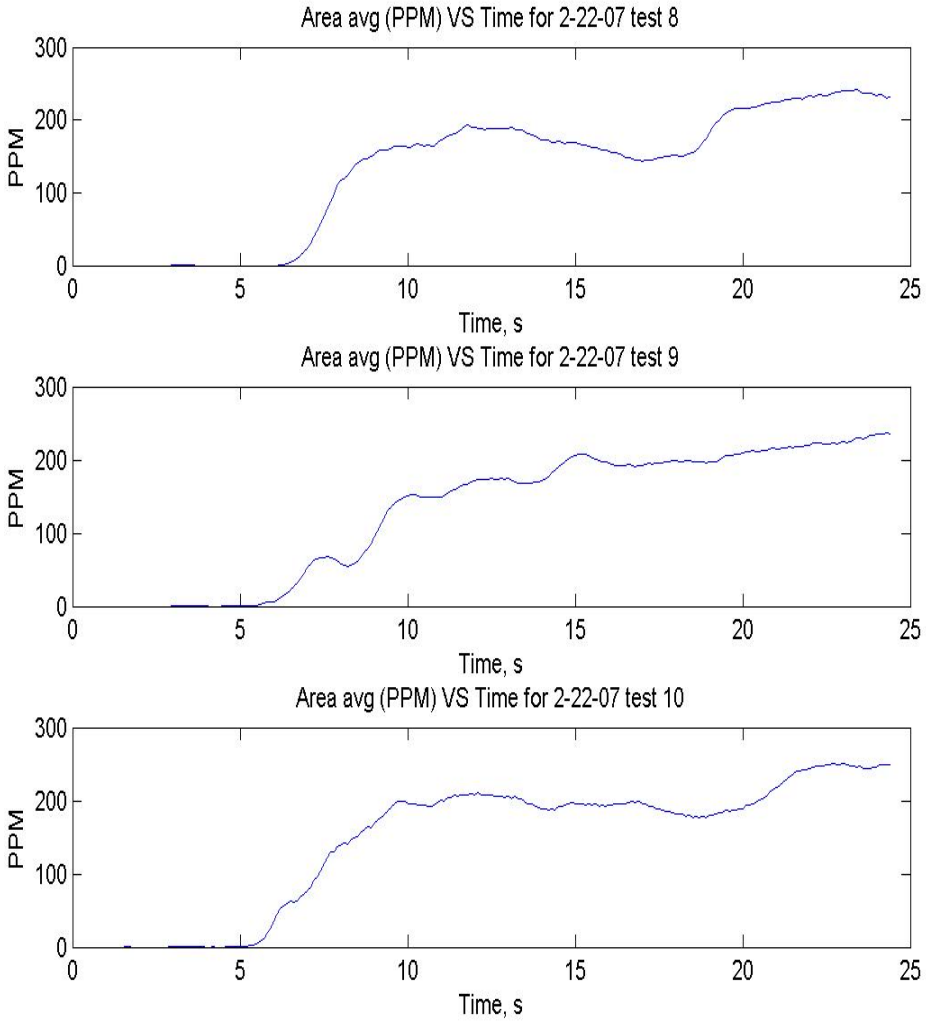

Figure B.8: Concentration histories for tests 8, 9, and 10 at the 3.18 cm plate separation on 2-22-07.

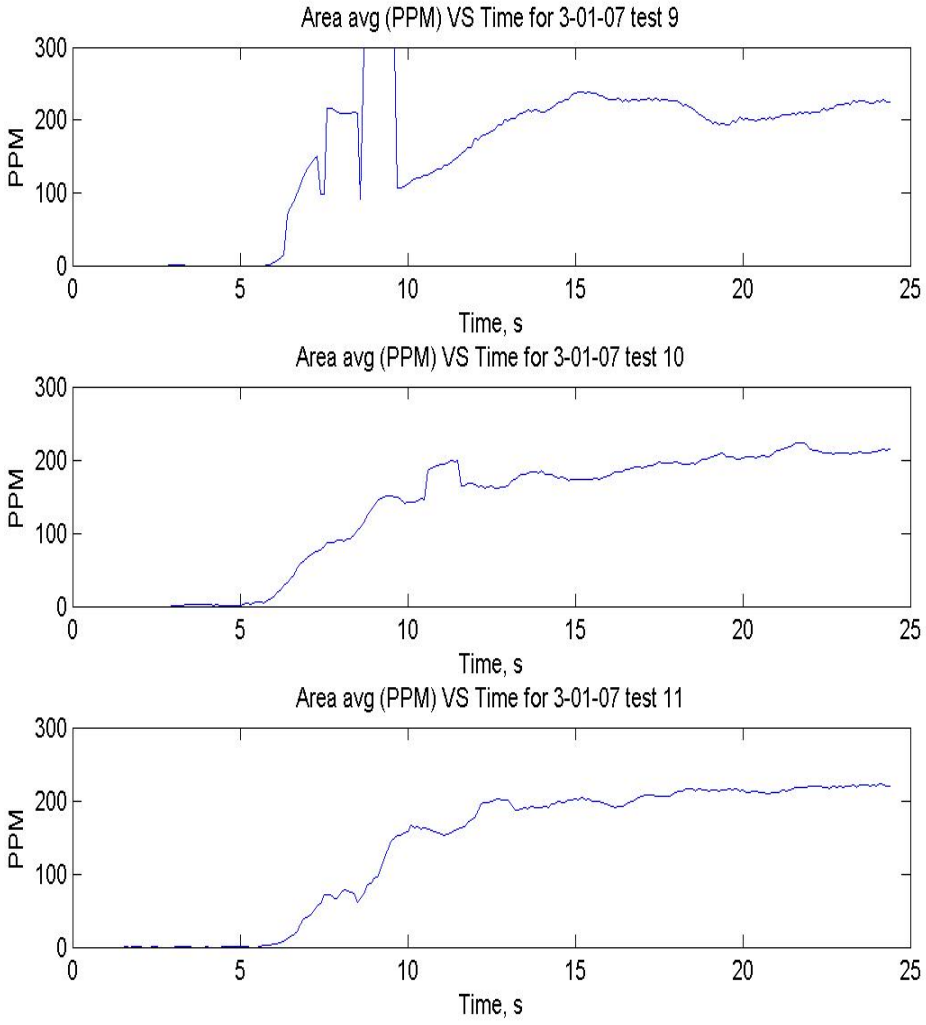

Figure B.9: Concentration histories for tests 9, 10, and 11 at the 3.18 cm plate separation on 3-01-07.

Appendix C – PIV Velocity Data

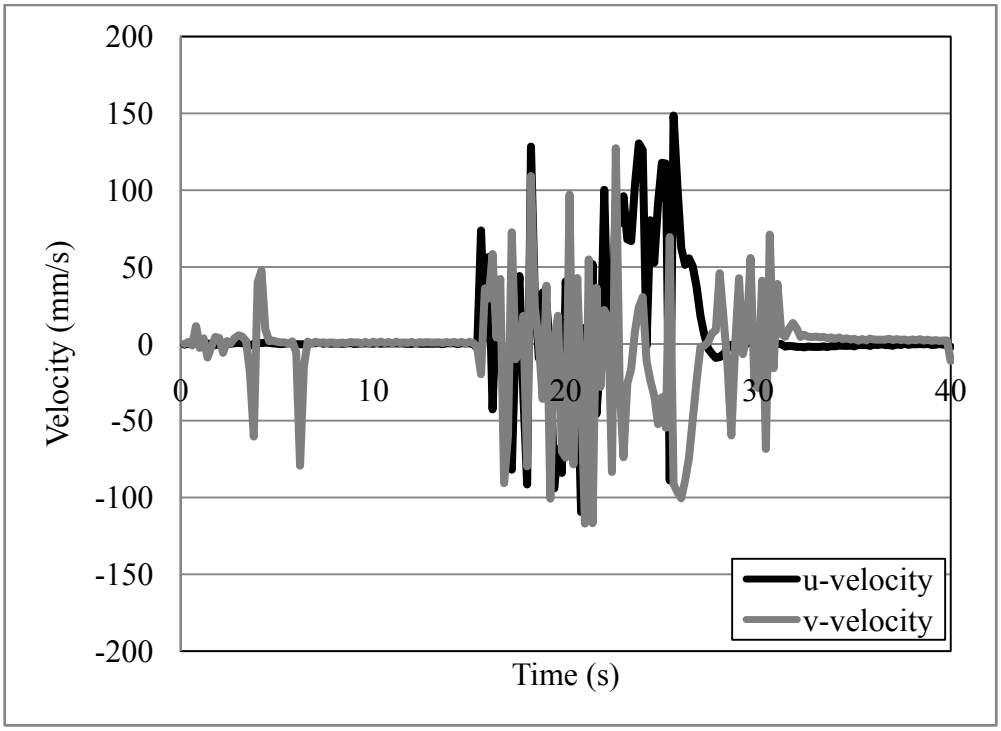

Figure C.1: Lower left velocity component data for the 1.27 cm plate separation.

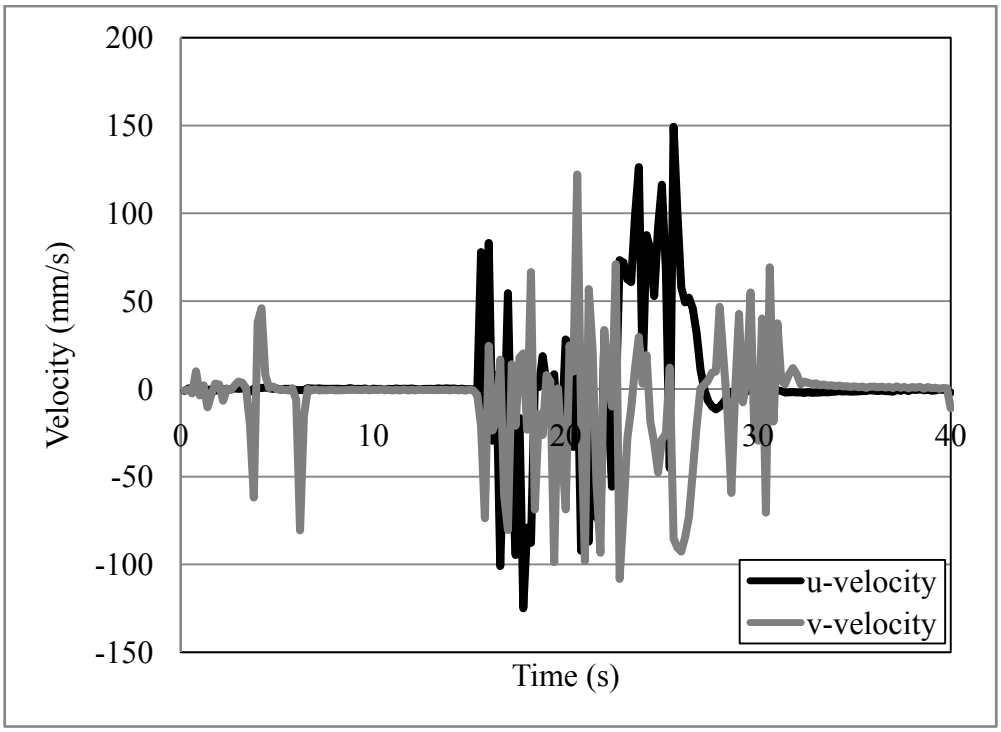

Figure C.2: Lower right velocity component data for the 1.27 cm plate separation.

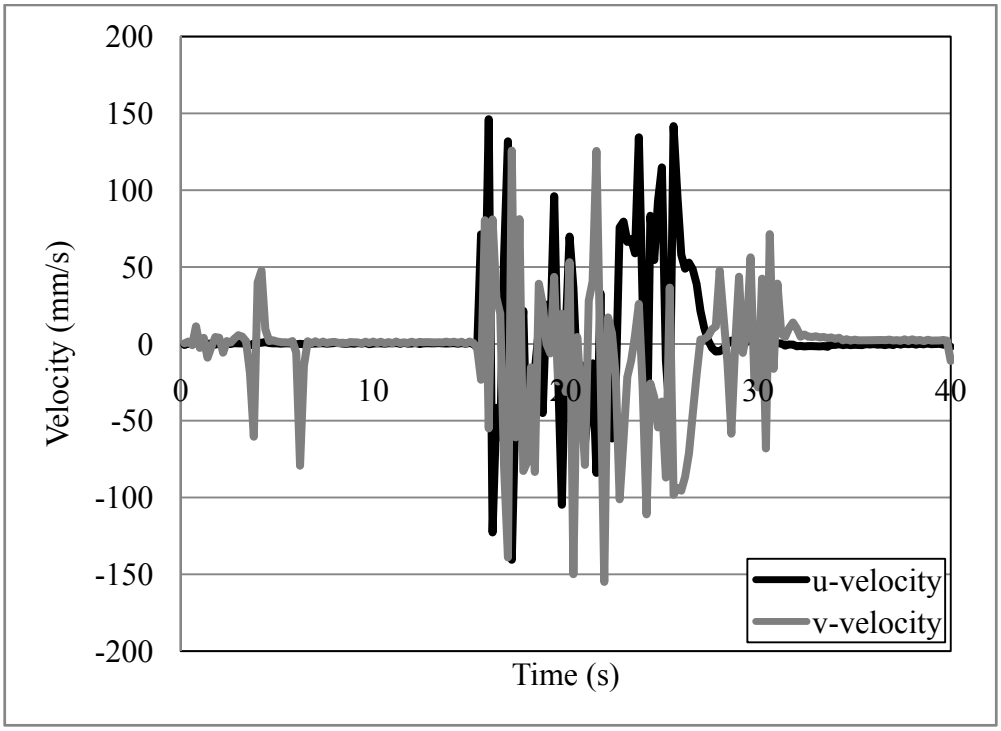

Figure C.3: Upper left velocity component data for the 1.27 cm plate separation.

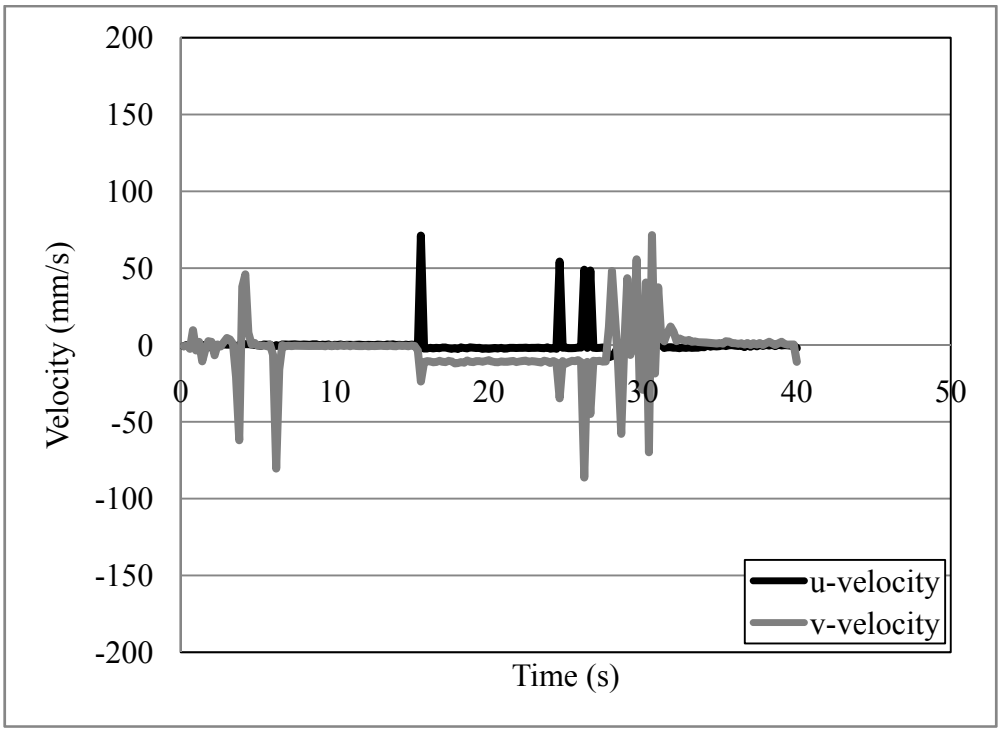

Figure C.4: Upper right velocity component data for the 1.27 cm plate separation.

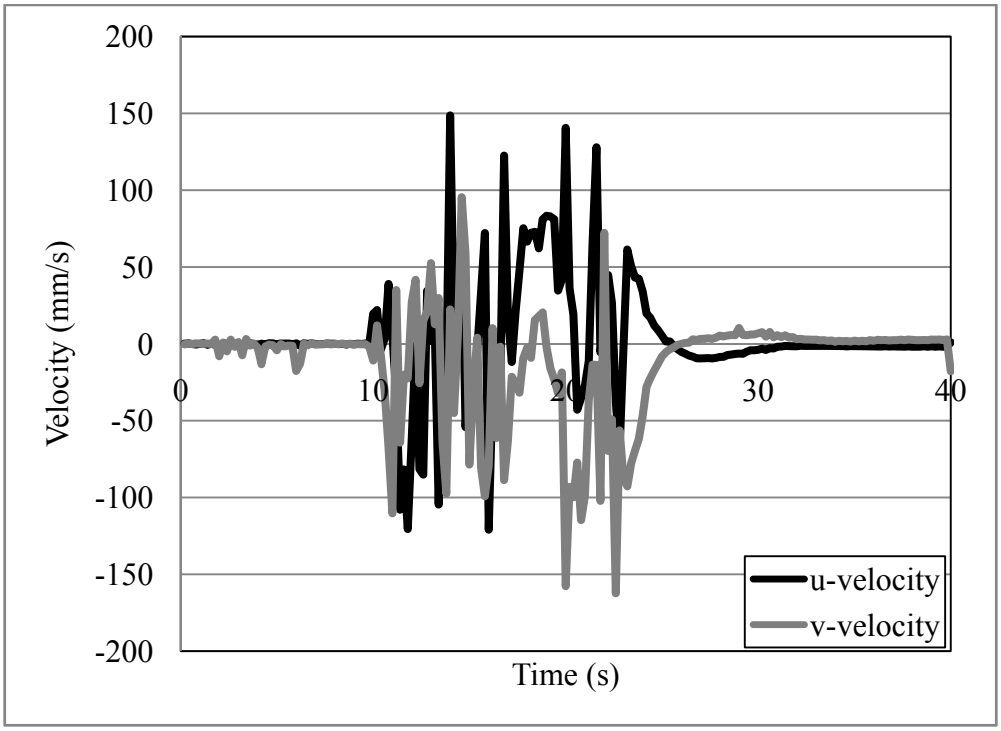

Figure C.5: Lower left velocity component data for the 1.91 cm plate separation.

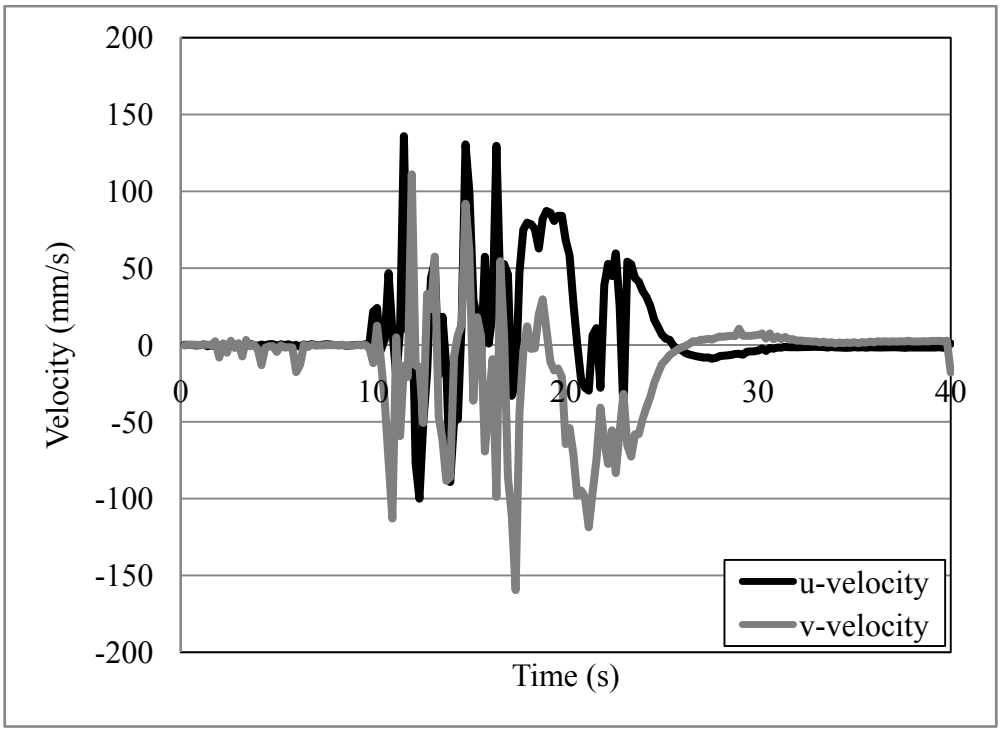

Figure C.6: Lower right velocity component data for the 1.91 cm plate separation.

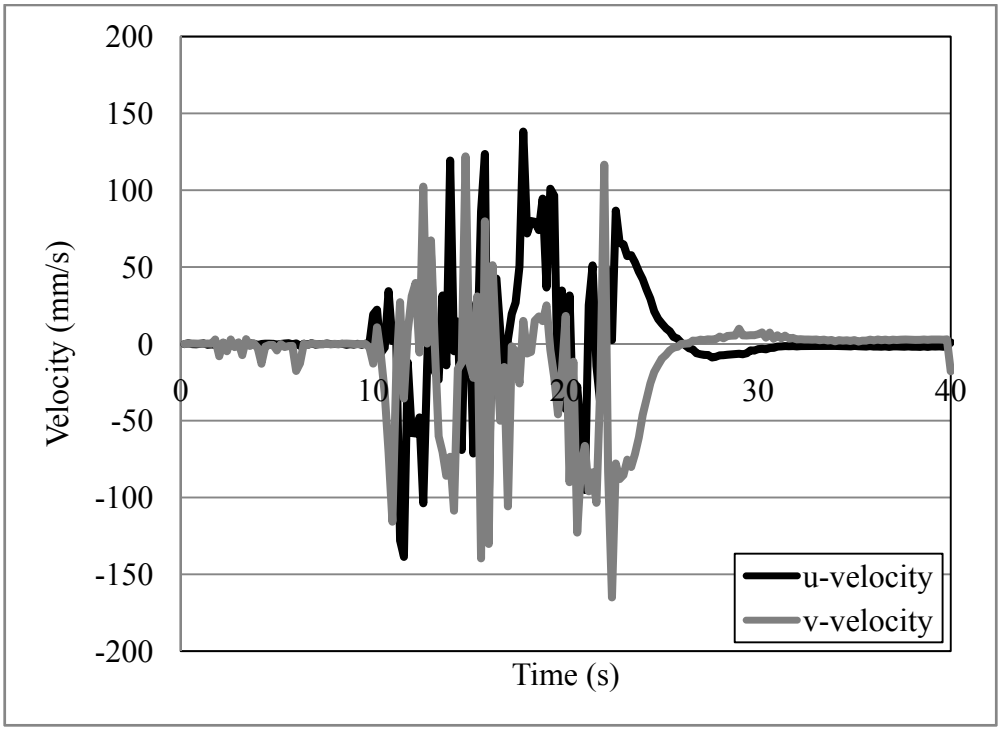

Figure C.7: Upper left velocity component data for the 1.91 cm plate separation.

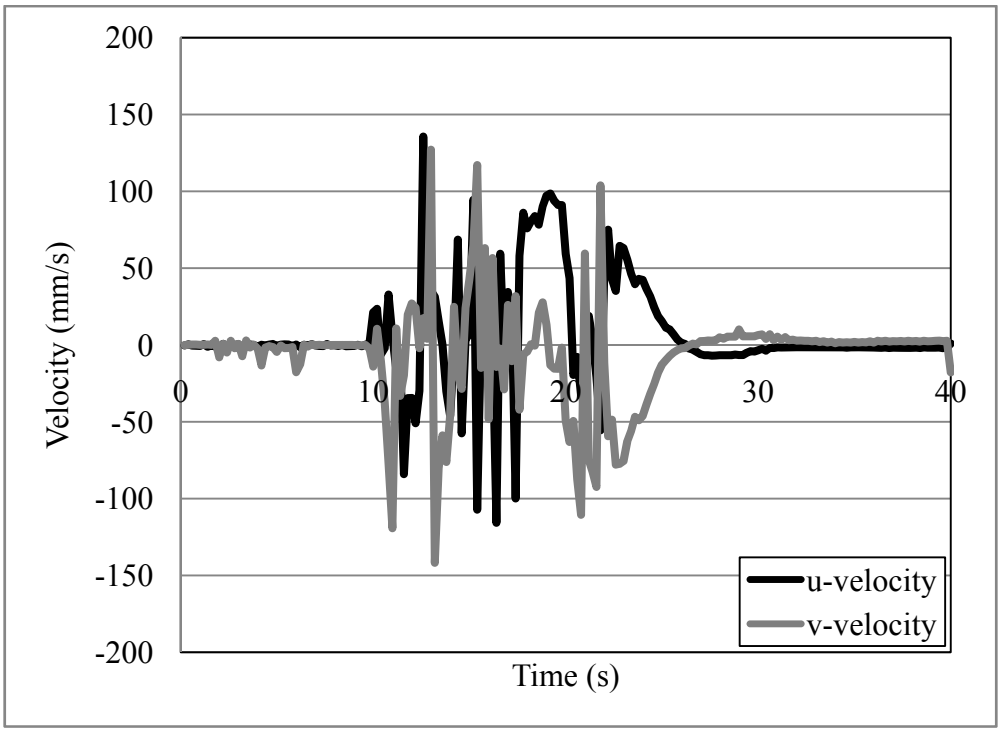

Figure C.8: Upper right velocity component data for the 1.91 cm plate separation.

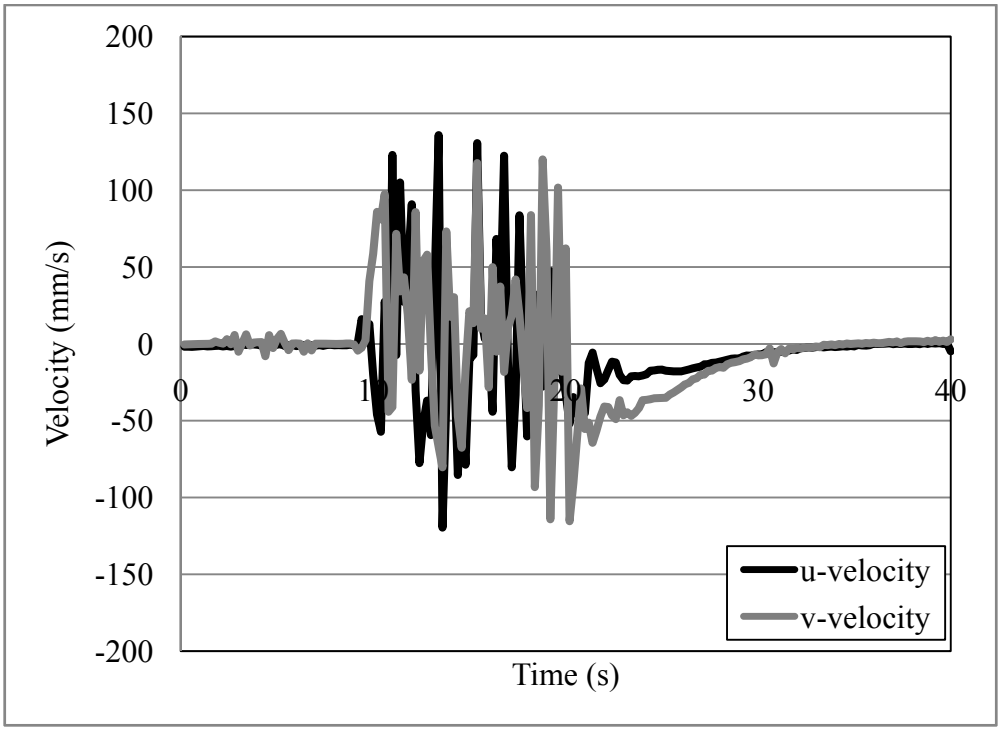

Figure C.9: Lower left velocity component data for the 3.18 cm plate separation.

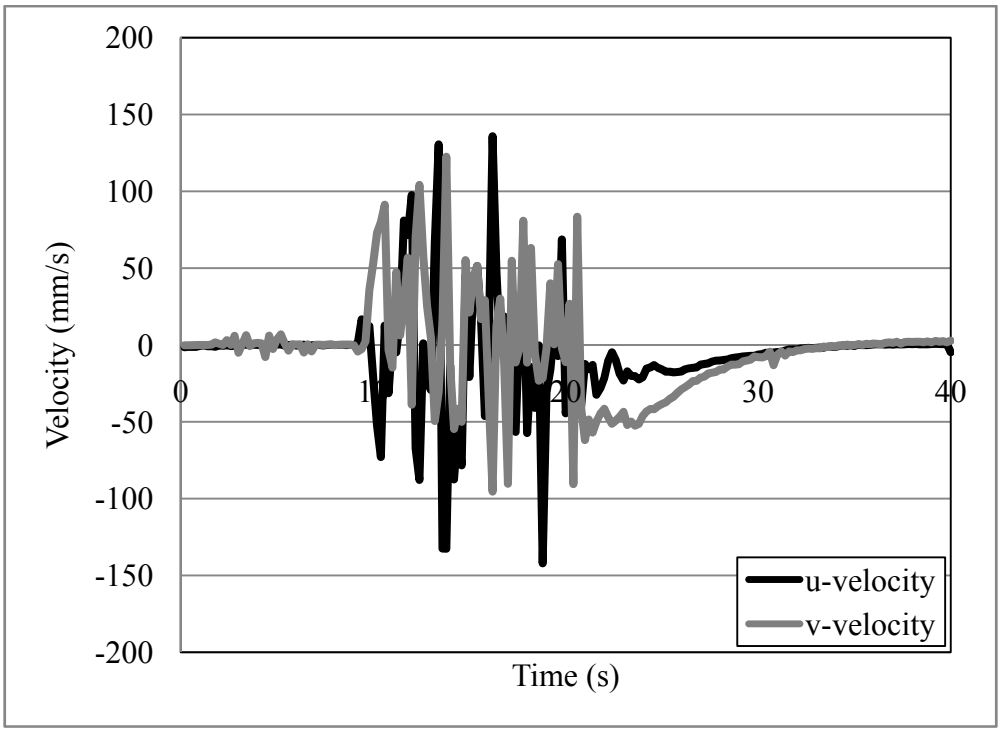

Figure C.10: Lower right velocity component data for the 3.18 cm plate separation.

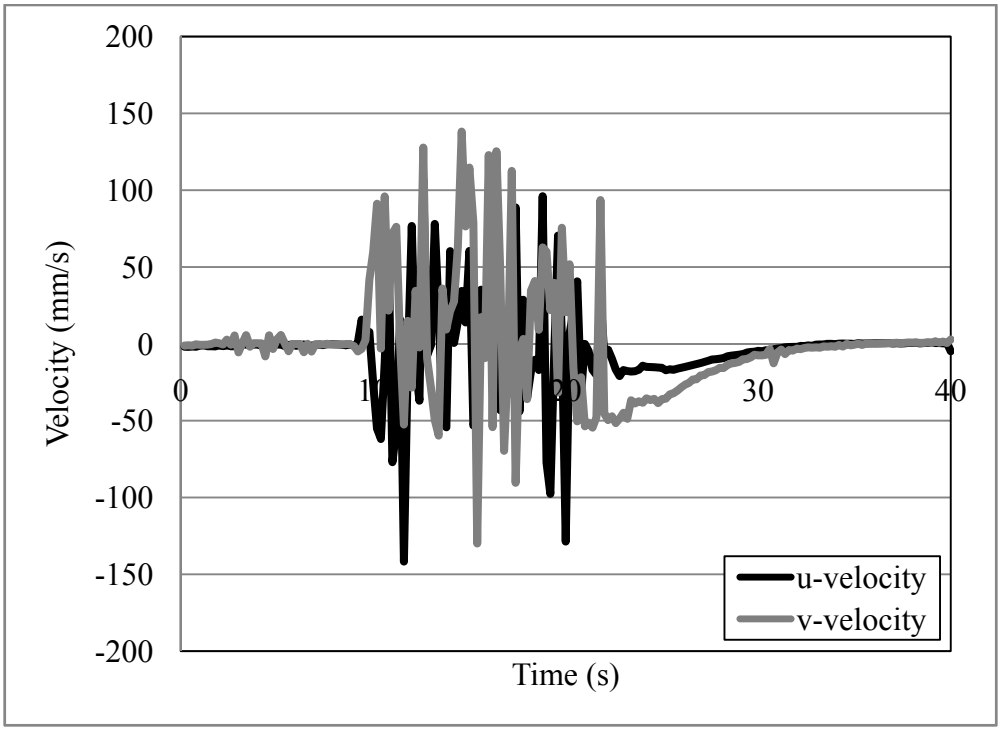

Figure C.11: Upper left velocity component data for the 3.18 cm plate separation.

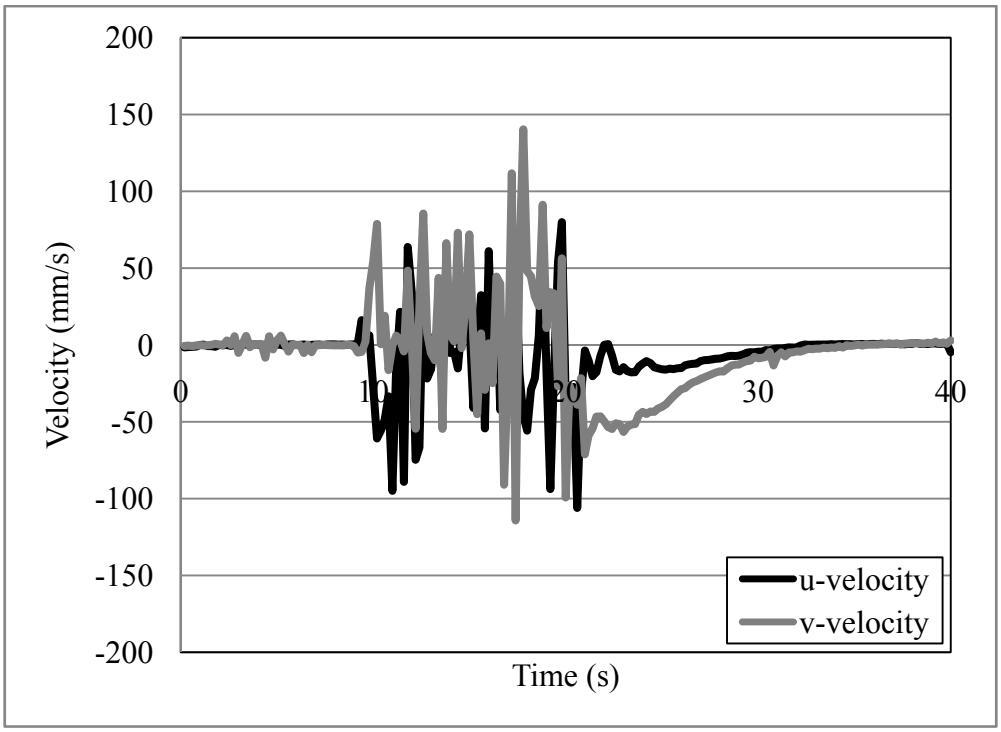

Figure C.12: Upper right velocity component data for the 3.18 cm plate separation.

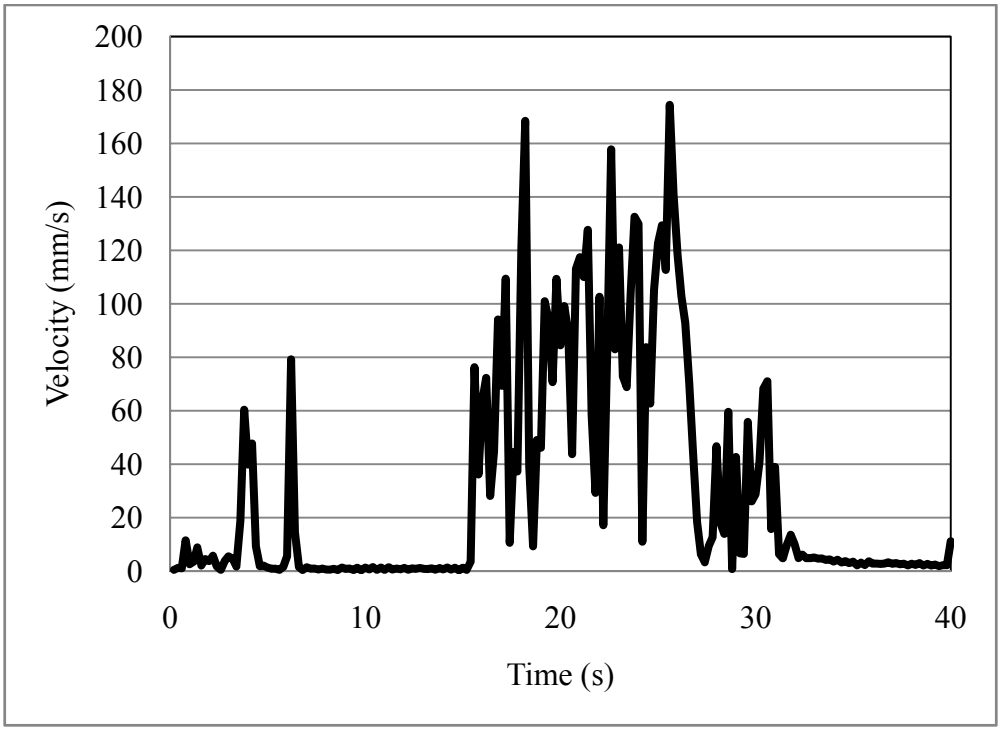

Figure C.13: Lower left velocity magnitude data for the 1.27 cm plate separation.

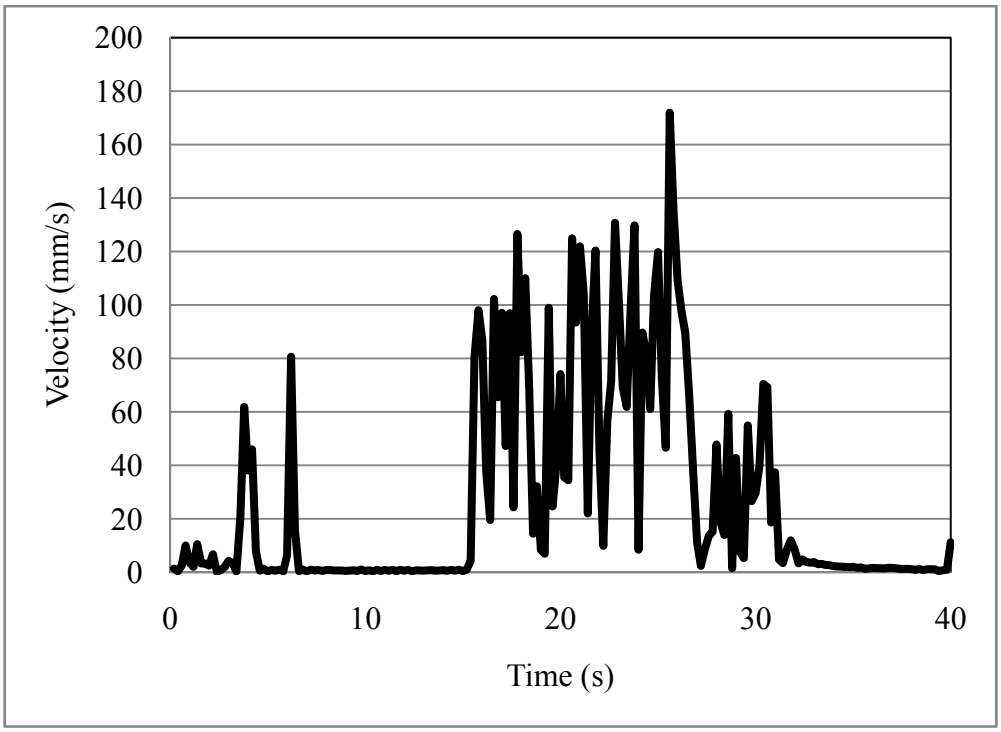

Figure C.14: Lower right velocity magnitude data for the 1.27 cm plate separation.

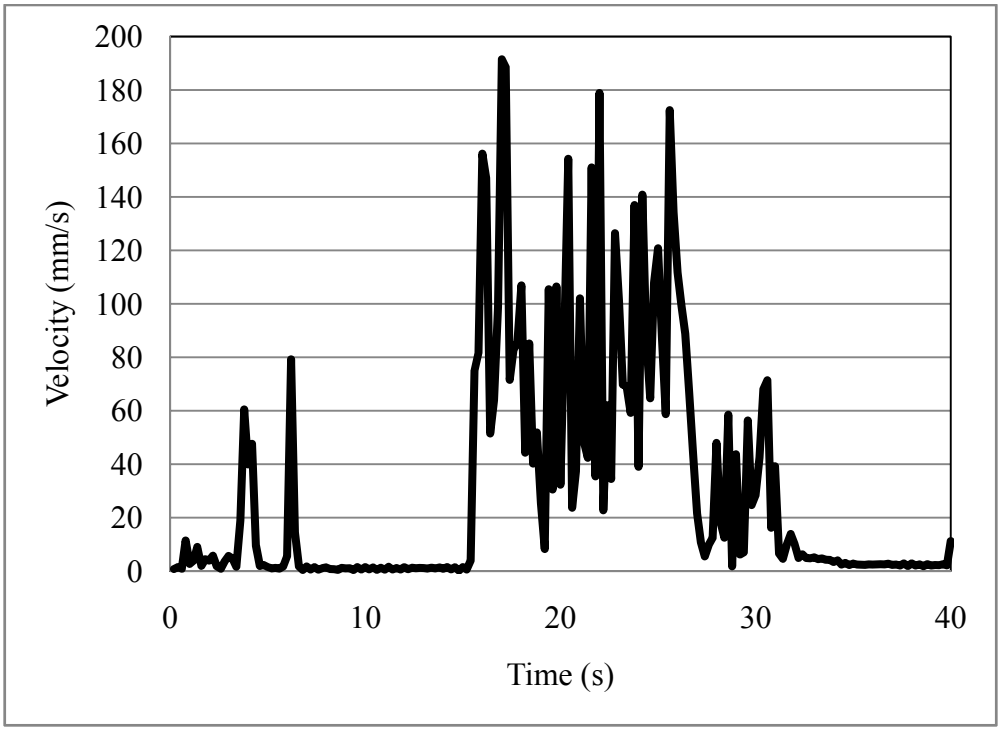

Figure C.15: Upper left velocity magnitude data for the 1.27 cm plate separation.

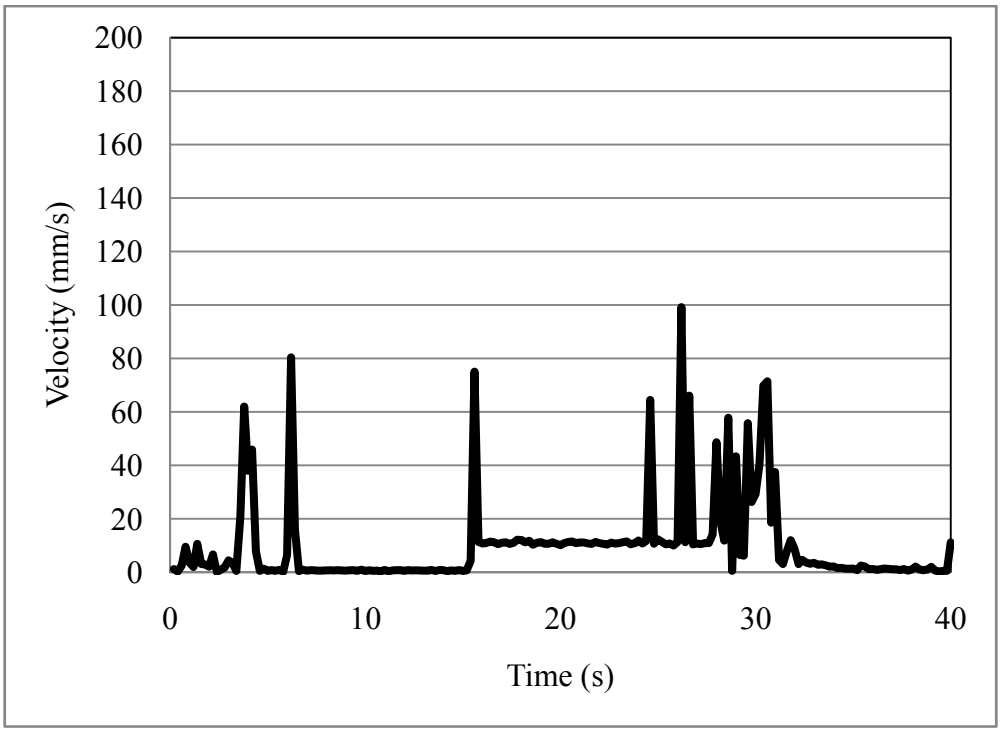

Figure C.16: Upper right velocity magnitude data for the 1.27 cm plate separation.

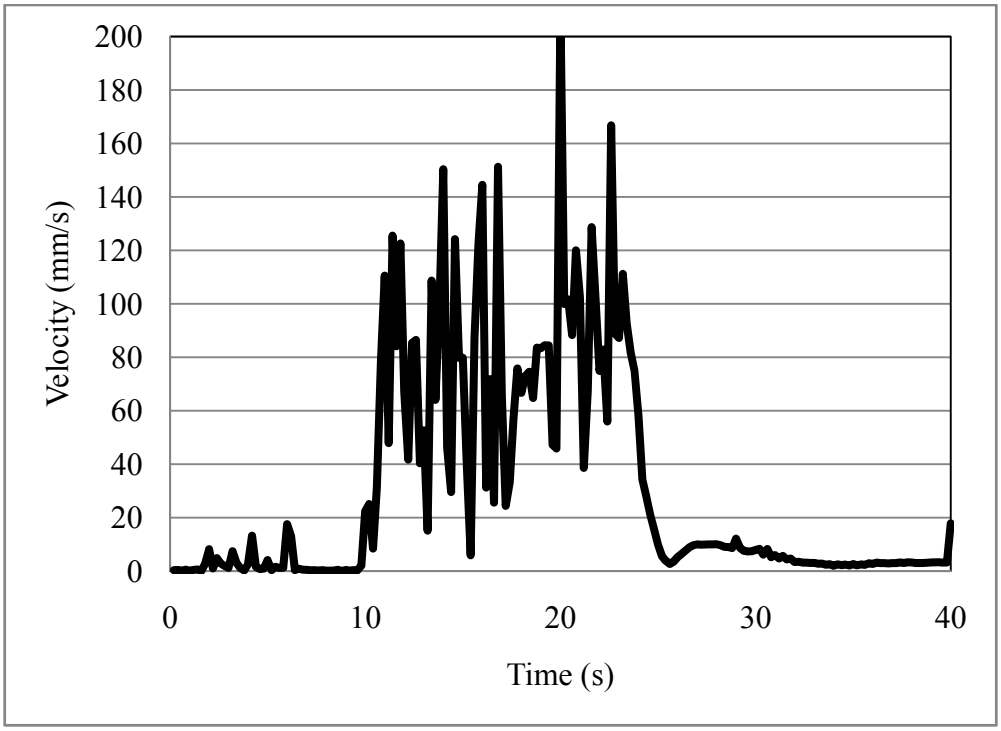

Figure C.17: Lower left velocity magnitude data for the 1.91 cm plate separation.

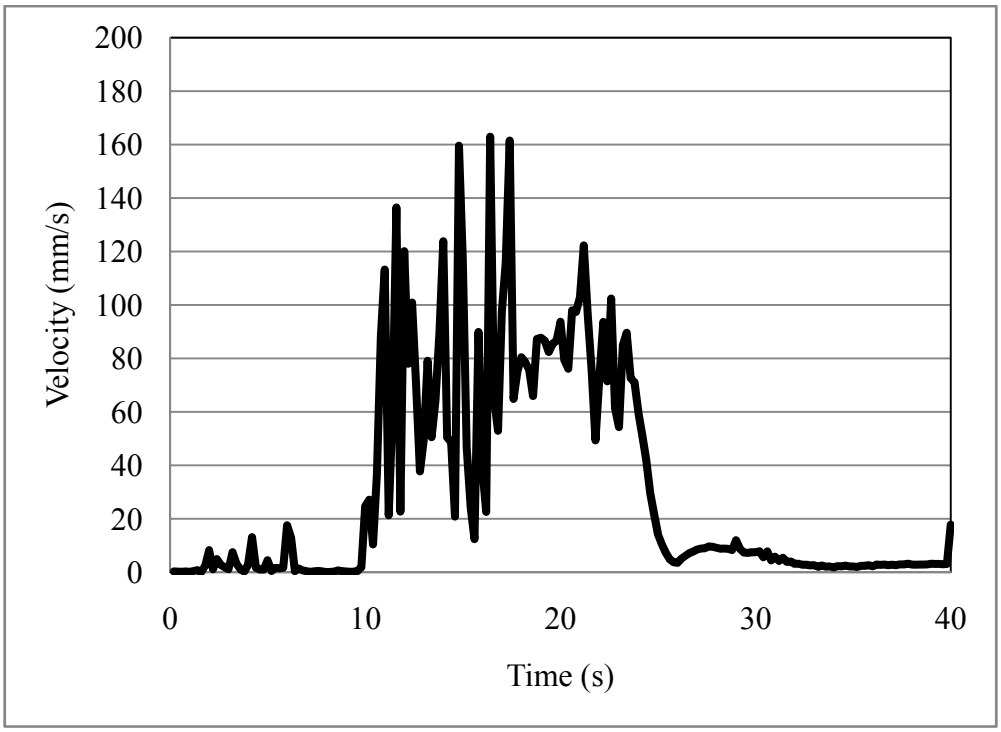

Figure C.18: Lower right velocity magnitude data for the 1.91 cm plate separation.

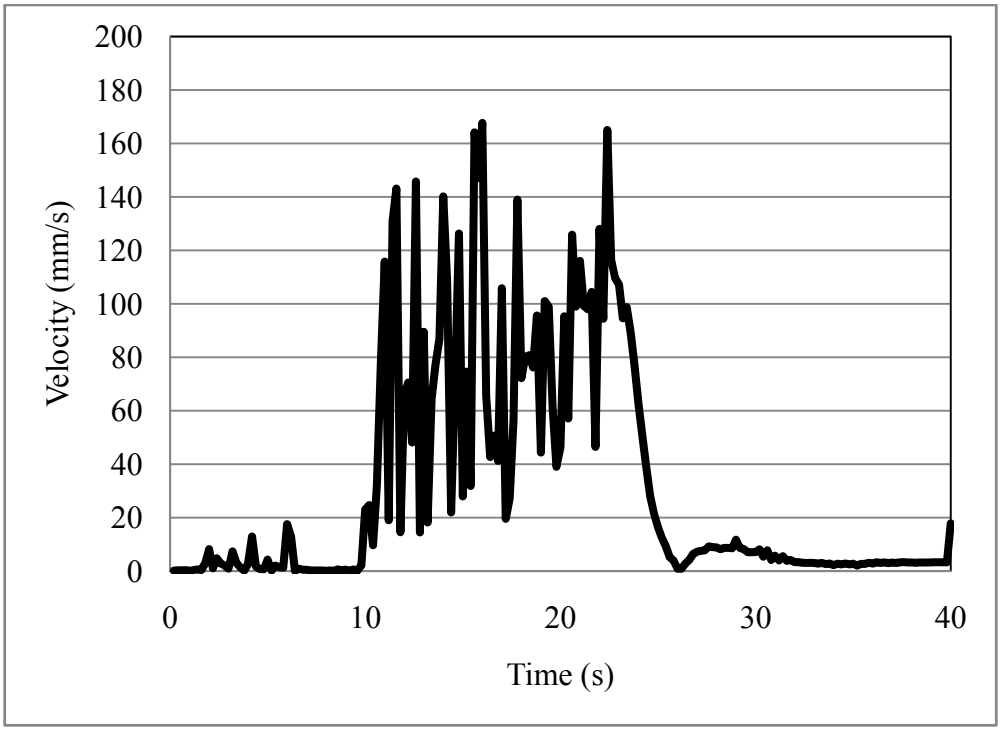

Figure C.19: Upper left velocity magnitude data for the 1.91 cm plate separation.

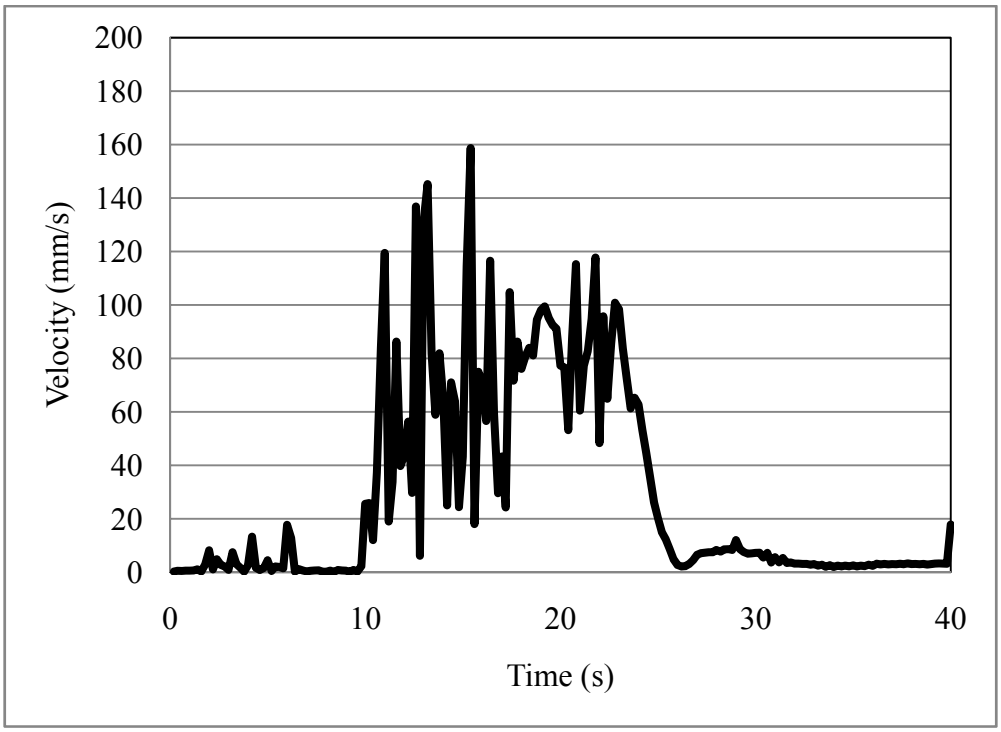

Figure C.20: Upper right velocity magnitude data for the 1.91 cm plate separation.

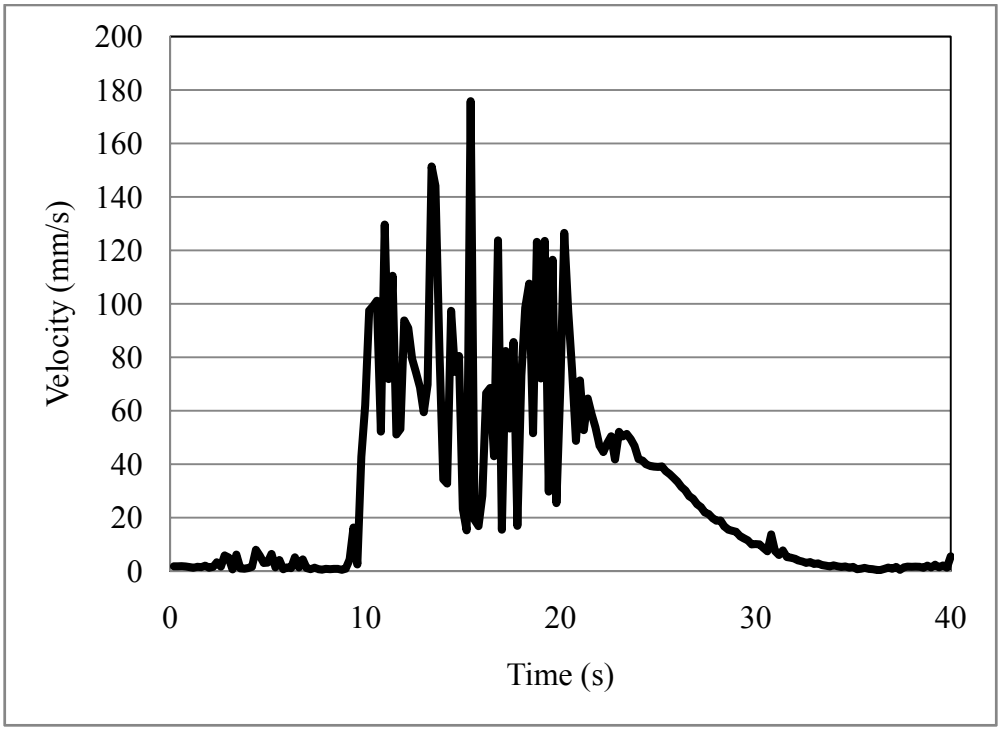

Figure C.21: Lower left velocity magnitude data for the 3.18 cm plate separation.

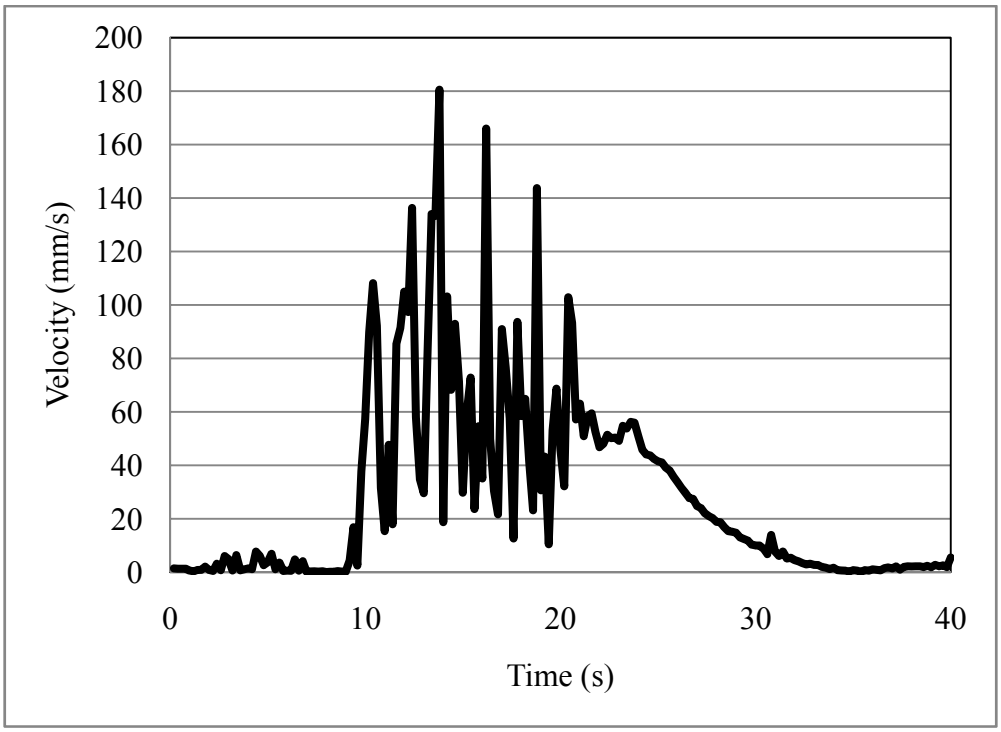

Figure C.22: Lower right velocity magnitude data for the 3.18 cm plate separation.

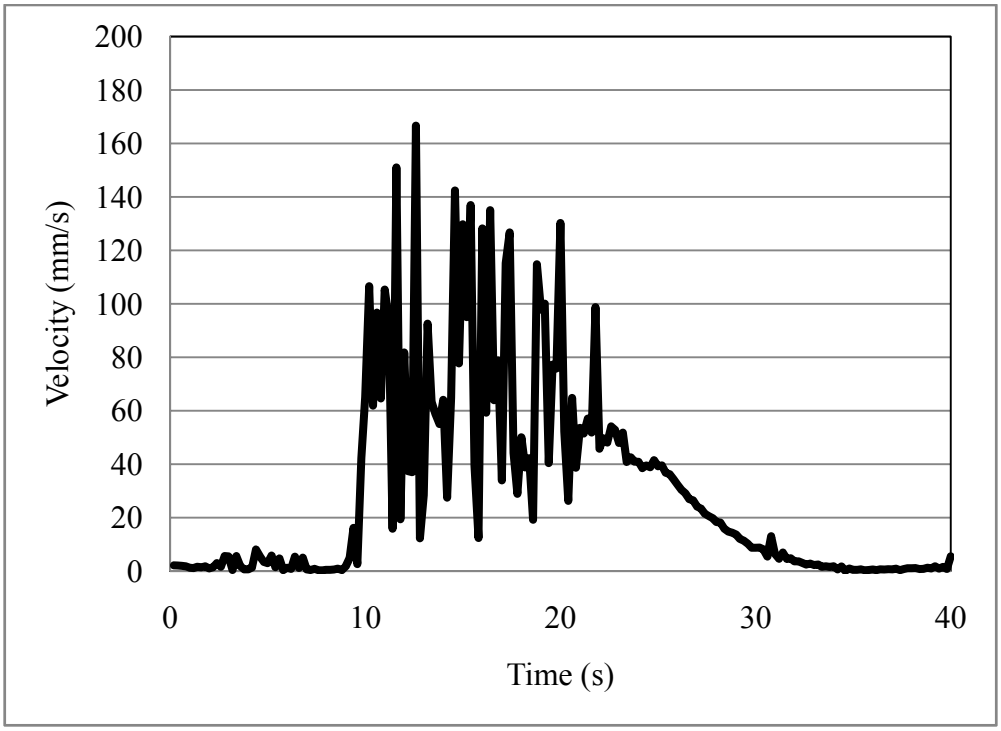

Figure C.23: Upper left velocity magnitude data for the 3.18 cm plate separation.

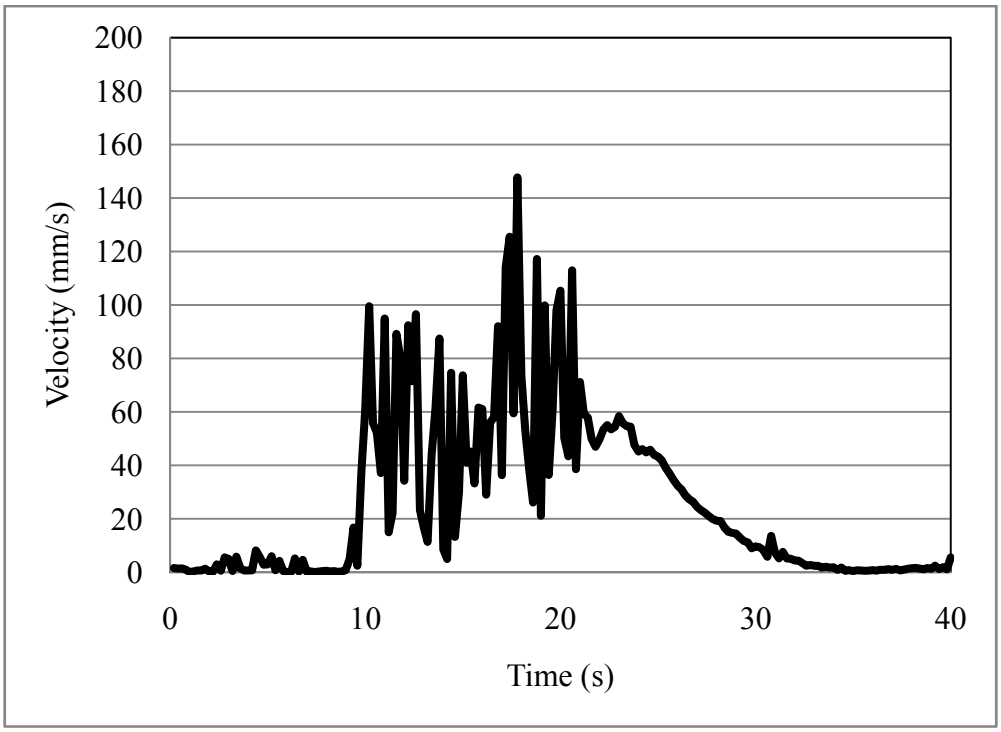

Figure C.24: Upper right velocity magnitude data for the 3.18 cm plate separation.

Appendix D – Model Development and Results Using FDS

D.1. Model Development in FDS

The FDS model was constructed to scale with the identical dimensions as those of the experimental apparatus (refer to Chapter 5). A layer of fluid cells four cells thick was added around the experimental apparatus with open pressure boundaries to ensure that the internal pressure of the model did not rise unrealistically. All geometric features present in the experimental apparatus were accounted for and included in the model representation. These features included the parallel plates, the walls of the experimental apparatus, the ventilation holes for the apparatus, the laser beam dump structure, and the exhaust housing, which was located on the exterior of the apparatus. Figure D.1 shows a diagram of the FDS model representation of the experimental apparatus.

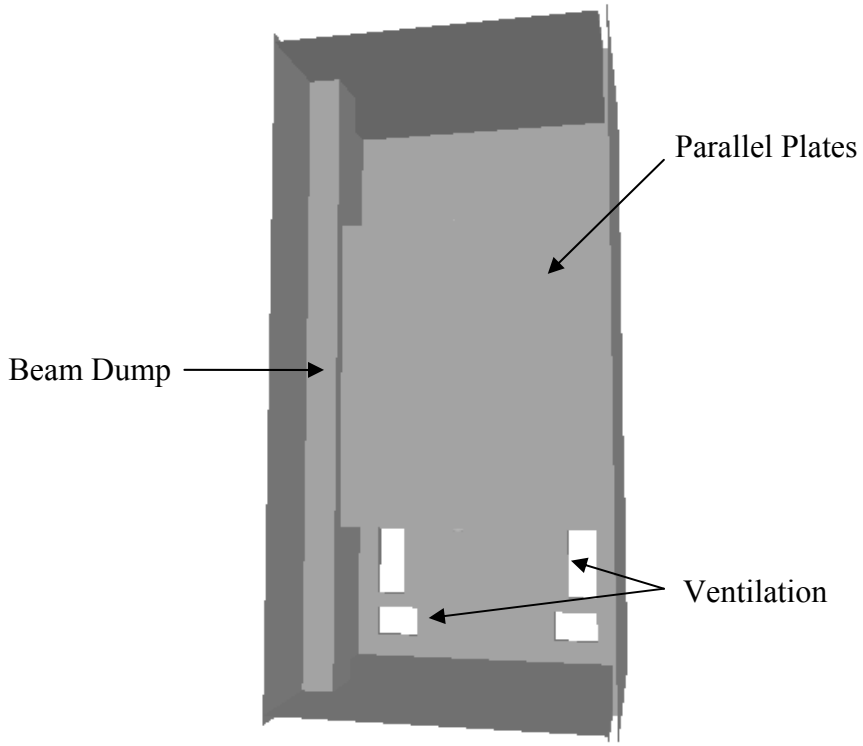

Figure D.1: FDS modelling representation of the experimental apparatus.

Due to the inability of the FDS code to fully represent a physical reconstruction of the inlet nozzle, an approximation of the boundary condition was made using several additional geometric features. These were introduced into the model to provide a means of expressing the flow of gas from the inlet. The geometric features were small, solid cell blockages placed within the experimental apparatus to provide a means for expressing the flow from the inlet gas boundary conditions. The approximation had to be used due to the lack of possible cell resolution in the vicinity of the inlet nozzle. Figure D.2 depicts the location and placement of the geometrical structures used in the model to anchor the boundary surfaces.

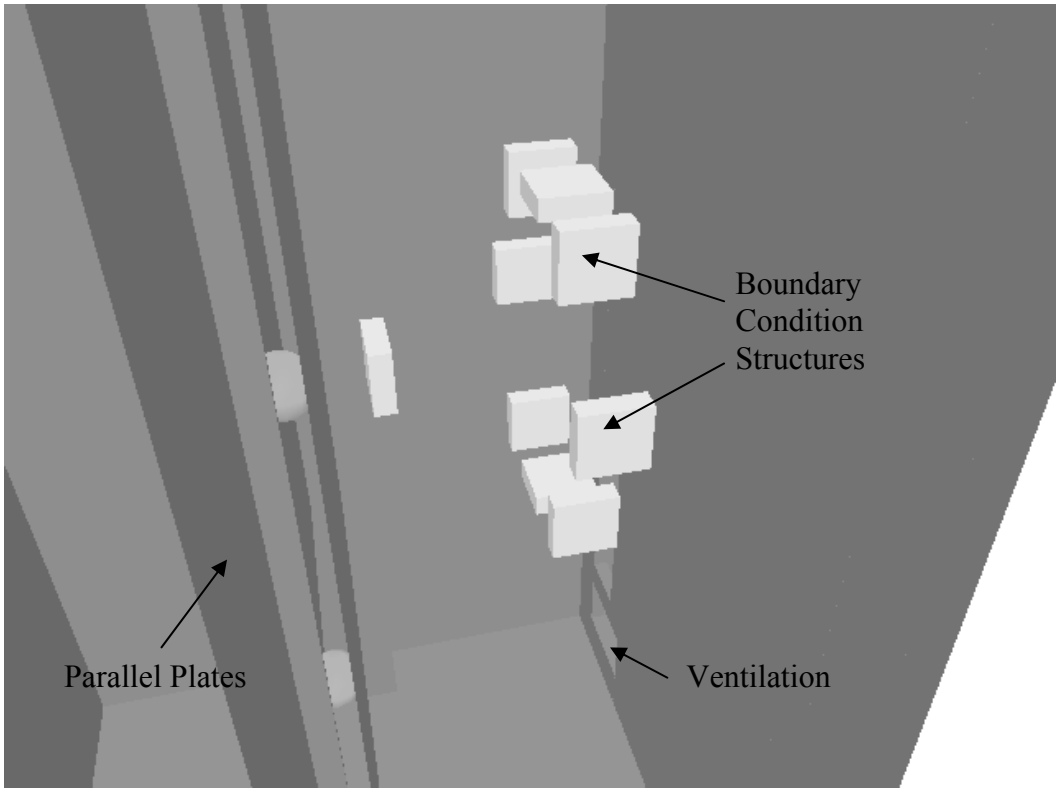

Figure D.2: Closer view of additional geometrical surfaces added into the FDS model for boundary condition placement.

The lack of possible cell resolution was due to inherent computational issues within FDS. The length scales needed to describe the inlet nozzle in space are on the order of millimeters. If those scales were used as a basic square cell in FDS, the resolution within the model would be on the order of 250 million cells. This level of cell

density is far beyond modern computing power. The adaptive meshing features of FLUENT provide a more ideal solution when building a computational mesh capable of recreating the experimental apparatus.

Overall, the FDS model created contained 1,013,760 cells. The largest cells were approximately 1.27 cm in the x, y, and z directions. The resolution was increased in the local modelled area around the plates to more accurately describe the flow field. The first increase in cell density occurred just outside of the area where the parallel plates were modelled. In this region, which was symmetrical on both sides of the parallel plates, the cells were 0.635 cm in the x, y, and z directions. A second increase occurred in the local area directly between the parallel plates. In this region, the cell size was further reduced to 0.318 cm in the x, y, and z directions. Figure D.3 illustrates the increasing cell density of the grid used in the FDS models.

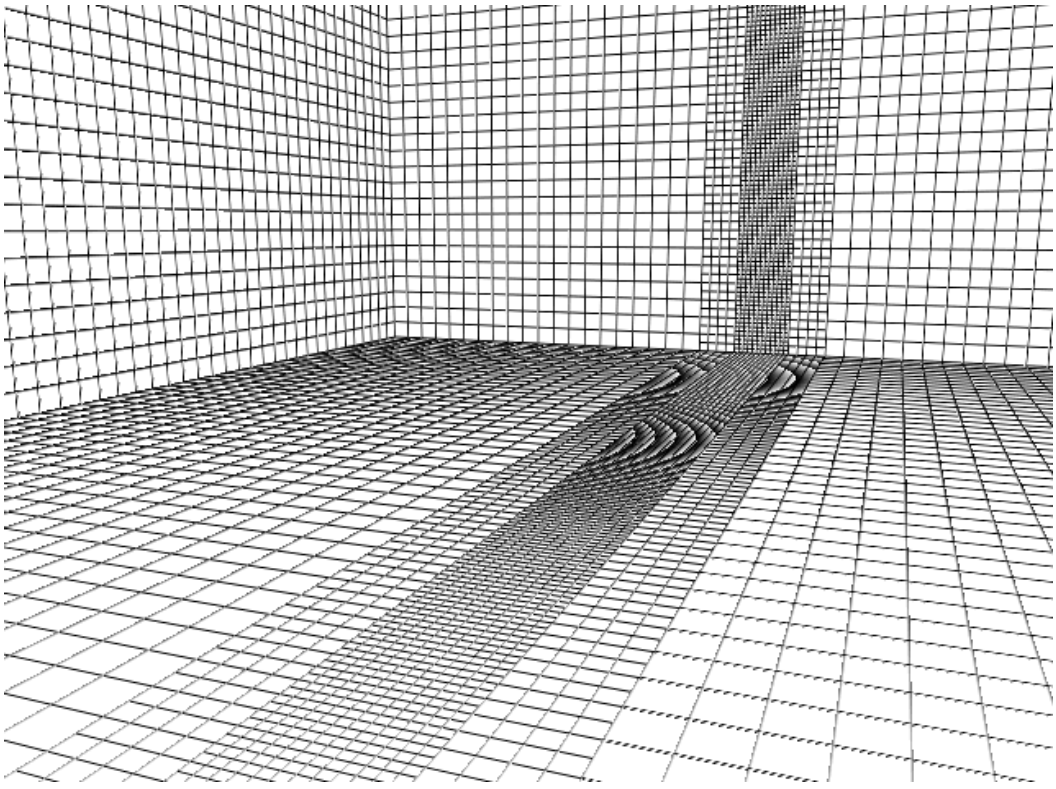

Figure D.3: Grid layout and increasing cell density in the local vicinity of the parallel plates for the FDS model.

All of the model variations were conducted using the default standard LES solver routine. The resulting data was transient in nature. The model tracked the flow of the inlet gas mixture (e.g., nitrogen and nitrogen dioxide mixture) over a 40-second period. The initial time-step was 0.02 seconds.

D.2. FDS Model Results

The use of the FDS code for modelling this particular application was problematic. In general, the FDS code could not account for the range of boundary conditions necessary to provide an adequate solution to the transport aspect of the experiment designed in this work. To arrive at this conclusion, a matrix of various run conditions was developed. This matrix is presented in Table D.1.

Run #	Plate Separation (cm)	Slip Condition	Smagorinsky Number	Cell Density Between Plates	Hood Flow Condition (m^3/s)	Influx Condition	32-bit or 64-bit fds.exe
box01	1.27	0.5	0.20	8	0.00	Original Ramp	32-bit
box02	1.27	0.5	0.20	8	0.51	Original Ramp	32-bit
box03	1.27	0.5	0.20	8	0.00	Corrected Ramp	32-bit
box04	1.27	1.0	0.20	8	0.00	Corrected Ramp	32-bit
box05	1.27	1.0	0.20	16	0.00	Corrected Ramp	64-bit
box06	1.27	1.0	1.00	8	0.00	Corrected Ramp	32-bit
box07	1.27	1.0	0.30	8	0.00	Corrected Ramp	32-bit
box08	1.27	0.5	0.10	8	0.00	Corrected Ramp	32-bit
box09	1.91	0.5	0.20	8	0.00	Original Ramp	32-bit
box10	1.91	0.5	0.20	8	0.51	Original Ramp	32-bit
box11	1.91	0.5	0.20	8	0.00	Corrected Ramp	32-bit
box12	1.91	1.0	0.20	8	0.00	Corrected Ramp	32-bit
box13	1.91	1.0	0.20	16	0.00	Corrected Ramp	64-bit
box14	1.91	1.0	1.00	8	0.00	Corrected Ramp	32-bit
box15	1.91	1.0	0.30	8	0.00	Corrected Ramp	32-bit
box16	1.91	0.5	0.10	8	0.00	Corrected Ramp	32-bit
box17	3.18	0.5	0.20	8	0.00	Original Ramp	32-bit
box18	3.18	0.5	0.20	8	0.51	Original Ramp	32-bit
box19	3.18	0.5	0.20	8	0.00	Corrected Ramp	32-bit
box20	3.18	1.0	0.20	8	0.00	Corrected Ramp	32-bit
box21	3.18	1.0	0.20	16	0.00	Corrected Ramp	64-bit
box22	3.18	1.0	1.00	8	0.00	Corrected Ramp	32-bit
box23	3.18	1.0	0.30	8	0.00	Corrected Ramp	32-bit
box24	3.18	0.5	0.10	8	0.00	Corrected Ramp	32-bit

Table D.1: Matrix of various FDS runs used in investigation.

In general, the above parameters could not be adjusted enough to compensate for the poorly expressed boundary condition of the high-momentum jet nozzle. The extremely high velocities of the gas release through the small nozzle openings could not be accurately represented by the creation of a square boundary vent to account for each jet downstream issuing from the nozzle. Additionally, the modifications made to the Smagorinsky number and the slip conditions did not result in an improvement in the results.

With regard to the slip conditions, the modelling results seemed to indicate that the results for the flow conditions between the plates improved with an adjustment to free-slip conditions. Unfortunately, free-slip conditions between the plates also resulted in the gas arriving much earlier between the plates than was expected from the experimental results, which resulted in increasingly worse predictions.

With regard to the Smagorinsky number, the modelling results appeared to show that modification of this parameter does not produce better results. The perturbation of this parameter may provide balance between two competing aspects of the problem: a high-momentum, turbulent, multiple-jet flow at the beginning of the modelled scenario and a low-momentum, laminar flow between the plates towards the end of the experimental scenario. By varying the Smagorinsky number to improve the flow results for the turbulent flow, the laminar flow result began to suffer. Similarly, by adjusting the Smagorinsky number to better capture the laminar flow between the plates, the initial turbulent jet was not well predicted, which again resulted in grossly wrong predictions of the steady-state concentrations and flow field.

Figures D.4 through D.10 provide some illustrative examples of the general trends based on the predictions made by FDS for the concentration of the nitrogen dioxide. All of the results are for the 1.27 cm plate separation distance and are labeled according to Table D.1.

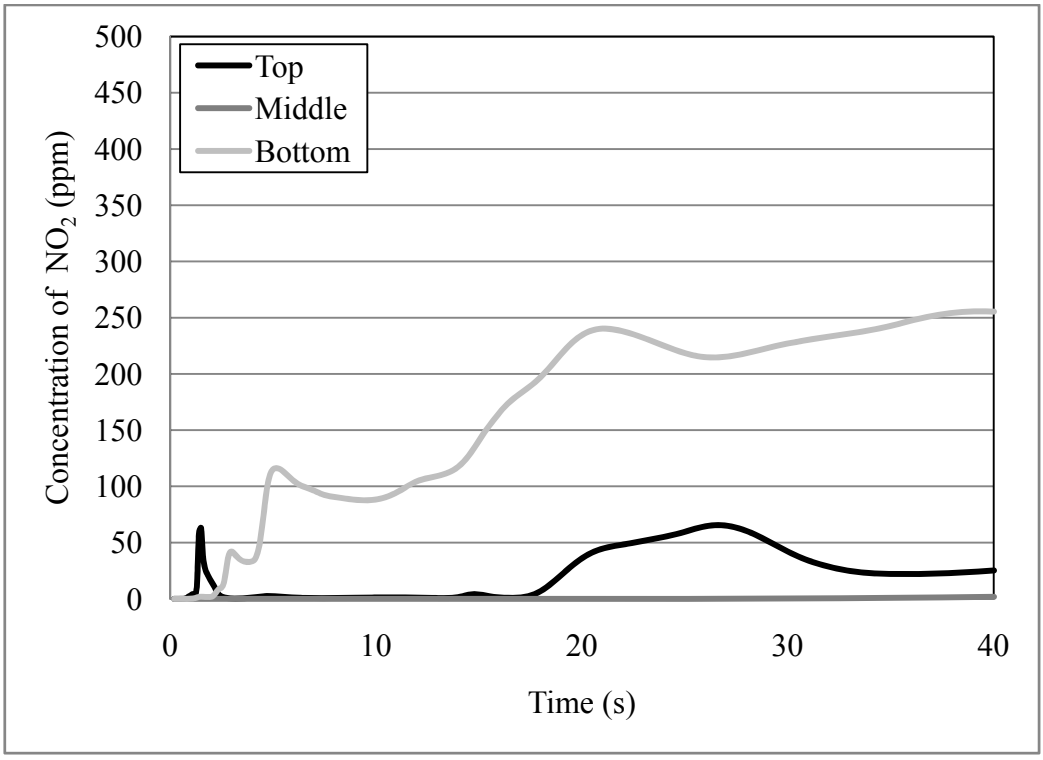

Figure D.4: FDS predictions of NO_2 at the 1.27 cm plate separation for case box01.

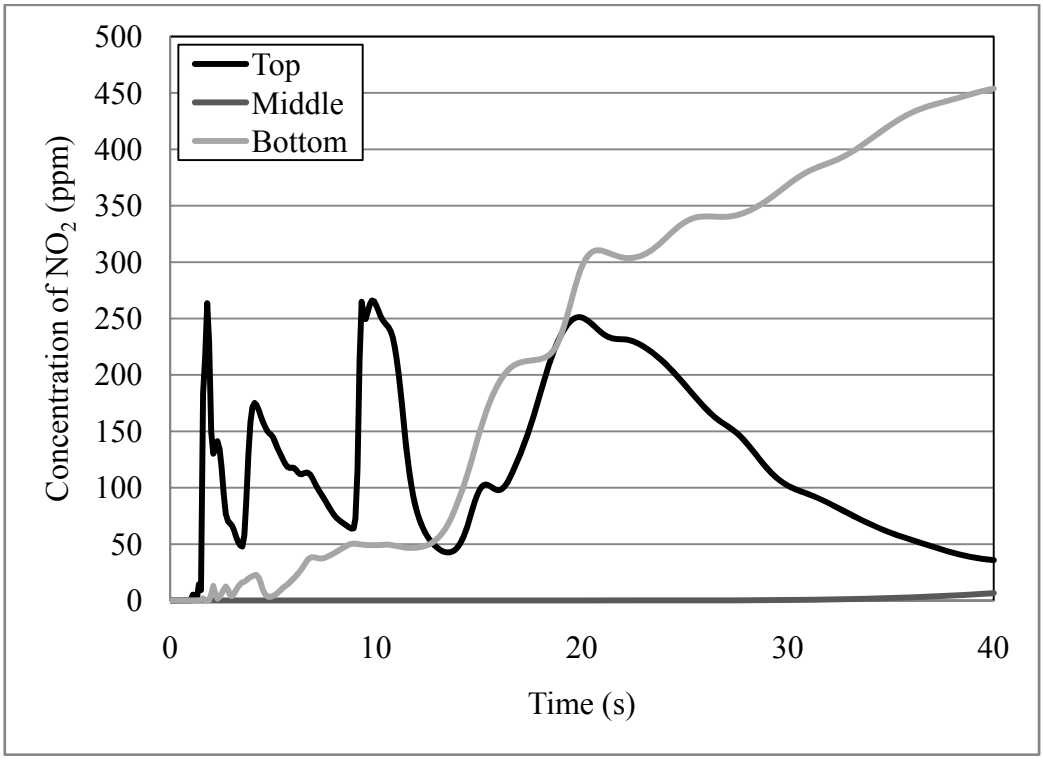

Figure D.5: FDS predictions of NO_2 at the 1.27 cm plate separation for case box03.

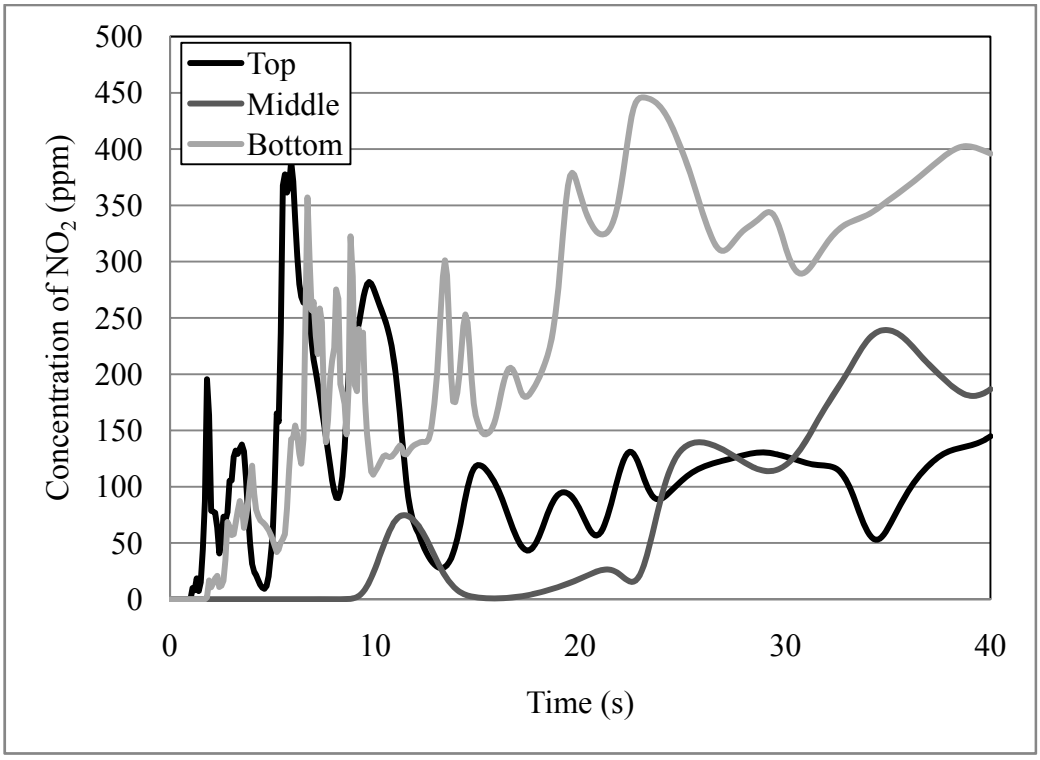

Figure D.6: FDS predictions of NO_2 at the 1.27 cm plate separation for case box04.

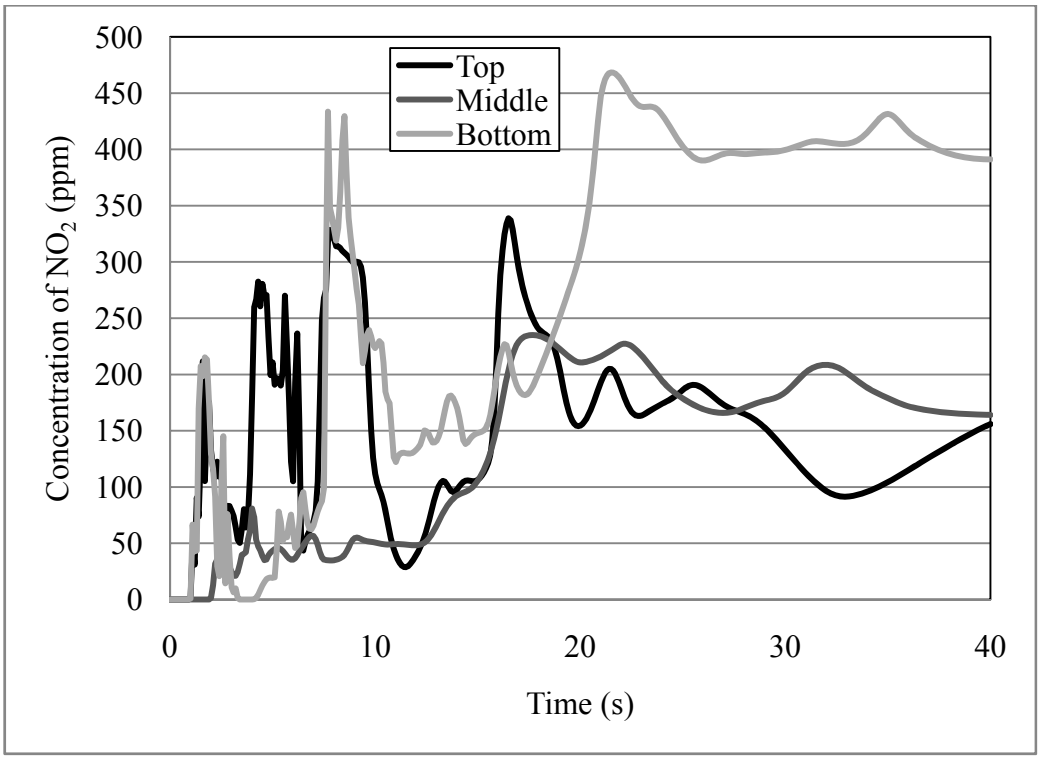

Figure D.7: FDS predictions of NO_2 at the 1.27 cm plate separation for case box05.

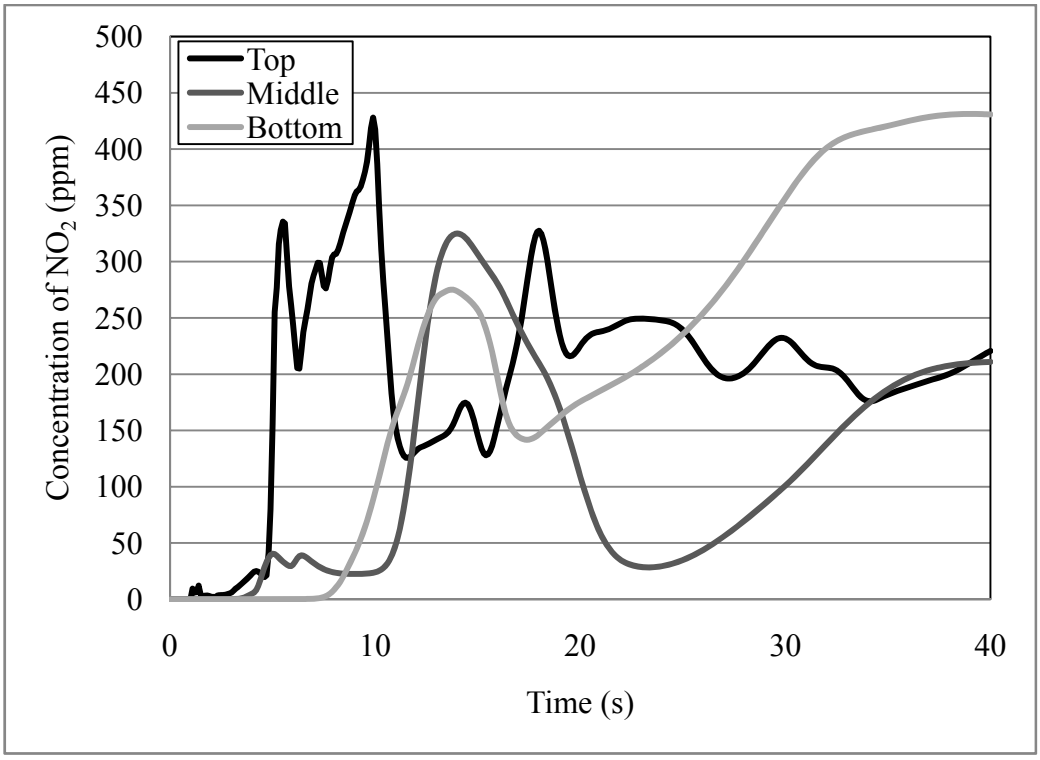

Figure D.8: FDS predictions of NO_2 at the 1.27 cm plate separation for case box06.

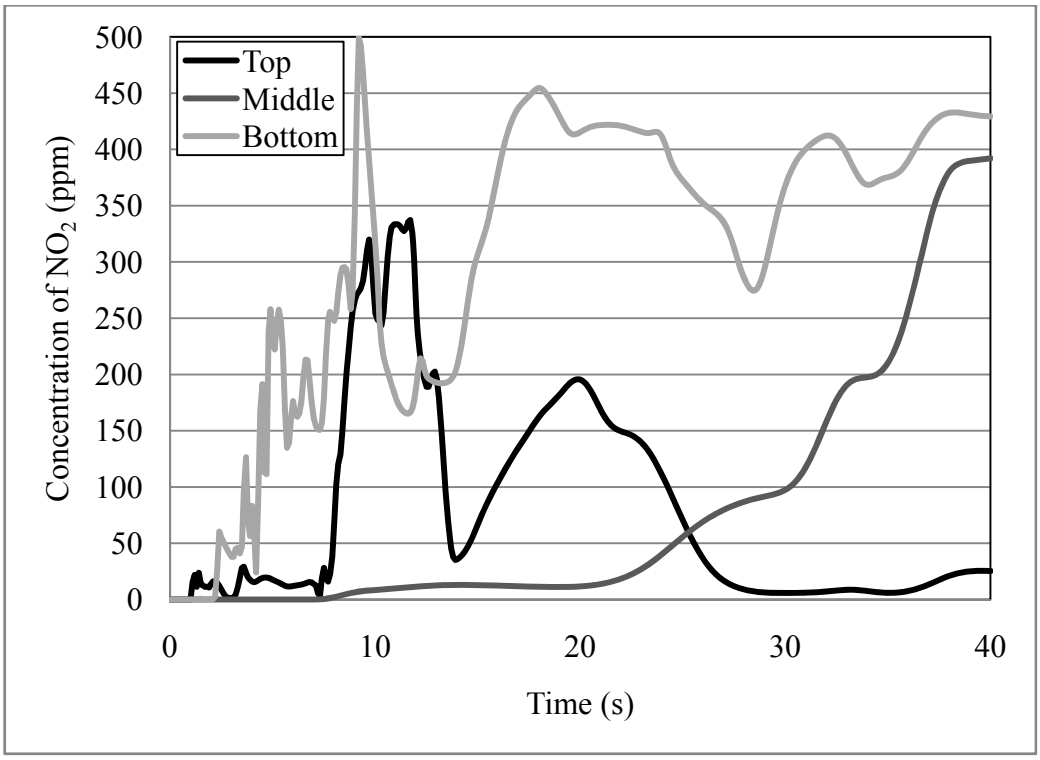

Figure D.9: FDS predictions of NO_2 at the 1.27 cm plate separation for case box07.

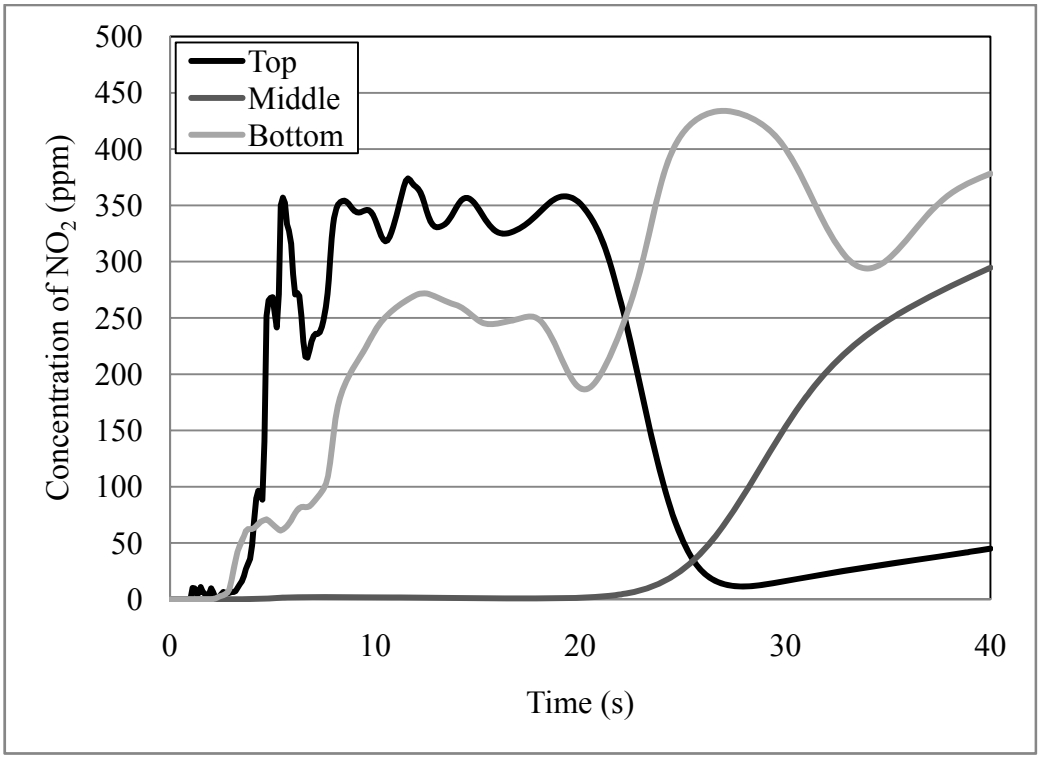

Figure D.10: FDS predictions of NO_2 at the 1.27 cm plate separation for case box08.